PROGRESSIVE COLLAPSE OF TITANIUM ALLOY MICRO-LATTICE STRUCTURES MANUFACTURED USING SELECTIVE LASER MELTING

Thesis submitted in accordance with the requirements of the

University of Liverpool for the degree of Doctor in Philosophy

by

Rafidah Hasan

February 2013

ABSTRACT

The starting point for this research was the viability of the Selective Laser Melted (SLM) titanium alloy Ti-6Al-4V micro-lattice structure for applications in Foreign Object Impact (FOI) situations in aerospace sandwich constructions. To this end, the mechanical behaviour of single struts and the compression behaviour of micro-lattice blocks were studied. Detailed characterizations of dimensional accuracy, circularity and microstructure, as well as clarifications of deformation behaviour and failure of single manufactured struts under tensile loading were done. The variability in stress-strain curve of struts which was derived using compliance correction method was found to arise from the variations in strut diameters, due to outer surface roughness of the material. Post-manufacture heat-treatment processes improved the surface roughness and variations of strut diameters as well as the microstructure of the α/β titanium alloy, hence reduced the scatter in the stress-strain curve of single struts. The deformation of the SLM Ti-6Al-4V micro-lattice blocks with Body Centred Cubic (BCC) structure was elucidated using combined experimental studies and computational analysis. Detailed analysis of geometry and diameter variations in struts of the micro-lattice blocks were done and compared to that of single manufactured struts. Node formation and manufactured quality of the micro-lattice structure were revealed from a 45° angle diagonal plane of sectioned block. The compressive deformation behaviour of the BCC micro-lattice block structures was then studied. Effects of different manufacturing routes and parameters as well as post-manufacture treatments in the compressed micro-lattice structures were discussed. Finite element analysis was performed using a validated model of BCC micro-lattice unit cell. The progressive collapse of the micro-lattice block structure was shown to be comparable with the prediction from the finite element model of a unit cell. The numerical simulation was then used to quantify the effect of parent material properties on block collapse. In this way, the relations between SLM manufacturing route, material properties and structural performance are highlighted.

ACKNOWLEDGEMENT

Thanks to the one and only God for giving a good health and mind which enable me to complete this thesis. May peace and blessings be upon the one after whom there is no other Prophet.

I would like to express my deepest appreciation to my dedicated Supervisor, Dr. R.A.W. Mines, who gave me the opportunity to do this research and spent his time and offered for many ideas, suggestions and guidance during the entire study.

Appreciation is also extended to all lecturers, staffs and colleagues at the Department of Engineering and the University of Liverpool, especially to Prof. W.J. Cantwell, Dr. P. Fox, Dr. C.J. Sutcliffe, Dr. M.I.H. Smith, Dr. Y. Shen, Dr. S. Tsopanos, Mr. S. Pennington, Mr. D. Atkinson, Dr. P. Beahan, Mr. P. Cross (Chemistry Department), Dr. T. Joyce, Dr. Y. Zhao, Dr. L. Zhang, Dr. K. Dawson, Ms. D. Bain, Ms. L. Swain, Mr. C. Addison, Mr. R. Gumruk, Mr. M.R. Rejab, Ms. S.H.S.M. Fadzullah and Dr. M.Z. Hassan. To many more that I missed to mention, all your helps and supports are highly appreciated. Special thanks to my special friends, Dr. Z. Shamsudin (Sheffield) and Dr. R. Ismail (Glasgow), for their prayers, thoughts and motivations.

I am also grateful for the scholarship, financial support and encouragement from The Ministry of Higher Education, Malaysia and my employer, Universiti Teknikal Malaysia Melaka (UTeM).

Finally, I would like to thank my beloved husband, Azman, my brilliant children, Muhammad and Ibrahim, and all family members in Malaysia, especially my Mom and Dad, for their love, patience and encouragement at all times.

CONTENTS

CHAPTER 3: INVESTIGATION ON PROPERTIES AND BEHAVIOURS OF SLM Ti-6Al-4V BCC MICRO-LATTICE BLOCKS

CHAPTER 1: INTRODUCTION, LITERATURE REVIEW AND OVERVIEW OF MATERIALS

1.1 AIMS AND OBJECTIVES OF RESEARCH

This research aims to study the behaviour and properties of Selective Laser Melting (SLM) Titanium alloy Ti-6Al-4V micro-lattice structure for sandwich construction in aerospace applications. The following objectives were identified:

- To investigate the viability of the SLM Ti-6Al-4V micro-lattice structure application in Foreign Object Impact (FOI) of aerospace sandwich construction.
- To quantify the quality of microstructure and material as well as dimensional accuracy and circularity of Ti-6Al-4V struts manufactured by the SLM.
- To measure the mechanical properties of SLM Ti-6Al-4V struts and to obtain stress-strain data of the SLM Ti-6Al-4V micro-lattice block with selected manufacturing parameters. Post-process heat-treatment was applied to improve the material properties.
- To analyze the progressive collapse of the Body Centered Cubic (BCC) SLM Ti-6Al-4V micro-lattice structure by studying the elastic, plastic and rupture deformation of finite element model of a unit cell.

1.2 GENERAL INTRODUCTION TO RESEARCH

The increasing application of sandwich structures in wide areas including aerospace, marine and automotive industries has led to numerous studies on the improvement of existing materials as well as the development of new skin, adhesive and core materials of the structures. Mechanical properties of skin and core have been extensively studied in designing high performance sandwich structures, especially during foreign object impact such as tyre debris or bird strike. Studies in core

materials of sandwich structure are mostly aimed to improve energy absorption performance of the materials, thus enhancement of the crash performance of the whole sandwich structure. The most studied core material is honeycomb, specifically aluminium honeycomb, which offers high stiffness and strength-to-weight ratio, especially in the 'out-of-plane' direction. Cellular materials such as foams also offer good energy absorption property. This type of core material has been widely studied, which has led to great understanding of the material [Gibson and Ashby (1999)]. Another type of core material that is increasingly attracting the interest of researchers is lattice materials, which was initiated from the approximation approach of microstructural models for foams. With current development of various manufacturing techniques, especially the use of rapid prototyping manufacturing technology, lattice material down to micrometre scale can be produced, and called micro-lattice material. Figure 1.1 shows the difference of physical appearance between honeycomb, open-cell foam, and micro-lattice structure.

Figure 1.1: Different physical appearance between materials; from left: honeycomb, open-cell foam (duocell), micro-lattice structure (pictures are from own collections)

Advanced manufacturing techniques such as the rapid prototyping selective laser melting (SLM) technique have strongly contributed to the initial study on the metallic micro-lattice structure at the University of Liverpool. Works have been carried out in studying the mechanical properties, crush behaviours, as well as impact properties of the SLM stainless steel (SS316L) and titanium alloy (Ti-6Al-4V) micro-lattices [Mines (2008), Santorinaios et al. (2006), McKown et al. (2007), Mines et al. (2008), McKown et al. (2008)]. Previous work showed that the specific strength of Ti-6Al-4V micro-lattice structures is competitive with that of aluminum

honeycomb [Mines et al. (2009)] and this is especially true if the energy density is high (higher laser powers and long exposure times) during the SLM process. In previous work on stainless steel (SS316L) [Tsopanos et al. (2010)], it has been shown that laser power and exposure has influence on strut diameter and properties. In the case of Ti-6Al-4V, no systematic study has been completed as yet, but from a preliminary study, a power of 200 Watts (W) and an exposure time of 1000 micro-seconds (μs) gave an acceptable quality of micro-lattice [Shen (2009)]. This combination of parameters for the Ti-6Al-4V micro-lattice structure core resulted in a more localized impact area in the sandwich constructions for foreign object impact as compared to aluminum honeycomb core [Hasan et al. (2010)]. A more localized impact area means that a smaller area is affected by impact damage, and this is preferred by the aircraft manufacturer [Morteau and Fualdes (2006)]. However, it has been observed that the impacted area of the Ti-6Al-4V micro-lattice structure core experienced surprisingly 'brittle-like' failure, which macroscopically, the failed struts showing almost flat fracture surfaces. Since plasticity is an important criterion for energy absorption in load-bearing structure performance, especially in aerospace applications, the failure of these SLM Ti-6Al-4V micro-lattice structures needs to be further studied and analyzed.

This thesis reports on research undertaken to investigate viability of SLM Ti-6Al-4V micro-lattice structure as core material in sandwich construction, especially for foreign object impact in aerospace applications. The study has undertaken the task of clarifying and quantifying issues related to quality, dimensional accuracy, circularity, as well as microstructure of material, where all of these are related to the previously observed failure. Mechanical properties of the material were measured from the SLM Ti-6Al-4V struts, and stress-strain data was determined for the micro-lattice block material with selected manufacturing parameters. Post-process heat-treatment for the material was introduced, in order to improve properties of SLM Ti-6Al-4V micro-lattice structure with similar manufacturing parameters. To complete the research, the progressive collapse of SLM Ti-6Al-4V Body Centred Cubic (BCC) micro-lattice structure was studied. For this task, simulation analysis of a BCC unit cell was carried out using Abaqus software.

1.2.1 General Outline of Research

A literature review for the current research is described in the following section. In Chapter 2, details on the SLM Ti-6Al-4V struts used in this research are presented. This includes investigation and discussion on issues related to material geometry, dimensional accuracy, microstructure and quality of material that influence the structure formation and performance of micro-lattice blocks. Post-process heat-treatment is suggested to improve the mechanical properties of the material. Clarifying all these issues is the main original contribution of this research, as this will improve the understanding of the SLM Ti-6Al-4V micro-lattice's strange failure that was mentioned in previous studies. Further details on the manufacturing process and procedures, and accuracy of manufactured node and strut in BCC micro-lattice arrangement are discussed in Chapter 3. Detailed descriptions on macro and micro deformation and failure of node and strut, with and without heat-treatment are also discussed. In Chapter 4, the progressive collapse of BCC SLM Ti-6Al-4V micro-lattice unit cell is modelled using Abaqus finite element software. The model was modified from a validated model of SLM SS316L micro-lattice structure, developed in another study. Finally, in Chapter 5, the main conclusions from the investigations are drawn together and suggestions for further work are put forward.

1.3 LITERATURE REVIEW

An extensive number of publications relating to cellular material and micro-lattice structure produced from a variety of manufacturing routes are available. However, a discussion on all these published works would result in a review which is too general on the issues pertinent to the present work. Hence discussions will instead be limited to selected publications with a focus on research related to:

- general aspect of cellular structure, with emphasis on the open-cell type
- the SLM process, with the emphasis on producing porous material and micro-lattice structure

- other competing processes in producing micro-lattice materials
- lattice structures, with the emphasis on mechanical properties such as strength, stiffness, and topology of material
- static, impact, and Foreign Object Impact (FOI) of SLM micro-lattice structure
- titanium alloy Ti-6Al-4V, with the emphasis on plasticity and failure theory of the material

1.3.1 Cellular Structure

As given by Gibson and Ashby (1999), cellular solids are made up of interconnected networks of solid struts or plates which form the edges and faces of cells. Cellular materials can be natural such as woods and bone; as well as man-made material such as polymeric foams that can be found anywhere includes disposable coffee cups. Two-dimensional cellular materials are called honeycomb while three-dimensional polyhedral cells are called foams. Foam made with cell edges only is called open-cell foam, and foam with sealed off cell is called closed-cell foam. Some foam is partly open and partly closed. The open and closed-cell configurations determine the porosity of cellular structure. A most important feature of cellular solid is its relative density ρ^*/ρ_s ; that is, the density of cellular material, ρ^*, divided by that of the solid from which the cell walls are made, ρ_s . In ideal cellular materials, plastic yielding and collapse occur simultaneously, which result in a distinct yield strength coincident with a plateau flow stress [Gibson and Ashby (1999)]. However, it was mentioned by Evans et al. (1998) that in commercial materials, yielding and collapse are not coincident. Local yielding initiates at cell nodes almost immediately upon loading. This is followed by rapid strain hardening, resulting in narrow deformation bands that extend across the test configuration.

While Gibson and Ashby (1999) discussed wide range of data analysis on cellular materials including wood, bone, metals, ceramics, glasses and composites, Banhart

(2001) compiled research focussing on cellular metallic materials. There are four conditions that have to be considered when assigning appropriate cellular metallic materials for applications, which are; morphology, metallurgy, processing and economy. The morphology, a crucial factor, includes type and amount of porosity needed, size and scale of porosity desired, and total internal surface area of cellular material required. Degrees of 'openness' of cellular structures depend on the applications, whether it is 'functional' or 'structural'. A 'very open' cell is more applicable for 'functional' application such as for high rate fluid flow in heat exchangers, while a 'completely closed' cell is more efficient for 'structural' application such as for load-bearing components in aircrafts. Figure 1.2 maps out the type of porosity required for various application fields. Meanwhile, the second important factor is the metallurgy, which means selecting suitable metals or alloys that can be manufactured according to given type of cellular structure. For example, light weight alloys such as aluminium, magnesium or titanium foams are preferred for structural, load bearing parts applications. Finally, the processing and cost are also important considerations in selecting cellular metallic materials, and therefore, any technology adapted to produce any shape of the material should offer reasonable price of manufactured products.

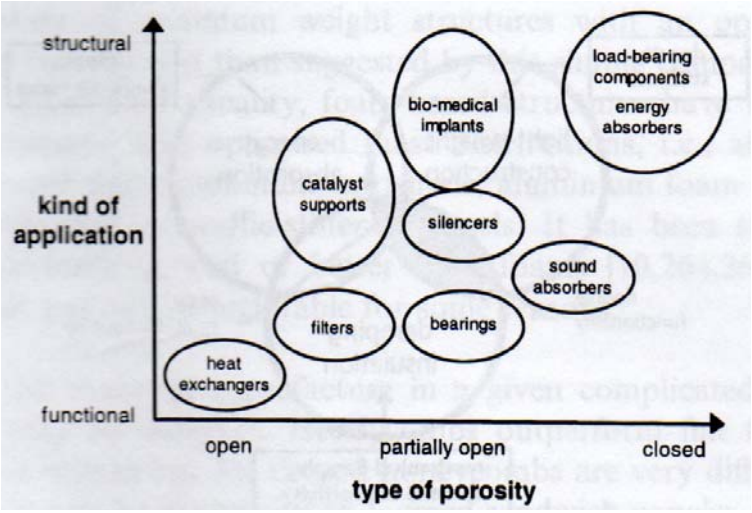

Figure 1.2: Application of cellular metallic materials grouped according to type of porosity [Banhart (2001)]

Not much is stated in earlier literature about another type of cellular material which is called a lattice structure. Later, Rehme (2010) highlighted that the three-dimensional periodicity of cellular material yields a lattice structure or also called truss structure. Micro-sized lattice structure has another term called micro-lattice structure, where, it is an approximation from the open-cell foam cellular structure such as found in cancellous bone. Luxner et al. (2009) had analysed both regular (periodic) and disordered (stochastic) open-cell structure of simple cubic arrangements of struts. The study suggested that highly ordered lattices are stronger than more disordered ones, but they are extremely sensitive to strain localization, therefore, accumulate high amounts of localized damage in certain orientation. However, Rehme (2010) presented contradictory statements, stating that better mechanical properties can be expected from regularly arranged cell structures than from randomly distributed formations which show low connectivity of the joints due to a small number of cell walls or struts linked in respective edges or vertices. Similar to Luxner et al. (2009), Mullen et al. (2009) also reported that randomization in cell structures enhance the mechanical properties of the structures by eliminating the natural fault planes that commonly occur in ordered structures. Producing randomized or stochastic structures is sophisticated; Mullen et al. (2009) applied a layer based manufacturing process which is the Selective Laser Melting (SLM) process, since the technology has the unique ability that permits the manufacture of the structures. Figure 1.3 maps out the classification of cellular material, adapted from Rehme (2010).

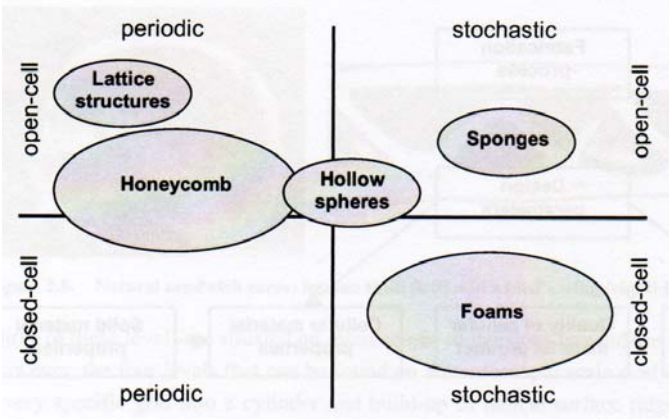

Figure 1.3: Classification of cellular materials [Rehme (2010)]

1.3.2 Selective Laser Melting

Selective Laser Melting (SLM) is a process which belongs to Rapid Manufacturing (RM), which directly produces end-use products or parts. The RM is a direction of Rapid Prototyping (RP) technology, other than Rapid Tooling (RT) [Yadroitsev (2009)]. The SLM name emerged after the Selective Laser Sintering (SLS) process, when powder metals experience complete melting rather than sintering or partial melting. This is a technological evolution of Laser Freeform Fabrication (LFF), which utilizes laser beam in fusing together powder particles [Rehme (2010)]. Early research on fully melted powder particles aimed to achieve a nearly full density. Kruth et al. (2004) reported that this technology can realize near net-shaped products which can avoid wastage of material, compared to machined parts from bulk block material. A wide range of metal powders can be processed using the SLM including stainless steel, copper, nickel, chromium, titanium as well as superalloys.

The development of systems using laser beams to fuse metal powder in the manufacture of solid objects was summarized by Yadroitsev (2009). Figure 1.4 lists the early inventors in the development of the system and the founding years of companies which use the process. Currently, there are five leading companies which produce equipment for the SLM of metal powders which use scanning laser beam to build up 3-dimensional shapes. The companies are EOS GmbH, MTT Technologies Group, 3D Systems Corporation, Concept Laser GmbH and Phenix Systems [Yadroitsev (2009)]. Although the same laser beam concept is applied, variations in systems and machine performances could result in different properties of produced parts from equipments supplied by different companies. In this study, the SLM250 Realizer from the MTT Technologies Group was used in the manufacture of the Ti-6Al-4V micro-lattice specimens. There are other systems supplied by the MTT Technologies Group, and the systems from this company are well suited for a broad range of medical, dental, aerospace, automotive, electronics and military applications as well as for cooling and conformal cooling applications that require accurate, fully dense metal parts produced from a wide selection of metals [Yadroitsev (2009)].

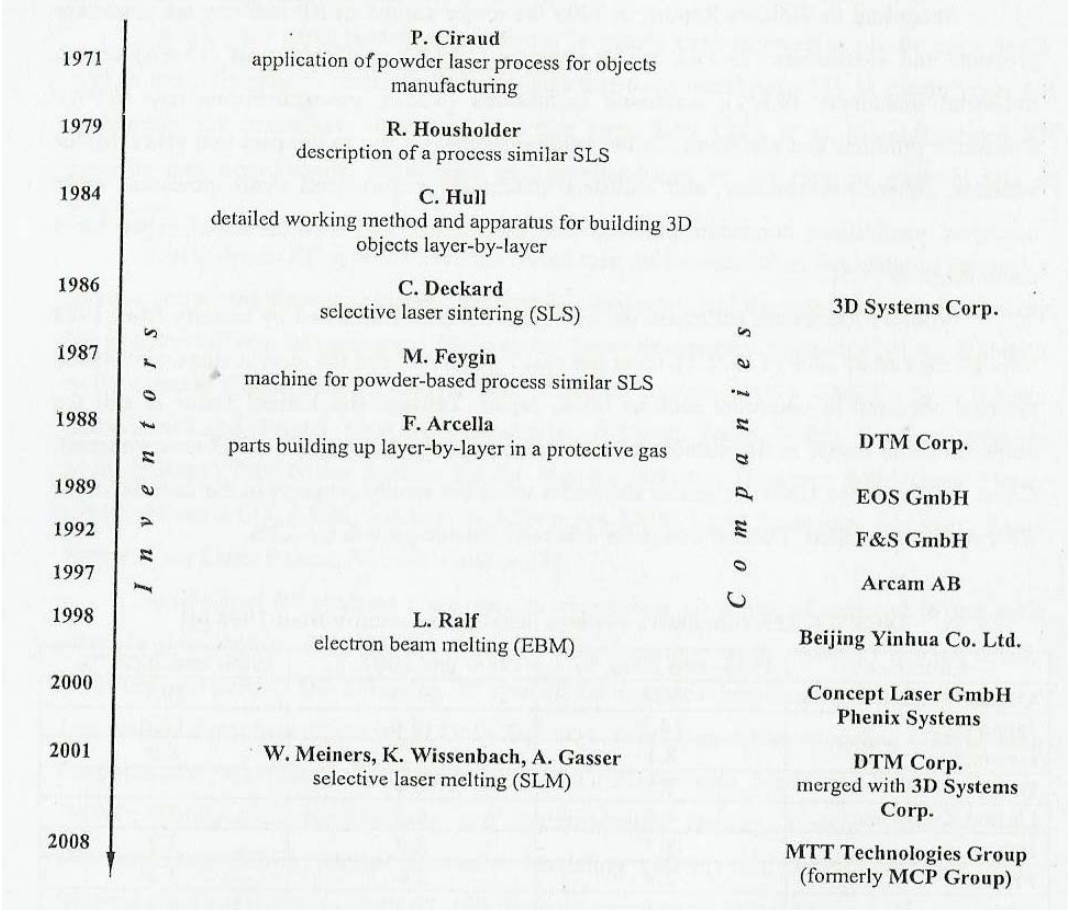

Figure 1.4: Scheme of patent history and founding years of direct metal sintering companies [Yadroitsev (2009)]

As reported by Yadroitsev (2009), two major direction of SLM activities are the manufacturing of complex three-dimensional (3D) shape parts and the synthesizing of functionally graded materials (FGM), such as complicated cooling channels for heat transfer applications and artificial hip joints for biomedical applications. It was reported that biocompatible material titanium alloys can be optimized up to 99.98% densities when produced using the SLM [Vandenbroucke and Kruth (2007)]. On the other hand, Rehme (2010) highlighted that the SLM is the process of choice for the realization of LFF open-cell lattice structure materials, for both periodic and stochastic types. The developments of research efforts to produce high porosity (~70%) structures using the SLM are seen to be promising [Mullen et al. (2009B); Stamp et al. (2009); Wang et al. (2010)].

The SLM process is based on a principle that the powder is applied in very thin layers on a building platform and melted due to the thermal energy induced by a laser beam [Rehme (2010)]. The cross-section area of a part is built by laser beam melting and resolidification of the powder particles in each layer, before the building platform is lowered and a new layer of powder is deposited and levelled by a wiper. By following a computer-generated pattern, the laser beam is being redirected across the surface of the powder bed by scanner optics in such a way that the powder particles can be selectively melted where desired. The fusion between metal powders in part's formation was reported as affected by the processing parameters [Yadroitsev et al. (2010)].

Rehme (2010) distinguished more than 150 different parameters that take effect on the SLM process. Figure 1.5 summarized the main influences of the process towards the quality of produced parts and the manufacturing cost and time.

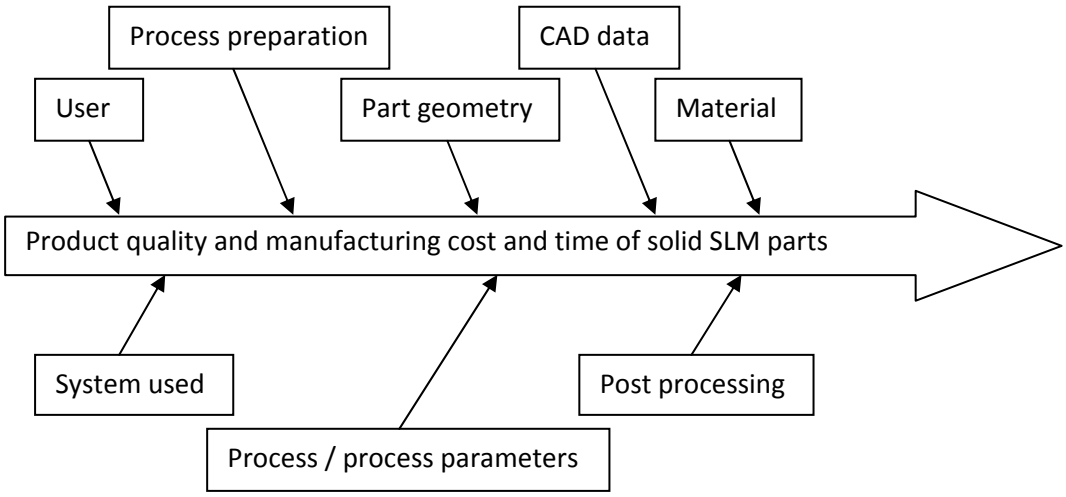

Figure 1.5: Diagram of SLM influence parameters [adapted from Rehme (2010)]

From all the identified parameters, Rehme (2010) identified that only 13 are crucial to the resulting quality properties of produced parts, and these are further divided into control parameters and disturbance variables. Those listed as control parameters

are beam power, speed of laser beam focus as it moves across the powder surface, hatch distance (distance between adjacent scan tracks in scanned area), layer thickness, exposure sequence strategy of which the scan vector length is an important factor. A dominant control parameter that affects the density of SLM products is energy density, E. The energy density (in J m^{-3}) is influence by the laser power, P, divided by the product of scan speed, v, hatch distance, h, and layer thickness, l, as shown in Equation 1.1.

$$E = \frac{P}{v\,.h\,.l} \qquad [1.1]$$

The quality properties of the produced SLM parts are resulted from crucial control parameters that are mentioned earlier. The properties can be characterized such as surface finish (surface roughness), strength (ultimate strength, yield strength, Young's modulus, break strain), accuracy to shape and size, hardness as a value for resistance to wear, density in terms of pore-free microstructure and residual stress behaviour (which leads to warping or cracking of parts during the process or after) [Rehme (2010)].

Tsopanos et al. (2010) studied the influencing SLM parameters on mechanical properties of stainless steel micro-lattice blocks structures. It was reported that there was a relative linear relationship between plateau stress and elastic modulus to the measured relative density. The study highlighted that laser power and exposure time has influence on strut diameter and properties of the material. For a body centred cubic (BCC) micro-lattice block, strut diameter, d, was derived in terms of mass of the block, m_b, density of the steel, ρ_s, number of cells along the cube side, N^3, and the cell length, L, as shown in Equation 1.2.

$$d = \sqrt{\frac{m_b}{\rho_S.\pi\,.N^3.L\,.\sqrt{3}}} \qquad [1.2]$$

Stamp et al. (2009) demonstrated that the SLM process can produce porous structure of controlled porosity using beam overlap procedure. The biocompatible

commercially pure titanium (CpTi) porous structure was reported to fulfil important requirements for pore size, porosity and mechanical strength of medical applications. Post manufacture high vacuum sintering was then applied in the study in order to increase the compression strength and enhance the surface topology of the produced porous structures.

The additive layer manufacture or layer by layer building of the SLM process for virtually any design arrangement can realize the manufacturing of hierarchical micro-lattice structure with extreme complexity. Mines (2008) suggested that the flexibility of the SLM process can make it capable to manufacture open-cell lattice structure, with the possibility of having micro-lattice core architectures with greater strength and stiffness to weight ratios than those offered by traditionally manufactured lattice structure core materials in sandwich construction application.

It should be noted that a major issue with additive layer manufacture such as the SLM is the potential to create actual metallic engineering components [Gibson et al. (2010)]. This requires not only full definition of the performance of the component which is the subject of this thesis, but also ensuring that the cost and environmental performance of the manufacturing process are competitive or better than, state of the art structural solutions. The SLM process is still being improved, and Kellens et al. (2011) identify the need to improve machine costs, energy and gas consumption, production time, and amount of waste (contaminated powder). Aerospace companies are investigating the potential of the SLM and other additive layer manufacturing processes for the manufacture of small numbers of high value structural components. Work on qualifying SLM on civil aircraft has begun with low risk parts for secondary structures such as the stainless steel fan cowl brackets and hinges [Warwick (2010)]. This qualification work concerns solid SLM components, and the thin sectioned micro-lattice struts discussed in this thesis are currently at a lower level of technology readiness.

1.3.3 Other Competing Processes in Producing Metallic Lattice Structure

There are many different fabrication processes available for producing cellular materials, but only a few will be discussed in this sub-section, mainly the periodic metallic lattice structure with struts such as tetrahedral, pyramidal and Kagome. Reviews from several authors [Wadley et al. (2003); Sypeck (2005); Rehme (2010)] on well established processes such as investment casting, deformation forming and metal textile approaches will be referred to in brief discussions. Latest process which utilizes laser such as electron beam melting (EBM) will also be discussed.

One of the earlier generation processes was the investment casting process, as studied by Deshpande et al. (2001). In the study, octet-truss lattice-material from aluminium alloy was manufactured, where triangulated layers with locating holes at the nodes, and tetrahedral cores with locating pins at the nodes, were injection moulded in polystyrene. The octet-truss structure was then constructed by adhering the triangulated layers in an 'ABCABC...' arrangement with alternating layers of the tetrahedral core. This polystyrene was used as the sacrificial pattern in a 'lost-wax' investment casting process to produce the lattice material. The process produced octet-truss material with solid cylindrical struts of radius a = 1 mm and length l = 14 mm, and the overall specimen dimension was 280 mm x 140 mm x 60 mm, with five tetrahedral core layers as shown in Figure 1.6(a). It was reported that the strength and stiffness of the octet-truss material are stretching-dominated and comparable to corresponding properties of metallic foams. Another study on structure produced by the investment casting is by Wang et al. (2003), where the performance of truss core based on 3D Kagome was investigated. In this study, rapid prototyped acrylonitrile butadiene styrene (ABS) was used as sacrificial pattern for investment casting of Cu-2%Be alloy. Panel with core member diameters of 1.25 mm with an overall panel size 246 x 66 x 14.4 mm were constructed. It was reported that the 3D Kagome design was showing superior performance relative to tetrahedron truss design, and greater resistance to plastic buckling at equivalent core density. Figure 1.6(b) shows an example of 3D Kagome core sandwich panel from investment cast.

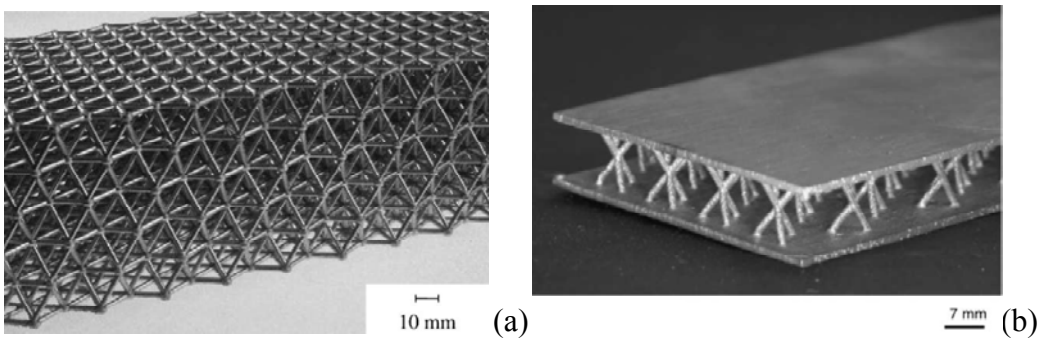

Figure 1.6: Periodic lattice structures from investment casting process; (a) octet-truss lattice material from cast aluminium alloy [Deshpande et al. (2001)]; (b) 3D Kagome core sandwich panel, from Cu-1.8%Be alloy [Wadley et al. (2003)]

Another method of producing lattice material is deformation forming, which can be rather said as a simple way to obtain periodic open-cell structures by press forming operation. It utilizes sheet perforation and shaping techniques. Tetrahedron lattice structure can be produced by deforming hexagonally perforated metal sheet, as illustrated in Figure 1.7. The processed material requires annealing treatment in order to soften the strain-hardened struts. Wadley et al. (2003) reported that lattice structure manufactured from this process showed much greater ductility than their investment cast counterparts. Besides perforating and shaping, another technique in deformation forming process is by shearing and expanding metal sheets techniques. As studied by Lim et al. (2009), low carbon steel sheet was uniquely cut by laser, and expanded width-wise to be a metal mesh, and then was bent along the lines connecting the longer ends of the diamond shapes into the corrugated sheet. Finally, the shorter struts were rotated by a 120° angle, and a quasi Kagome truss was produced. Figure 1.8 illustrates the shearing, expanding and corrugating processes.

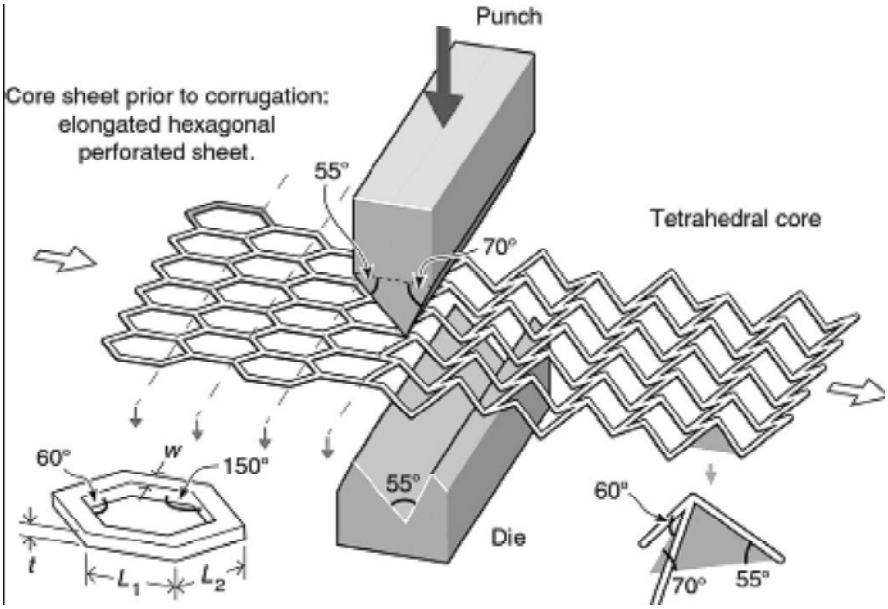

Figure 1.7: Illustration explaining on deformation forming process for tetrahedral lattice structure [Wadley et al. (2003)]

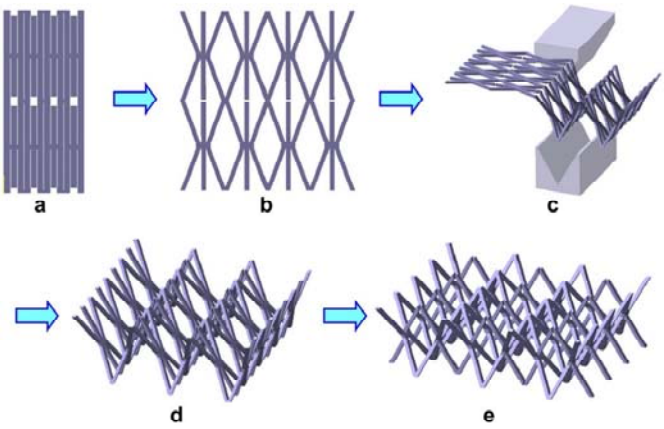

Figure 1.8: Illustration explaining the slicing, expanding and corrugating processes in producing a quasi Kagome truss [Lim et al. (2009)]

One more reviewed technique for producing periodic metallic lattice structure is the mature technology metal textile approach. It consists of inexpensive methods and controllable positions of weaving, braiding and sewing of any alloy that can be drawn into wire, to produce an open-cell woven structure. The wire orientation can be arranged in any angle such as 0/90° and 45° as shown in Figure 1.9. Extensive discussions on this process were given by Wadley et al. (2003) and Sypeck (2005). It

was reported that linear behaviour of the produced structure from the metal textile approach outperforms open and closed-cell stochastic foams at low relative density [Sypeck (2005)].

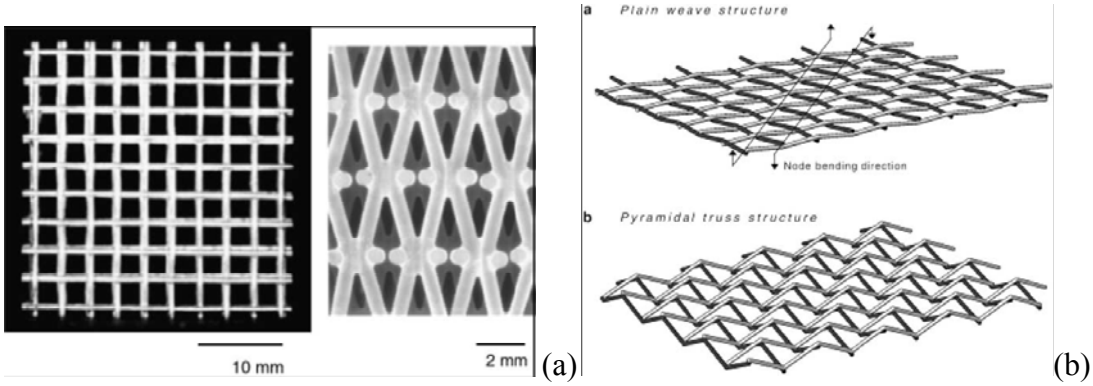

Figure 1.9: (a) A 0°/90° orientation of inconel textile from front and side view; (b) Pyramidal truss can be produced by shearing a plain weave fabric and bending the node at 45° orientation [Wadley (2003)]

Other than the established techniques of investment casting, deformation forming and metal textile, there is an advanced method in producing the periodic lattice structure. The process is similar with the selective laser melting (SLM) as discussed in previous sub-section, but instead of using laser, this technology uses an electron beam as the energy source to melt layers of metal powders in vacuum, and the process is called electron beam melting (EBM). Cansizoglu et al. (2008) studied the fabrication of non-stochastic lattice structure using electron beam melting. In the EBM process, the electron beam is generated by heating a tungsten filament and accelerating the electrons towards the metal powder at the build platform using an accelerating voltage of 60kV. The electron beam is focused and deflected using electromagnetic coils. As in SLM, the EBM also utilizes layer by layer build to manufacture 3D object, until the structure completed. The difference is that, in the EBM, the base metal plate and the powder bed need to be preheated prior to electron scanning. The grain size in an EBM part is a function of cooling rate. The cooling rate is a function of both process parameters and part geometry, and the rate depends on the size of melting area. In Cansizoglu et al. (2008B), the effect of build angle on

manufacturing of Ti-6Al-4V lattice structure was studied. It was reported that when thin beams are built at an angle, each layer of that beam consists of a relatively small cross-section that is slightly shifted from one layer to the next, as shown in Figure 1.10. This will affect structural stiffness of lattice structure struts manufactured using this process.

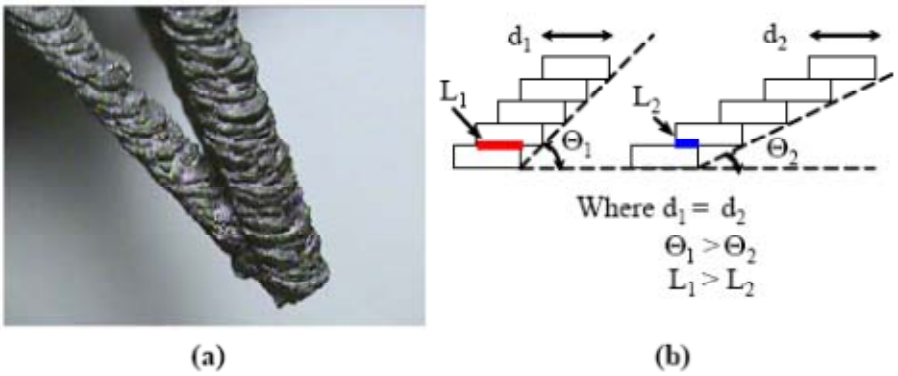

Figure 1.10: (a) A thin low-angled beam structure manufactured using EBM; (b) effect of low-build angle on thin beam structure [Cansizoglu et al. (2008B)]

From discussions on manufacturing processes of periodic metallic lattice structure materials, every method has their own strength and advantage in producing core structure that suitable with different sandwich structure applications. However, there are common aspects in general mechanical properties of the lattice structure materials that can be discussed, especially in sandwich structure and load bearing applications.

1.3.4 Mechanical Properties of Lattice Structure

The discussions on mechanical properties of open-cell lattice structures need to be started from general properties of cellular materials. Besides depending on the parent material, the properties of cellular materials also depend on cell size, cell shape, periodicity and connectivity between cell walls or struts, porosity type, and relative density of the materials [Rehme (2010)].

A basic guideline in classifying type of cellular materials is from observation on general compressive stress-strain curve, whether the material behaviour is bending-dominated or stretch-dominated. General compressive behaviour of cellular solids as sketched in Rehme (2010) is shown in Figure 1.11. In most cases, bending-dominated behaviour is associated with open-cell or with stochastic materials; while stretch-dominated behaviour is often correlated with closed-cell or sometimes open-cell periodic counterparts. At a given relative density, a stretch-dominated cellular material always shows higher relative strength.

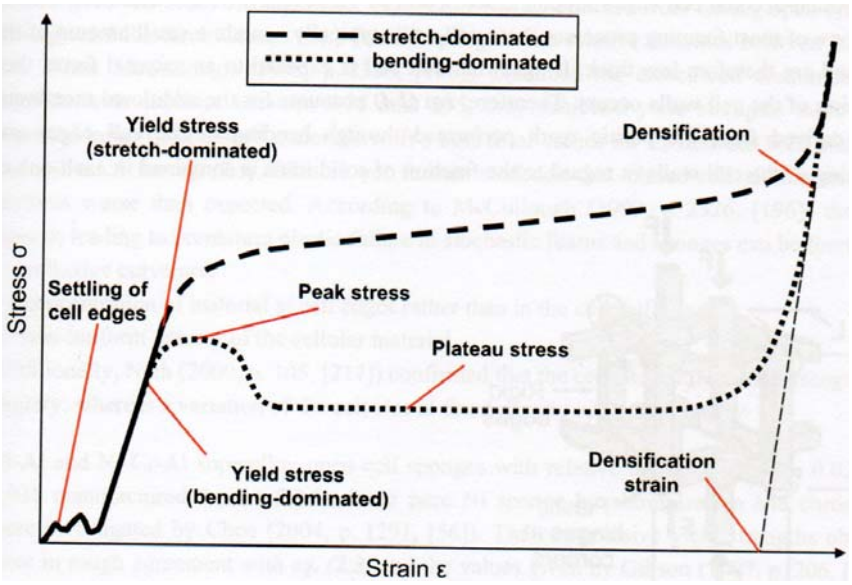

Figure 1.11: General compressive behaviour of cellular solids [Rehme (2010)]

Comparison on micro-failure mechanism of typical lattice truss materials as shown in Figure 1.12 was studied by Fan et al. (2008). It was reported that three main micro-failure mechanisms of the lattice materials are tension yield, compression yield, and compression buckling of struts. The study suggested that the diamond cell type is an undesirable sandwich core material due to low stiffness, uniaxial strength and shearing strength; while pyramidal lattice is a desirable core material for sandwich panels due to larger shearing strength than the uniaxial strength. Two design criterion were suggested; (1) the relative density, ρ^* of the lattice materials must be greater than certain critical values that suggested in the study; and (2) the number and stacking mode of struts can be pre-designed according to the loading conditions. The uniaxial strength and stiffness would be much larger in the direction where the struts are much more densely stacked. Figure l.13 lists the mechanical properties of 3D lattice materials as given in Fan et al. (2008).

It should be noted that the octahedral cell as shown in Figure 1.12 is also known as body centred cubic (BCC) cell. Mines (2008) reported that the compressive collapse of the BCC structure is controlled by plasticity at the strut nodes. The BCC, octet-truss, tetrahedral and Kagome structures were reviewed in the paper [Mines (2008)]. In general, the preferred core topologies are those of stretch and compression without bending [Deshpande et al. (2001)]. It was reported that the tetrahedral trusses are good for plates [Deshpande and Fleck (2001)]; Kagome trusses have superior isotropy and greater resistance to softening modes such as plastic buckling [Wang et al. (2003)]; and octet-trusses are good for stretching without bending behaviour but they are complex to manufacture [Deshpande et al. (2001)]. It was also reported that the progressive collapse of the lattice structures are non-optimal, but there is an active interest in the analysis and optimisation of the lattice core structures, with both the micromechanical and the homogenisation approaches are being pursued [Mines (2008)].

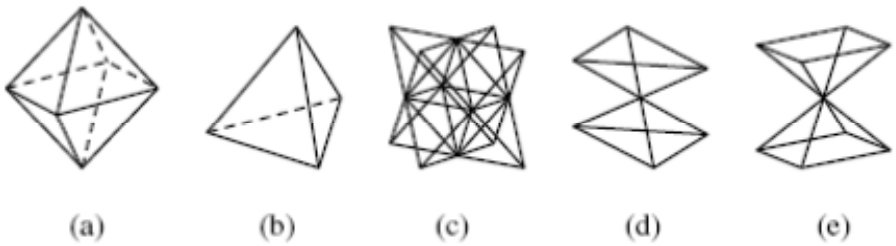

Figure 1.12: Periodic unit cell of typical lattice truss materials: (a) octahedral cell; (b) tetrahedral cell; (c) octet-truss cell; (d) diamond cell; and (e) pyramid cell [Fan et al. (2008)]

Cell	Specific stiffness			Specific uniaxial strength			Specific shearing strength		
	x	y	z	x	y	z	xy	yz	zx
	$0.167\rho^*$			$0.333\rho^*$			$0.167\rho^*$		
	$0.153\rho^*$	$0.153\rho^*$	$0.296\rho^*$	$0.111\rho^*$	$0.167\rho^*$	$0.444\rho^*$	$0.096\rho^*$	$0.157\rho^*$	$0.181\rho^*$
	$0.15\rho^*$	$0.15\rho^*$	$0.2\rho^*$	$0.1\rho^*$	$0.1\rho^*$	$0.2\rho^*$	$0.2\rho^*$	$0.283\rho^*$	$0.283\rho^*$
	$0.216\rho^*$	$0.216\rho^*$	$0.135\rho^*$	$0.17\rho^*$	$0.17\rho^*$	$0.27\rho^*$	$0.163\rho^*$	$0.193\rho^*$	$0.193\rho^*$

Figure 1.13: Mechanical properties of 3D lattice materials [Fan et al. (2008)]

Compression and shear properties of pyramidal lattice core sandwich structures from titanium alloy which was fabricated by using forming and diffusion bonding methods were investigated by Queheillalt and Wadley (2009). It was found that during compressive and shear loading, the stress-strain responses were similar to other lattice truss based materials and the peak strengths corresponded to the onset of truss member buckling. The collapse strength of a lattice core was mentioned to be determined by the mechanism of strut failure which depends on the cell geometry, strut material properties and the mode of failure during loading (plastic yielding and elastic or plastic buckling). Figure 1.14 shows comparison of compressive peak strength in Queheillalt and Wadley (2009) study with other studies in their literatures. For comparison, the compressive peak strength of the SLM SS316L BCC micro-lattice block as reported in Mines et al. (2007) is annotated in the figure. The study of SLM SS316L BCC micro-lattice structure was the earlier research which

led to the current study of SLM Ti-6Al-4V BCC micro-lattice structure reported in this study.

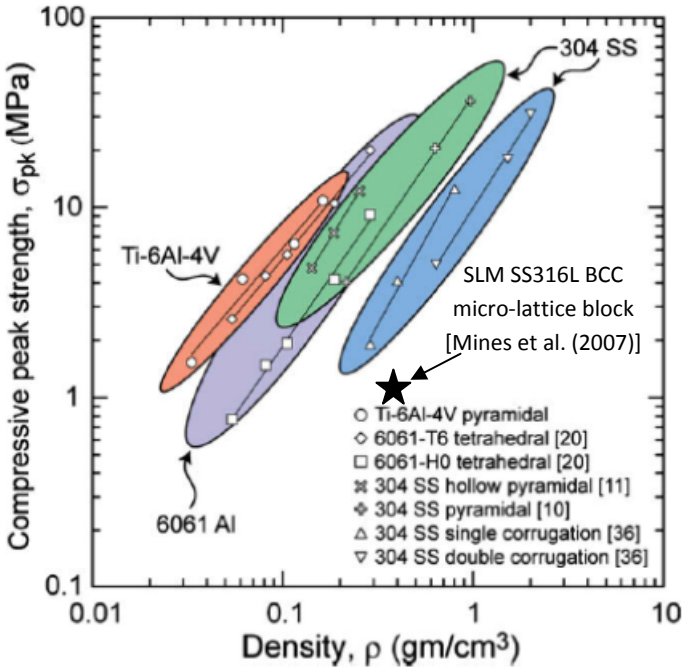

Figure 1.14: Compressive peak strength versus density for various sandwich core topologies [Queheillalt and Wadley (2009)]

Doyoyo and Hu (2006) studied on the failure of metallic strut lattices subjected to multi-axial loads, by carrying out parametric investigation on two microscopic parameters related to the geometry of struts; (1) strut-level strengthening; and (2) slenderness ratios. Both parameters are key design parameters for the strut lattice. The slenderness ratio is given by $= L_{eff}/\sqrt{I/A}$; where L_{eff} , I and A are the effective strut length, strut's moment of inertia, and strut's cross-sectional area respectively. In a 3D Warren truss material (Figure 1.15), the strengthening ratio, η is defined as the cross-sectional area of struts in the cubic lattice, a^{cub}, divided by the cross-sectional area of struts in the octet lattice, a^{oct} . The strengthening ratio relation is given by $\eta = (a^{cub}/a^{oct})^2$.

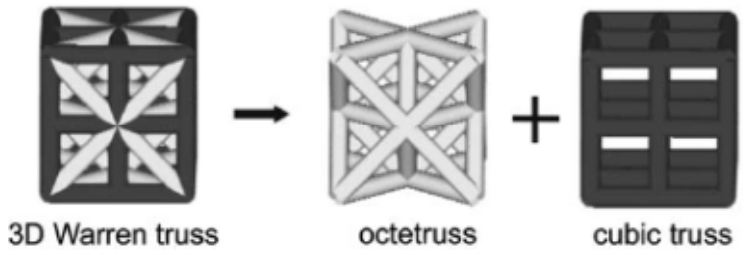

Figure 1.15: The 3D Warren truss composed of octetruss and cubic truss [Doyoyo and Hu (2006)]

Ushijima et al. (2011) highlighted the complexity of parametric modelling on models with various deformation modes and micro-strut boundary conditions assumptions of selectively laser melted (SLM) stainless steel body centred cubic (BCC) micro-lattice structure. It was predicted that specific stiffness E^* and strength σ^* values increase with increasing d/L (strut diameter over cell size), and there is no optimum, as shown in Figure 1.16.

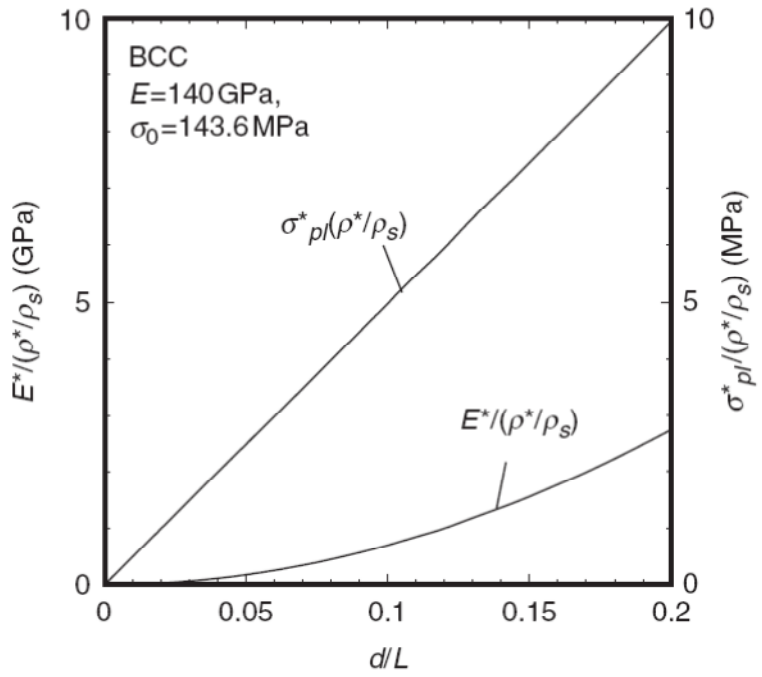

Figure 1.16: Variations of specific stiffness and strength from analytic model of Ushijima et al. (2011)

Studies on mechanical properties of lattice structure usually assumed that the strut members have uniform microstructure and mechanical properties. However, the local properties of the individual struts may be significantly affected by variations in defect sizes/content, local changes in microchemistry and differences in microstructure, and thus investigation of individual struts is needed to obtain individual data as input for numerical simulation analysis. Zhou et al. (2004) explored the effects of strut properties on the deformation behaviour of aluminium lattice block structures. An elastic-plastic beam behaviour of lattice block structures was simulated using a pyramidal unit cell model, incorporating the stress-strain data from multiple compressive deformation experiments. The study suggested that the measured variations in the strut tensile and compressive properties may be used to estimate the bounds in the deformation behaviour of lattice block structures.

1.3.5 Static, Impact and Foreign Object Impact of SLM Micro-lattice

McKown et al. (2008) reports about early studies that investigated micro-lattice structures using the advanced selective laser melting process (SLM) for high performance load-bearing applications. Quasi-static, dynamic and blast loading responses of pillar-octahedral (0°, ±45°) and octahedral (±45°) stainless steel 316L lattices with different unit-cell sizes were studied. Figure 1.17 shows the schematic of unit-cell geometry used in the study. Two unit-cell sizes of 2.5 mm and 1.5 mm were tested and considered as low density and high density respectively. In the quasi-static study, it was reported that the pillar-octahedral geometry showing approximately 3.5 times higher yield strength compared to the octahedral geometry, at both low and high cell density. Figure 1.18 shows the quasi-static response of block structures in the study. The octahedral exhibited smooth stress-strain trace with no discernible yield points shown by lattice C and D curves in the figure while the pillar-octahedral exhibited an initial peak yield point associated with plastic bending of the vertical strands as shown by lattice A and B curves. For the dynamic response, the study suggested that the compression strength of the lattice material increased steadily with loading rate, with the value at 3 m/s (150 s-1) being approximately 25% higher than its quasi-static value as shown in Figure 1.19. On the other hand it was reported that the crush behaviour of the lattice under blast loading conditions produced the similar deformation mechanisms as the quasi static results.

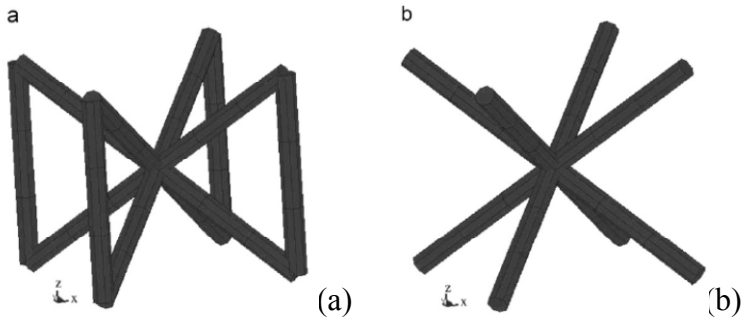

Figure 1.17: Schematic of the unit cell geometry in McKown et al. (2008) study; (a) pillar octahedral lattice; and (b) octahedral lattice

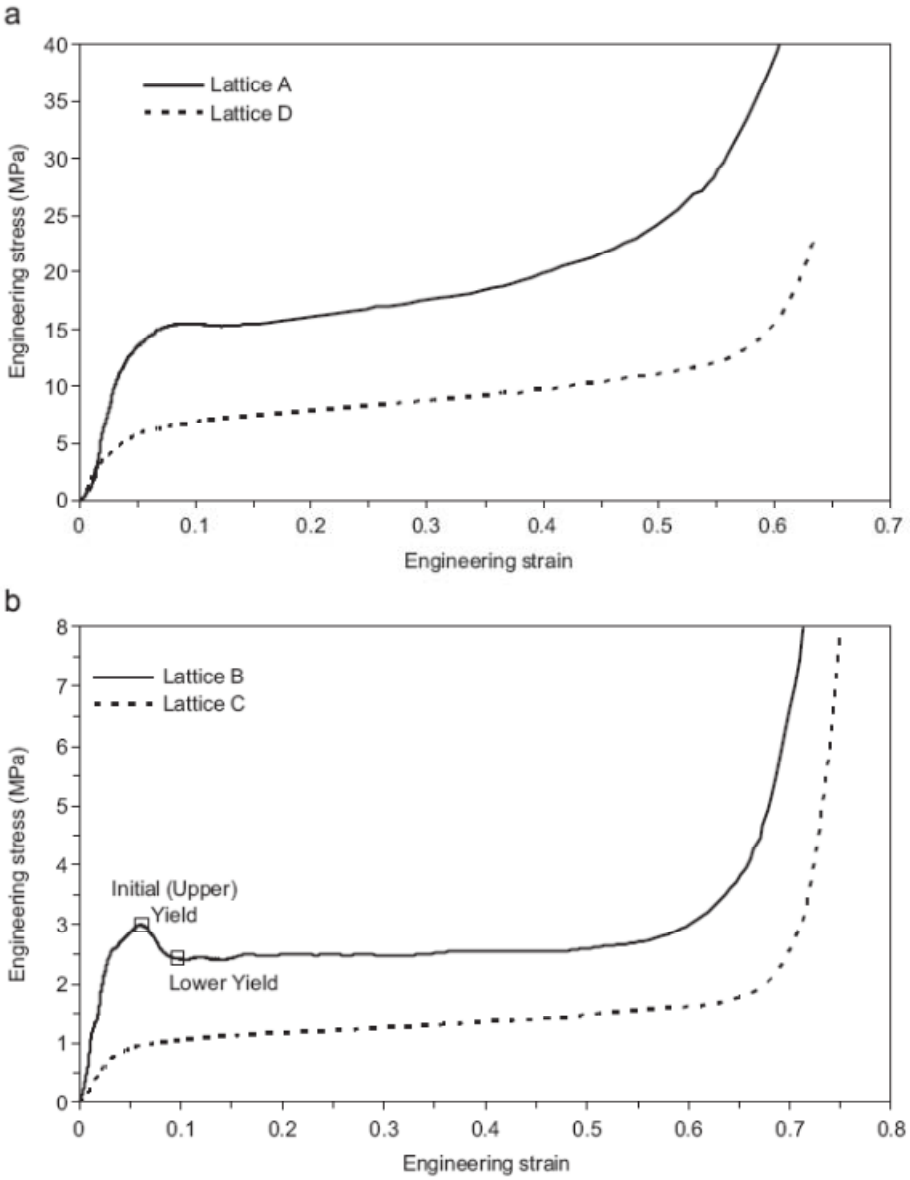

Figure 1.18: Typical quasi-static stress-strain curves for (a) higher density lattices A and D; and (b) lower density lattices B and C [McKown et al. (2008)]

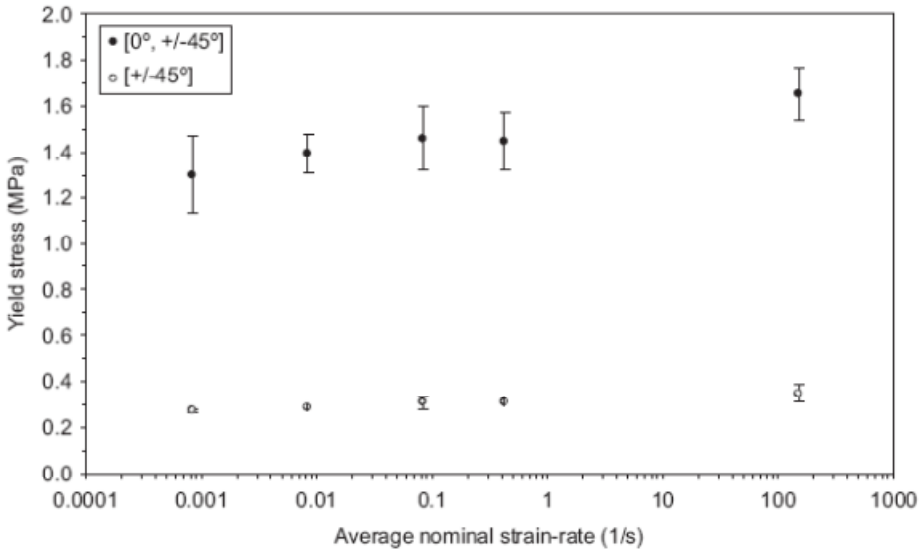

Figure 1.19: The variation of yield stress with crosshead displacement rate for the pillar-octahedral lattice (0°, ±45°) and octahedral lattice (±45°) structures [McKown et al. (2008)]

Mines (2008) identified five basic mechanisms for the core during foreign object impact of sandwich structures, namely global elastic response (global stiffness and strength), local elastic response (giving rise to skin core debonding), local crush response (during perforation), boundary response (connections) and post-impact response (one-off load and fatigue strength). In the paper, it was highlighted that the ability of the SLM process to tailor micro-lattice cellular structures can realise graded structures with finer cellular structure nearer the skin and a more coarse cellular structure towards the centre, which is the interest in foreign object impact of sandwich panels.

The third mechanism during foreign object impact that was identified by Mines (2008), which is perforation core crushing, was studied on sandwich panel with stainless steel micro-lattice core and compared to Alporas aluminium foam [Mines et al. (2008)]. In the study, static penetration tests and low velocity impact tests were carried out. At similar density, the micro mechanics of penetration for the two structures were completely different, but the specific energy absorption was similar. In impact test, it was found that the failure modes of the skins were similar,

suggesting that the progressive degradation of skin support leading to skin rupture is similar, as shown in Figure 1.20. From the comparable results between BCC stainless steel 316L micro-lattice structure and Alporas aluminium, Mines et al. (2008) suggested that there is scope to improve the specific perforation performance of the micro-lattice by changing the micro structure or the parent material (i.e. to titanium).

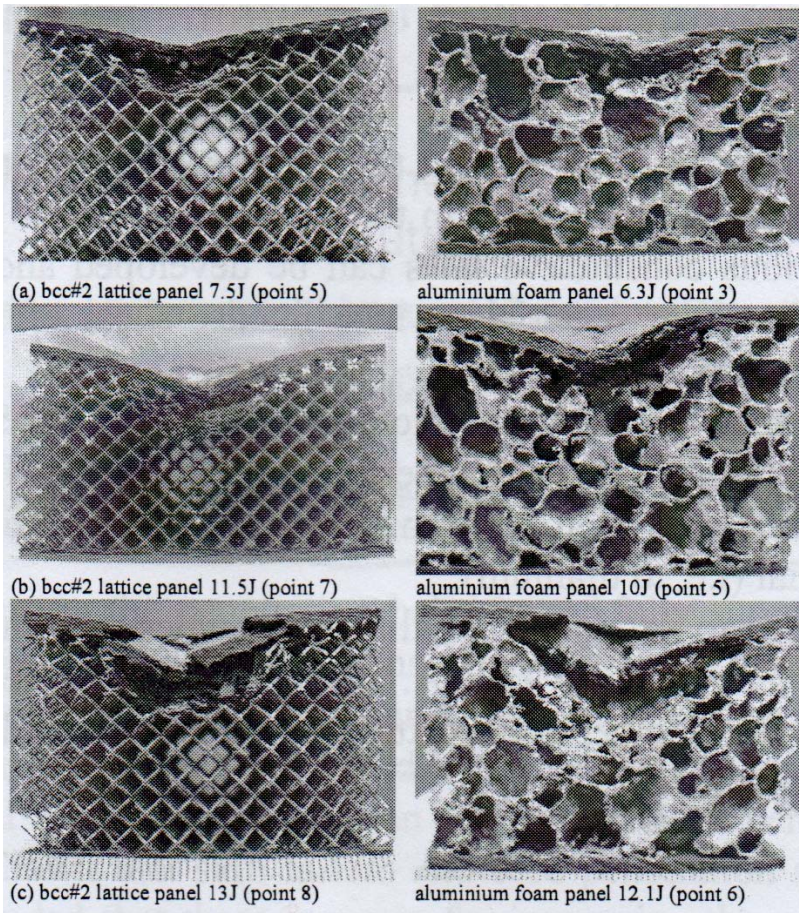

Figure 1.20: Comparison on sandwich panel cross-sections of SLM BCC stainless steel micro-lattice core and Alporas aluminium alloy at various impact energies [Mines et al. (2008)]

On top of extensive study on SLM stainless steel micro-lattice structure as core material in sandwich structure, Shen (2009) also investigated the feasibility of SLM titanium Ti-6Al-4V micro-lattice structure as the core material. Impact tests were

done on sandwich panels with four different core materials, and impact energies were normalised by their respective densities. The SLM Ti-6Al-4V micro-lattice core was shown to be better than SLM stainless steel micro-lattice core, and also comparable to Alporas aluminium foam core, although still outperformed by the aluminium honeycomb core. Figure 1.21 shows the specific impact energy versus dent depth of four different core materials as reviewed from Shen (2009). The comparison on impact performance of sandwich panels with SLM Ti-6Al-4V micro-lattice core and aluminium honeycomb core was also reported in Hasan et al. (2010). On top of being comparable in impact resistance with the aluminium honeycomb, the SLM Ti-6Al-4V micro-lattice core was also showing more localized damage, which means that less replacement area needed for a particular sandwich structure, and this can fulfil the requirement outlined by the aircraft manufacturer [Morteau and Fualdes (2006)].

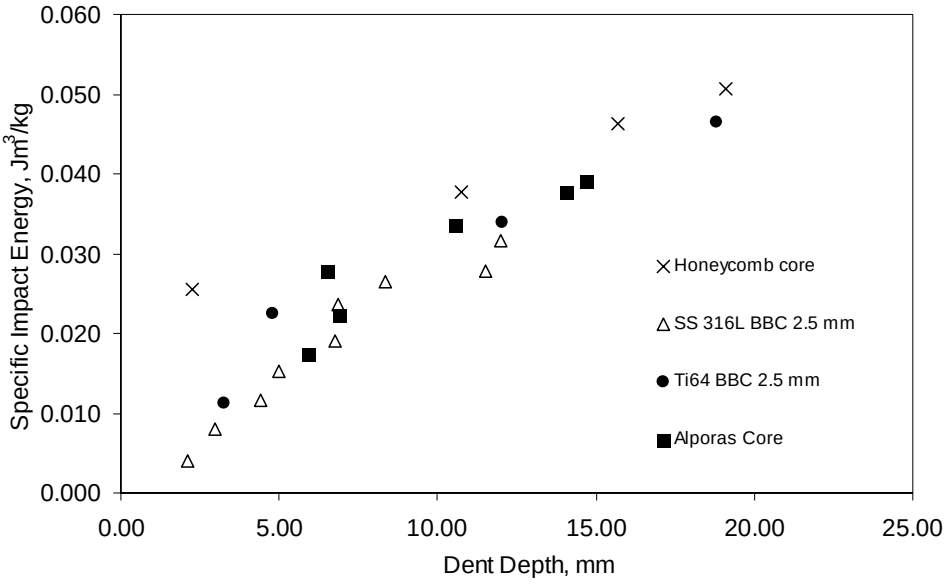

Figure 1.21: Comparison of performance for sandwich panels with four different types of core materials [Shen (2009)]

1.3.6 Titanium Alloy Ti-6Al-4V

From the preliminary studies on the performance of the SLM Ti-6Al-4V micro-lattice structure as core material in sandwich construction to address foreign object impact, it can be seen that this material has significant potential that merits further examination and analysis [Hasan et al. (2010)]. The Ti-6Al-4V alloy was already known as having great potential in future aerospace applications, although other materials offer competitive production costs [Polmear (2006)]. Wu (2006) mentioned that civil aircraft companies are committed to use titanium alloy in the next generation of aero-engines, and this is an encouraging factor for the further development of the material. It is also known that the specific strength of Ti-6Al-4V is almost seven fold that of stainless steel [Boyer et al. (1994)].

Table 1.1: Component elements in Ti-6Al-4V [Boyer et al. (1994)]

Element	Al	V	C	H	Fe	N	O	Ti
Percentage of composition	5.5% - 6.75%	3.5% - 4.5%	≤ 0.08%	≤ 0.015%	≤ 0.4%	≤ 0.03%	≤ 0.2%	As balance

Table 1.1 shows element composition of titanium alloy Ti-6Al-4V. It is an α/β alloy, where the aluminium reduces the density of the alloy by stabilizing and strengthening the α-phase, while the vanadium improves ductility by stabilizing β-phase during hot working. The Ti-6Al-4V offers good tensile properties at room temperature, and the applications includes blades, discs, bolts, fasteners, springs and biomedical implants, as well as aerospace metal. This alloy shows resistance to fatigue, crack propagation as well as corrosion. Table 1.2 shows properties of the material, as given by Boyer et al. (1994).

Table 1.2: Properties of Ti-6Al-4V (Grade 5), Annealed [Boyer et al. (1994)]

Density	Ultimate Tensile Strength	Tensile Yield Strength	Elongation at Break	Modulus of Elasticity	Poissons Ratio
4.43 g/cc	950 MPa	880 MPa	14%	113.8 GPa	0.342

The titanium alloy can be produced from several processes such as forgings, castings and powder metallurgy. However, different manufacturing processes contribute to the differences in properties. Since the titanium alloy can be manufactured from powder metallurgy, the powder can be also processed using the Selective Laser Melting (SLM).

Murr et al. (2009) studied microstructure and mechanical behaviour of Ti-6Al-6V produced by the SLM process. It was reported that the SLM products were having a microstructure which give rise to a mechanical behaviour similar to and superior to wrought or cast Ti-6Al-4V products. Tensile strengths ranged from 0.9 to 1.45 GPa, which was 50% increase over wrought products; with corresponding elongations ranging from 25% to 4.4%.

Facchini et al. (2010) studied the ductility of Ti-6Al-4V alloy produced by the SLM. It was reported that SLM applied to Ti-6Al-4V alloy produced a material with a martensitic microstructure, which were less ductile as compared to the wrought alloy. Some microcracks, due to the effect of incomplete homologous wetting and residual stresses produced by the large solidification undercooling of the melt pool, are observable in the matrix. A post-manufacture heat-treatment was suggested to transform the metastable martensite into dual phase $\alpha+\beta$, with a morphology that depends on the heat treatment. The stabilization of the microstructure resulted in an improvement in ductility, which is comparable to the wrought alloy.

Martensitic microstructure in the SLM Ti-6Al-4V was also observed by Thijs et al. (2010). It was due to the fast cooling during the SLM process. It was reported that there was segregation of aluminium (Al) element due to the rapid solidification, which was affected by amount of heat and scanning strategy, thus lead to the precipitation of an intermetallic Ti_3Al phase. This makes the melt pool boundaries visible on etching. The amount of precipitation increases with the reduction of scanning speed. The melt pool phenomena reported in this study supported the finding in Facchini et al. (2010) and further clarified the formation of microcracks in the material.

Another issue that can be a drawback for some applications of the SLM Ti-6Al-4V material is the relatively high-surface roughness. Many factors contribute to the surface roughness of the SLM products such as material, powder particle size, layer thickness, laser and scan parameters, scan strategy and surface post-treatment. 'Stair effect' due to the layer-wise production is also one of the main factors. Vandenbroucke and Kruth (2007) have addressed this issue and investigated on the influence of sloping angle, layer properties and post-treatments on the surface roughness of the SLM Ti-6Al-4V. It was reported that simple surface post-treatments such as glass blasting and ultrasonic ceramic filling removed partial molten particles on the surface, leading to strong reduction of roughness. A study by Pazos et al. (2010) also reported that there was a strong dependence of fatigue crack nucleation mechanism on the surface condition of the titanium material. There was an improvement in fatigue behaviour of the material with shot blasting treatment.

Recent study by Leuders et al. (2012) aimed to evaluate the fatigue behaviour of Ti-6Al-4V manufactured by selective laser melting. A thorough analysis of microstructure and defects was conducted in the study in order to establish a profound mechanical property and microstructure relationships. Post-manufacture heat-treatments for 2 hours duration with temperature below and above β-transus (800°C and 1050°C, respectively), as well as hot isostatic pressing (HIP) treatments

were carried out on standard cylindrical fatigue-test specimens (12.1 mm diameter x 120 mm length). For the HIP treatment, the specimens were treated under Argon gas atmosphere at 920°C with a pressure of 1000 bar for 2 hours duration. It was reported that reduction of pores size due to HIP treatment led to significant improvement in fatigue strength of the SLM Ti-6Al-4V material.

HIP treatment was also applied on SLM Ti-6Al-4V micro-lattice specimens during early study of this research [Shen (2009); Hasan et al. (2011)] which will be further discussed in Chapter 3. The HIP was done at 930°C and 100 MPa pressure under Argon gas atmosphere for 2 hours duration. It was reported that the HIP treatment stabilized the stress-strain response of the micro-lattice block specimens with low manufacturing parameters (180 W x 500 μs). However, no improvement was observed in the micro-lattice specimens with high manufacturing parameters (200 W x 1000 μs).

Song et al. (2012) suggested the melting mechanism of Ti-6Al-4V powder in the manufacture of a perfect SLM part, based on two main parameters, i.e., laser power and scanning speed (in the current thesis study, instead of scanning speed, the laser exposure time is considered, which can be a function of the inverse scanning speed). Over a range of laser powers and scanning speeds, Song et al. (2012) summarized three processing windows which correspond to three different melting mechanisms, as listed below.

I. *Melting with cracks* – This is a high energy input zone. At a high laser power combined with a relatively low scanning speed, the single Ti-6Al-4V track could be completely melted and even broke up due to the excessive shrinkage and the high residual stresses, producing many visible cracks.
II. *Continuous melting* – The energy input was so comfortable that continuous single tracks were obtained by means of the complete melting of Ti-6Al-4V powders.

III. *Partial melting* – The insufficient energy input could not induce significant melting of Ti-6Al-4V powders. This will inevitably induce a laminated structure formed by Ti-6Al-4V powders.

The mechanical properties of the three zones proposed by Song et al. (2012) can be indicated by the microhardness of the SLM Ti-6Al-4V parts of the three zones, as shown in Figure 1.22. It can be concluded that the processing parameters have an important influence on the mechanical properties indicated by the microhardness. This is because the microhardness has a direct relationship with the densification level, which corresponds to the resistance to plastic deformation or rupture.

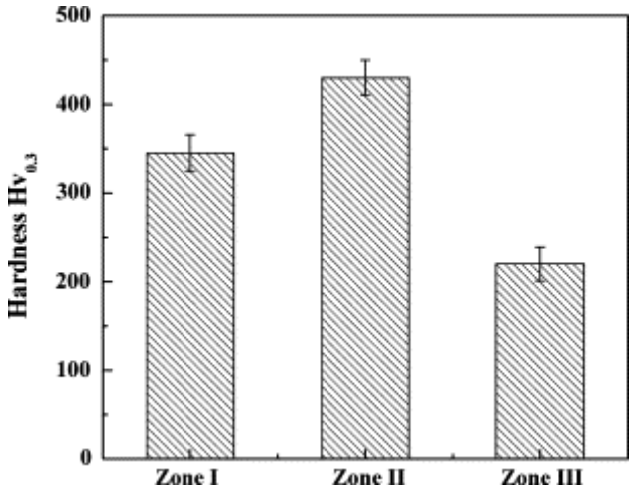

Figure 1.22: Microhardness of selective laser melted Ti-6Al-4V parts [Song et al. (2012)]

There was an attempt to estimate the mechanical properties of the SLM Ti-6Al-4V octahedral porous material by Sun et al. (2012). This material is similar with the body centred cubic (BCC) micro-lattice structure in the current thesis, but both their strut diameters and cell sizes are larger. Sun et al. (2012) estimated that the theoretically calculated load of the octahedral unit satisfies Equation 1.3 and the deformation displacement satisfies Equation 1.4.

$$F = \frac{2\pi\sigma d^3}{d\cos\theta + 8l\sin\theta} \quad [1.3]$$

$$K\delta_{compression} = F \quad [1.4]$$

Where $K = \frac{8EIA}{l^3A+4Il}$, δ is deformation displacement, F is load, E is Young's modulus, I is moment of inertia, A is strut's cross-section area, l is strut's length, d is strut's diameter, θ is angle between the holding strut and the vertical direction. It was observed that the compression curves reported in Sun et al. (2012) were not comparable to the nominal compression curves reported in the current thesis and other earlier studies [McKown et al. (2008); Shen (2009); Tsopanos et al. (2010)], therefore Sun et al. (2012) estimations were not adapted in this study.

The potential of the SLM Ti-6Al-4V material as high performance parts in aerospace, automotive and medical applications is actively being explored by researchers and companies throughout the world. Serious efforts from manufacturers to implement the material in future systems are supported by the ASTM Committee on Standards with the publication of a document for standard manufacturing of the selective laser melted components [ASTM Standard (2012)]. This promising document motivates the researchers to come out with more recent advancements with this technology application.

1.3.7 Plasticity and Failure Criterion

As reported by Facchini et al. (2010), the SLM Ti-6Al-4V alloy exhibited a ductile behaviour. Therefore, the plasticity theory can be applied in modelling the material. A simple tensile test can provide a wealth of information on the plasticity of a material. Basic plasticity equations from the tensile test are as outlined in the following paragraph [Lemaitre and Chaboche (1990); Tan (2009)].

In the tensile test, the original cross sectional area, A_0 , and gage length, l_0 , are measured prior to conducting the test. The applied load P and instantaneous gage length l_1 (when facilities available) are continuously measured throughout the test using computer-based data acquisition. For uniaxial loading, the engineering stress, σ_{eng} , is defined by

$$\sigma_{eng} = \frac{P}{A_0} . \quad [1.5]$$

The engineering strain is defined according to

$$\varepsilon_{eng} = \frac{l_1 - l_0}{l_0} . \quad [1.6]$$

The strain (true strain) is the change in length divided by the instantaneous length,

$$d\varepsilon = \frac{dl}{l} . \quad [1.7]$$

The integration gives

$$\varepsilon = \int_0^{\varepsilon} d\varepsilon = \int_{l_0}^{l_1} \frac{dl}{l} = \ln \frac{l_1}{l_0} . \quad [1.8]$$

The stress (true stress) is the applied load divided by the instantaneous cross-sectional area, A,

$$\sigma = \frac{P}{A} . \quad [1.9]$$

The fundamental distinction between true stress and engineering stress, and true strain and engineering strain, concerns the interrelation between gage length and diameter changes associated with plastic deformation. From Equation 1.8, the relation between the strain (true) and engineering strain is

$$\varepsilon = \ln(1 + \varepsilon_{eng}). \quad [1.10]$$

Since plastic deformation is a constant-volume process such that

$$A_0 l_0 = Al = \text{constant} , \quad [1.11]$$

any extension of the original gage length would produce a corresponding contraction of the gauge cross-sectional area. The relation between true stress σ and engineering stress σ_{eng} is

$$\sigma = \frac{P}{A} = \frac{P}{A_0}\frac{A_0}{A} = \frac{P}{A_0}\frac{l}{l_0} = \sigma_{eng}(1 + \varepsilon_{eng}) \ . \qquad [1.12]$$

Due to the complex nature of the stress-strain curve of a mechanical test such as tensile test, it has become customary to idealize this curve in various ways as in Figure 1.23 [Tan (2009)]. A perfectly plastic material shows an unlimited amount of deformation or strain, at constant stress, and after the removal of load, the plastic strain or deformation cannot be recovered. The stress-strain curve for an ideal elastic-plastic material is illustrated in Figure 1.23 curve I. If the elastic deformation is negligibly small, the rigid-plastic idealization is valid (curve II of Figure 1.23), and for linear-hardening material, curve III could be a reasonable approximation.

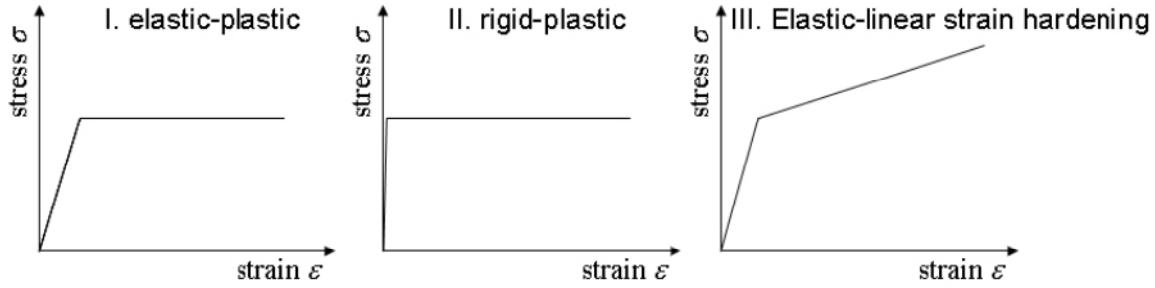

Figure 1.23: Idealized stress-strain curve [Tan (2009)]

A basic assumption of elastic-plastic models is that the deformation can be divided into an elastic part and an inelastic (plastic) part. A general form of this statement is written as in Equation 1.13 [Abaqus Theory Manual (2009)].

$$\mathbf{F} = \mathbf{F}^{el} \cdot \mathbf{F}^{pl} \qquad [1.13]$$

where F is the total deformation gradient, $\mathbf{F}^{el}$ is the fully recoverable part of the deformation at the point under consideration, and $\mathbf{F}^{pl} = [\mathbf{F}^{el}]^{-1} \cdot \mathbf{F}$.

This decomposition can be used directly to formulate the plasticity model. Historically, an additive strain rate decomposition,

$$\dot{\varepsilon} = \dot{\varepsilon}^{el} + \dot{\varepsilon}^{pl} \qquad [1.14]$$

has been used in its place . Here, $\dot{\varepsilon}$ is the total (mechanical) strain rate, $\dot{\varepsilon}^{el}$ is the elastic strain rate, and $\dot{\varepsilon}^{pl}$ is the plastic strain rate.

The ductile criterion is a phenomenological model for predicting the onset of damage due to nucleation, growth and coalescence of voids in ductile materials [Abaqus Theory Manual (2009)]. The model assumes that the equivalent plastic strain at the onset of damage, $\bar{\varepsilon}_{\mathrm{D}}^{pl}$, is a function of stress triaxiality and strain rate:

$$\bar{\varepsilon}_{\mathrm{D}}^{pl}(\eta\,,\dot{\bar{\varepsilon}}^{pl}) \qquad [1.15]$$

where $\eta = -p/q$ is the stress triaxiallity, p is the pressure stress, q is the Mises equivalent stress, and $\dot{\bar{\varepsilon}}^{pl}$ is the equivalent plastic strain rate. The criterion for damage initiation is met when the following condition is satisfied:

$$\omega_{\mathrm{D}} = \int \frac{\mathrm{d}\bar{\varepsilon}^{pl}}{\bar{\varepsilon}_{\mathrm{D}}^{pl}(\eta\,,\dot{\bar{\varepsilon}}^{pl})} = 1 \qquad [1.16]$$

where ω_{D} is a state variable that increases monotonically with plastic deformation. At each increment during the analysis the incremental increase in ω_{D} is computed as

$$\Delta\omega_{\mathrm{D}} = \frac{\Delta\bar{\varepsilon}^{pl}}{\bar{\varepsilon}_{\mathrm{D}}^{pl}(\eta\,,\dot{\bar{\varepsilon}}^{pl})} \geq 0\,. \qquad [1.17]$$

In Abaqus/Standard the ductile criterion can be used in conjuction with the Mises, Hill, and Drucker-Prager plasticity models.

The ductile criterion as mentioned in Equation [1.15] to [1.17] was based on studies reported in Hooputra et al. (2004). The approaches used in the studies involve a number of different failure mechanism representations, such as necking (due to local instabilities), as well as ductile and shear fracture. The plastic strain based parameter that was derived in the studies was from the application of initial imperfection which was assumed triggering the instability and forming a localised necking; the main mechanism that leading to fracture in ductile sheet metals. It should be noted that the studies were carried out on thin-wall double chamber extrusion parts made from aluminium alloy EN AW-7108 T6.

Wierzbicki et al. (2005) calibrated and evaluated seven fracture models which include the constant equivalent strain criterion, the Xue-Wierzbicki (X-W) fracture criterion, the Wilkins (W) fracture model, the Johnson-Cook (J-C) fracture model, the CrachFEM fracture model, the maximum shear (MS) stress model and the fracture forming limit diagram (FFLD). In the study, a set of 15 tests were conducted on 2024-T351 aluminium alloy. It was found that the MS stress fracture model closely follows the trend of almost all tests. The X-W criterion and the CrachFEM models predict correctly fracture in all types of experiments. The W criterion is working well in certain ranges of the stress triaxiality. Whereas, the remaining three fracture criteria i.e. the J-C model, the FFLD approach and the constant equivalent strain method can only be used in situation when the stress triaxiality and/or the deviatoric state parameter vary in very narrow ranges.

There is recent study by Giglio et al. (2012) on calibration of ductile fracture locus of titanium alloy Ti-6Al-4V. The study is based on multiaxial experimental tests and numerical simulations of detailed finite element (FE) models, to calibrate the Bao-Wierzbicki failure criterion based on phenomenological ductile criteria, as given in relation in Equation [1.18].

$$\varepsilon_f = \begin{cases} \frac{D_1}{(1+3\eta)} + D_2 & -1/2 < \eta \leq 0 \\ D_3\eta_2 + D_4\eta + D_5 & 0 < \eta \leq \eta_{\mathrm{T}} \\ D_6 + D_7 e^{(-D_6\eta)} & \eta_{\mathrm{T}} \leq \eta \end{cases} \qquad [1.18]$$

where ε_f is failure strain function, D is damage parameter, η is stress triaxiality, and η_{T} is transition stress triaxiality point. This set of equations takes the cut-off triaxiality value and the relative minimum failure strain value at pure shear conditions into account; and these failure locus features have not been referred to by the earlier mentioned Hooputra model [Hooputra et al. (2004)].

1.3.8 Critical Assessment of Issues and Results of Previous Works

Previous works of micro-lattice structures manufactured using the SLM for the applications of foreign object impact in sandwich constructions were mainly using SS316L stainless steel as the material. Shen et al. (2010) reported on the modes of failure of these micro-lattice structures. Other than the modes of failure, the effect of cell size to the collapse of the unconstrained body centred cubic (BCC) micro-lattice structures was investigated by Ushijima et al. (2011). In addition to Ushijima et al. (2011) works, Gumruk and Mines (2013) investigated on the effect of micro-scaled geometry to the collapse of stainless steel micro-lattice structures. Earlier, a key paper for the micro-lattice structures research works was published by Tsopanos et al. (2010) which studied the effects of SLM manufacturing parameters on the properties and dimensions of the produced stainless steel micro-lattice structures. All of these previous works provide an important background to the investigations of micro-lattice structures manufactured from different types of metallic materials. Due to the different mechanisms of materials during the SLM process, the modes of failure as well as the collapse behaviours of the stainless steel micro-lattice structures as reported in previous works [Shen et al. (2010); Ushijima et al. (2011)] were not necessarily applicable to micro-lattice structures manufactured from other materials such as Ti-6Al-4V titanium alloy. There are several issues need to be addressed in the SLM manufacturing of titanium alloy micro-lattice structures, and the definition of issues with this material was recently published in Mines et al. (2013).

The main issue to be clarified in the micro-lattice structure research is the potential of BCC Ti-6Al-4V micro-lattice structures for foreign object impact applications. The previously explored stainless steel micro-lattice structures have low specific strength and are less suited to high performance applications. Therefore, material such as Ti-6Al-4V with higher specific strength could be the next focus. However, the Ti-6Al-4V material is more sensitive to the SLM manufacturing process [Yadroitsev (2009)], and therefore the performance of this material depends on the quality of the produced SLM structures. In order to fully utilize the Ti-6Al-4V micro-lattice structures manufactured from the SLM technology, two major issues

need to be further addressed, which are the quality and the properties of the micro-lattice structure, arise from the relations between process-material-structural performance.

An approach comprises of four areas was taken in an attempt to address the issues. The four areas include the manufacturing technology, microstructural characterisation, mechanical testing and finite element modelling. For the manufacturing technology which involves the SLM, the same apparatus and procedures as applied in the production of the stainless steel micro-lattice structures were used due to the confidence in the established approach by Tsopanos et al. (2010). For the microstructural characterization, images from the optical microscopy and scanning electron microscopy were used to determine the macrostructure and microstructure as well as the diameter and circularity of the micro-struts. Image analysis system was not fully applied in this study due to its complexity, and the system was only used for capturing images of optical microscopy. Other method that could be used for microstructural characterization is the combination of light microscopy and image analysis which was reported in other researches such as in Kobryn et al. (2000). For mechanical testing of micro-struts, tensile test was applied and the compliance correction method was used in the determination of mechanical properties of the material. This method was widely used in high modulus fiber testing [Li and Langley (1985); ASTM D 3379-75 (1999)] and was chosen for its simplicity and reliability. The only drawback for this testing is it may not represent the real condition of micro-struts in a BCC micro-lattice structure under loading condition. Other than micro-tensile test, micro-compression test and strut bending test could also be considered for the micro-struts testing. However, the micro-compression test would be much more complicated with the issues of alignment, buckling and end constraints [Hemker and Sharpe (2007)], while the strut bending test would need a sophisticated support system for strain measurement such as the digital image correlation (DIC) system. For the finite element modelling, it was decided to use the existing approach of Smith (2012). The model in the study worked well for the stainless steel micro-lattice structure, and therefore, for this study, the model was improved to suit the diameter and material properties of the Ti-6Al-4V micro-lattice structure.

1.4 OVERVIEW OF MATERIALS

Throughout this study, the specimens used were the materials manufactured between the year of 2008 and 2009, which was the same period of time with the specimens used in Shen (2009) and Tsopanos et al. (2010). The machine and manufacturing conditions were the same with that described in Tsopanos et al. (2010). The study of SLM stainless steel SS316L micro-lattice structures [Tsopanos et al. (2010)] inspired the current study of SLM Ti-6Al-4V micro-lattice structures, where the effects of manufacturing parameters as studied in Tsopanos et al. (2010) were applied. With the rest of the conditions the same, only the powder material was changed from SS316L to Ti-6Al-4V. The condition with laser power of 200 W and exposure time of 1000 μs was applied in the manufacturing of Ti-6Al-4V, and a reasonable structure of Ti-6Al-4V micro-lattices were produced [Shen (2009)].

The machine used to produce the specimens was the MCP Realizer II (commercial SLM workstation supplied by MCP (UK) Ltd.) with a build envelope of 250 mm X 250 mm X 240 mm. The machine which was also known as the SLM250, was located at the previous SLM laboratory before being re-located at a new laboratory in year 2011. The machine was re-calibrated at the new location, and this gives a different manufacturing route as compared to that of Tsopanos et al. (2010) and Shen (2009).

The aim of the current study is to define and fully clarify issues on the behaviour of the SLM Ti-6Al-4V micro-lattice structure. It is known that the manufacturing route is critical to the produced SLM materials, which could result in change of properties with change of manufacturing route. Therefore, specimens manufactured at the same period of time with the earlier studies were used. There were restricted numbers of specimens at restricted manufacturing parameters at the selected set up of the SLM250. Table 1.3 listed all the specimens reported in this study with the respective identifications. Some of the specimens from earlier studies were included in the list since they were used in data comparison with the current study.

Table 1.3: List of specimens used throughout the study of SLM Ti-6Al-4V micro-lattice structures (*comparison data)

Type	Year produced	Material ID used in this study	Architecture / Build angle	Dimension	Specimen numbers	Manufacturing parameters	Post-processing treatment	Remarks
Block	2008 (Specimens were produced by Dr. S. Tsopanos)	B(1-3)-200-1000-AR	BCC 2.5 mm	20x20x20mm^3	# 1 – 3	200Wx1000µs	As-received	Hasan et al. (2011)
		B(1-3)-200-1000-HIP	BCC 2.5 mm	20x20x20mm^3	# 1 – 3	200Wx1000µs	HIPped	*Reported in Shen (2009)
		B(1-3)-180-500-AR	BCC 2.5 mm	20x20x20mm^3	# 1 – 3	180Wx500µs	As-received	*Reported in Shen (2009)
		B(1-3)-180-500-HIP	BCC 2.5 mm	20x20x20mm^3	# 1 – 3	180Wx500µs	HIPped	*Reported in Shen (2009)
		B1-180-1000-AR-M	BCC 2.5 mm	20x20x20mm^3	# 1	180Wx1000µs	As-received	Node & microstructure analysis
		B1-180-1000-AR	BCC 2.5 mm	20x20x20mm^3	# 1	180Wx1000µs	As-received	Compression test
		B(1-2)-160-1000-AR	BCC 2.5 mm	20x20x19mm^3	# 1 – 2	160Wx1000µs	As-received	Compression test/geometry analysis
		B(1-2)-160-1000-HT	BCC 2.5 mm	20x20x19mm^3	# 1 – 2	160Wx1000µs	Heat-treated	Compression test/geometry analysis
		B1-160-1000-HT-M	BCC 2.5 mm	20x20x19mm^3	# 1	160Wx1000µs	Heat-treated	Node/microstructure analysis
Single Strut	2009 (Specimens were produced by Dr. S. Tsopanos)	S(1-2)-90-200-1000-AR	90°	23 mm	# 1 – 2	200Wx1000µs	As-received	Microstructure/geometry analysis
		S1-90-200-1000-HT(A)-M	90°	23 mm	# 1	200Wx1000µs	Heat-treated (A)	Microstructure analysis
		S1-90-200-1000-HT(B)-M	90°	23 mm	# 1	200Wx1000µs	Heat-treated (B)	Microstructure analysis
		S1-35-200-1000-AR-M	35°	43 mm	# 1	200Wx1000µs	As-received	Microstructure/geometry analysis
		S(1-15)-35-200-1000-AR	35°	43 mm	# 1 – 15	200Wx1000µs	As-received	Tensile test/geometry analysis
		S(1-9)-35-200-1000-HT(B)	35°	43 mm	# 1 – 9	200Wx1000µs	Heat-treated (B)	Tensile test/geometry analysis

1.5 FOCUS OF THE STUDY

The focus of this study is the understanding and use of a new and innovative micro-lattice core material manufactured using selective laser melting (SLM) [Yadroitsev (2009); Rehme (2010)]. In this process, metallic powder is selectively melted to form spatial micro-lattice structures. Previous papers on micro-lattice structures have discussed the manufacturing process for stainless steel micro-lattices [Tsopanos et al. (2010)], some testing of micro-lattice blocks and beams [Shen et al. (2010)] and some theoretical parametric studies [Ushijima et al. (2011)]. A feature of the SLM manufacturing process is the ability to realize lattice structures with 50 micron features, which means that the lattice structures can be tailored with the application in mind. Once the manufacturing process is refined, this shifts emphasis to detailed study and optimisation of cellular materials, which includes structural engineering at the small scale. Ushijima et al. (2011) developed parametric compressive models for the body centred cubic micro-lattice geometry in the form of blocks, and showed the complexity of parametric modelling. These ideas need to be developed further so as to fully exploit the manufacturing process.

It should be noted that there are other manufacturing processes for micro-lattice structures. For example, micro-lattice structures have been realized in thiolene polymer using ultra violet light [Jacobsen et al. (2007)]. Strut diameters of the order of 200 micrometers and cell sizes of the order of 1mm have been obtained. Cansizoglu et al. (2008) realised a hexagonal/rectangular hybrid micro-lattice structure with a cell size of 5mm and a strut diameter of 500μm. Electron beam melting is faster and more economic compared to selective laser melting, but the surface quality of components is not as good [Gibson et al. (2010)]. A common theme in this study is ensuring good mechanical properties for parent materials and ensuring good quality lattice construction. The definition of the process-material-property relation has been identified as being critical for the full exploitation of additive manufacturing technology [Gibson et al. (2010)]. These issues will be addressed in this study.

One of the major performance issues of aerospace twin skinned construction is their foreign object impact performance [Mines et al. (1998)]. This can be a result of dropped tools, hail, runway debris, and bird strike. Impact can give rise to sub critical damage, or partial and full penetration. Impact behaviour is dependent the skin and the core, and in this study, the focus will be on cores. The foreign object impact performance of the cores could be further enhanced by quantifying micro-inertia and material strain rate effects in the core and by adapting micro-lattice structure architecture to improve impact performance [Mines et al. (2013)]. For the SS316L BCC case, progressive collapse is dominated by plastic hinges in the vicinity of the node and so impact effects will relate to beam bending dynamics and rate dependence of the yield stress of the parent material [Mines et al. (2013)]. For the Ti-6Al-4V BCC case in this study, material rupture becomes an issue.

The study addresses the application of a novel manufacturing technology to a widely used structural application, which is the open cellular core. If the manufacturing technology is to be fully utilised, two major issues need to be addressed further. The most immediate major issue is to fully define, in detail, the quality of the micro-lattice structure. This includes dimensional accuracy, surface quality, residual stresses, material microstructure, trace impurities, and hence variabilities in material and structural performance. The longer term major issue is to rigorously define the relation between process-material-structural performances, which leads to the study presented in this thesis. Figure 1.24 shows a diagram which simplifies the approach taken for this study.

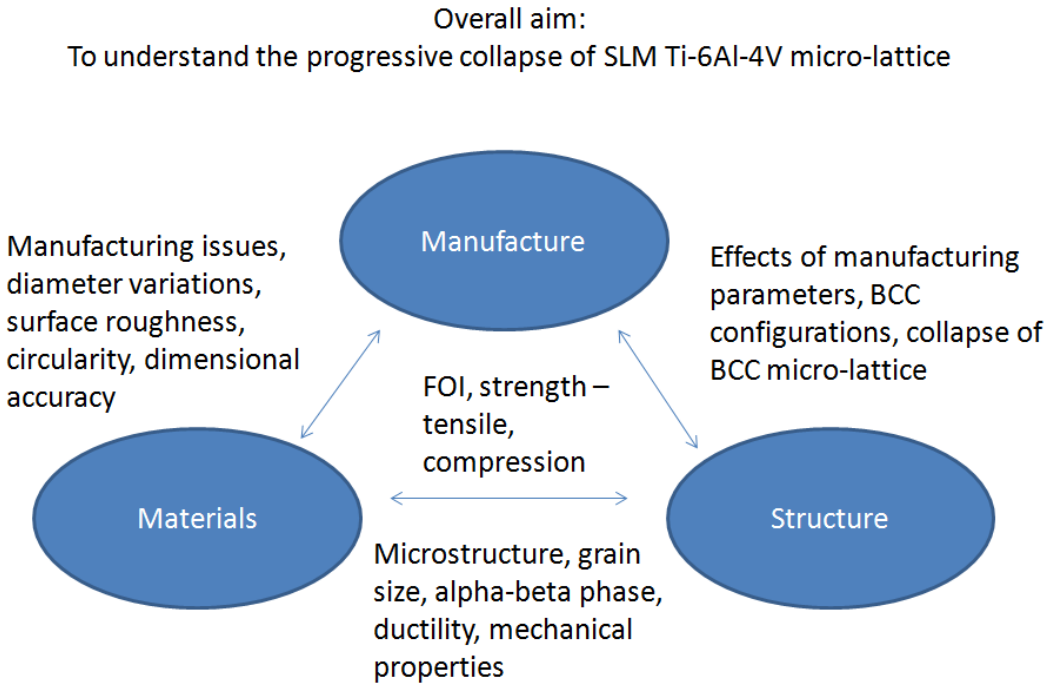

Figure 1.24: Diagram showing the approach taken in this thesis

1.6 SUMMARY OF CHAPTER 1

The background of the current research has been discussed in the form of a general discussion on cellular material, the SLM process, competing manufacturing processes, mechanical properties of lattice material, lattice material response on static and impact loading, titanium alloy as parent material, as well as plasticity and ductile failure theory. It has been mentioned that periodic open-cell cellular material is known as lattice structure, which has predictable properties and can be suggested to be used in structural applications for energy absorption. The complexity in manufacturing of open-cell lattice structure can be realized with the selective laser melting (SLM) process, but the properties and quality of the structure strongly depend on control parameters of the process [Rehme (2010)]. Before the emergence of SLM, there were already manufacturing processes to produce lattice materials, however, the SLM is the process that can deliver a wide range of product requirements for various applications [Kruth et al. (2004)]. Among several topologies of periodic lattice structures, it was found that the pyramidal truss arrangement is desirable for its strength and properties, although the progressive collapse of the lattice structures are non-optimal [Fan et al. (2008); Mines (2008)]. The pyramidal truss unit cell can be rearranged to be the octahedral or octet truss unit cell. The octahedral arrangement is also known as the body centered cubic (BCC) arrangement. There were many studies on the octet truss including studies on response of stainless steel octahedral lattice structures produced by the SLM process, which was found comparable to the response of Alporas aluminium foam [McKown et al. (2007)]. The SLM process was then extended to produce the Ti-6Al-4V micro-lattice structure, since the material is thought to be more applicable to foreign object impact in aerospace applications. Studies revealed that the strength of SLM Ti-6Al-4V material was comparable to its bulk material, but post-manufacturing heat-treatment was suggested for the material to improve its properties. The study of plasticity and collapse of the SLM Ti-6Al-4V BCC micro-lattice structure is set as the focus in this research, to fill the gap identified in current literature, and with the aim to investigate the viability of this material for applications in Foreign Object Impact (FOI) in aerospace sandwich constructions.

REFERENCES OF CHAPTER 1

Abaqus Theory Manual (2009) Abaqus 6.9-EF Online Documentation. Dassault Systemes Simulia Corp. Providence, RI, USA.

ASTM D 3379-75 (Reapproved 1989) (1999) 'Standard test method for tensile strength and Young's modulus for high-modulus single-filament materials'. *Annual Book of ASTM Standards*, pp. 732-735.

ASTM Standard (2012) '*Standard specification for Addititive Manufacturing Titanium-6 Aluminum-4 Vanadium with Powder Bed Fusion*', ASTM International, DOI: 10.1520/F2924-12.

Banhart, J. (2001) 'Manufacture, characterisation and application of cellular metals and metal foams'. *Progress in Materials Science*, 46: 559-632.

Boyer, R., Welsch, G., Collings, E.W. (Eds.) (1994) Material Properties Handbook *Titanium Alloys*. ASM International: Material Park, OH. http://www.matweb.com

Cansizoglu, O., Harrysson, O., Cormier, D., West, H., Mahale, T. (2008) 'Properties of Ti-6Al-4V non-stochastic lattice structures fabricated via electron beam melting'. *Materials Science and Engineering A*, 492: 468-474.

Cansizoglu, O., Harrysson, O.L., West, H.A., Cormier, D.R., Mahale, T. (2008B) 'Applications of structural optimization in direct metal fabrication'. *Rapid Prototyping Journal*, 14(2): 114-122.

Deshpande, V.S. and Fleck, N.A. (2001) 'Collapse of truss core sandwich beams in 3 point bending'. *International Journal of Solids and Structures*, 39: 6275-6305.

Deshpande, V.S., Fleck, N.A., Ashby, M.F. (2001) 'Effective properties of the octet-truss lattice material'. *Journal of the Mechanics and Physics of Solids*, 49(8): 1747-1769.

Doyoyo, M. and Hu, J.W. (2006) 'Multi-axial failure of metallic strut-lattice materials composed of short and slender struts'. *International Journal of Solids and Structures*, 43: 6115-6139.

Evans, A.G., Hutchinson, J.W. and Ashby, M.F. (1998) 'Cellular metals'. *Current Opinion in Solid State & Material Science*, 3: 288-303.

Facchini, L., Magalini, E., Robotti, P., Molinari, A., Hoges, S., Wissenbach, K. (2010) 'Ductility of a Ti-6Al-4V alloy produced by selective laser melting of prealloyed powders'. *Rapid Prototyping Journal*, 16/6: 450-459.

Fan, H.L., Fang, D.N., Jing, F.N. (2008) 'Yield surfaces and micro-failure mechanism of block lattice truss materials'. *Materials and Design*, 29: 2038-2042.

Gibson, L.J., and Ashby, M.F. (1999) *Cellular Solids: Structure and Properties*. 2nd Edition. Cambridge University Press, United Kingdom.

Gibson, I, Rosen, D.W., Stucker, B. (2010) *Additive Manufacturing Technologies*. Springer, New York, USA.

Giglio, M., Manes, A., Vigano, F. (2012) 'Ductile fracture locus of Ti-6Al-4V titanium alloy'. *International Journal of Mechanical Sciences*, 54:121-135.

Gumruk, R. And Mines, R.A.W. (2013) 'Compressive Behaviour of Stainless Steel Micro-lattice Structures'. *International Journal of Mechanical Sciences*, 68: 125-139.

Hasan, R., Mines, R., Shen, E., Tsopanos, S., Cantwell, W., Brooks, W., Sutcliffe, C. (2010) 'Comparison of the drop weight impact performance of sandwich panels with aluminium honeycomb and titanium alloy micro-lattice cores'. *Applied Mechanics and Materials*, 24-25: 413-418.

Hasan, R., Mines, R., Shen, E., Tsopanos, S., Cantwell, W. (2011) 'Comparison on compressive behaviour of aluminium honeycomb and titanium alloy micro lattice blocks'. *Key Engineering Materials*, 462-463: Pp. 213-218.

Hemker, K.J. and Sharpe, Jr.W.N. (2007) 'Microscale Characterization of Mechanical Properties'. *Annual Review of Materials Research*, 37: 93-126.

Hooputra, H., Gese, H., Dell, H., Werner, H. (2004) 'A comprehensive failure model for crashworthiness simulation of aluminium extrusions'. *International Journal of Crashworthiness*, 9(5): 449-463.

Jacobsen, A.J., Barvosa-Carter, W., Nutt, S. (2007) 'Compression behaviour of micro scale truss structures formed from self propagating polymer wave guides'. *Acta Materialia*, 55: 6724-6733.

Kellens, K., Yasa, E., Renaldi, Dewulf, W., Kruth, J.P., Duflou, J.R. (2011) 'Energy and resource efficiency of SLS/SLM processes'. *22nd International Solid Freeform Symposium*, Austin, Texas, pp. 1-16.

Kobryn, P.A., Moore, E.H., Semiatin, S.L. (2000) 'The Effect of Laser Power and Traverse Speed on Microstructure, Porosity, and Build Height in Laser-Deposited Ti-6Al-6V'. *Scripta Materialia*, 43: 299-305.

Kruth, J.P., Froyen, L., Van Vaerenbergh, J., Mercelis, P., Rombouts, M., Lauwers, B. (2004) 'Selective laser melting of iron-based powder'. *Journal of Materials Processing Technology*, 149: 616-622.

Lemaitre, L. and Chaboche, J.L. (1990) *Mechanics of Solid Materials*. Cambridge University Press, UK.

Leuders, S., Thone, M., Riemer, A., Niendorf, T., Troster, T., Richard, H.A., Maier, H.J. (in press – corrected proof, November 2012) 'On the mechanical behaviour of titanium alloy TiAl6V4 manufactured by selective laser melting: Fatigue resistance and crack growth performance'. *International Journal of Fatigue*,

http://dx.doi.org.ezproxy.liv.ac.uk/10.1016/j.ijfatigue.2012.11.011

Li, C.T. and Langley, N.R. (1985) 'Improvement in fiber testing of high-modulus single-filament materials'. *Journal of American Ceramic Society*, Vol. 68: C-202-C-204.

Lim, C.H., Jeon, I., Kang, K.J. (2009) 'A new type of sandwich panel with periodic cellular metal cores and its mechanical performances'. *Material and Design*, 30: 3082-3093.

Luxner, M.H., Woesz, A., Stampfl, J., Fratzl, P., Pettermann, H.E. (2009) 'A finite element study on the effects of disorder in cellular structures'. *Acta Biomaterialia*, 5: 381-390.

McKown, S., Cantwell, W.J., Brooks, W.K., Mines, R.A.W., Tsopanos, S., Sutcliffe, C.J. (2007) 'High performance sandwich structures with hierarchical lattice cores'. *Proceedings of the 28th International European SAMPE*, Europe. 396-401.

McKown, S., Shen, Y., Brooks, W.K., Sutcliffe, C.J., Cantwell, W.J., Langdon, G.S., Nurick, G.N., Theobald, M.D. (2008) 'The quasi-static and blast loading response of lattice structures'. *International Journal of Impact Engineering*, 35: 795-810.

Mines, R.A.W., Worrall, C.M., Gibson, A.G. (1998) 'Low Velocity Perforation Behaviour of Polymer Composite Sandwich Panels'. *International Journal of Impact Engineering*, 21(10): 855-879.

Mines, R.A.W., McKown, S., Cantwell, W., Tsopanos, S., Brooks, W., Sutcliffe, C.J. (2007) 'On the progressive collapse of micro-lattice structures'. *Proceedings of the 13th International Conference on Experimental Mechanics, Alexandroupolis*, Greece, Paper No. 158.

Mines, R.A.W. (2008) 'On the characterization of foam and micro-lattice materials used in sandwich construction'. *Strain*, 44: 71-83.

Mines, R.A.W., McKown, S., Tsopanos, S., Shen, E., Cantwell, W., Brooks, W., Sutcliffe, C. (2008) 'Local effects during indentationh of fully supported sandwich panels with micro lattice cores'. *Applied Mechanics and Materials*, 13-14: 85-90.

Mines, R., Girard, Y., Fascio, V. (2009) 'On the development of conventional and micro-lattice cellular metals as core materials in aerospace sandwich construction'. *SAMPE Europe Conference & Exhibition*, Paris. Paper no. 248-256.

Mines, R.A.W., Tsopanos, S., Shen, Y., Hasan, R., McKown, S.T. (2013) 'Drop Weight Impact Behaviour of Sandwich Panels with Metallic Micro-lattice Cores'. *International Journal of Impact Engineering*, 60: 120-132.

Morteau, E. and Fualdes, C. (2006) 'Composites @ Airbus Damage Tolerance Methodology'. ESAC – Ref X029 PR0608046. National Institute for Aviation Research, Chicago, USA.

Mullen, L., Stamp, R.C., Fox, P., Jones, E., Ngo, C., Sutcliffe, C.J. (2009) 'Selective Laser Melting: A unit cell approach for the manufacture of porous, titanium, bone in-growth constructs, suitable for orthopedic applications. II. Randomized structures'. *Journal of Biomedical Material Research Part B: Appliaed Biomaterial*, 92B: 178-188.

Mullen, L., Stamp, R.C., Brooks, W.K, Jones, E., Sutcliffe, C.J. (2009B) 'Selective Laser Melting: A regular unit cell approach for the manufacture of porous, titanium, bone in-growth constructs, suitable for orthopedic applications'. *Journal of Biomedical Material Research Part B: Applied Biomaterial*, 89B: 325-334.

Murr, L.E., Quinones, S.A., Gaytan, S.M., Lopez, M.I., Rodela, A., Martinez, E.Y., Hernandez, D.H., Martinez, E., Medina, F., Wicker, R.B. (2009) 'Microstructure and mechanical behaviour of Ti-6Al-4V produced by rapid-layer manufacturing, for biomedical applications'. *Journal of the Mechanical Behaviour of Biomedical Materials*, 2: 20-32.

Polmear, I.J. (2006) *Light alloys: From traditional alloys to nanocrystals*. 4th ed, Elsevier/Butterworth-Heinemann, Amsterdam.

Pazos, L., Corengia, P., Svoboda, H. (2010) 'Effect of surface treatments on the fatigue life of titanium for biomedical applications'. *Journal of the Mechanical Behaviour of Biomedical Materials*, 3: 416-424.

Queheillalt, D.T. and Wadley, H.N.G. (2009) 'Titanium alloy lattice truss structures'. *Material and Design* 30: 1966-1975.

Rehme, O. (2010) *Cellular Design for Laser Freeform Fabrication*. Cuvillier Verlag, Gottingen.

Santorinaios, M., Brooks, W., Sutcliffe, C.J., Mines, R.A.W. (2006) WIT Trans. Built Environ. 85: 481-490.

Shen, Y. (2009) *High performance sandwich structures based on novel metal cores*. Thesis PhD. University of Liverpool, UK.

Shen, Y., McKown, S., Tsopanos, S., Sutcliffe, C.J., Mines, R.A.W., Cantwell, W.J. (2010) 'The Mechanical Properties of Sandwich Structures Based on Metal Lattice Architectures'. *Journal of Sandwich Structures and Materials*, 12: 159-180.

Smith, M.I.H. (2012) *The compressive response of novel lattice structures subjected to static and dynamic loading*, PhD Thesis, University of Liverpool, United Kingdom.

Song, B., Dong, S., Zhang, B., Liao, H., Coddet, C. (2012) 'Effects of processing parameters on microstructure and mechanical property of selective laser melted Ti6Al4V'. *Materials & Design*, 35: 120-125.

Stamp, R., Fox, P., O'Neill, W., Jones, E., Sutcliffe, C. (2009) 'The development of a scanning strategy for the manufacture of porous biomaterials by selective laser melting'. *Journal of Material Science: Material Medic*, 20: 1839-1848.

Sun, J., Yang, Y., Wang, D. (2012) 'Mechanical properties of Ti-6Al-4V octahedral porous material unit formed by selective laser melting'. *Advances in Mechanical Engineering*, Article ID 427386, doi: 10.1155/2012/427386

Sypeck, D.J. (2005) 'Cellular Truss Core Sandwich Structures'. *Applied Composite Materials*, 12: 229-246.

Thijs, L., Verhaeghe, F., Craeghs, T., Humbeeck, J.V., Kruth, J.P. (2010) 'A study of the microstructural evolution during selective laser melting of Ti-6Al-4V'. *Acta Materialia*, 58: 3303-3312.

Tsopanos, S., Mines, R.A.W., McKown, S., Shen, Y., Cantwell, W.J., Brooks, W., Sutcliffe, C.J. (2010) 'The influence of processing parameters on the mechanical properties of selectively laser melted stainless steel microlattice

structures'. *Journal of Manufacturing Science and Engineering*, 132: 041011-1 - 140111-12.

Tan, H. (2009) *Flow Theory of Plasticity*. Lecture notes, University of Aberdeen. http://homepages.abdn.ac.uk/h.tan/pages/teaching/plasticity/Flow.pdf

Ushijima, K., Cantwell, W.J., Mines, R.A.W., Tsopanos, S., Smith, M. (2011) 'An investigation into the compressive properties of stainless steel micro-lattice structures'. *Journal of Sandwich Structures and Materials*, 13: 303-329.

Vandenbroucke, B. and Kruth, J.P. (2007) 'Selective laser melting of biocompatible metals for rapid manufacturing of medical parts'. *Rapid Prototyping Journal*, 13/4: 196-203.

Wadley, H.N.G., Fleck, N.A., Evans, A.G. (2003) 'Fabrication and structural performance of periodic cellular metal sandwich structures'. *Composites Science and Technology*, 63: 2331-2343.

Wang, J., Evans, A.G., Darmasena, K., Wadley, H.N.G. (2003) 'On the performance of truss panels with Kagome core'. *International Journal of Solids and Structures*, 40(25): 6981-6988.

Wang, Y., Shen, Y., Wang, Z., Yang, J., Liu, N., Huang, W. (2010) 'Development of highly porous titanium scaffolds by selective laser melting'. *Material Letters*, 64: 674-676.

Warwick, G. (2010) 'Adding value: Additive manufacturing could bring much needed affordability to aerospace products'. *Aviation Week and Space Technology*, November 1/8, pp. 80-83.

Wierzbicki, T., Bao, Y., Lee, Y.W., Bai, Y. (2005) 'Calibration and evaluation of seven fracture models'. *International Journal of Mechanical Sciences*, 47: 719-743.

Wu, X. (2006) 'Review of alloy and process development of TiAl alloys'. *Intermetallics*, 14: 1114-1122.

Yadroitsev, I. (2009) *Selective laser melting Direct manufacturing of 3-D objects by selective laser melting of metal powders*. Lambert Academic Publishing AG & Co. KG, Germany.

Yadroitsev, I., Gusarov, A., Yadroitsava, I., Smurov, I. (2010) 'Single track formation in selective laser melting of metal powders'. *Journal of Materials Processing Technology*, 210: 1624-1631.

Zhou, J., Shrotriya, P., Soboyejo, W.O. (2004) 'On the deformation of aluminum lattice block structures: from struts to structures'. *Mechanics of Materials*, 36: 723-737.

CHAPTER 2: CHARACTERIZATION STUDY ON SELECTIVELY LASER MELTED (SLM) Ti-6Al-4V MICRO-STRUT

2.1 INTRODUCTION

The decision to use titanium alloy Ti-6Al-4V in modern aircraft parts is based on properties of the material that make it suitable for the purpose, such as high strength-to-weight ratio and high temperature resistance of the material. However, competition from aluminium alloys in terms of cost will affect the continued usage of titanium alloy in the future. It is believed that the application of titanium alloy could be increased by investing in improved and advanced technology in production and manufacturing of the material [Polmear (2006)]. Research in improving the performance of the material and its development is still ongoing. In addition to this there are also some remaining challenges especially in temperature-microstructure-properties inter-relations [Wu (2006)]. Since the titanium alloys can be manufactured from its powder form, the advanced technology of Selective Laser Melting (SLM) was found to be suitable to produce solid titanium parts directly from the metal powder [Rehme (2010)]. However, in order to accomplish the aerospace application requirements and standards, further explorations of properties and behaviours of the novel material need to be done.

Experimental tests and analyses of the SLM Ti-6Al-4V micro-lattice structure as core material in sandwich construction for aerospace applications has been carried out in the University of Liverpool, since it has been reported that its specific strength is comparable to the aluminum honeycomb [Mines et al. (2009)]. Despite showing a comparable strength, a major drawback of this material is that it exhibits surprisingly 'brittle-like' fracture failure [Hasan et al. (2010)], while it is known than the Ti-6Al-4V alloy is having relatively high strength and formability [Polmear (2006)]. In order to fully understand the properties and behaviours of the SLM Ti-6Al-4V micro-lattice structure manufactured in this university, it is important to characterize the basic unit of the material, which is the micro-strut.

In this study, geometrical analysis of micro-strut was done to quantify the dimensional accuracy and quality of the material. Material analysis was carried out in order to investigate the resulting microstructure from manufacturing process which affects fracture and mechanical properties of micro-strut. Some of specimens were heat-treated and the effects of resultant microstructure on the properties of the micro-struts were observed. The main deliverable of this study is the suggestion of the stress-strain curve for the micro-strut. The determined elastic modulus and yield stress values are essentials for future use in analytical and numerical studies of the materials.

2.2 MATERIALS AND SLM MANUFACTURING PROCESS

The SLM Ti-6Al-4V micro-lattice was manufactured from Titanium Powder Grade 5 ASTM (Ti-6Al-4V), produced by TLS Technik GmbH & Co., Germany, with chemical composition of elements as shown in Table 2.1. The average particle size of this powder was less than 45 μm [Shen (2009)]. For this study, the micro-lattices were manufactured using an MCP Realizer II (commercial SLM workstation supplied by MCP (UK) Ltd.) with a build envelope of 250 mm X 250 mm X 240 mm. It was fitted with a 200 W continuous wave Ytterbium fiber laser operating at a wavelength of 1068 – 1095 nm and was the apparatus by Tsopanos et al. (2010) where further details can be found. To manufacture the titanium and its alloys, it is important to avoid oxygen pick up by the molten metal and therefore an argon atmosphere, with no more than 0.2% oxygen, was maintained with an overpressure of 10-15 mbars. As the Realizer II was used for a range of materials, the machine was carefully cleaned on change over using a standard procedure [Sutcliffe (n.d)]. More discussions of manufacturing process are described in Chapter 3 which focuses on micro-lattice block formation.

Based on preliminary research in SLM Ti-6Al-4V micro-lattice structure [Shen (2009)], a set of manufacturing parameters with 200 W laser power and 1000 µs laser exposure time were selected since it gave an acceptable micro-lattice structure performance. This combination of parameters for the Ti-6Al-4V micro-lattice structure core resulted in a more localized impact area in the sandwich constructions for foreign object impact as compared to aluminium honeycomb core [Hasan et al. (2010)].

Table 2.1: Chemical composition of elements for Titanium Powder Grade 5 ASTM from TLS Technik GmbH & Co.

Element	Al	V	Fe	Si	O	C	N	H
Max.	5.5-6.5	3.4-4.5	0.25	n.a	0.13	0.08	0.05	0.012
Typical	5.9	3.9	0.19	n.a	0.12	0.01	0.01	0.004

In this study, material analysis was based on a unit of SLM Ti-6Al-4V micro-lattice structure, which was built from micro-struts with length of $\sqrt{3}/2$ from a unit cell length l in Body-Centred-Cubic (BCC) architecture. Figure 2.1(a) illustrates a unit cell for BCC structure while Figure 2.1(b) defines geometry of the BCC unit cell, as been adapted from Ushijima et al. (2011).

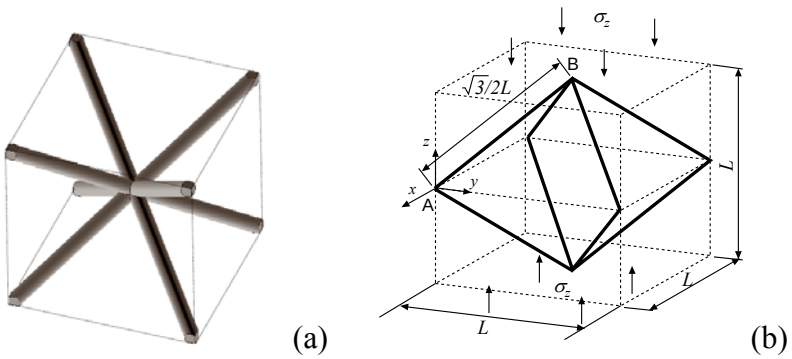

Figure 2.1: (a) A schematic of unit cell for BCC structure; (b) Geometry of the BCC unit cell [Ushijima et al. (2011)]

2.2.1 The As-received SLM Ti-6Al-4V Micro-Struts

Single micro-struts were manufactured using the same parameters of that for micro-lattice structure, which were at 200 W laser power and 1000 μs laser exposure time. The rest of manufacturing conditions were assumed to be the same; hence the single micro-strut properties can be assumed to represent the micro-lattice structure properties. Since the arrangement of micro-struts in BCC architecture was at 35° angle from horizontal, the single struts were manufactured at similar build angle, with maximum length limited to 43 mm, due to manufacturing restriction. However, there are also few struts manufactured at 90° build angle with 23 mm length, for geometry and quality comparison purposes. This will be further discussed in the next sections.

The SLM process produced the micro-struts by accumulating laser melted powder layers of 50 μm thicknesses. The thickness was the distance of build platform movement prior to every new powder layer being spread, scanned and melted according to specific-computer generated pattern. The single-pass laser melted powder of each layer fused to each other, forming thin solid micro-struts towards the end of the process. In producing the 90° build angle micro-struts, the melted layers were directly fused on top of each preceding layer, while for the 35° build angle micro-struts, a part of the successive layers were shifted to one side from top of preceding layer in order to build up slanted struts with approximately 35° angle from horizontal. Figure 2.2 illustrates schematic of micro-strut builds for both 90° and 35° build angle respectively. The example of SLM micro-struts builds were given in Figure 2.3, which showed the SLM stainless steel SS316L micro-struts as reported in Tsopanos et al. (2010).

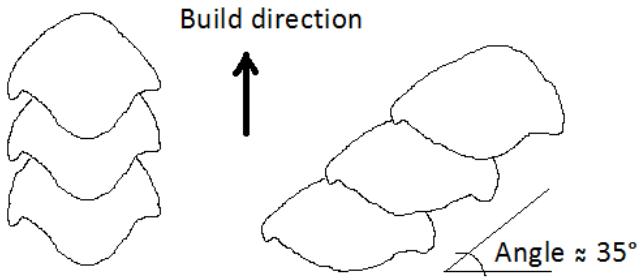

Figure 2.2: Schematic of micro-strut manufactured at 90° build angle (left) and 35° build angle (right)

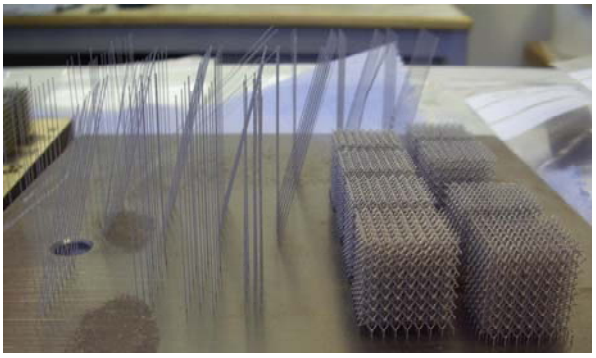

Figure 2.3: SLM SS316L struts and micro-lattice blocks prior to removal from steel substrate [Tsopanos et al. (2010)]

It should be noted that there might be some effect in properties between different build angles of single struts. As reported by Shen (2009), the titanium alloy struts built at an angle of 35° have larger (14%) diameter than the struts built vertical to the laser beam. Figure 2.4(a) shows a front view image of the SLM Ti-6Al-4V BCC micro-lattice structure block; and Figure 2.4(b) shows two types of the SLM Ti-6Al-4V micro-struts materials produced for this research at the University of Liverpool. Meanwhile, Figure 2.5(a) and (b) show the optical microscopic image of longitudinal cross-sections for both micro-struts built at 90° and 35° angles. It was noticed that there was a difference in both struts, specifically, variations in outer surface, and these were comparable to that of the schematic which was illustrated in Figure 2.2. The geometrical variations will be discussed later in the following sections. Figure 2.6 shows the microstructure of the as-received micro-strut (35° build angle) at a higher magnification than that of Figure 2.5(b). The microstructure observed was

similar to that of an 'as-welded' Ti-6Al-4V alloy with a dendritic 'ghost' β phase structure, formed on freezing, inside which was a needle martensite structure, formed on cooling to room temperature. There will be further discussions on the microstructure in the following sections within this chapter.

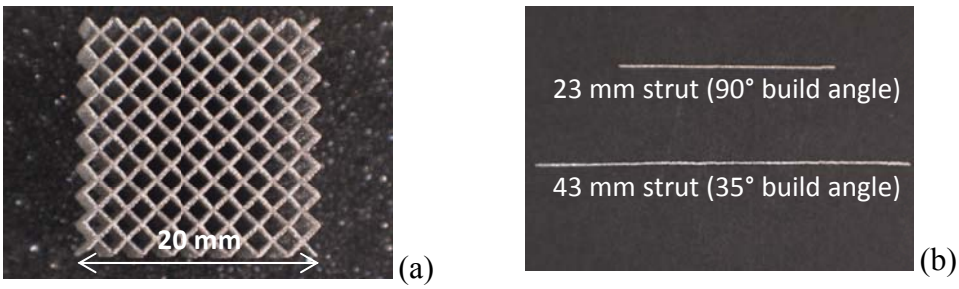

(a) (b)

Figure 2.4: (a) A side view of 20 mm cubed BCC micro-lattice structure block [B(1-3)-200-1000-AR]; (b) the SLM Ti-6Al-4V micro-struts [S1-90-200-1000-AR and S1-35-200-1000-AR-M]

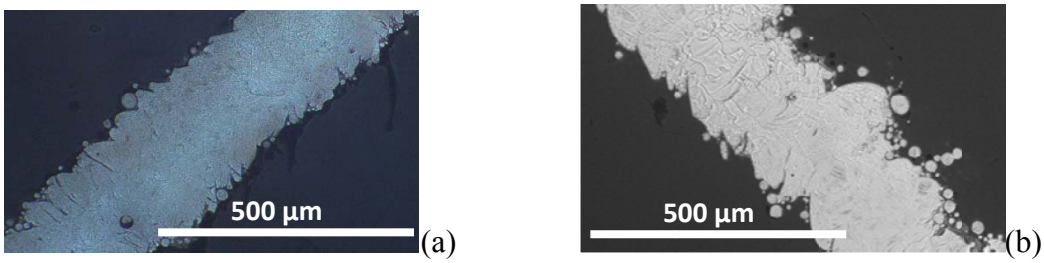

(a) (b)

Figure 2.5: The optical microscopic image of longitudinal cross-sections for micro-struts at (a) 90° [S1-90-200-1000-AR]; and (b) 35° [S1-35-200-1000-AR-M] build angles

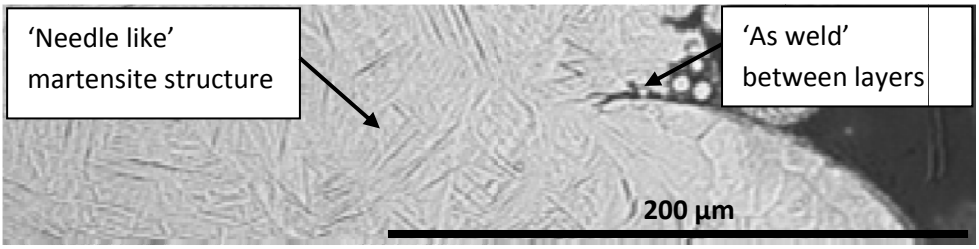

Figure 2.6: Microstructure of the as-received SLM Ti-6Al-4V micro-strut (35° build angle) manufactured at 200 W X 1000 µs parameters [S1-35-200-1000-AR-M]

2.2.2 Heat-Treated SLM Ti-6Al-4V Micro-Struts

From the literature, it has been mentioned that the Ti-6Al-4V is classified under α/β group of titanium alloy. Titanium alloy which fall either within α/β or β groups is very responsive to heat treatment and this affect its resultant microstructure, as compared to α group alloy [Polmear (2006)]. It was reported that different heat treatment process produces different strength and properties of Ti-6Al-4V alloy. This is due to phase transformation of β at high temperature, and different routes of subsequent cooling rate affects β to α phase transition, thus produces different composition of α+β phase as well as different microstructure morphology and properties in final product. Schematic diagram of microstructure range for α/β alloy heat-treatment can be referred in literature [Polmear (2006)] and will be shortly shown in the following section. Research specifically in the SLM Ti-6Al-4V material [Facchini et al. (2010)] suggested a post-manufacture heat-treatment to transform the metastable martensite into dual phase α+β, which resulted in an improvement in ductility, but a reduction in strength values. Besides traditional heat-treatment, hot isostatic pressing (HIP) has also been mentioned to improve porosity in powder manufactured titanium alloy products [Polmear (2006)], or to improve final microstructure in cast titanium alloy products [Wu and Hu (2005)].

In Shen's study (2009), HIP process has been done but the results showed that the process gave no significant improvement on specific strength of SLM Ti-6Al-4V micro-lattice cores with high manufacturing parameters i.e. 200 W laser power and 1000 μs laser exposure time. Only low set manufacturing parameters of HIP micro-lattice cores i.e. 180 W laser power and 500 μs laser exposure time, showed more stable deformation during compression test as compared to un-HIP cores. These findings were taken into consideration in the current study on microstructure of SLM Ti-6Al-4V micro-strut; where due to high cost of the HIP process which involved sophisticated facilities, basic post-manufacture heat-treatment using simple facilities was suggested and will be discussed in this thesis. The objective of the introduction of heat-treatment process was to control the final microstructure of the specimen, and hence for improvement in the strength of material.

In ASM Handbook [Gilbert and Shannon (1998)], it was mentioned that titanium alloy reacts with oxygen, water and carbon dioxide normally found in heat-treating atmospheres and also with hydrogen formed by decomposition of water vapour. A brittle oxide layer which is commonly called α case, as a result from interaction between oxygen and titanium surface, need to be removed before the heat-treated product can be used. A table was given in the handbook, which suggested minimum layer thickness of metal removal after thermal exposure of titanium alloys in an oxidizing atmosphere. It was found that minimum of 145 μm surface removal is suggested for 1 hour heat-treatment at temperature around 1000°C.

In this study, micro-struts of 200 W and 1000 μs parameters with build angle of 90° and 35° were subjected to a heat-treatment process using simple available facilities, in order to compare the effects on the SLM Ti-6Al-4V microstructure transformations and its mechanical properties. The process was expected to introduce some improvement in the ductility and behaviours of material. Extra care was taken since the micro-struts were having cross sectional diameter of not more than 400 μm. Oxidized surface removal after the heat-treatment was thought to be not practical, since it will leave less than half of the diameter, which would mean that at the end only around 110 μm would remain. Therefore, a vacuum atmospheric condition (0.1 mbar) with the usage of sealed quartz tubes was introduced in order to avoid the oxidizing environment in a normal heat-treatment furnace oven. Figure 2.7(a) shows a photograph of the furnace oven facility which was used in the heat-treatment process. In this study, each micro-strut was sealed inside a vacuumed quartz tube as shown in Figure 2.7(b), prepared from a glass-blowing process. The glass-blowing process [Barbour (1978)] was done at the Chemistry Department, University of Liverpool.

(a)

(b)

Figure 2.7: The facilities involved in heat-treatment process (a) a furnace oven; (b) an example of a vacuum sealed quartz tube with a 23 mm length micro-strut inside [S1-90-200-1000-AR]

In order to compare the microstructure developments, two types of heat-treatment processes were done. The first process or Process A involved solution treatment at 920°C for 1 hour and water quench, which resulted more α than β phase microstructure. In the second process or Process B, the vacuum sealed micro-strut was solution treated at 1000°C for 1 hour, water quenched and precipitation heat treated at 540°C for 4 hours. The resulted microstructure showed a more balanced α+β phase, and was found comparable to the schematic illustration of double solution treated α/β titanium alloys that can be found in Polmear (2006). Table 2.2 summarizes the heat-treatment processes used in this study. Meanwhile, Figure 2.8 and 2.9 illustrate schematics of temperature versus time plots of two processes that were done for both heat-treatment processes, with the resultant microstructure images (observed under an optical microscope) respectively.

Table 2.2: Summary of both heat treatment processes

Materials identification	Micro-strut parameters	First solution treatment	Second solution treatment
As-received [S1-35-200-1000-AR-M]	200 W X 1000 µs; 35° b.a.	-	-
Process A [S1-90-200-1000-HT(A)-M]	200 W X 1000 µs; 90° b.a.	Heat up to 920°C for 1 hour and water quench	-
Process B [S1-90-200-1000-HT(B)-M] and [S(1-9)-35-200-1000-HT(B)]	200 W X 1000 µs; 90° and 35° b.a.	Heat up to 1000°C for 1 hour and water quench	Heat up to 540°C for 4 hours and air cooled to room temperature

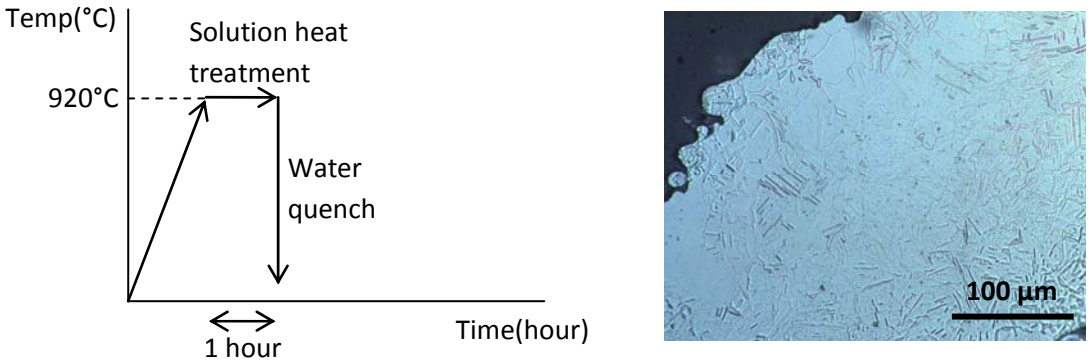

(a) (b)

Figure 2.8: (a) A schematic of temperature versus time plot for solution heat treatment on the SLM Ti-6Al-4V micro-strut (Process A) and; (b) the resultant microstructure from the process (strut with 200 W X 1000 µs parameters) [S1-90-200-1000-HT(A)-M]

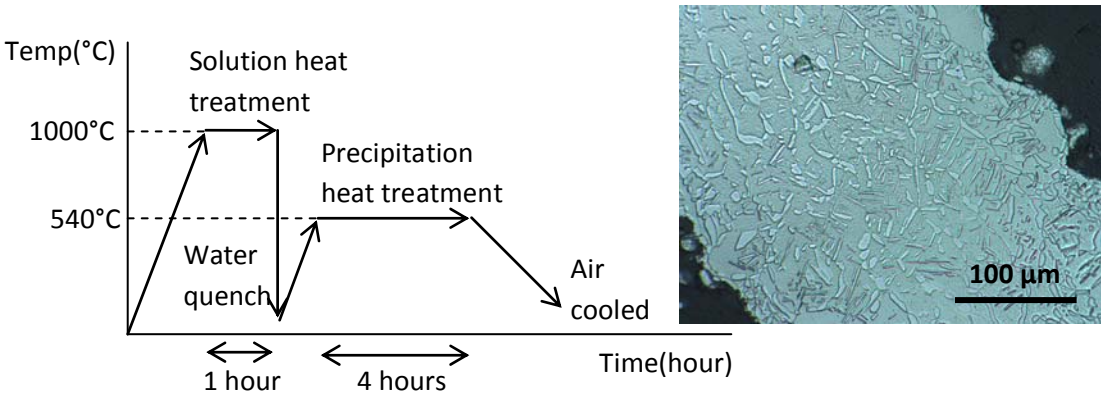

(a) (b)

Figure 2.9: (a) A schematic of temperature versus time plot for both solution and precipitation heat-treatments on the SLM Ti-6Al-4V micro-strut (Process B) and; (b) the resultant microstructure from the process which shows balance α+β phase (strut with 200 W X 1000 µs parameters) [S1-90-200-1000-HT(B)-M]

2.2.3 A Brief Note on Ti-6Al-4V Alloy System

It is important to include a brief discussion on Ti-6Al-4V alloy, in order to provide a quick revision for the material. As mentioned in the previous section, the Ti-6Al-4V material is the most common type of α+β alloy. Figure 2.10 shows the ternary phase diagram of Ti-Al-V alloy for isothermal section at 980°C, given in ASM Handbook (1992). The '**X**' marks the estimated composition of Ti-6Al-4V alloy. The Ti-6Al-4V alloy is designed for high strength at low-to-moderate temperatures. The strengthening of α+β alloy can be achieved by rapidly cool the alloy from a temperature high in the α+β range or even above the beta transus. Then, it is followed by an intermediate-temperature treatment (aging) to produce an appropriate mixture of α and transformed β products. Response to heat treatment is a function of cooling rate from the solution temperature and therefore may be affected by section size [Lampman (1990)]. Figure 2.11(b) to (e) show the resultant microstructure subjected to the rapid cooling temperature of Ti-6Al-4V. Acicular structures (Figure 2.11(c)) are formed by working or heat-treating above the β transus and rapid cooling. Meanwhile, rapid cooling from temperatures high in the α+β range (Figure 2.11(d) and (e)) will result in equiaxed primary α and acicular α from the transformation of β structures [Lampman (1990)]. To assist understanding, marks '**X**' in both Figure 2.10 and 2.11(a) represent the Ti-6Al-4V alloy with almost the same composition.

Under the SLM conditions, the resulting microstructure of the Ti-6Al-4V is composed of the martensite α' phase, with the shape of very fine needles (around 360 nm) due to the extremely high cooling rate from the β domain estimated around 10^4 K/s [Vilaro et al. (2011)]. For a quick comparison, the estimated cooling rate for the vacuum sealed strut used in this study was 490 K/s.

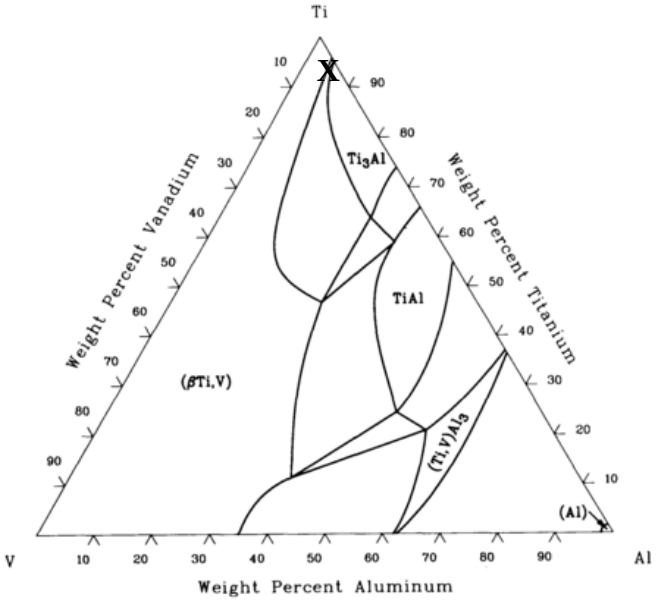

Figure 2.10: Ternary phase diagram of Ti-Al-V for isothermal section at 980°C [ASM Handbook (1992)]

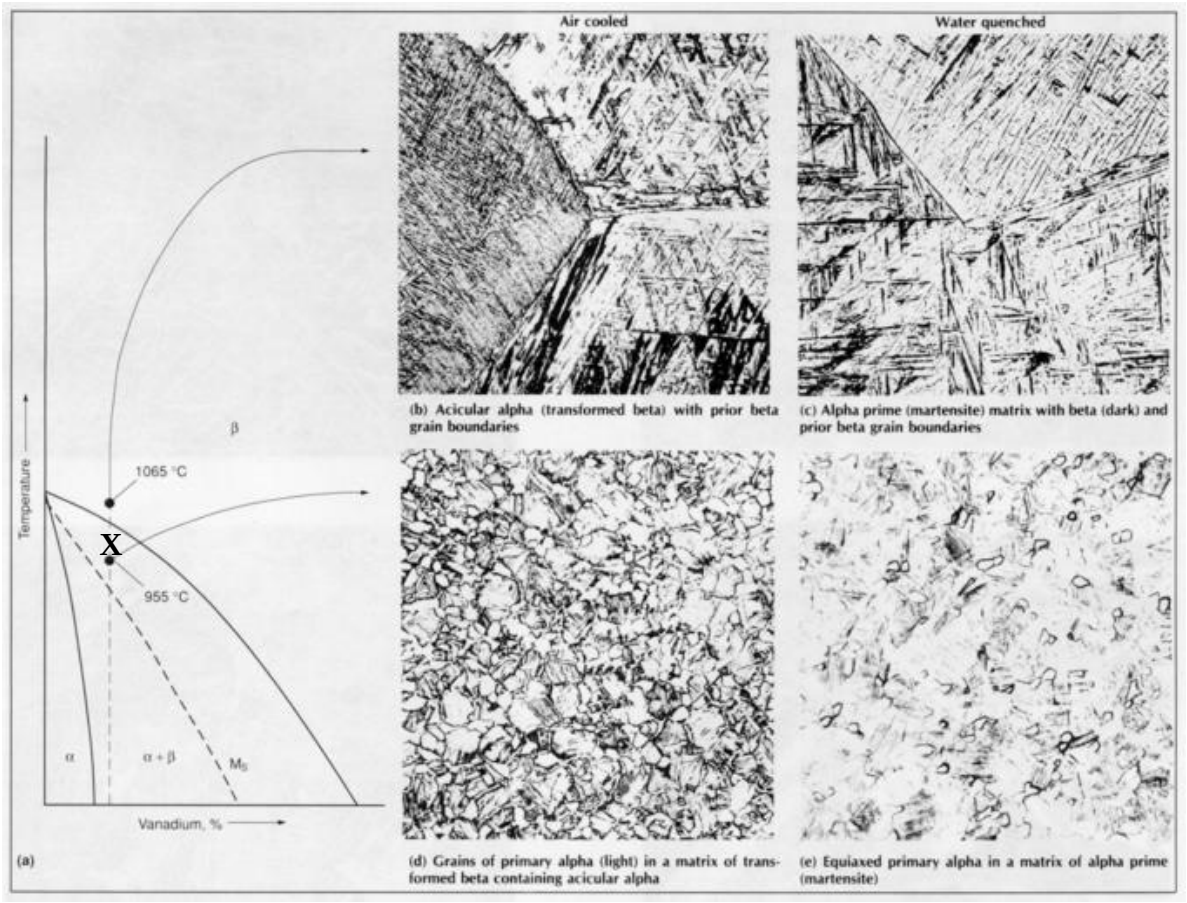

Figure 2.11: Microstructures of alloy Ti-6Al-4V ((b) to (e)) after cooling from different areas of the phase field shown in (a). Specimen in micrograph (e) provided the best combination of strength and ductility after aging [Lampman (1990)]

2.3 MATERIALS CHARACTERIZATION ON MICRO-STRUT

Material analysis study of the SLM Ti-6Al-4V micro-struts involved a Nikon/EPIPHOT optical microscope and a JSM-6610-JEOL scanning electron microscope (SEM) for microstructure observations. The SEM facility was also equipped with PentaFET Precision-Oxford Intruments-INCA X-act electron dispersive spectroscopy (EDS) for metallic elements observations. Vickers micro-hardness tester from Matsuzawa Seiki Co. Ltd. was also used in this study in order to briefly differentiate the hardness of the materials, and to estimate diameter variations along the micro-struts. Figure 2.12(a), (b) and (c) show the photograph images of the optical microscope, the SEM machine incorporated with the EDS, and the micro-hardness tester respectively.

(a)

(b)

(c)

Figure 2.12: Images of (a) an optical microscope; (b) a SEM machine incorporated with EDS and; (c) a micro-hardness tester

2.3.1 Metallographic Samples Preparation

Prior to material analysis, metallurgical samples of micro-strut were prepared by hot-mounting the micro-struts in conductive resin using 20 mm diameter moulds. The samples were then gradually polished by emery papers and diamond paste up to 1 micron, following standard metallurgical procedure. The polishing process per sample took approximately 2 to 3 hours to be completed until the samples gave images of plain flat mirror-like cross-section of micro-struts. To observe the microstructure, the polished samples were etched by the general use Keller's reagent (mixture of 1% hydrofluoric acid, 1% hydrochloric acid, and 2.5% nitric acid). Figure 2.13(a), (b), (c) and (d) show photographs of mounted samples, hot-mounting machine and polishing machines.

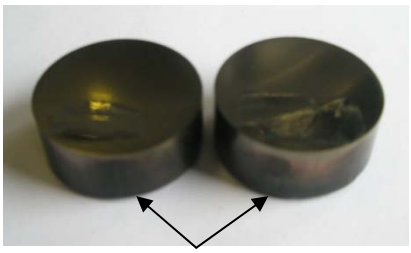

The mounted micro-strut specimens

(a)

(b)

(c)

(d)

Figure 2.13: Photograph images of (a) mounted samples [S1-90-200-1000-AR and S1-35-200-1000-AR-M]; (b) hot-mounting machine; and (c)-(d) polishing machines

2.3.2 Analysis on Diameter Measurement of Micro-Strut

It is important to carefully define the diameter of the micro-strut, since all further derivations in determining the properties are dependent on the definition of this basic unit. Three methods were applied in this study; using vernier calliper, shadow measurement of optical microscope images, and estimation using micro-hardness tester. Values obtained from the three methods were compared and justifications were given in selection of a robust definition for SLM Ti-6Al-4V strut diameter produced at 200 W and 1000 µs manufacturing parameters. In all methods,

uncertainties were taken from standard deviation values of average measured diameters.

It should be noted that images from optical microscopy were taken for the analysis due to a more straightforward procedure and cost effective when compared to the usage of images from the SEM. The specimen preparation time for the SEM is longer and the cost of gold coating of the specimen is higher when compared to the optical analysis procedure.

The as-received micro-strut diameter measurements were taken using vernier calliper, from specimens prepared for tensile test. The average diameter was determined as (0.375 ± 0.004) mm, and all the measurements were as showed in Figure 2.14.

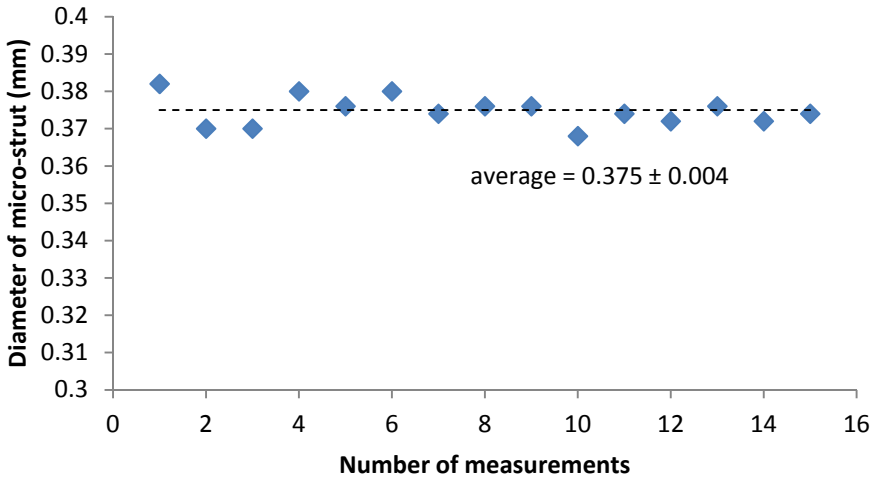

Figure 2.14: As-received micro-strut diameter measurements using vernier calliper [S(1-15)-35-200-1000-AR]

The micro-strut diameter was also determined from shadow measurements of optical microscope images, as shown in Table 2.3. Besides the as-received micro-strut, this

method was also applied to the heat-treated micro-strut, since it offered detailed values of diameter variations within a specimen that were hardly noticed using a vernier calliper. For the shadow measurement, Kohler illumination was used [Nikon (2013)]. In this condition, the light was set up in a way to obtain a very uniform intensity.

Table 2.3: Shadow measurements of optical microscope images for micro-strut diameters [S(1-15)-35-200-1000-AR and S(1-9)-35-200-1000-HT(B)]

As-received micro-strut	Heat-treated micro-strut
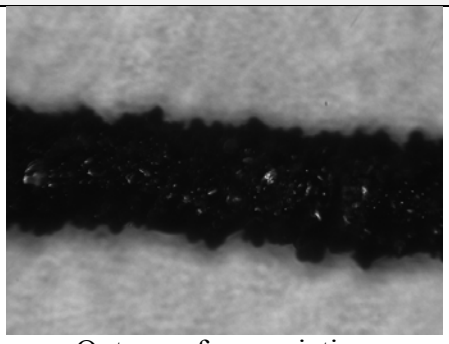 Outer surface variation	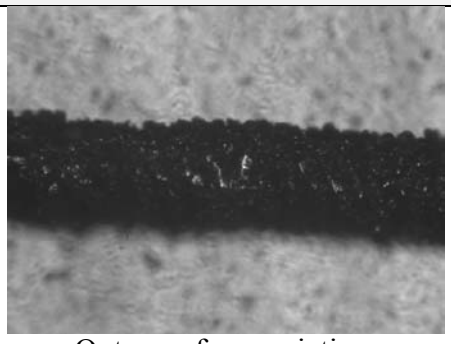 Outer surface variation
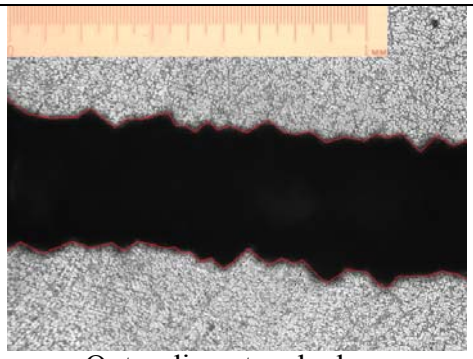 Outer diameter shadow	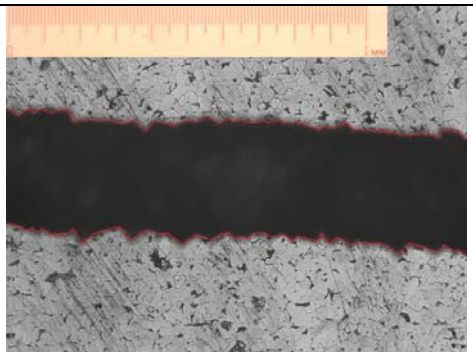 Outer diameter shadow
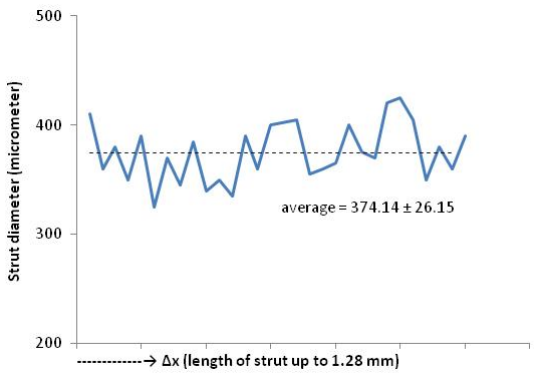	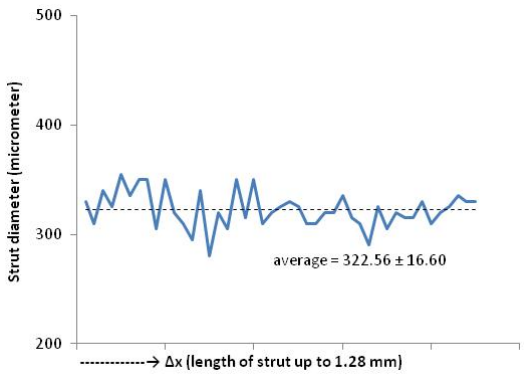

The maximum scale showed in the figures of Table 2.3 was 1 mm or 1000 µm. Strut diameter variations were taken from three samples. The average micro-strut diameters that were obtained from the shadow measurement method were (374.14 ± 26.15) µm and (322.56 ± 16.60) µm for both the as-received and the heat-treated micro-struts respectively. The variations in strut diameters also indicated that the outer surfaces were not smooth. Analysis of surface roughness will be discussed in the next section.

Another method to determine the micro-strut diameter was from the estimation of distance using the micro-hardness tester Matsuzawa Seiki (earlier Figure 2.12(c)). Knife edges of the tester were adjusted to both sides of a strut, and the equipment then displayed the value of calculated distance between the knife edges. The system calculated dimensions based on 40x magnification, however, the diameter of the strut was too large to be measured at this magnification. Therefore, magnification of 10x was set to fit in the whole diameter of a micro-strut. The value then was multiplied by 4 to give the real dimensions. Fifteen measurements were taken from three samples (i.e. five diameter variations for each sample), as showed in Figure 2.15. The average strut diameter was estimated as (370.40 ± 17.88) µm.

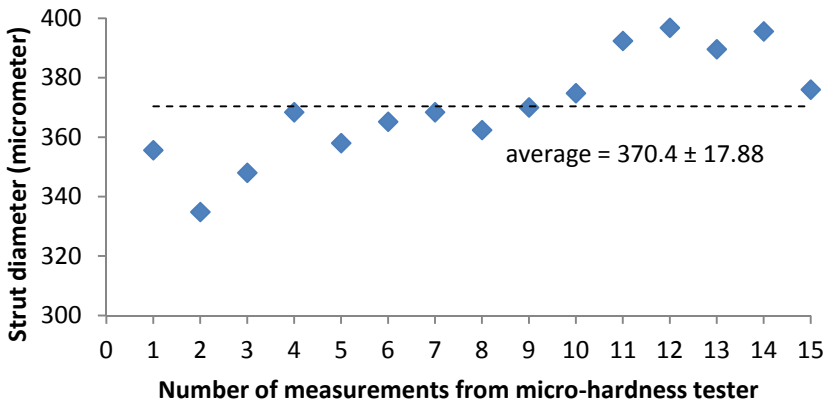

Figure 2.15: As-received micro-strut diameter measurements estimated from micro-hardness tester [S(1-3)-35-200-1000-AR]

Table 2.4 compares the as-received micro-strut diameter measurement results from the three methods. It tabulates the average value from each method, with their respective minimum and maximum range. It was shown that the minimum and maximum values from all three methods were within 95% confidence interval or ±2σ value (two times standard deviation). Figure 2.16 further compares the three average values. All of the values showed good agreement between each other, with the vernier calliper measurement giving the smallest scatter while the shadow measurement gave the largest scatter. As shown in earlier Table 2.3 (shadow measurement table), the diameter variations due to surface irregularities were measured along the shadow line of a micro-strut. Therefore, shadow measurement method detected details on deepest valleys and highest peaks along the surfaces which led to an amount of scatter in the measurement. Noticeable scatter was also seen in the result of measurement using the micro-hardness tester method, which involved variations within a micro-strut sample.

Table 2.4: Micro-strut diameter values of the as-received SLM Ti-6Al-4V struts (200 W x 1000 µs @ 35° build angle) from three different measurement methods

Range of strut diameter value		Vernier calliper measurement	Shadow measurement of optical microscope image	Estimation from micro-hardness tester
Minimum value (µm)	-2σ	367	321.84	334.64
	Measured	368	325	334.8
Average value ± σ (µm)		375 ± 4	374.14 ± 26.15	370.40 ± 17.88
Maximum value (µm)	Measured	382	425	396.8
	+2σ	383	426.44	406.16

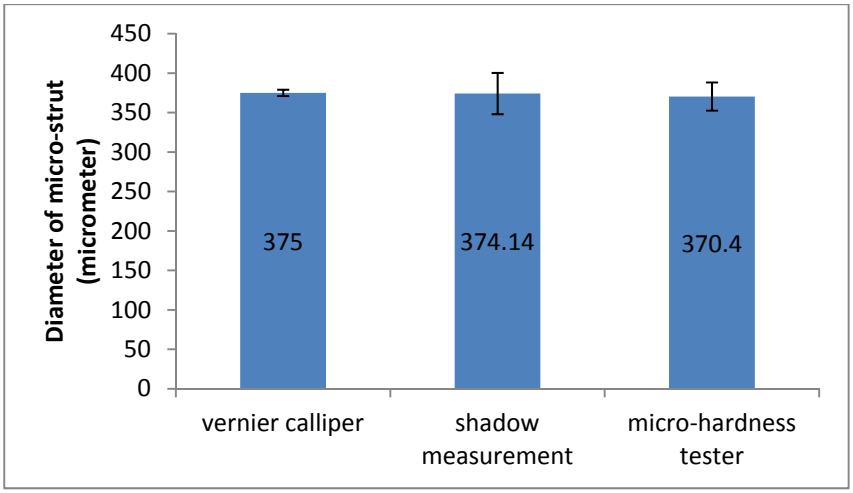

Figure 2.16: Comparison of average diameter values of the as-received SLM Ti-6Al-4V strut (200 W x 1000 µs @ 35° build angle) from three methods with their respective standard deviations

Based on a good agreement between each strut diameter result, it is therefore suggested that the result from shadow measurement method is taken as a reference value to be used for analysis of the SLM Ti-6Al-4V micro-strut manufactured at 200 W and 1000 µs parameters, with 35° build angle. The large scatter in the method covered ranges of lower and upper bounds for the average diameter values of all three measurement methods. Therefore, the average diameter of the as-received micro-strut was determined as (374.14 ± 26.15) µm, with minimum range of 321.84 µm and maximum range of 426.44 µm.

2.3.3 Circularity Measurement and Dimensional Accuracy of the Micro-struts

Figure 2.17 shows the nominally circular cross-sections of the as-received SLM Ti-6Al-4V micro-struts built at 35° (Left) and 90° (Right) angles to the powder bed. It showed that the micro-strut manufactured at 35° build angle has a larger diameter compared to the strut manufactured at 90° build angle. This is also confirmed with Shen's report (2009), which stated that struts built at 35° build angle have diameter of 14% larger than struts built at 90° angle. It was noticed that the diameter of the

35° build angle strut was not a perfect circle, having a partially distorted part due to laser melted powder arrangement in the 35° build, as illustrated in the earlier schematic of Figure 2.2 and the longitudinal cross-section images of Figure 2.5. By referring to the scale bar in Figure 2.17, the diameter measurements of longest ends for the 35° and 90° build angle struts were estimated to be approximately 380 µm and 330 µm, respectively.

The estimation of distorted diameter, 380 µm, shown in Figure 2.17 was found to be about 1.6% larger than the determined average strut diameter from the shadow measurement method of (374.14 ± 26.15) µm. Since the estimated value was within the ±2σ range of the average value, this further confirmed that the average value could be the accepted diameter value for further analysis of the SLM Ti-6Al-4V micro-strut.

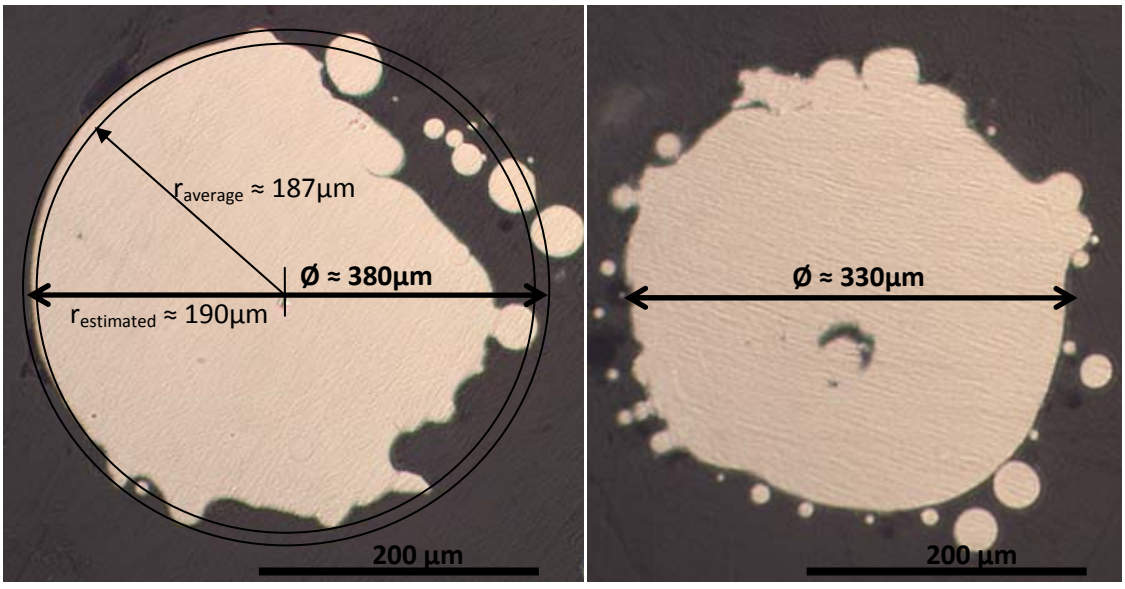

Figure 2.17: The nominally circular cross-sections (end parts) of the as-received SLM Ti-6Al-4V micro-strut built at 35° (Left) [S1-35-200-1000-AR-M] and 90° (Right) [S1-90-200-1000-AR] angles (with 200 W X 1000 µs manufacturing parameters)

The circularity of micro-strut can be represented by a circularity index (*CI*), using simple geometrical expressions, which has been widely used in the research of natural fibres [Skau (1951); Petkar et al. (1980); Diao et al. (1999)]. By taking *A* as the overall area of cross-section; *P* as the perimeter of cross-section; A_{max} as area of the circle the perimeter of which is *P*; *r* as radius of circle the parameter of which is *P*; an expression of circularity, *C*, as in Equation 2.4 was derived.

It is known that, $A_{max} = \pi r^2$ [2.1]

and $P = 2\pi r$. [2.2]

Therefore, $A_{max} = \frac{P^2}{4\pi}$ [2.3]

and $C = \frac{A}{A_{max}} = \frac{4\pi A}{P^2}$. [2.4]

The circularity, *C*, or circularity index, *CI*, may vary in value from unity, for a circle; to zero, for a cross-section having a finite perimeter and zero area.

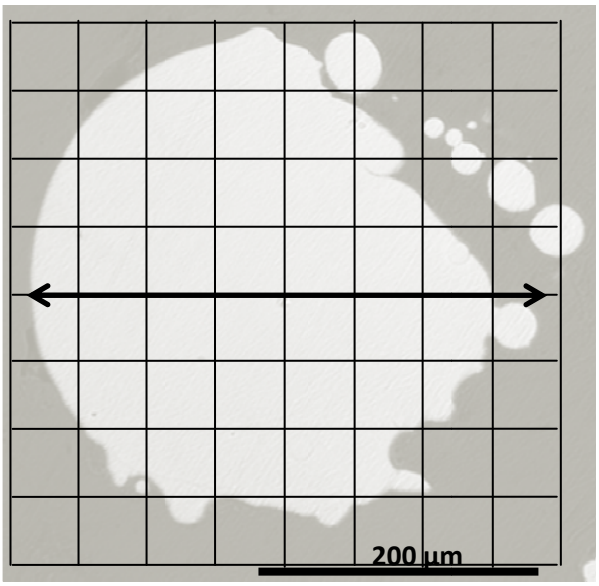

Figure 2.18: Grids of 2500 µm^2 in cross-section area calculation [S1-35-200-1000-AR-M]

In this study, the area *A* of the cross-section was calculated manually using grid method, as shown in Figure 2.18, where 2500 μm^2 grids were used in the estimation. The perimeter was calculated from measurement of the equivalent line length surrounding the cross-section area. The circularity index was measured twice for each 35° and 90° build angle respectively, and the results were shown in Table 2.5.

Table 2.5: Circularity index of as-received SLM Ti-6Al-4V strut build at 35° [S1-35-200-1000-AR-M] and 90° angle [S(1-2)-90-200-1000-AR] (200 W and 1000 μs manufacturing parameters)

Build angle	Diameter (μm)	Cross-sectional area, *A* (μm^2)	Perimeter, *P* (μm)	Circularity index, *CI*	Average *CI* (± standard deviation)
35°	Specimen 1				0.8238 (± 0.0475)
	380	86250	1171.14	0.7902	
	Specimen 2				
	372	76250	1057.14	0.8574	
90°	Specimen 1				0.8996 (± 0.0199)
	330	81250	1057.14	0.9136	
	Specimen 2				
	325	78750	1057.14	0.8855	

It should be noted that the Image analysis system by LUMENERA Corp. with 'Infinity 2-2C-175675' camera and 'Infinity Analyze' software is equipped at the optical microscope as shown in earlier Figure 2.12(a) of section 2.3. For this study, only the camera was utilized but not the software. This is because the usage of available software is quite complicated when compared to the usage of manual estimation with grids. In this case, simplicity was chosen in order to avoid complexity in the estimation.

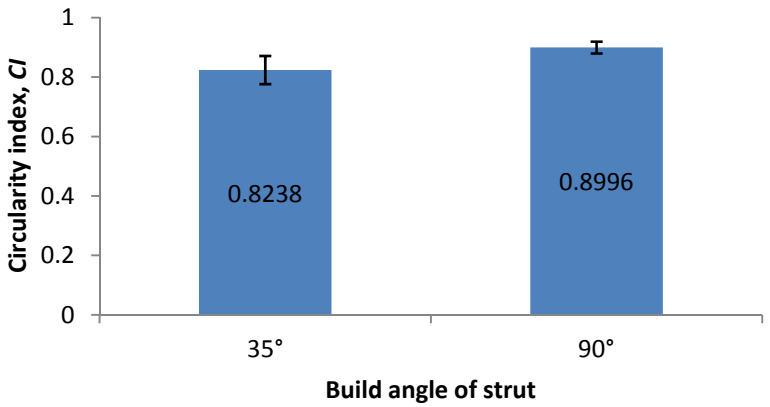

Figure 2.19: Circularity index for the as-received SLM Ti-6Al-6V struts manufactured at 35° and 90° build angle (200 W and 1000 µs manufacturing parameters)

As shown in Figure 2.19, it was confirmed that the strut built at 90° angle was more circular than the one built at 35° angle. The difference between circularity of struts manufactured at both build angles was approximately 9%. Besides the effect of build angle, the circularity was also affected by surface variations of struts. This was the reason of non-circularity of the theoretically fully dense solid cylindrical strut built at 90° angle, which can be also seen in earlier Figure 2.5.

There was also an interest to analyze the effect of heat-treatment on the circularity of micro-strut. For this case, diameter variations from the shadow measurement method were used. Formulas used by Kude and Khairnar (2004) were utilized. The strut diameter can be obtained from the maximum measured radius, A, and minimum measured radius, B, as given by the following Equation 2.5.

$$Diameter = 2\left(\sqrt{\frac{A^2+B^2}{2}}\right) \quad [2.5]$$

The non-circularity measured in terms of percentage is given by the following relation of Equation 2.6.

$$Non-circularity = \left\{\left(\frac{A-B}{Diameter}\right) \times 200\right\}\% \quad [2.6]$$

The results of using these formulas were shown in Table 2.6.

Table 2.6: The as-received [S(1-15)-35-200-1000-AR] and heat-treated [S(1-9)-35-200-1000-HT(B)] SLM Ti-6Al-4V micro-struts geometry estimations by using formulas from Kude and Khairnar (2004)

Material	Diameter (μm)	Non-circularity (%)
As-received strut (35° build angle)	378.32	26.43
Heat-treated strut (35° build angle)	316.94	22.09

From the results in Table 2.6, the heat-treated strut was shown to be more circular than the as-received strut. The calculated strut diameters were slightly different from the average values found using the shadow measurement method. The differences were 1.12% and 1.74% for the as-received and heat-treated struts, respectively. The value of non-circularity of as-received strut was compared to the circularity index *CI* that was found previously. In order to be comparable, the percentage of non-circularity was converted into a circularity index, by the subtraction of the value from unity. Table 2.7 shows the comparisons of diameters and circularities calculated using Kude and Khairnar (2004) formulas, with the values obtained from shadow measurement and circularity index calculation, respectively. Differences of 1.12% and 10.69% were observed for the diameter and circularity results, respectively. The good agreement between the results of diameter and circularity has confirmed that the as-received SLM Ti-6Al-4V strut can be assumed as a cylindrical solid with an average diameter of (374.14 ± 26.15) μm, within the range of minimum value of 321.84 μm and maximum value of 426.44 μm. Meanwhile, the heat-treated SLM Ti-6Al-4V strut was assumed to be a cylindrical solid with a smaller average diameter of (322.56 ± 16.60) μm within the minimum and maximum range of 289.36 μm and 355.76 μm.

Table 2.7: Comparison of diameters and circularities of the 35° build angle as-received SLM Ti-6Al-4V strut (200 W x 1000 µs) [S(1-15)-35-200-1000-AR], determined from different methods

Diameter (µm)		Circularity index (*CI*)	
Using Formula from Kude and Khairnar (2004)	378.32	Conversion from non-circularity result	0.7357
Average value from shadow measurement method	374.14	Measurement of circularity index	0.8238
Difference	1.12%	Difference	10.69%

The effects of circularity on the properties of the SLM Ti-6Al-4V micro-struts will be discussed in Section 2.5. As for brief discussion, Figure 2.20 shows the influence of the circularity on the Young's modulus (*E*) of the micro-struts in this study. It is shown that higher Young's modulus can be obtained from an improved circularity of the heat-treated micro-struts. While circularity is referred to the fullness of a cross-section of the micro-strut, it should be noted that a better definition for dimensional accuracy is the variations of diameter along the micro-struts. However, the terms 'circularity' and 'dimensional accuracy' are always mixed together in the usage, as applied in the formula of Kude and Khairnar (2004). Figure 2.21 shows the parallel improvements in both the circularity and dimensional accuracy of the respective as-received and heat-treated micro-struts.

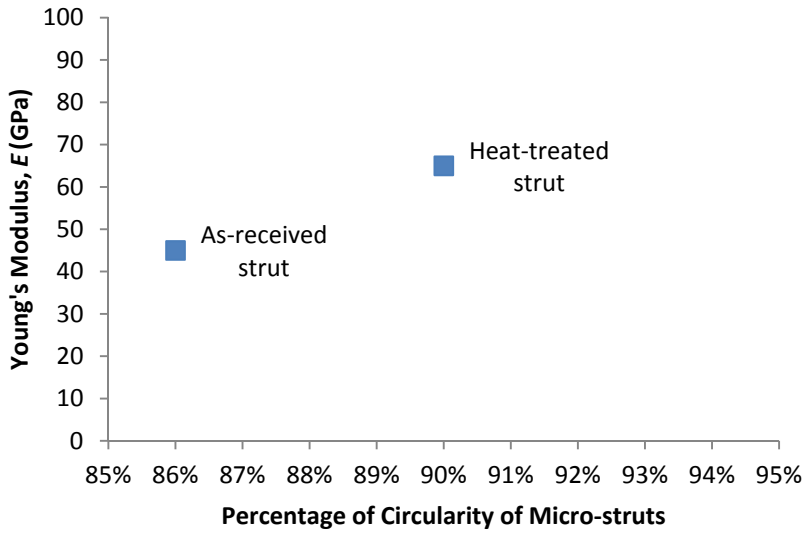

Figure 2.20: Influence of circularity on the Young's modulus (E) of the micro-struts

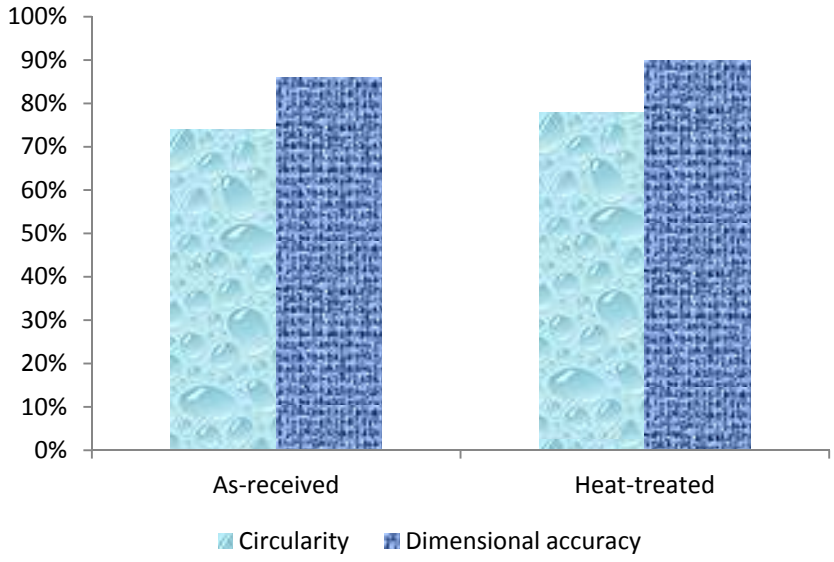

Figure 2.21: Parallel improvement in both the circularity and dimensional accuracy of the respective as-received and heat-treated micro-struts

2.3.4 Analysis of Surface Roughness and Stress Concentration of Micro-Strut

From the shadow measurement method as discussed in the previous section 2.3.2, it was shown that there were irregularities along the outer surfaces of the struts. As mentioned by Van Bael et al. (2011), waviness and roughness of strut surfaces, due to attached powder particles, will result in local heterogeneities and stress concentrations leading to a lower stiffness and lower compressive strength of the material. Moreover, it will complicate the accurate prediction of mechanical properties by means of analytical models and finite element analysis (FEA). Therefore, on top of the determination of strut diameter, the surface roughness profiles of the SLM Ti-6Al-4V struts in this research were also deduced from the shadow measurements, as shown in Table 2.8.

Table 2.8: Surface roughness profiles and parameters that were deduced from shadow measurement method for both the as-received and heat-treated SLM Ti-6Al-4V struts (200 W and 1000 µs manufacturing parameters, at 35° build angle) [S(1-15)-35-200-1000-AR and S(1-9)-35-200-1000-HT(B)]

As-received micro-strut	Heat-treated micro-strut
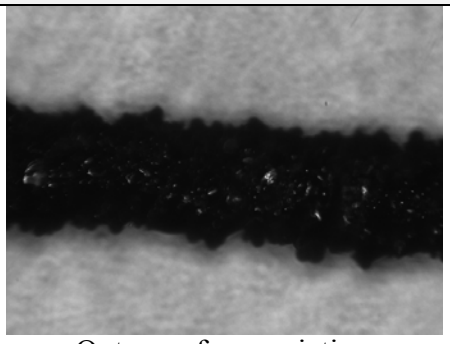 Outer surface variation	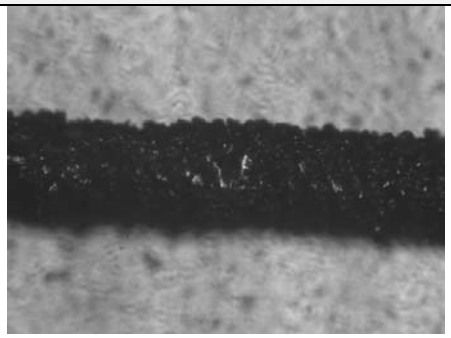 Outer surface variation
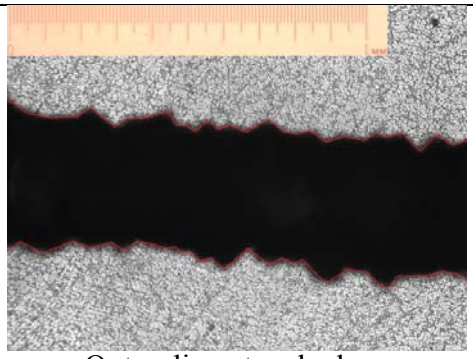 Outer diameter shadow	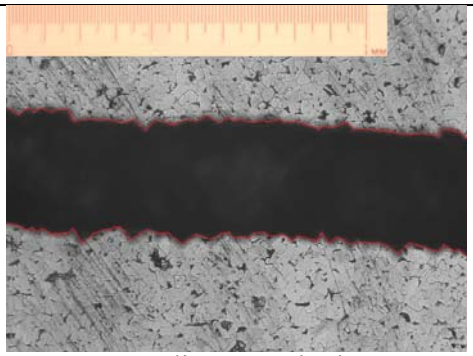 Outer diameter shadow
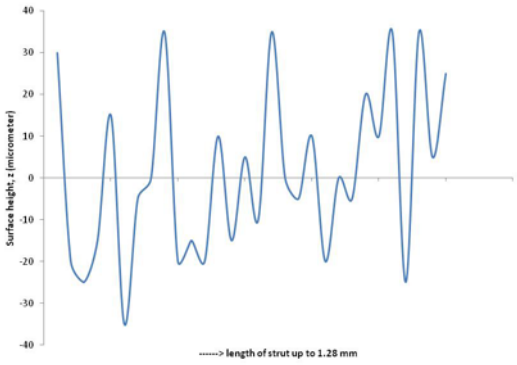 Surface roughness profile of as-received strut	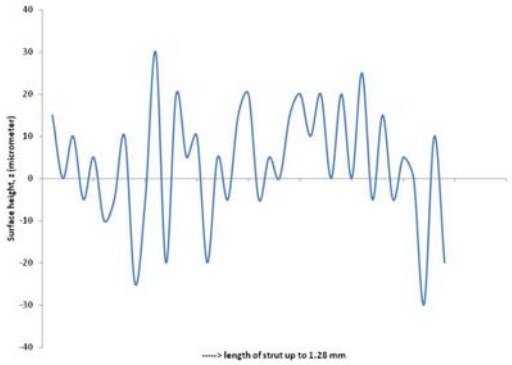 Surface roughness profile of heat-treated strut
R_a = 16.8 µm	R_a = 11.5 µm
R_y = 70 µm	R_y = 60 µm
R_z = 59 µm	R_z = 46 µm

The standard surface topography components; average roughness (R_a), peak-to-valley height roughness (R_y), and 10-point roughness (R_z); are represented by the following equations:

$$R_a = \frac{1}{L}\int_0^L |z|\, dx \qquad [2.7]$$

$$R_y = |z_{max} - z_{min}| \qquad [2.8]$$

$$R_z = \frac{1}{5}\left[\sum_{i=1}^{5}(z_i)_{max} + \sum_{j=1}^{5}\left|(z_j)_{min}\right|\right] \qquad [2.9]$$

Figure 2.22 further explains the surface roughness parameters definitions. Based on the standard equations, surface roughness parameters for the as-received and heat-treated SLM Ti-6Al-4V micro-struts were determined. Differences of R_a, R_y and R_z between the as-received and heat-treated struts were 31.5%, 14.3% and 22% respectively, as shown in Table 2.8.

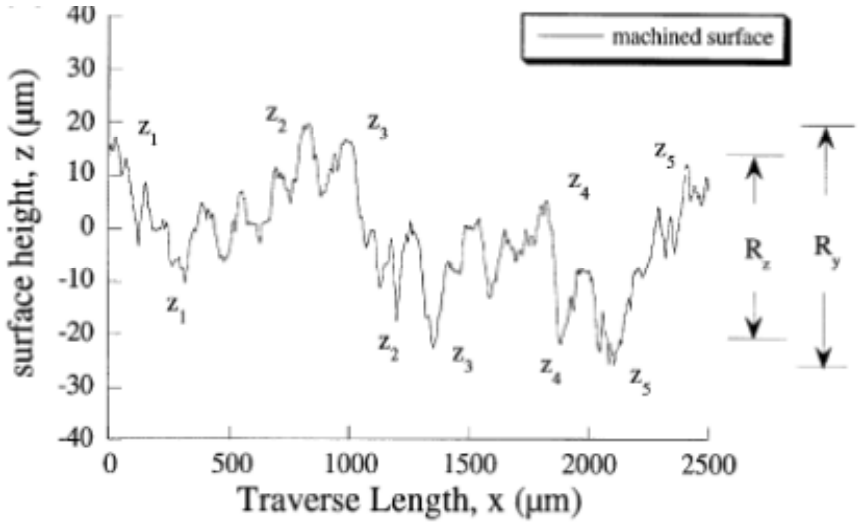

Figure 2.22: Arbitrary surface profile and the standard surface roughness parameters [Adapted from Arola and Williams (2002)]

There was also an interest to study the stress concentrations along the micro-struts surfaces due to the surface roughness. A semi empirical relationship for surface stress concentration factor, K_t, using standard roughness parameters was given by Neuber rule, as being applied by Arola and Williams (2002), as shown in Equation 2.10.

$$K_t = 1 + n\sqrt{\lambda \frac{R_z}{\rho}} \qquad [2.10]$$

Where R_z is the 10-point surface height, ρ is the notch root radius, n is the stress state (n=1 for shear and n=2 for tension), and λ is the ratio between spacing and height of surface irregularities.

An alternative expression which was more suitable for the stress concentration imposed by surface texture was given by Arola-Ramulu model [Arola and Ramulu (1999)]. The effective stress concentration, $\overline{K}_t$, for a process-dependant surface texture was defined in terms of dominant profile valleys and the corresponding average valley radii, as in Equation 2.11.

$$\overline{K}_t = 1 + n\left(\frac{R_a}{\bar{\rho}}\right)\left(\frac{R_y}{R_z}\right) \qquad [2.11]$$

Where R_a, R_y and R_z are the average roughness, peak-to-valley height, and 10-point roughness respectively; parameter $\bar{\rho}$ is the effective profile valley radius determined from the dominant profile valleys as shown in Figure 2.23; and n is the stress state (n=1 for shear and n=2 for tension).

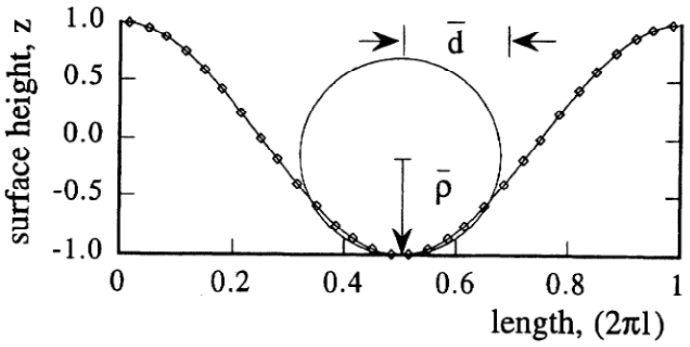

Figure 2.23: Definitions of effective profile valley radius [Arola and William (2002)]

By referring to Arola and Williams (2002), the effective notch root radius $\bar{\rho}$ was estimated from the surface profiles using a graphical radius method. A best-fit circle defined by the maximum area of contact was inscribed in the root of at least three deepest valleys of the examined profile. The average of these profile valley radii was then calculated to establish $\bar{\rho}$ for both the as-received and heat-treated struts. The $\bar{\rho}$ value for the as-received strut was estimated as (36.7 ± 9.5) μm, and the $\bar{\rho}$ value for the heat-treated strut was estimated as (32.3 ± 3.4) μm. The effective stress concentration factors, $\overline{K}_t$, for both the as-received and heat-treated SLM Ti-6Al-4V struts surfaces were calculated using the Arola-Ramulu model according to Equation 2.11 and were related to the surface roughness as shown in Figure 2.24 below. It was shown that the stress concentration was higher for the higher surface roughness of the as-received strut. This means that, the strength of the as-received strut would be lower as compared to the heat-treated strut. The effects of surface roughness on the properties of the SLM Ti-6Al-4V micro-struts will be discussed in Section 2.5. Figure 2.25 shows the relation between the surface roughness and the ultimate strength of the micro-struts in this study.

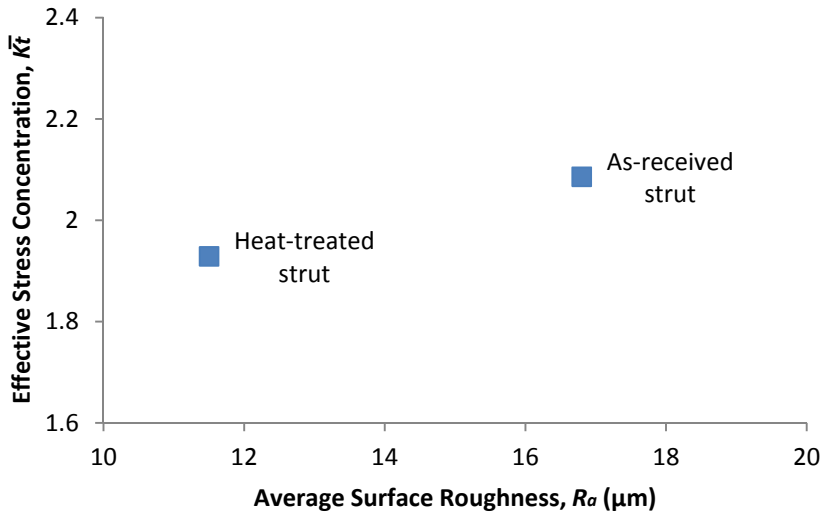

Figure 2.24: The stress concentration of the as-received and heat-treated SLM Ti-6Al-4V struts (200 W and 1000 µs, at 35° build angle) [S(1-15)-35-200-1000-AR and S(1-9)-35-200-1000-HT(B)] given as the effective stress concentration factors, $\overline{K}_t$, in terms of the average surface roughness, R_a

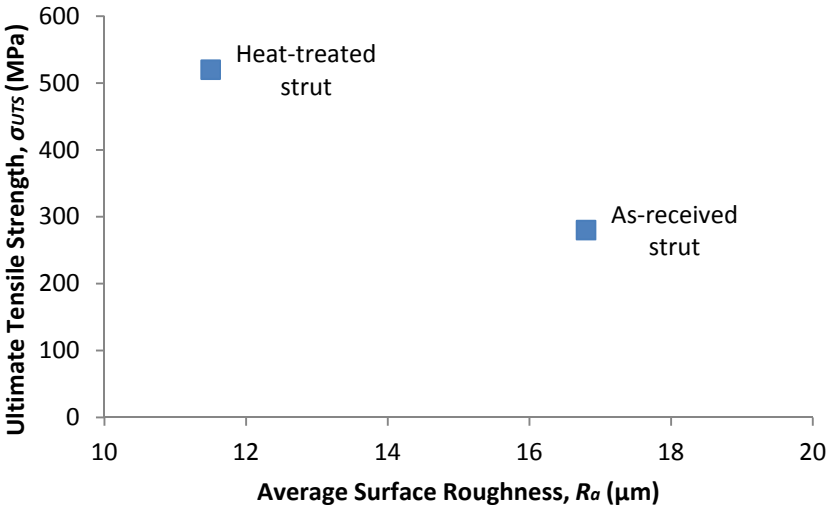

Figure 2.25: The effect of surface roughness R_a on the ultimate tensile strength σ_{UTS} of the SLM Ti-6Al-4V struts (200 W and 1000 µs, at 35° build angle) [S(1-15)-35-200-1000-AR and S(1-9)-35-200-1000-HT(B)]

2.3.5 Comparison between the As-Received and Heat-treated Microstructure of Micro-Struts

Table 2.9 compares the microstructure images of the as-received and heat-treated SLM Ti-6Al-4V micro-struts that have been already shown in sections 2.2.1 and 2.2.2 respectively. Definition of materials should be referred to the earlier Table 2.2. In Table 2.9, microstructure of the 'As-received' material was observed as similar to that of an 'as-welded' Ti-6Al-4V alloy with a dendritic 'ghost' β phase structure, formed on freezing, inside which is a needle martensite structure, formed on cooling to room temperature. It was similar to the microstructure reported in Facchini et al. (2010), although it was different to that of standard Ti-6Al-4V alloy [Boyer et al. (1994)]. Within the microstructure were regions that, although dendritic, looked very different from the bulk of material. These dendritic looking regions have attracted our attention because although they were small they may have a significant effect upon the mechanical behaviour of the micro-struts. Therefore, further analysis was carried out for clarifications and will be discussed in the following section.

Heat-treatment processes were carried out as been explained in section 2.2.2, in order to obtain a more balanced α+β phase Ti-6Al-4V material, as it should be. The 'Process A' heat-treatment only involved partial process of solution treatment and quenching, while the complete 'Process B' included ageing process for precipitation heat-treatment. The earlier process showed more α than β structure, as a result of the quenching process which is always associated with hard martensitic structure. The later process however, showed a comparable microstructure with the schematic shown in Figure 2.26, with a balanced α+β phase, which was reported to produce high tensile strength and effective in crack resistance, thus improving fracture toughness of the material [Polmear (2006)]. The resultant microstructure from 'Process B' also showed the disappearance of the 'dendritic' structure and the formation of a more uniform structure, which is therefore likely to produce struts without regions of weakness, whilst avoiding significant grain growth that may produce regions of the struts that are single grains. The presence of a large grain size

within such small struts would significantly affect their strength as overall slip would be limited by the slip planes within the single crystal.

Table 2.9: Microstructure comparison between the as-received and heat-treated SLM Ti-6Al-4V micro-struts (note: b.a. = build angle)

Materials identification	Microstructure image	Observation
As-received 200 W X 1000 µs (35° b.a.) [S1-35-200-1000-AR-M]	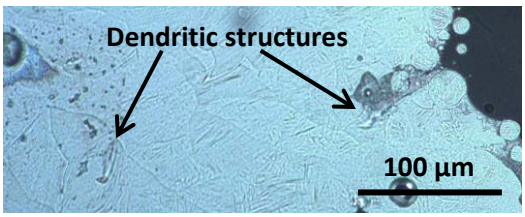	'Needle-like' martensite α-phase with 'ghost' β-phase structure; similar to 'as-welded' structure; existence of dendritic structure
Process A 200 W X 1000 µs (90° b.a.) [S1-90-200-1000-HT(A)-M]	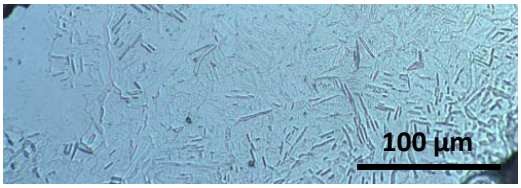	Martensitic quenched structure with more α than β phase; coarser than the as-received; no dendritic structure observed
Process B 200 W X 1000 µs (90° b.a.) [S1-90-200-1000-HT(B)-M]	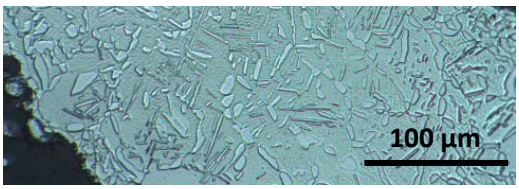	More balanced α and β phase; i.e. α precipitation in β matrix; no dendritic structure observed

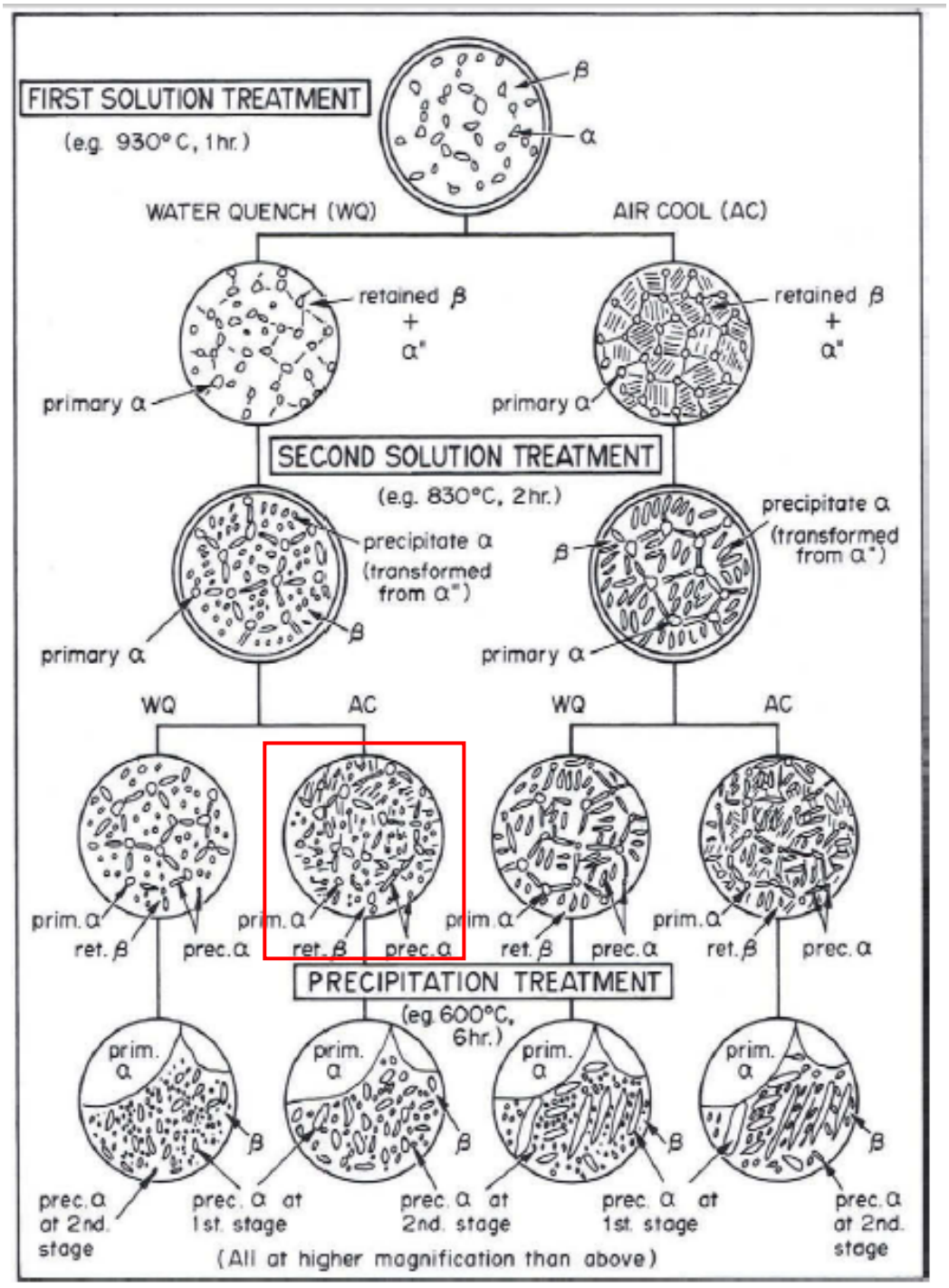

Figure 2.26: Schematic diagram showing range of microstructures obtained by double solution treatment [adapted from Figure 6.19 in Polmear (2006)]. The microstructure in the red-square is similar to the microstructure from 'Process B', as shown in Table 2.9.

2.3.6 Element Analysis and Hardness of As-received Micro-Struts

As shown in Table 2.9, there was an existence of dendritic structures in the microstructures of the 'As-received' SLM Ti-6Al-4V micro-struts. Figure 2.27 showed an SEM image of the as-received microstructure with dendritic structures at grain boundaries regions while Figure 2.28 showed the higher magnification image of one of those dendritic structures. Elemental analysis was carried out on a longitudinal cross-section of the as-received SLM Ti-6Al-4V micro-struts using the Energy Dispersive Spectroscopy (EDS). As the EDS is known to be used in a semi-quantitative mode to determine chemical composition by peak-height ratio, the discussions in this study are more towards a qualitative explanation of the detected elements. Detailed explanation of the EDS can be found in many available references [Brown and Gallagher (2008)].

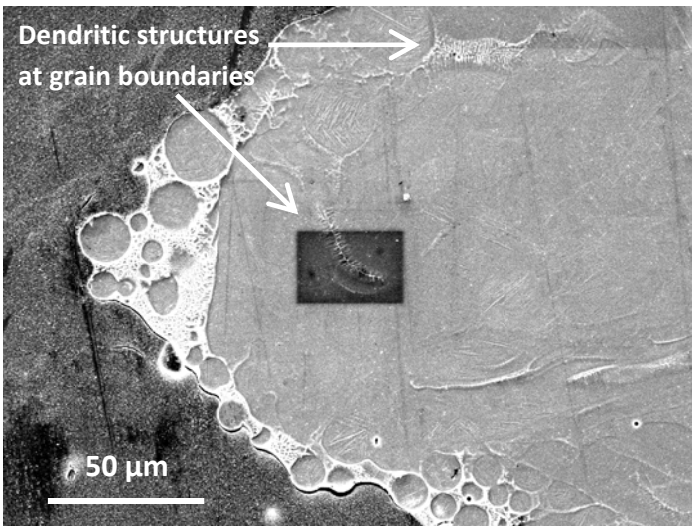

Figure 2.27: The SEM image of As-received SLM Ti-6Al-4V (200 W x 1000 µs) microstructure with dendritic structures at grain boundaries regions [S1-35-200-1000-AR-M]

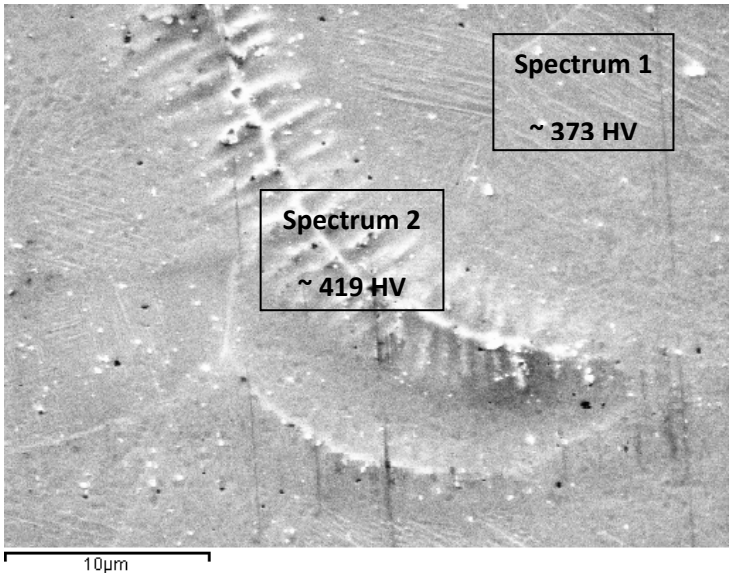

Figure 2.28: A larger image of dendritic structure as shown in Figure 2.27, with indicated points of Spectrum 1 and 2 for elemental analysis in Figure 2.29 and 2.30

The EDS Spectrum 1 (Figure 2.29), from a region away from the dendritic structure, detected the major elements of Ti-6Al-4V (Table 2.1) as approximately 89.9wt% titanium (Ti), 5.9wt% aluminium (Al) and 3.9wt% vanadium (V), with no iron detected. Iron may be present as another residue element, but the maximum allowed quantity is 0.25wt%. Meanwhile, Spectrum 2 (Figure 2.30) from the dendritic structure (Figure 2.28) showed relatively high levels of iron (Fe) and some chromium (Cr). The peak height-ratio for Ti and Fe showed that the level of iron present was high, whilst analysis of the surrounding area showed that the iron was localized to this structure. The presence of this iron rich region was surprising as iron has a high solubility in β titanium (but not α) and this structure had features more like those formed on freezing. The detection of Cr was also surprising as it is not present in the alloy. It appeared that these regions were forming as the residue elements from suspected small amount of stainless steel powder that was present in the SLM machine from previous manufacture using stainless steel powder, and became incorporated into the titanium build. The most likely source was the powder feed system, as the argon atmosphere was carefully filtered to remove powder particulate residues from the recycled gas [Tsopanos et al. (2010)]. However, no

quantitative measurement on particulate amount was applied in the filtering system, and therefore there is still room for improvement on the strategy that can be taken to minimize residue elements in the SLM manufacturing.

Most of the dendritic structures were found at boundaries and within inter-layer areas in the micro-strut. These phases probably occurred during freezing rather than by precipitation in the solid, and given the size of the regions formed, they were probably due to single powder particles of stainless steel material. It was likely that the stainless steel particle dissolved in the melt pool but due to the short time the region was molten, it was not diluted significantly by the titanium; and on freezing, the iron concentration still exceeded the solid solubility of iron in titanium, led to the formation of Ti-Fe intermetallic by a eutectic reaction [Murray (1992)].

It likely that this dendrite formation affected the mechanical properties, as they were likely to be brittle and acted as a weak points in the micro-strut, initiating cracking across the strut in that region, the strut only being as strong as the weakest point. It was found that these structures were significantly harder (419 ± 19 HV compared with 373 ± 11 HV) than the bulk of the structure (Fig 2.28), which would be expected if Ti-Fe was formed. However, although a possible reaction was identified from the phase diagrams, it has not yet been possible to confirm this by determining the phases present in these regions.

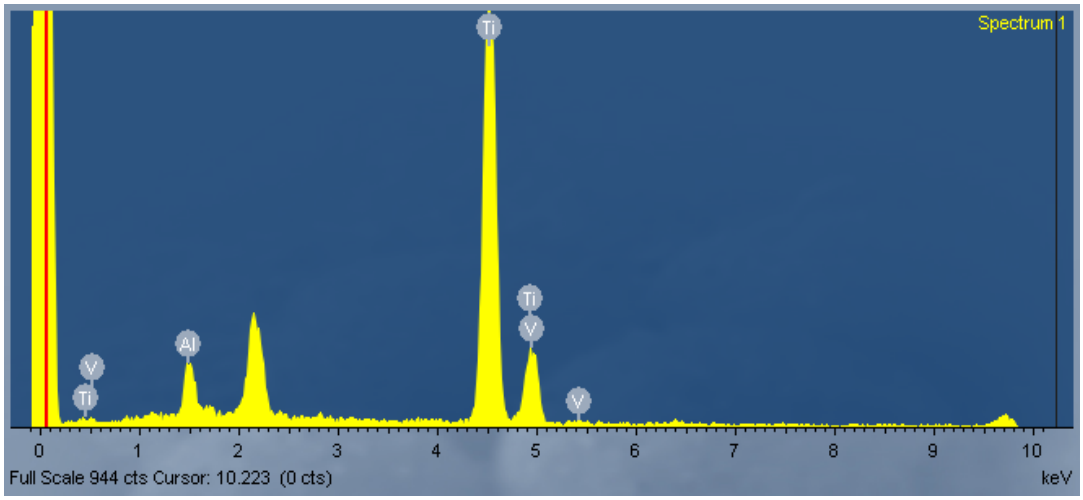

Figure 2.29: The EDS plot of Spectrum 1 for elemental analysis of As-received micro-strut which confirms with Ti-6Al-4V major elements as in Table 2.1 [S1-35-200-1000-AR-M]

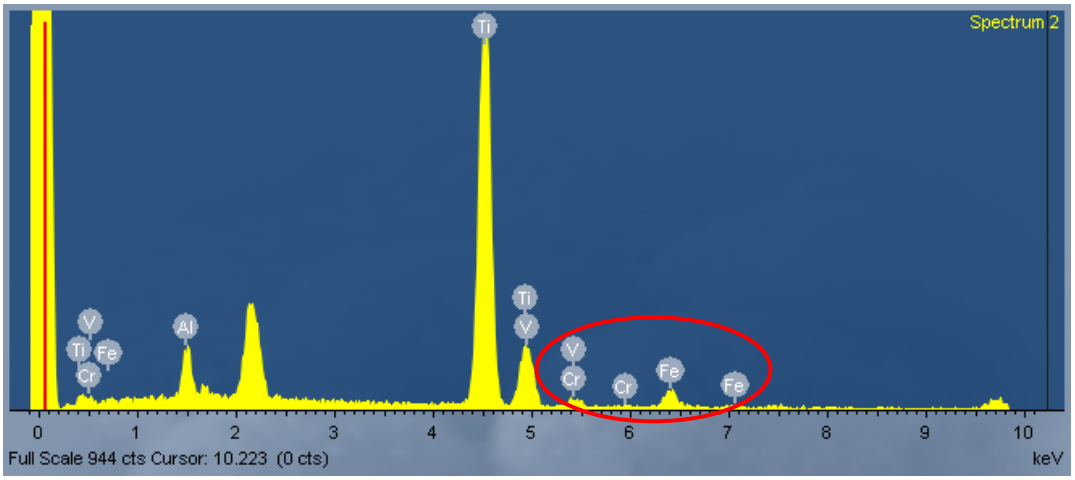

Figure 2.30: The EDS plot of Spectrum 2 for elemental analysis of As-received micro-strut with the existence of Fe and Cr peaks, suspected due to residue elements [S1-35-200-1000-AR-M]

2.3.7 Element Analysis and Hardness of Heat-treated Micro-Struts (Process A)

Figure 2.31 shows the SEM image of the microstructure for heat-treated SLM Ti-6Al-4V micro-strut, after the solution treatment and quenching process (Process A). An optical microscope image of the microstructure was shown in previous Table 2.9. In Figure 2.31, none of the dendritic structure was observed and the microstructure was uniform throughout the section. The micro-structure was observed as closer to that normally found in the Ti-6Al-4V alloy, in which any segregation of elements was redistributed. The heat-treated micro-strut was analysed under the EDS.

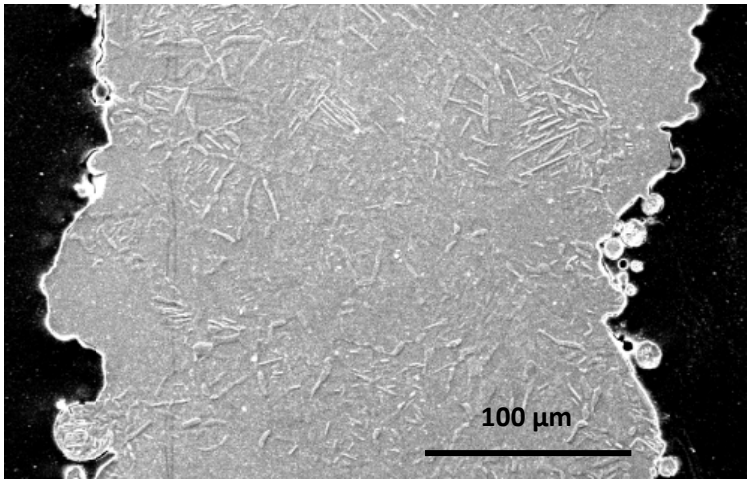

Figure 2.31: SEM image of microstructure for heat-treated SLM Ti-6Al-4V micro-strut (200 W X 1000 µs), after solution treatment and quenching process (Process A) [S1-90-200-1000-HT(A)-M]

As shown in Figure 2.32, line scan analysis of EDS was done in a selected area, where each shown spot represented one EDS scan part. Out of all ten spectrums acquired from ten spots, only three spectrums showed relatively low amount of iron (Fe) in the material, as in Figure 2.33. These were normal amounts of Fe expected in the Ti-6Al-4V alloy, whilst no chromium (Cr) was detected throughout the sampled area, as the overall level of residues was below the detection limit of the EDS system. This can be considered as a positive finding and the effect of the

redistribution of elements due to heat-treatment on the mechanical properties of micro-strut needs to be further studied. For a quick comparison, the hardness value of the heat-treated material was found to be approximately 424 HV.

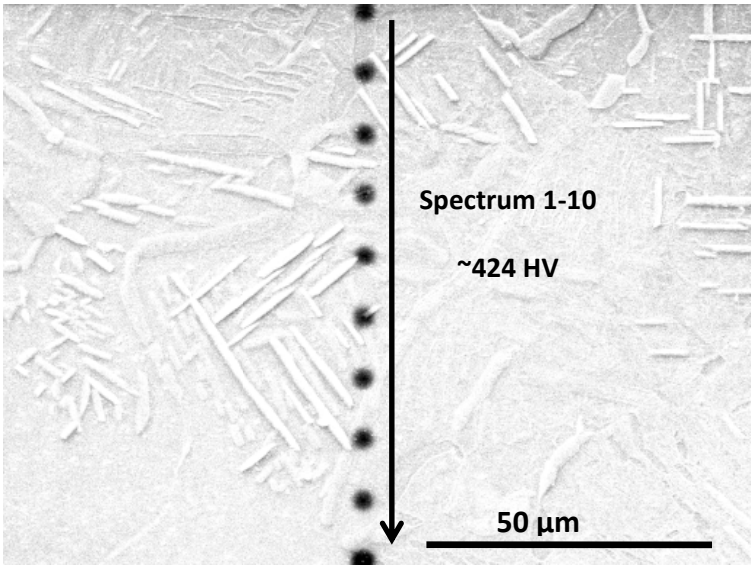

Figure 2.32: Ten spots of line scan analysis for heat-treated micro-strut (Process A) under the EDS [S1-90-200-1000-HT(A)-M]

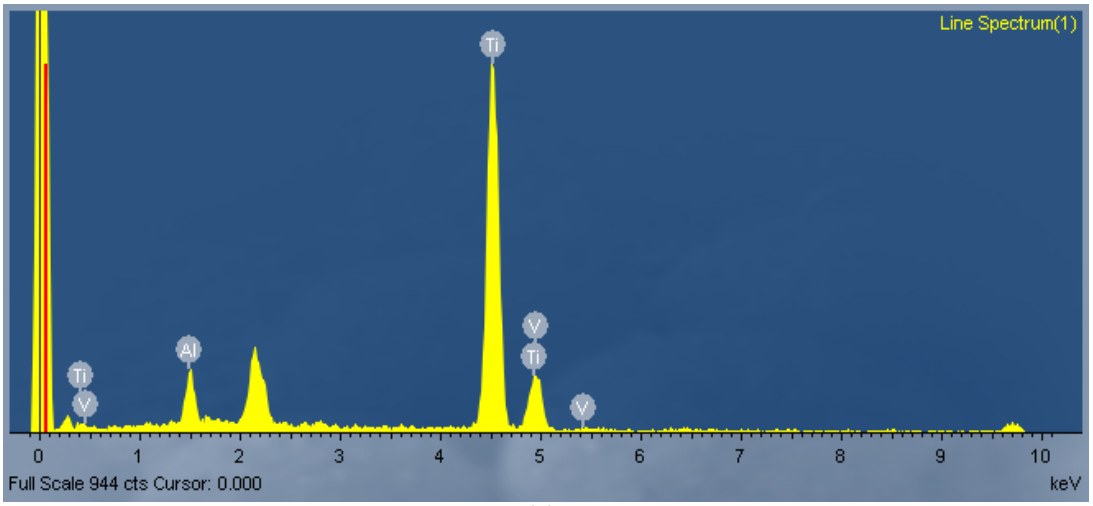

(a)

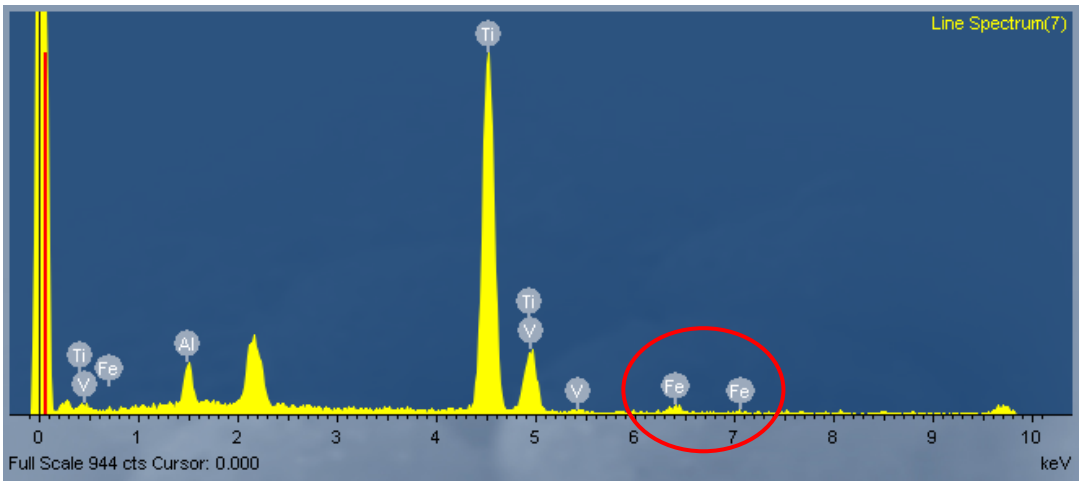

(b)

Figure 2.33: Examples of spectrums acquired from ten spots of EDS; (a) one out of seven normal Ti-6Al-4V spectrums; (b) one out of three spectrums which showed relatively low amount of Fe in the heat-treated material [S1-90-200-1000-HT(A)-M]

Table 2.10 lists the maximum level which is permitted for the Fe and other residue element (Cr) in the SLM Ti-6Al-4V material according to a recently published ASTM standard (2012). It can be concluded that, although the existence of residue elements cannot be eliminated from the micro-struts, the heat-treatment mitigates the residue elements throughout the material. The effects of heat-treatment to the mechanical properties of the SLM Ti-6Al-4V micro-struts are discussed in the following sections and summarized in Section 2.5.

Table 2.10: Comparison of the permitted level of residue elements according to the ASTM standard (2012) and the level of elements found in this study

Residue element	ASTM Standard (2012)	SLM Ti-6Al-4V micro-struts (Table 2.1)	
		As-received	Heat-treated
Iron (Fe) (Observation from the EDS)	Max. Element = 0.30 weight%	Max. Element = 0.25 weight%	
		High level of Fe detected at dendritic structures throughout the material	Fe was detected only at 30% of the sample area and no dendritic structures were observed
Chromium (Cr) (Observation from the EDS)	Max. Element = 0.10 weight%	Max. Element = not expected	
		Cr was detected at dendritic structures throughout the material	No Cr was detected (below the detection level of the EDS)

2.4 TENSILE TEST ON THE SLM Ti-6Al-4V MICRO-STRUTS

In previous research of stainless steel micro-lattice structure manufactured from rapid prototyping technology using selective laser melting (SLM) technique, the tensile properties of the individual as-received micro-strut was studied in order to evaluate the performance of stainless steel SS316L micro-lattice structure [Shen (2009)]. By using an extensometer, elastic modulus value of around 50 GPa or only 26% of stainless steel SS316L bulk material's modulus was determined. The low elastic modulus value was expected from the strain calculation of the extensometer, which was derived from the crosshead displacement during the tensile test. Thus, a compliance correction using finite element analysis was then applied in order to achieve a value of 140 GPa or approximately 74% of SS316L bulk material's value [Tsopanos et al. (2009)]. It should be noted that in previous study, no microstructural consideration was given in determining the mechanical properties.

In the current study, a simple and reliable method of determining tensile properties such as elastic modulus value will be suggested and applied, rather than using the finite element analysis procedure. The elastic modulus of the as-received and heat-treated SLM Ti-6Al-4V micro-struts were investigated using a basic experimental compliance correction method as found in literatures [Sergueeva et al. (2009); Kalidindi et al. (1997); Turek (1993)]. With the prior information on geometry and microstructure of struts used in this study, the difference in the results compared to standard values of the particular properties should therefore be fairly evaluated based on reality of manufactured specimen.

2.4.1 Assumptions and Justifications for Selected Micro-strut Geometry

Before further analysis in the derivation of mechanical properties, it should be noted that, an assumption was given, where the micro-strut was considered as a solid thin cylindrical shape. Based on justifications made during the analysis of micro-strut diameter, the average diameter of (374.14 ± 26.15) μm, within the range of minimum value of 321.84 μm and maximum value of 426.44 μm, were selected for the as-received strut. However, the average diameter value obtained from the vernier calliper measurements of five gauge lengths in micro-tensile tests was also used in the early stage of elastic modulus determination for the as-received struts, since the value of (0.375 ± 0.004) mm was within the range of the selected average diameter value ((374.14 ± 26.15) μm). Meanwhile, the heat-treated strut was also assumed as a cylindrical solid, but with a smaller average diameter of (322.56 ± 16.60) μm within the minimum and maximum range of 289.36 μm and 355.76 μm respectively. This can be attributed to the effects of heat-treatment on the surface irregularities of the struts.

It should be noted that, the maximum and minimum ranges of the diameter values gave the lower and upper boundaries estimations of micro-struts mechanical

properties. On assigning the boundaries estimations, justifications based on circularities of struts were also considered. Based on the previous Table 2.6, the non-circularity of 26% and 22% were estimated for the as-received and heat-treated struts, respectively. Comparison of percentage of non-circularities with maximum and minimum areas of micro-struts, further confirmed the selection of diameter values for the lower and upper boundaries in the derived mechanical properties of micro-struts. Table 2.11 tabulates the comparison of the minimum and maximum cross-sectional area values with the non-circularity of as-received and heat-treated micro-struts. It was shown that percentage of differences for maximum and minimum cross-sectional areas were comparable to the percentage of non-circularity for both the as-received and heat-treated micro-struts.

Table 2.11: Comparison on the minimum and maximum cross-sectional area values with the non-circularity of as-received and heat-treated micro-struts

	As-received micro-strut			Heat-treated micro-strut		
	Minimum	Average	Maximum	Minimum	Average	Maximum
Diameter (mm)	0.322	0.374	0.426	0.289	0.323	0.356
Cross-sectional area (mm^2)	0.08136	0.10995	0.14284	0.06577	0.08173	0.09942
Difference from average value	26.00%	-	29.91%	19.53%	-	21.64%
Non-circularity (Table 2.6)	26.43% Comparable % values			22.09% Comparable % values		

2.4.2 Testing Procedure

The tensile tests for the SLM Ti-6Al-4V micro-struts were conducted on a small bench top servo-hydraulic testing machine (Instron 3342 machine controlled by a computer using Instron Bluehill software), with 500 N load cell, due to the small size of the micro-struts. The load accuracy of the machine was 0.5% of the indicated load [Instron (2013)]. Such test machines are regularly used for testing fibre filaments and wires [Shen (2009)]. Loading velocity of 0.1 mm/minute was applied throughout the test, without the application of extensometer for strain measurement. The strain-rate, determined by dividing the loading velocity by the gauge length, was approximately 10^{-4} s^{-1} throughout the entire test. The load was recorded by a dedicated computer. The strain was derived directly from the crosshead displacement and the compliance correction method was applied. Limited by the manufactured specimen length of 43 mm, only five different gauge lengths, L, were tested; 5 mm, 8 mm, 10 mm, 22 mm and 30 mm, with three repeat tests for each gauge length. Figure 2.34(a) to (e) show the arrangement of the machine for the tensile tests of different gauge lengths. The gauge length measurements were set by using a ruler; and for repetition tests, the setting measurements at the machine were used. This meant that for each gauge length, a same measurement length was used in all repetitions. Both specimen ends were manually tightened at jaw grippers. The faces of the test machine grippers were glued with 240 grit emery papers which were expected to minimize the slippage effects of the micro-struts during the tests. The emery papers were replaced after about five tests took place, in order to make sure that gripping mechanism was similar for all tests. A disadvantage of this tensile test procedure was that it was highly operator dependence. Thus, an operator needs to familiarize him/herself with the apparatus, software and micro-strut specimen handling before conducting the tests.

Throughout the study, the engineering stress-strain curves were converted to the true stress-strain curves based on the Equations [1.5] to [1.12] as discussed in Chapter 1. It was noticed that the differences between the true stress-strain curves and the

engineering stress-strain curves were minimum and were shown in the following discussions.

(a) (b) (c) (d) (e)

Figure 2.34: Micro-tensile tests of the SLM Ti-6Al-4V micro-struts at different gauge lengths; (a) 5 mm; (b) 8 mm; (c) 10 mm; (d) 22 mm; (e) 30 mm [S(1-15)-35-200-1000-AR]

2.4.3 Basic Theory of Compliance Correction Method

The fundamental concept behind the compliance correction method is based on the assumption that the specimen and testing fixture can be modelled as a system with two springs in series. When subjected to a same applied load F, the total measured displacement can be taken as the sum of the displacements in the specimen and the loading system, as represented by Equation 2.12.

$$\delta_T = \delta_S + \delta_C \qquad [2.12]$$

δ_T is the total measured displacement, while δ_S is the specimen deformation and δ_C is the displacement in the loading system, i.e. the machine compliance factor. If both the specimen and the loading system are assumed as linear elastic springs, it can be shown that the apparent compliance factor, C_a $(= \delta_T/F)$, is related to the machine compliance factor, C_m $(= \delta_C/F)$, as given in Equation 2.13.

$$C_a = C_m + (1/EA)L \quad [2.13]$$

E is the elastic modulus of the tested specimen while A and L are the cross-sectional area and the length of the specimen, respectively. As suggested in a withdrawn but still reliable standard (ASTM D 3379-75), C_m is the zero gauge length intercept on a plot of C_a versus L for a given material, and the corrected elastic modulus, E, of the material can be extracted from the slope of this plot, or calculated from Equation 2.14, where E_u is the uncorrected elastic modulus of the tested material.

$$E = \frac{(L/A)}{(C_a - C_m)} = \frac{(E_u C_a)}{(C_a - C_m)} \quad [2.14]$$

However, for a more accurate compliance factor, Equation 2.13 can be modified as shown in Equation 2.15, with C_m is the zero gauge length intercept on a plot of C_a versus L/D^2 , where D is the diameter of the specimen [Li and Langley (1985)].

$$C_a = C_m + (4/\pi E)(L/D^2) \quad [2.15]$$

2.4.4 Determination of Elastic Modulus and Mechanical Properties of the As-Received Micro-Strut

Figure 2.35 shows the measured elastic modulus values for the as-received SLM Ti-6Al-4V micro-struts at several gauge lengths, between 5 to 30 mm. The tests were repeated three times for each gauge length. Each gauge length has its own average diameter value from vernier calliper measurements, as shown in Table 2.12, and the average diameter values for all gauge lengths were still within the range of the selected average diameter value from the shadow measurement method.

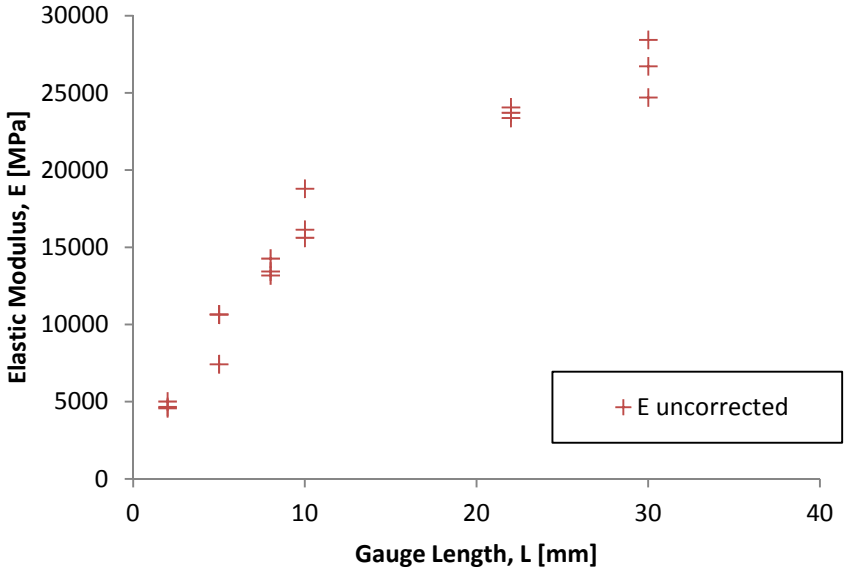

Figure 2.35: Plot of Elastic Modulus versus Gauge Length for the as-received SLM Ti-6Al-4V micro-struts with 35° build angle at 200 W laser power and 1000 µs laser exposure time [S(1-15)-35-200-1000-AR]

The micro-tensile test results showed that higher elastic modulus values were obtained for longer gauge lengths. The repeatability of the results can be seen from the scatter between values for each gauge length in Figure 2.35. The values scatter between 1% (at 22 mm gauge length) and 20% (at 5 mm gauge length). By using the experimental compliance correction method, as explained in previous section, the elastic modulus was corrected. Figure 2.36 shows a plot of apparent compliance factor versus gauge length over square of diameter, which was tabulated in order to obtain a machine compliance factor of 0.0042 mm/N from y-axis intersection. The machine compliance factor is important in the determination of the corrected elastic modulus value.

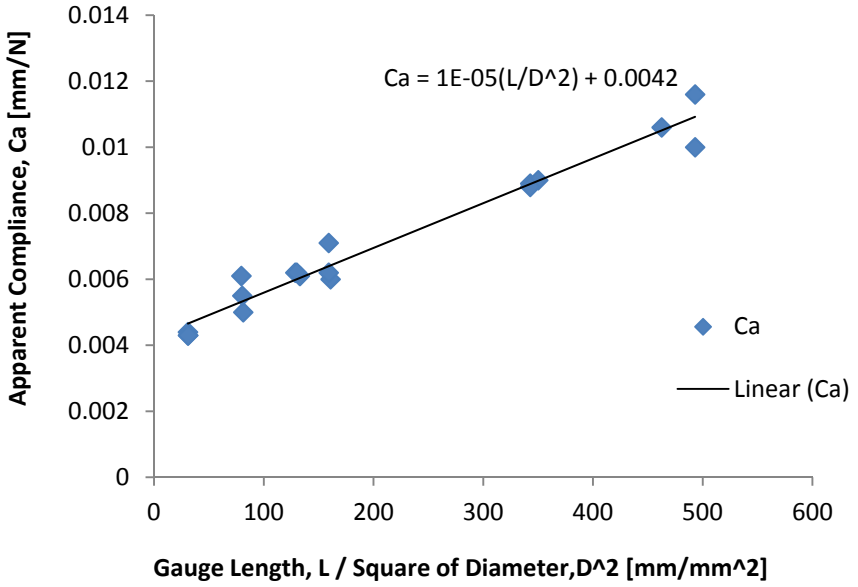

Figure 2.36: Plot of C_a versus L/D^2 for micro-strut tensile test of as-received SLM Ti-6Al-4V [S(1-15)-35-200-1000-AR]

Table 2.12: List of corrected elastic modulus values for different gauge lengths of micro-tensile test result for the as-received SLM Ti-6Al-4V micro-struts (The ± values are from standard deviation values of each repetition) [S(1-15)-35-200-1000-AR]

Gauge length [mm]	Average diameter [mm]	Average apparent compliance for test [mm/N]	Average uncorrected E value [GPa]	Average corrected E value [GPa]
30	0.374 ± 0.007	0.0107 ± 0.0008	27 ± 1.9	44 ± 5.2
22	0.379 ± 0.002	0.0089 ± 0.0001	24 ± 0.3	45 ± 0.9
10	0.375 ± 0.001	0.0064 ± 0.0006	17 ± 1.7	50 ± 12
8	0.371 ± 0.003	0.0062 ± 0.00006	14 ± 0.6	43 ± 1.7
5	0.374 ± 0.002	0.0055 ± 0.0006	10 ± 1.9	45 ± 21
	0.375 ± 0.004		Ave. E from all gauge lengths	45 ± 9.9

Table 2.12 lists the corrected elastic modulus values for the different gauge lengths. From the table, it can be seen that the average corrected elastic modulus (E) value for the as-received SLM Ti-6Al-4V micro-strut was about 40% (45 ± 9.9 GPa) of that standard Ti-6Al-4V value (114 GPa) [Boyer et al. (1994)]. It was noted that the E value of the 22 mm gauge length was the nearest to the average value. In this case, the 22 mm gauge length was chosen in further analysis, based on the lowest scatter between the results and the nearest to the average corrected E value. Figure 2.37 shows the uncorrected and corrected stress-strain curves determined using the experimental compliance correction method. From these curves, properties such as yield strength (YS), ultimate tensile strength (UTS) and elongation to failure were also obtained.

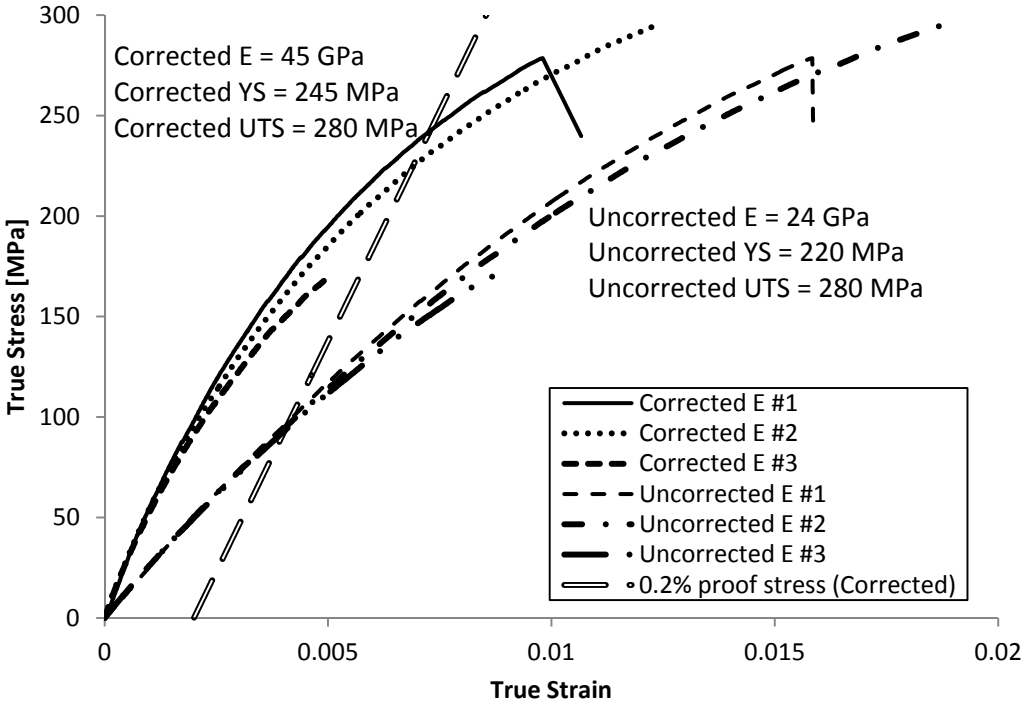

Figure 2.37: Stress-strain curves of uncorrected and corrected elastic modulus value for 22 mm gauge length for as-received SLM Ti-6Al-4V micro-struts (with repeat tests) [S(1-15)-35-200-1000-AR]

Table 2.13 lists the properties of the as-received SLM Ti-6Al-4V micro-strut, compared to properties reported in literatures. It can be seen that there were

variations in the reported values, due to the differences in processing and manufacturing routes in these studies. Other than the standard annealed Ti-6Al-4V [Boyer et al. (1994)], the rest of the selected literatures used additive manufacturing (layer by layer powder melting) to build the specimen, either by selective laser melting (SLM), direct laser forming (DLF) or electron beam melting (EBM). None of these studies used the same processing parameters, therefore variations can also be seen in studies using similar processes. It was found that the material properties determined in this study were the lowest among the tabulated values. The SLM Ti-6Al-4V micro-strut in this study showed approximately 40% (45 ± 9.9 GPa) of E value, 28% (245 MPa) of YS value, 30% (280 MPa) of UTS value, and 1% of elongation, as compared to the standard annealed Ti-6Al-4V [Boyer et al. (1994)]. Yet, it can be seen that the elongation to rupture of micro-strut in this study was around 19% to 30% of the elongations reported in other SLM studies. It can be concluded that the micro-strut used in this study is lower in strength and ductility. These trends have also been found for stainless steel micro-struts manufactured used SLM [Tsopanos et al. (2010)].

One of the factors that contributed to this was the small size of the micro-strut as compared to other specimens. The average outer diameter of the micro-strut measured using vernier caliper was 0.375 ± 0.004 mm, and this build was manufactured by using single laser melting point (single pass) at each layer. Multiple laser melting points (multiple passes) were used in each layer to build the desired geometry of the specimens in other studies. Therefore, in this study, the strength of the micro-strut was highly dependent on the strength of the overlapping (welding) area between each melted powder layer. Another factor that may contribute to the low properties of the micro-strut is the assumption of the micro-strut as a solid cylindrical shape. In reality, the SLM micro-strut shape is not as smooth as a solid rod, since the geometry depends on the optical quality of the laser beam [Tsopanos et al. (2010)], the build angle [Cansizoglu et al. (2008)], and other manufacturing parameters, as discussed in section 2.3.2 to 2.3.4.

Table 2.13: Properties of the as-received SLM Ti-6Al-4V micro-strut in this study compared to other properties from literatures

Reference	Process		Material's structure / dimension	Properties			
				E (GPa)	YS (MPa)	UTS (MPa)	Elongation to failure (%)
This study	Selective laser melting (200 W, 1000 μs)		Circular micro-strut / 0.375 mm X 43 mm	45	245	280	1.5
Properties from Matweb [Boyer et al. (1994)]	Annealed		-	114	880	950	14.0
[Facchini et al. (2010)]	Selective laser melting (195 W, 225 mm/s scan speed)		Rectangular cross-section bar / 90 mm X 32 mm	110	990	1095	8.1
[Facchini et al. (2009)]	Electron beam melting (4 kW)	As-built	Rectangular cross-section bar / 90 mm X 32 mm	118	830	915	13.1
		Hipped		117	795	870	13.7
[Murr et al. (2009)]	Electron beam melting (102 kW/cm^2 energy density, 10^3 mm/s scan speed)		Cylindrical rod / 20 mm X 120 mm	-	1125	1150	20.0
	Selective laser melting (190 W, 7x10^3 mm/s scan speed)			-	1325	1400	4.5
[Vandenbroucke and Kruth (2007)]	Selective laser melting (95 W, 125 mm/s)		-	94	1125	1250	6.0
[Hollander et al. (2006)]	Direct laser forming	As-built	Round tensile specimen / 4 mm X 54 mm	118	1100	1211	6.5
		Annealed		118	960	1042	13.0

Figure 2.38 shows another plot of stress-strain curve for the as-received SLM Ti-6Al-4V micro-strut, with the lower and upper ranges estimation for the curve; by applying the maximum and minimum values of the selected diameter ranges in the derivation formulas, as well as consideration of 26% non-circularity of the as-received micro-strut (Table 2.11). Although a large range was covered by the upper and lower boundaries, which were approximately 35% and 25% from the curve, respectively; it was found comparable to the percentage of non-circularity of the micro-strut (Table 2.11). This suggested that the percentage of non-circularity can be used for rough estimation of deviations in mechanical properties of the micro-strut. Further confirmation can be found from the results of the heat-treated strut that will be discussed in the following section.

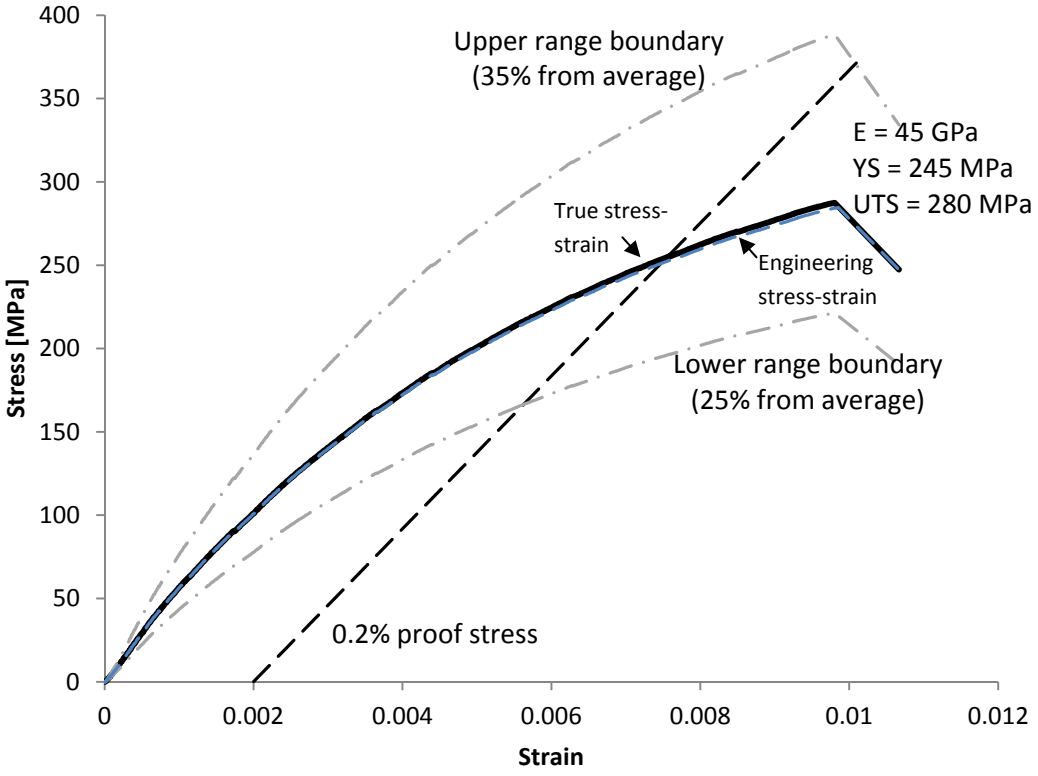

Figure 2.38: Stress-strain curves for the as-received SLM Ti-6Al-4V micro-strut with lower and upper range boundaries

2.4.5 Determination of Elastic Modulus and Mechanical Properties of the Heat-treated Micro-Struts

The uncorrected and corrected elastic modulus values for the heat-treated SLM Ti-6Al-4V micro-struts at gauge lengths between 5 mm to 30 mm were listed in Table 2.14. Due to limited number of specimen, repetitions were only done on tests at 10 mm and 22 mm gauge lengths. The heat-treated struts were assumed as cylindrical solids with an average diameter of (322.56 ± 16.60) μm, with the minimum and maximum range of 289.36 μm and 355.76 μm. A similar procedure as described in section 2.4.4 was applied to obtain a machine compliance factor from the tests, which was found to be 0.0034 mm/N, in the determination of the corrected elastic modulus value for the heat-treated micro-struts.

Table 2.14: List of corrected elastic modulus values for different gauge lengths of micro-tensile test result for the heat-treated SLM Ti-6Al-4V micro-struts [S(1-9)-35-200-1000-HT(B)]

Gauge length [mm]	Average diameter [mm]	Average apparent compliance for test [mm/N]	Average uncorrected E value [GPa]	Average corrected E value [GPa]
30	0.322 ± 0.017	0.0088	42	68
22	0.322 ± 0.017	0.0077 ± 0.0007	36 ± 3.3	65
10	0.322 ± 0.017	0.0052 ± 0.0005	28 ± 2.8	75
8	0.322 ± 0.017	0.0047	22	79
5	0.322 ± 0.017	0.0044	13	56
			Ave. E from all gauge lengths	69 ± 8.8

From Table 2.14, it can be seen that the average corrected elastic modulus (E) value for the heat-treated SLM Ti-6Al-4V micro-strut was increased to 53% from that of the as-received micro-strut, and was about 61% (69 ± 8.8 GPa) of that standard Ti-

6Al-4V value (114 GPa) [Boyer et al. (1994)]. In order to be comparable to the as-received micro-strut, test data of 22 mm gauge length was selected for further analysis of mechanical properties of the heat-treated micro-strut. It should be noted that there was a difference between the average elastic modulus value (69 GPa) and the elastic modulus of 22 mm gauge length (65 GPa). In this case, the estimation of mechanical properties was referred to the 22 mm gauge length properties.

Figure 2.39 shows the uncorrected and corrected stress-strain curves determined using the experimental compliance correction method for the heat-treated micro-struts at 22 mm gauge length. The heat-treated SLM Ti-6Al-4V micro-strut showed increased properties values from that of the as-received; which was approximately 39% (340 MPa) of yield strength (YS) value, 55% (520 MPa) of ultimate tensile strength (UTS) value, and 1.5% of elongation, as compared to the standard annealed Ti-6Al-4V [Boyer et al. (1994)].

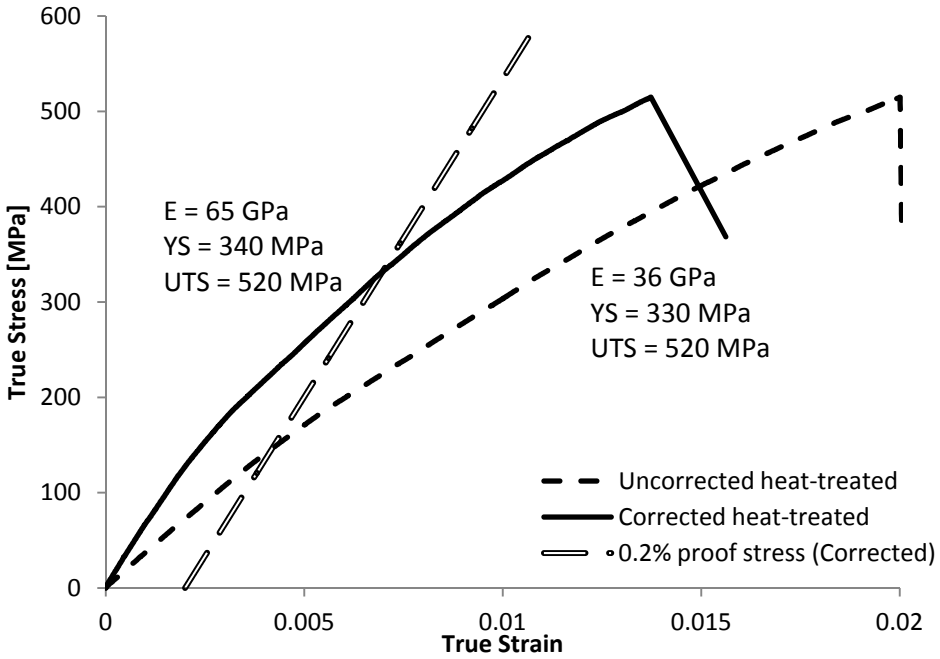

Figure 2.39: Stress-strain curves of uncorrected and corrected elastic modulus value for 22 mm gauge length for heat-treated SLM Ti-6Al-4V micro-strut

Figure 2.40 shows another plot of stress-strain curve for the heat-treated SLM Ti-6Al-4V micro-strut, with the upper and lower range boundary estimations. The upper boundary of 23% and lower boundary of 17% from the stress-strain curve of the heat-treated micro-strut were found to be comparable to the percentage of non-circularity of the heat-treated micro-strut, which was 22% (Table 2.11). As suggested in the previous section, the percentage of non-circularity can be used in rough estimation of deviations in mechanical properties of the micro-strut.

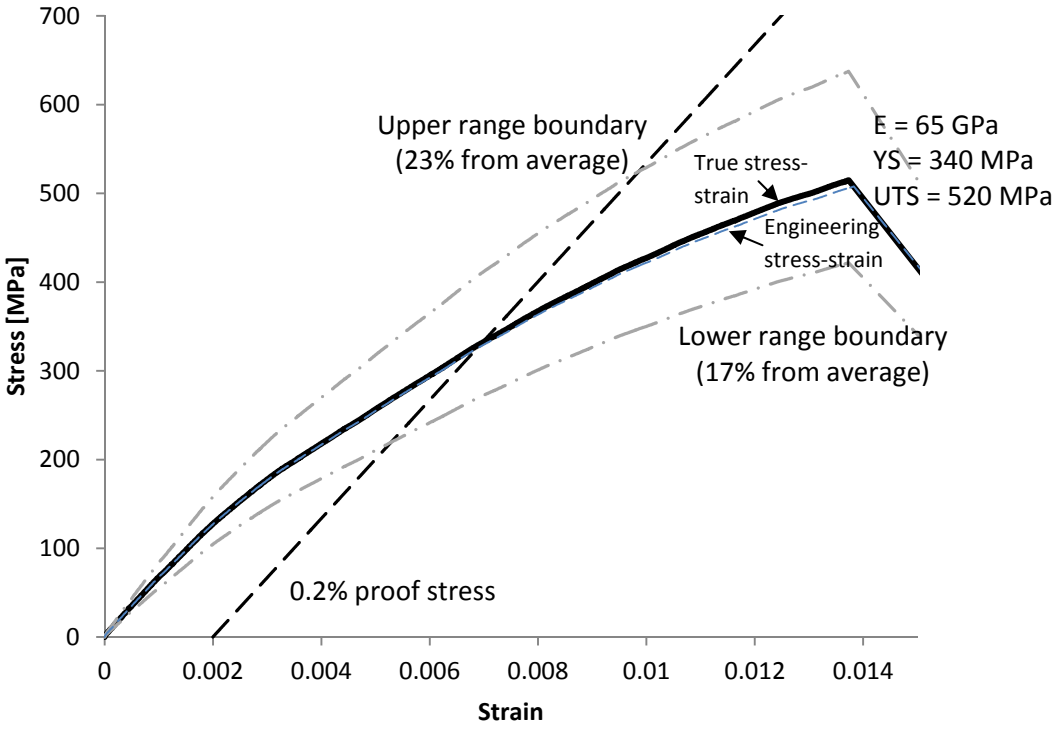

Figure 2.40: Stress-strain curve for the heat-treated SLM Ti-6Al-4V micro-strut with lower and upper range boundaries

2.4.6 Fracture Surface and Failure Mechanism of SLM Ti-6Al-4V Micro-Struts

Fracture surface of the as-received micro-strut after failure due to tensile loading was shown in Figure 2.41. In order to assist discussions, Figure 2.5(b) and 2.6 are re-presented and renumbered as Figure 2.42 below.

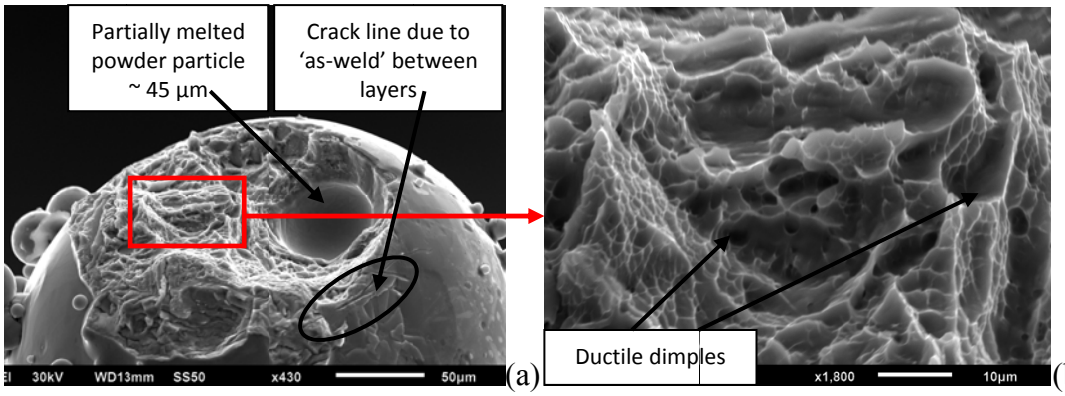

Figure 2.41: Fracture surface of as-received, 35° build angle strut of SLM Ti-6Al-4V manufactured at 200 W laser power and 1000 µs laser exposure time; (a) at lower magnification; (b) at higher magnification which shows ductile dimples [S1-35-200-1000-AR]

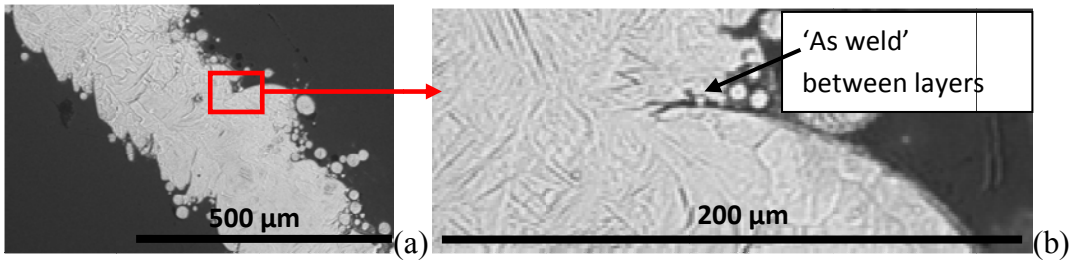

Figure 2.42: Images of cross sections for as-received micro-struts with 200 W X 1000 µs parameters at 35° build angle; (a) at lower magnification; (b) at higher magnification [S1-35-200-1000-AR-M]

Ductile dimples were clearly observed on the fracture surface of the as-received micro-strut as in Figure 2.41(b), indicating that ductile rupture has taken place. As

shown in Figure 2.41(a), there was evidence of porosity in the struts, due to partially melted powder particle with size approximately 45 µm. Near the porosity, a crack line was observed, and it was expected that this area was the area of 'as-weld' between layer, as shown in Figure 2.42. The 'as-weld' between layer areas contributed to irregularities along the micro-strut surface, where stress concentration took place. The rupture was expected to start from these weak regions which are also called 'stress raisers'. It was mentioned in literature that many fractures occur due to crack propagation from the vicinity of a macroscale stress raiser [Becker and McGarry (2002)]. This was also explained by Kerlins and Phillips (1987), where fracture of a stressed part is often caused by the presence of some internal or surface discontinuities such as laps, seams, cracks, porosity and inclusions.

In this study, during tensile test of a micro-strut, stress was concentrated at the most distinct 'as-weld' discontinuity area as shown in Figure 2.42, and crack occurred at that place. Once the crack initiated, fracture took place and propagated toward other discontinuities and weak points within the strut, such as areas with partially melted powder particles and microvoids. Afterwards, due to microvoids coalescence and ductile overload at the rest of the locations, the micro-strut ruptured with ductile fracture failure. An SEM image in Figure 2.43 showed another fracture surface of a micro-strut, with numbering that indicated the progression of failure that took place.

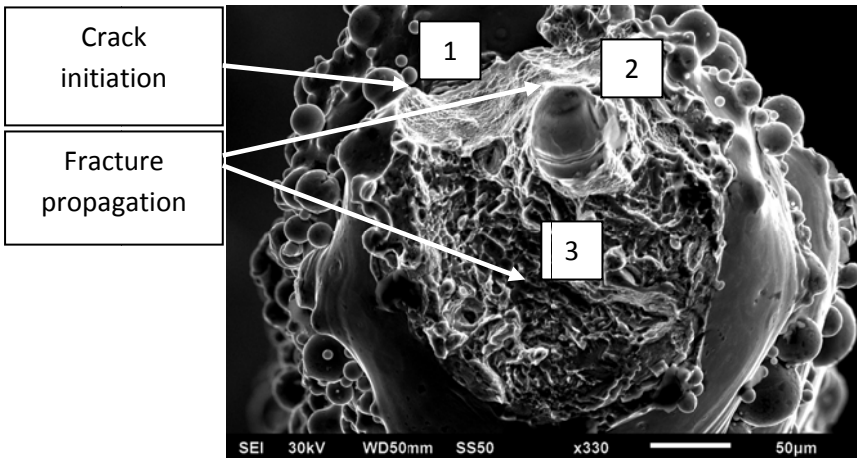

Figure 2.43: Progression of failure in the SLM Ti-6Al-4V micro-strut (200 W X 1000 µs, 35° build angle), due to tensile loading [S2-35-200-1000-AR]

The irregularities along the surface of micro-struts and the existence of voids inside the micro-struts contributed to the initiation of crack that resulted in ductile fracture of the material. Similar fracture was observed in the heat-treated micro-strut, as shown in Figure 2.44. There was an existence of void at the fracture surface, but none of the obvious discontinuities at outer surface was observed. The discontinuities were fused together and improved by the heat-treatment, hence smoothing the outer surface of strut and reducing the stress raiser. This has contributed to the improvement in the strength of the heat-treated strut as compared to the as-received strut. Figure 2.44(b) shows higher magnification of the fracture surface. There was evidence of ductile fracture having taken place, shown by the appearance of ductile dimples.

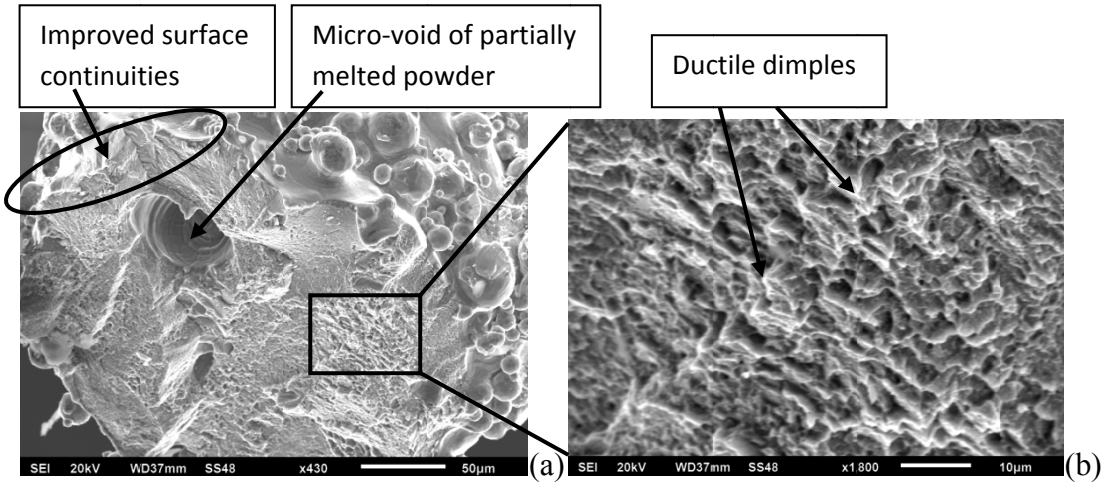

Figure 2.44: Fracture surface of the heat-treated micro-strut due to tensile loading (35° build angle, 200 W laser power and 1000 µs laser exposure time); (a) at lower magnification; (b) at higher magnification which shows ductile dimples [S1-35-200-1000-HT(B)]

As mentioned in Hooputra et al. (2004), the main mechanism that can cause the fracture of a ductile metal is the void nucleation, void growth and void coalescence. For ductile fracture, it is assumed that the equivalent fracture strain ε_{eq}^{**} is a function

of the stress triaxiality η, defined in Equation 2.16 by components in principal stress space.

$$\eta = \frac{3\sigma_m}{\sigma_{eq}} = \frac{\sigma_1 + \sigma_2 + \sigma_3}{\sqrt{\alpha_1^2 + \alpha_2^2 + \alpha_3^2 - \sigma_1\sigma_2 - \sigma_2\sigma_3 - \sigma_3\sigma_1}} \quad [2.16]$$

Where $\sigma_m = (\sigma_1 + \sigma_2 + \sigma_3)/3$; σ_{eq}= equivalent stress; $\alpha_{1,2,3}$ = ratio of minor principal strain (rate) to major principal strain (rate) and; $\sigma_{1,2,3}$ = principal components of stress tensor.

Typically, the dependence of the equivalent fracture strain on the stress triaxiality is expressed in the form of Equation 2.17.

$$\varepsilon_{eq}^{**} = d_0 \exp(-c\eta) \quad [2.17]$$

Where d_0 = material parameters in ductile fracture curve; c = directionally dependant material in ductile fracture curve; η = stress triaxiality.

On the other hand, Becker and McGarry (2002) discussed on model of void nucleation for ductile crack. One of the simpler models that predict a strain to fracture ε_f, is given by Equation 2.18.

$$\varepsilon_f = 2 \ln\frac{L}{w} \approx \ln\frac{1}{\rho} \quad [2.18]$$

Where L is the void spacing, w is the void size, and ρ is the void volume fraction. Figure 2.45 illustrates the definitions of parameters of Equation 2.18.

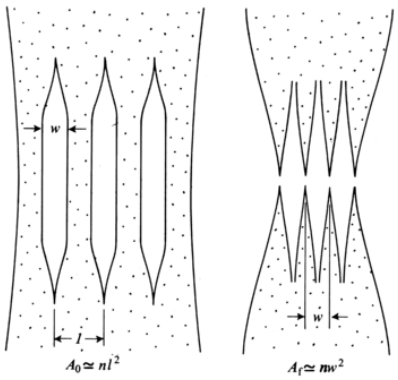

Figure 2.45: Parameters definition of Backofen's model for fracture from holes [Becker and McGarry (2002)]

2.4.7 Determination of Equivalent Plastic Strain from Micro-strut Tensile Test

As mentioned in previous section, the equivalent plastic strain is an important parameter in failure analysis of ductile materials. Therefore, it is one of the aims of this study to determine the equivalent plastic strain from the uniaxial micro-tensile test of the SLM Ti-6Al-4V micro-struts. The findings are to be used in the measurement of fracture and prediction of failure in the finite element analysis that will be discussed in Chapter 4.

A typical elastic-linear strain hardening curve is shown in Figure 2.46, where σ_Y is the yield stress, E is the Young's modulus, E_t is the tangential modulus after yielding. The figure shows a bilinear curve, as a simplification from reality, which is a continuous curve, as shown in Figure 2.47. Derivations of equations for hardening and flow rule are as in the following discussions [Tan (2009); Lemaitre and Chaboche (1990)].

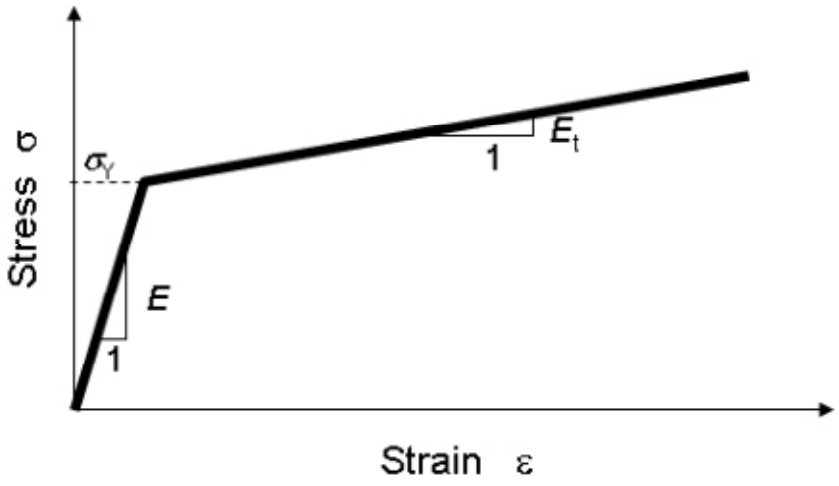

Figure 2.46: A typical stress (true) – strain (true) curve from a uniaxial test [Tan (2009)]

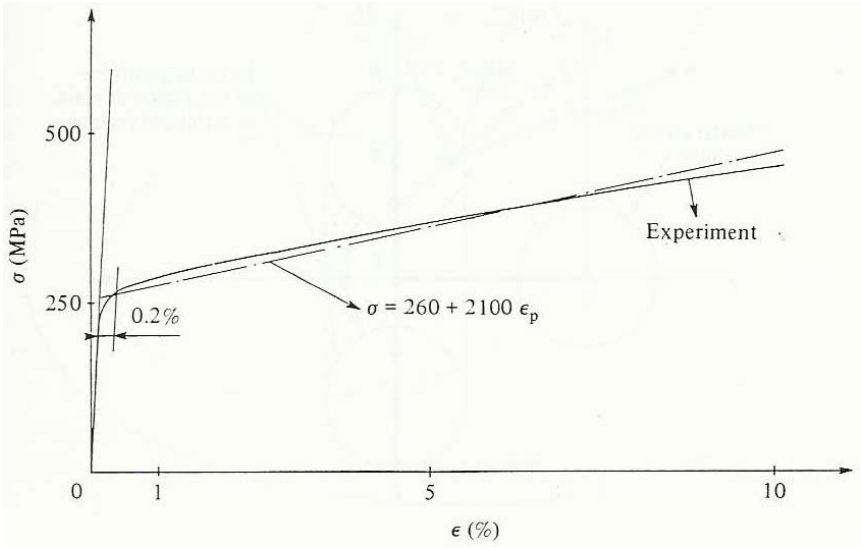

Figure 2.47: A continuous true stress-strain curve of A316 stainless steel with the identification of linear hardening in tension [Lemaitre and Chaboche (1990)]

The von Mises yield criterion can be expressed in another form;

$$\bar{\sigma} = \sigma_Y \,, \qquad [2.19]$$

Where $\bar{\sigma}$ is the equivalent yield stress which is defined as

$$\bar{\sigma} = \sqrt{3J_2} \,. \qquad [2.20]$$

Based on the relation between J_2 and the deviatoric stress tensor, one has

$$\bar{\sigma} = \sqrt{\frac{3}{2}\sigma'_{ij}\sigma'_{ij}} \,. \qquad [2.21]$$

The resistance to plastic flow of a deformed solid is known as strain hardening. The yield criterion will change with further development of plastic deformation. It is assumed that the yield criterion that can account for the hardening can be written as

$$\bar{\sigma} = Y(\bar{\varepsilon}^p) \,, \qquad [2.22]$$

where $\bar{\varepsilon}^p$, called equivalent plastic strain, is a scalar measure of plastic strain tensor defined through time integration of the equivalent plastic strain rate

$$\bar{\varepsilon}^p = \int_{t=0}^{t} \dot{\bar{\varepsilon}}^p dt \,, \qquad [2.23]$$

Where $\varepsilon_{ij}^{p} = 0$ at the time $t = 0$, and the equivalent plastic strain rate $\dot{\bar{\varepsilon}}^{p}$ is defined as

$$\dot{\bar{\varepsilon}}^{p} = \sqrt{\frac{2}{3}\dot{\varepsilon}_{ij}^{p}\dot{\varepsilon}_{ij}^{p}}\,. \qquad [2.24]$$

During plastic deformation, $\dot{\varepsilon}_{ii}^{p} = 0$, due to the incompressibility. Therefore, in a uniaxial tension, the plastic strain rate is $\dot{\varepsilon}^{p} = \begin{bmatrix} \dot{\varepsilon}^{p} & 0 & 0 \\ 0 & -\frac{1}{2}\dot{\varepsilon}^{p} & 0 \\ 0 & 0 & -\frac{1}{2}\dot{\varepsilon}^{p} \end{bmatrix}$, which gives the equivalent plastic strain as

$$\bar{\varepsilon}^{p} = \int \sqrt{\frac{2}{3}\left(\dot{\varepsilon}^{p}\dot{\varepsilon}_{11}^{p} + \dot{\varepsilon}_{22}^{p}\dot{\varepsilon}_{22}^{p} + \dot{\varepsilon}_{33}^{p}\dot{\varepsilon}_{33}^{p}\right)dt}$$

$$= \int \sqrt{\frac{2}{3}\left(\dot{\varepsilon}^{p}\dot{\varepsilon}^{p} + \frac{1}{4}\dot{\varepsilon}^{p}\dot{\varepsilon}^{p} + \frac{1}{4}\dot{\varepsilon}^{p}\dot{\varepsilon}^{p}\right)dt}$$

$$\bar{\varepsilon}^{p} = \int \dot{\varepsilon}^{p}dt = \varepsilon^{p} \qquad [2.25]$$

The equivalent yield stress as a function of equivalent plastic strain, $(\bar{\varepsilon}^{p})$, can be obtained from experiment, such as uniaxial test or torsion test, based on the condition that the yield criterion must be satisfied at all times during plastic straining.

In uniaxial stress state, letting axis 1 along the tensile direction, the stress tensor is

$$\boldsymbol{\sigma} = \begin{bmatrix} \sigma & 0 & 0 \\ 0 & 0 & 0 \\ 0 & 0 & 0 \end{bmatrix}, \qquad [2.26]$$

The deviatoric stress tensor is

$$\boldsymbol{\sigma}' = \begin{bmatrix} \frac{2}{3}\sigma & 0 & 0 \\ 0 & -\frac{1}{3}\sigma & 0 \\ 0 & 0 & -\frac{1}{3}\sigma \end{bmatrix}, \qquad [2.27]$$

Therefore the equivalent stress is $\bar{\sigma} = \sigma$. As shown in Equation 2.25 that the equivalent strain during uniaxial tensile test $\bar{\varepsilon}^{p} = \bar{\varepsilon}_{11}^{p}$. Thus, the uniaxial stress-strain can be employed to determine the hardening law for a general stress state.

As in previous Figure 2.46, the relation between the equivalent yield stress *Y* and the equivalent plastic strain $\bar{\varepsilon}^p$ can be derived. From the figure, during the plastic deformation

$$\sigma = \sigma_Y + E_t(\varepsilon - \varepsilon_Y) , \quad [2.28]$$

Where σ_Y is the initial yield stress, and $\varepsilon_Y = \frac{\sigma_Y}{E}$ is the strain at the yield point.

Since $= \varepsilon^e + \varepsilon^p$, where $\varepsilon^e = \frac{\sigma}{E}$ is the elastic part of the strain and ε^p is the plastic part, one has

$$\sigma = \sigma_Y + \frac{EE_t}{E-E_t}\varepsilon^p .$$

Since for uniaxial tension, the equivalent stress $\bar{\sigma} = \sigma$, and the equivalent plastic strain $\bar{\varepsilon}^p = \varepsilon^p$, the relation between the equivalent yield stress and the equivalent plastic strain as assumed in Equation 2.22 is

$$\bar{\sigma} = \sigma_Y + \frac{EE_t}{E-E_t}\bar{\varepsilon}^p . \quad [2.29]$$

Figure 2.48 shows a stress-strain curve of the as-received SLM Ti-6Al-4V micro-strut, with a projected tangent line (dashed line), for the extraction of tangential modulus after yielding E_t . The tangent was drawn passing both the yield strength value and the maximum point of the initial stress-strain curve. A curve which is similar to a typical stress-strain curve (Figure 2.46) is obtained, and shown in Figure 2.49. The initial modulus value *E* is 45 GPa while the yield stress value σ_Y is 245 MPa. From Figure 2.49, the tangential modulus after yielding E_t is determined as 6.7 GPa. By substitution of the required values into Equation 2.29, the relation between the equivalent yield stress and the equivalent plastic strain of the as-received SLM Ti-6Al-4V micro-strut is given by Equation 2.30.

$$\bar{\sigma} = [0.245 + 7.8721\bar{\varepsilon}^p]\text{GPa} \quad [2.30]$$

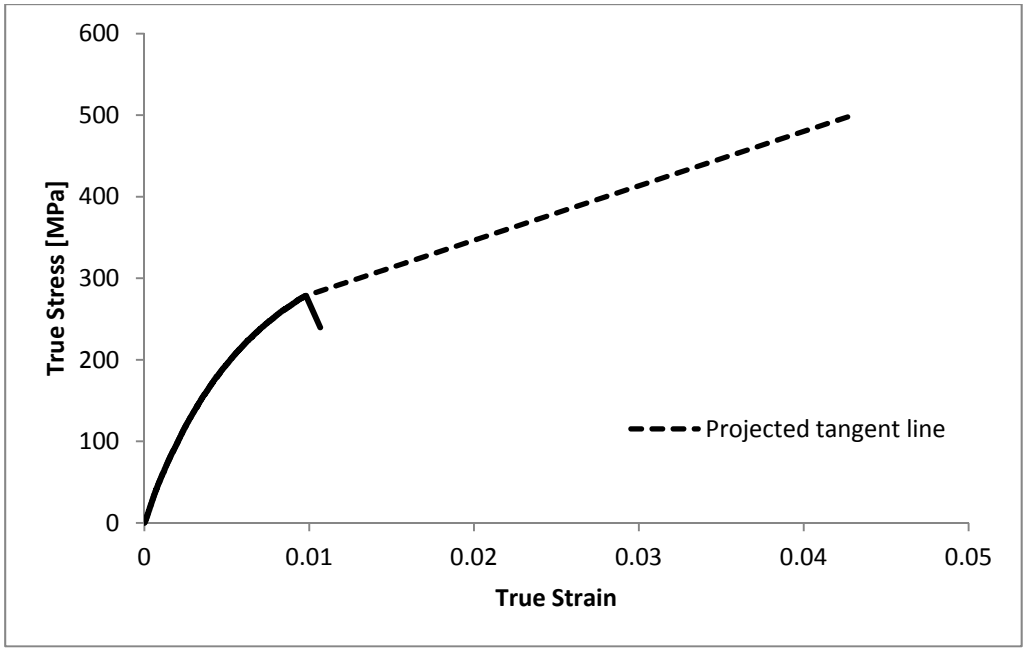

Figure 2.48: Stress-strain curve of the as-received SLM Ti-6Al-4V micro-strut, with a projected tangent line [S(1-15)-35-200-1000-AR]

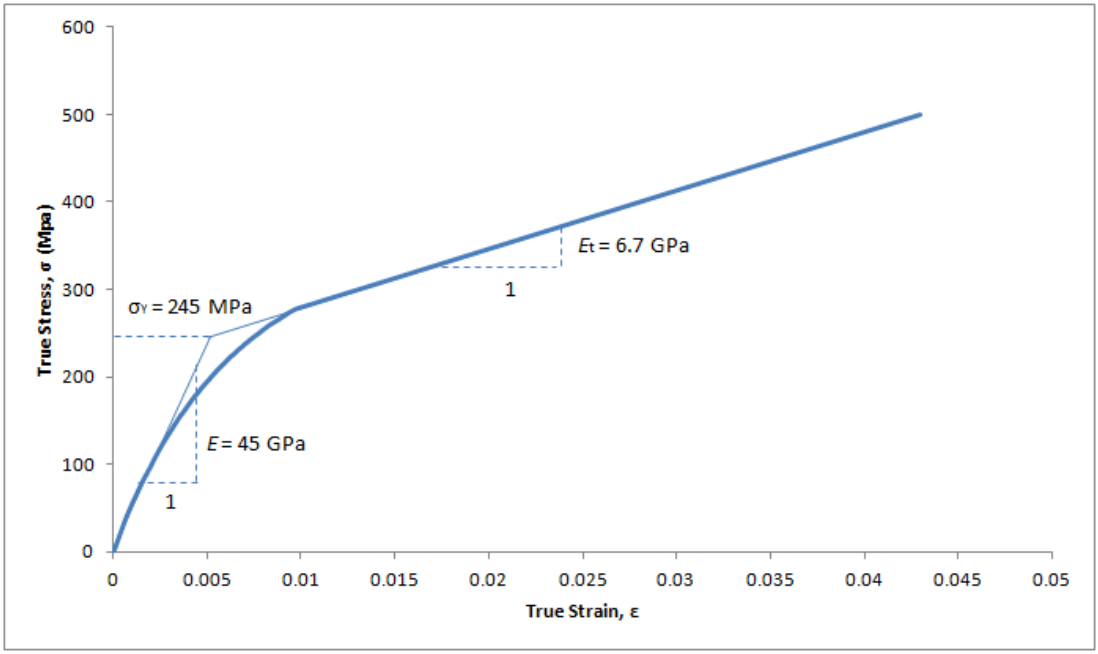

Figure 2.49: Stress-strain curve of the as-received SLM Ti-6Al-4V micro-strut, similar to the typical curve as in Figure 2.46

A similar procedure was applied to the stress-strain curve of the heat-treated SLM Ti-6Al-4V micro-strut, as shown in Figure 2.50. A projected tangent line (dashed line) was drawn passing both the yield strength value and the maximum point of the initial stress-strain curve. A similar curve to that of typical stress-strain curve (Figure 2.46) is obtained, and shown in Figure 2.51. The initial modulus value E for the heat-treated SLM Ti-6Al-4V strut is 65 GPa and the corresponding yield stress value σ_Y is 340 MPa. The tangential modulus after yielding E_t is determined as 20.1 GPa. After the substitution of all required values into Equation 2.29, the relation between the equivalent yield stress and the equivalent plastic strain of the heat-treated SLM Ti-6Al-4V micro-strut is given by Equation 2.31.

$$\bar{\sigma} = [0.34 + 29.098\bar{\varepsilon}^{p}]\text{GPa} \qquad [2.31]$$

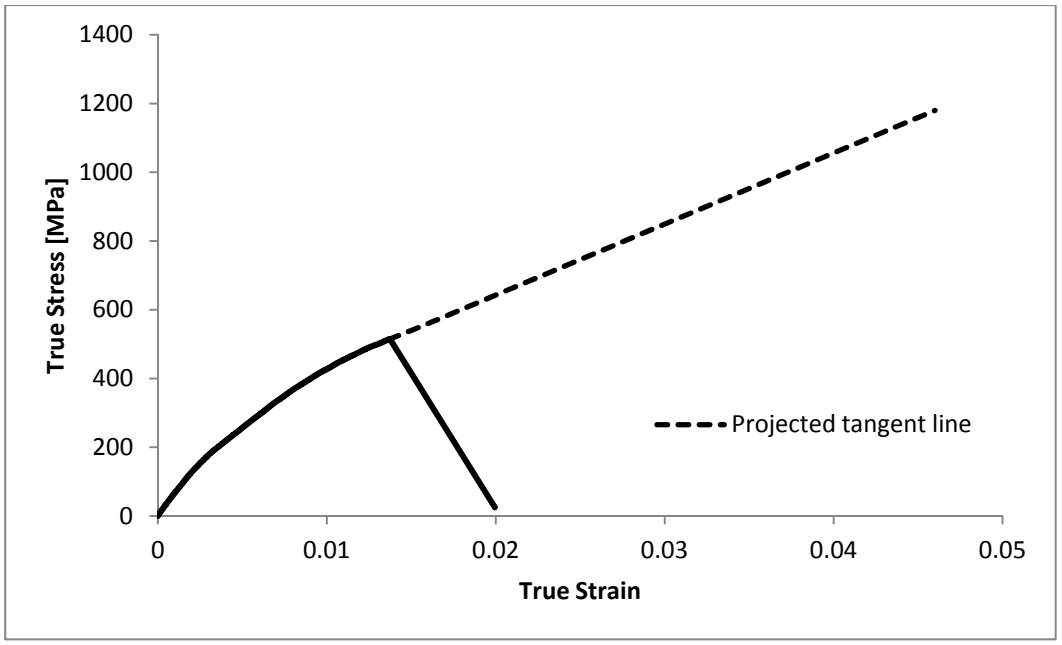

Figure 2.50: Stress-strain curve of the heat-treated SLM Ti-6Al-4V micro-strut, with a projected tangent line [S(1-9)-35-200-1000-HT(B)]

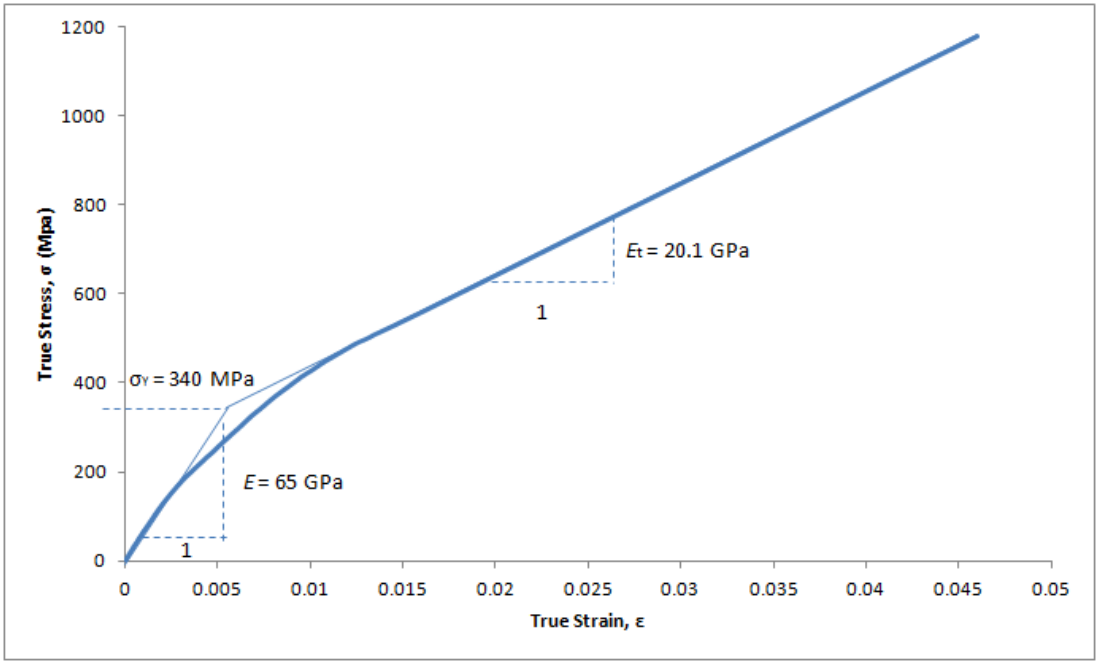

Figure 2.51: Stress-strain curve of the heat-treated SLM Ti-6Al-4V micro-strut, similar to the typical curve as in Figure 2.46

2.4.8 A Brief Note on Necking and Instability

As shown in the previous section, the plasticity relations of the as-received and the heat-treated micro-lattice struts were determined from the linear strain hardening curves. In this section, a short discussion on necking and instability is carried out, in order to evaluate the condition of the micro-struts when subjected to tensile loading.

In a typical metal bar subjected to a tensile load, it is known that after the load reaches a maximum value, necking occurs and the load gradually diminishes until fracture. The state corresponding to the maximum load is called plastic instability. The discussion of plastic instability condition was referred to the explanation in Vu and Blachut (2009), and determined by the equations in the following paragraphs.

The true stress σ at current load P is given by

$$P = \sigma A \qquad [2.32]$$

where A is the current cross-sectional area.

At the maximum load, $dP = 0$ and from Equation [2.32]

$$\sigma dA + Ad\sigma = 0 \qquad [2.33]$$

Assuming the material is incompressible, one has

$$A_0 L_0 = AL \qquad [2.34]$$

And consequently,

$$LdA + AdL = 0 \qquad [2.35]$$

where L is the current gauge length. The subscript is for original dimensions.

From Equations [2.33] and [2.35], the instability state is given by

$$\frac{d\sigma}{\sigma} = \frac{dL}{L} = d\varepsilon \quad \text{or} \quad \frac{d\sigma}{d\varepsilon} = \sigma \qquad [2.36]$$

where the true strain or logarithmic strain $\varepsilon = \int dL/L$.

In the true stress-strain curve, the instability state corresponds to a point at which the subtangent z measured along the strain axis is unity ($z = 1$), as shown in Figure 2.52. After the point of instability, necking takes place as indicated in the figure. The curve in Figure 2.52 is compared to the curves of the micro-struts in this study, shown in Figure 2.48 and 2.50. It can be observed that the curves of the micro-struts are not having the necking region after the instability point. Figure 2.48 and 2.50 show that the SLM Ti-6Al-4V micro-struts failed at a very low strain of approximately 0.01. This is shown by a sudden drop in strength after the instability point. Therefore, for the titanium alloy Ti-6Al-4V micro-strut in this study, necking is considered to be negligible and the discussion is not to be carried out under this topic. However, it should be noted that necking occurs in stainless steel SS316L material.

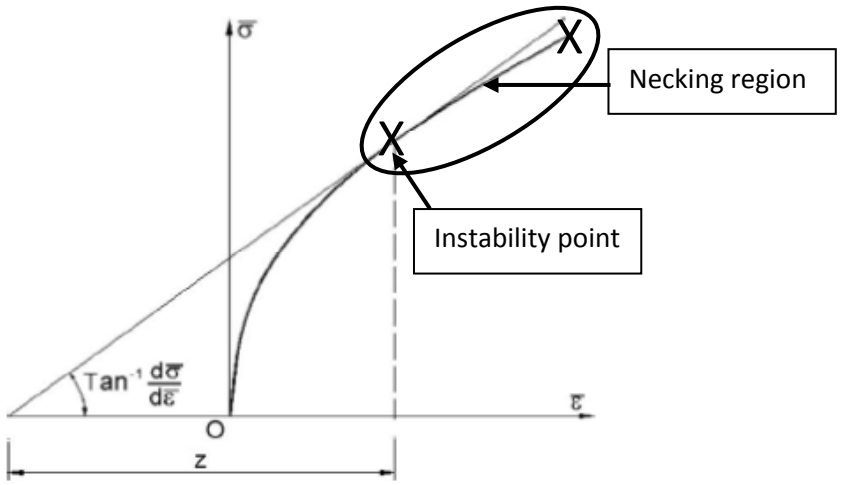

Figure 2.52: Critical subtangent *z* to the generalized instability strain hardening curve [adapted from Vu and Blachut (2009); cross-reference Swift (1952)]

2.5 IMPROVEMENTS IN SURFACE QUALITY, DIAMETER ACCURACY, CIRCULARITY, AND MECHANICAL PROPERTIES OF SLM Ti-6Al-4V MICRO-STRUTS

As concluded from previous Table 2.13, the as-received SLM Ti-6Al-4V micro-strut used in this study had low strength and ductility as compared to that of standard values; with approximately 40% (45 ± 9.9 GPa) of E value, 28% (245 MPa) of YS value, 30% (280 MPa) of UTS value, and 1% of elongation, as compared to the standard annealed Ti-6Al-4V [Boyer et al. (1994)]. Surface quality, diameter accuracy and circularity were identified as factors that contributed to these less than desirable properties of the micro-struts manufactured with 200 W laser power and 1000 μs laser exposure times, at 35° build angle.

In this study, it was found that diameter accuracy of micro-struts build at 35° angle were affected by diameter variations along the strut, which led to a range of minimum and maximum values in diameter as shown in Table 2.11. The variations of strut diameters manufactured at 35° build angle was related to the increase in diameter size, but led to a reduction in circularity of micro-strut cross-section as compared to the struts that were manufactured in vertical direction (90° build angle). Van Bael et al. (2011) also reported on the waviness of the struts that were manufactured under a 45° angle which was due to the staircase effect in additive manufactured parts, hence increased strut thickness.

Irregularities along outer surfaces contributed to the poor surface quality of SLM Ti-6Al-4V micro-struts used in this study. The irregularities were due to the bonded particles along the surfaces of micro-struts as shown in Figure 2.53(a). Similar phenomenon was observed in other studies of SLM Ti-6Al-4V porous structures [Van Bael et al. (2011)] and studies of SLM SS316L gyroid cellular structure [Yan et al. (2012)], as shown in Figure 2.53(b) and (c) respectively. As mentioned by Yan et al. (2012), the phenomenon was due to partially melted powder particles by the laser beam at the outside surfaces of micro-struts and significantly increased the

surface roughness of the material. Both Van Bael et al. (2011) and Yan et al. (2012) suggested that post processing cleaning such as sand blasting to be carefully carried out to remove a part of the bonded particles, resulting in smaller deviations of the surface irregularities. In another study, Pattanayak et al. (2011) used heat-treatment at 1300°C in an argon gas atmosphere to make partially melted pure titanium particles fused and bonded with the laser melted core parts thus smoothing the surface.

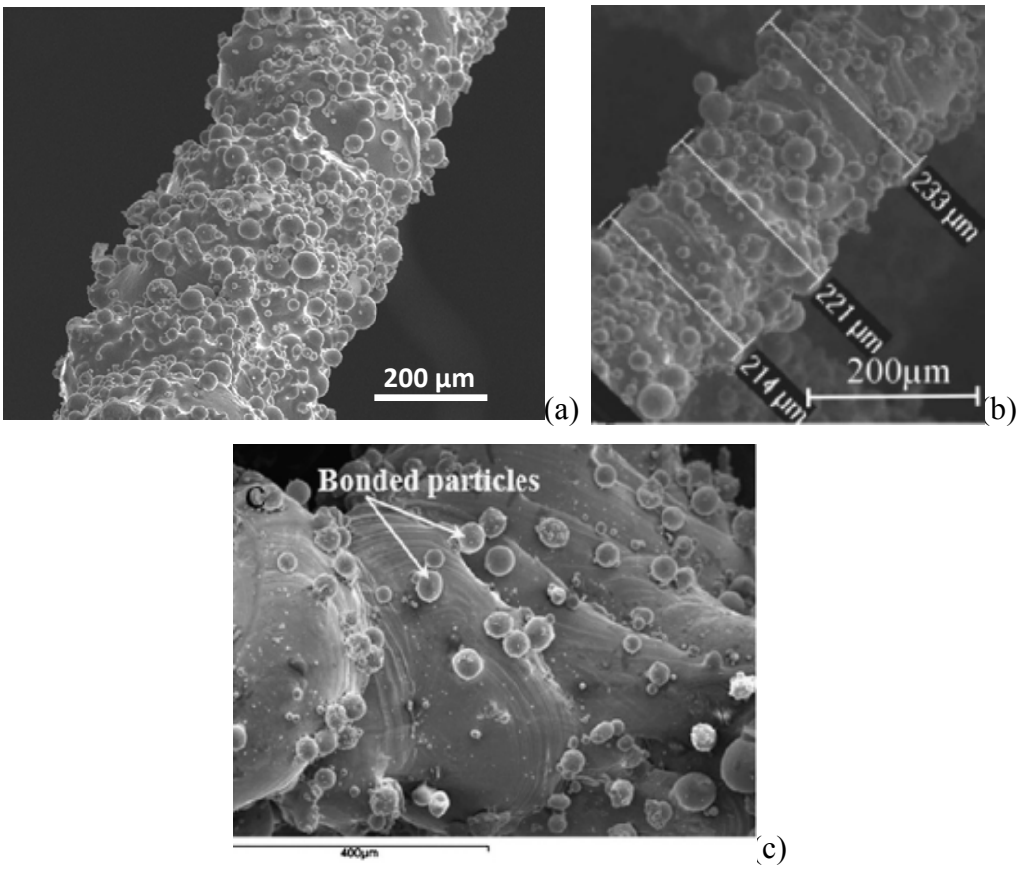

Figure 2.53: (a) Bonded particles along the surface of as-received micro-strut in this study [S1-35-200-1000-AR]; (b) surface of SLM Ti-6Al-4V porous structures [Van Bael et al. (2011)]; (c) surface of SLM SS316L gyroid cellular structure [Yan et al. (2012)]

A simple heat-treatment process was applied to the SLM Ti-6Al-4V struts in this study. The material was undergoing solution treatment at 1000°C for 1 hour

followed by water quenching and precipitation heat-treatment at 540°C for 4 hours in a vacuum condition. Besides improving the microstructure, it was shown that the heat-treatment also improved the surface quality, diameter accuracy and circularity of micro-struts. This was the result of the sintering mechanism in solid state diffusion during the heat-treatment [Murray (1992)]. A smoother heat-treated surface compared to the as-received surface can be seen in Figure 2.54(a) and (b), where discontinuities and bonded particles were re-melted and fused along the surface of heat-treated material. There were reductions in surface roughness and diameter variations, as well as improvement in circularity in the heat-treated micro-struts. Consequently, improvement in the mechanical properties of heat-treated SLM Ti-6Al-4V micro-strut was also found, as well as reduction in lower and upper bounds of uncertainty values in the stress-strain curve. Table 2.15 lists the improvements that have been achieved after the introduction of heat-treatment on the SLM Ti-6Al-4V micro-struts. Amongst the results, it is important to notice that the strain at failure for the heat-treated strut was increased by 50% as compared to the as-received, and the respective scatter in mechanical properties (bounds of stress-strain curve) was reduced by 33%.

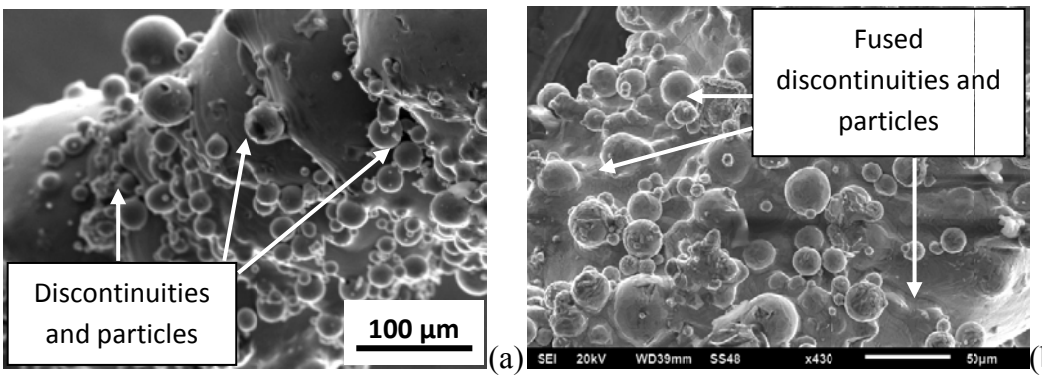

Figure 2.54: Micro-struts' outer surface; (a) discontinuities and particles of as-received strut [S2-35-200-1000-AR]; (b) fused discontinuities and particles of heat-treated strut [S1-35-200-1000-HT(B)]

Table 2.15: Improvements due to the introduction of heat-treatment on the SLM Ti-6Al-4V micro-struts

Properties	As-received strut	Heat-treated strut	Difference from the As-received
Diameter	(374.14 ± 26.15) µm	(322.56 ± 16.60) µm	-13.8%
Circularity	73.57%	77.91%	+5.9%
Surface roughness, R_a	16.8 µm	11.5 µm	-31.5%
Young's Modulus, E	45 GPa	65 GPa	+44.4%
Yield strength, YS	245 MPa	340 MPa	+38.8%
Ultimate tensile strength, UTS	280 MPa	520 MPa	+85.7%
Strain at failure, ε_f	1%	1.5%	+50.0%
Scatter in σ-ε curve	60%	40%	-33.3%

Based on the results, it was shown that the post-manufacture heat-treatment had improved the properties of the SLM Ti-6Al-4V micro-struts. It was the effect from the smoothing of outer surface irregularities and the emergence of a more balance α+β phase in the microstructure of the heat-treated struts. Improvement in surface roughness has led to the improvement of circularity, thus improvements in mechanical properties were also obtained. There was a reduction in uncertainty value by 33%, and it should be noted that further reduction in uncertainty would improve the confidence level of the results. Therefore, it was shown that the room for improvements of the SLM Ti-6Al-4V micro-struts is related to the improvements in geometrical aspects and quality of the material.

There are few suggestions to further improve the quality and geometry of the SLM Ti-6Al-4V micro-strut material as listed below.

- One more step of solution treatment-quenching-precipitation heat-treatment is suggested in order to produce a more equiaxed microstructure of micro-

struts, whilst a significant grain growth that may produce regions of the struts that are single grains should be avoided. The presence of a large grain size within such small struts would significantly affect their strength as overall slip would be limited by the slip planes within the single crystal.

- The application of heat-treatment processes within an environment that can produce good sintering effects to the particles bonded at the outer surfaces and the discontinuities along the struts due to the layered manufacturing process is also recommended for the SLM Ti-6Al-4V micro-strut, such as using the argon gas atmosphere.
- Another way to improve the micro-strut properties due to surface irregularities and variations is by using powder with smaller size of particles.
- Manufacturing strategy which can minimize the effect of layer by layer formation in the single laser melting point of the struts can be adapted. This can improve the circularity of the manufactured struts.
- Laser re-melting technique that was used by Yasa et al. (2011) can also be considered to be applied at every layer during micro-strut manufacturing in order to improve not only the outer surfaces, but also the porosity of the micro-struts, but this technique will definitely increase the total manufacturing time.

2.6 SUMMARY OF CHAPTER 2

In this chapter, two main research activities were reported; the material analysis and tensile test on micro-struts specimen. Both activities aimed to characterize the basic unit of the SLM Ti-6Al-4V micro-lattice structure and look for ways forward to improve the properties of the material manufactured in the University of Liverpool. Two types of materials were used; the as-received micro-struts and the heat-treated micro-struts by using a simple heat-treatment procedure.

In material analysis, the as-received and heat-treated micro-struts geometries were quantified using several methods. The average diameter of the as-received micro-strut was determined as (374.14 ± 26.15) μm, while the average diameter for the heat-treated micro-strut was (322.56 ± 16.60) μm. The percentages of non-circularity for the as-received and heat-treated micro-struts were found as 26% and 22% respectively. Surface roughness parameters were also determined, which were related to the stress concentration at the outer surfaces of micro-struts. Higher surface roughness of the as-received micro-struts has led to a higher stress concentration, thus lower the strength of the material, as compared to the heat-treated micro-struts. There was improvement in microstructure of the heat-treated micro-struts, where a more balanced α+β phase was achieved and the disappearance of dendritic structures was observed. These dendritic structures which were found at boundary regions were originated from trapped residues, which contributed to the weakness of material. The element analysis results showed that re-distribution of residue elements was observed in the heat-treated strut, which improved the properties of the material.

From the tensile test study, it was found that the compliance correction method can be used to determine the elastic modulus value of micro-struts. The variations in micro-struts geometries were taken into considerations in the derivation of mechanical properties of micro-struts. Stress-strain curves with lower and upper boundary ranges of uncertainties were determined for both the as-received and heat-

treated micro-struts. Improvements in mechanical properties were reported for the heat-treated micro-strut, as a consequence of the improvement in microstructure and geometries of the material. Further improvements of the material, especially to reduce uncertainties in micro-strut diameters could be done in future, as mentioned in section 2.5.

From this, characterization studies of micro-struts, relations of microstructures, geometries and properties of SLM Ti-6Al-4V micro-struts were shown. The determined geometries and mechanical properties of the materials are taken as reference values for FEA simulation study of SLM Ti-6Al-4V micro-lattice structure that will be discussed in Chapter 4. The fracture surfaces of the micro-struts that failed under tensile load will be compared to that of the micro-lattice blocks under compression load in Chapter 3, and failure of the materials will be compared with the FEA results in Chapter 4. In this chapter, the relationships between the equivalent stress and the equivalent plastic strain of both the as-received and heat-treated SLM Ti-6Al-4V micro-struts were derived, as given by Equation 2.30 and 2.31. These equations will be used in the prediction of failure of the materials.

It should be noticed that the determined value of Young's Modulus (E = 45 GPa) in this study is low compared to that of standard value (114 GPa) [Boyer et al. (1994)]. This could be one of the effects of the existence of residue elements in the strut material. The low E value trend can also be seen in other study using wrought Ti-6Al-4V material [Singh et al. (2012)]. Figure 2.55(a) shows the stress-strain curves from the standard value [Boyer et al. (1994)] and other study of Ti-6Al-4V [Singh et al. (2012)]. Meanwhile, Figure 2.55(b) shows the comparison of both curves with the curve which was determined for strut material in this study. With the consideration of upper range and lower range boundaries (as discussed in section 2.4.4), it can be seen from Figure 2.55(b) that the E value determined from the strut tensile test in this study can be considered as reasonable when compared to the standard value. The diameter variations along the struts gave the upper range and the lower range boundaries, where the maximum and minimum E values can be determined as 75 GPa and 35 GPa, respectively.

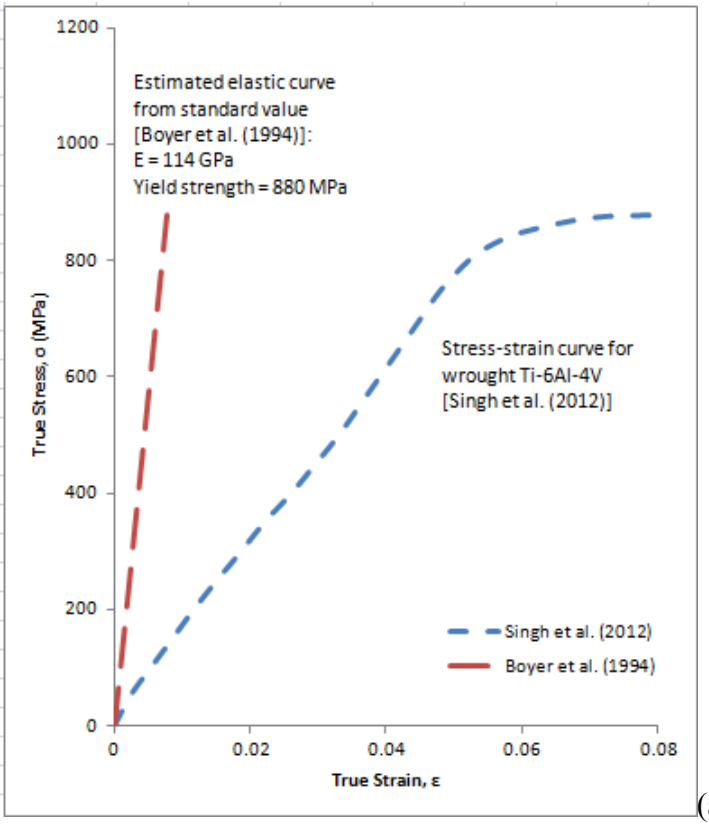

(a)

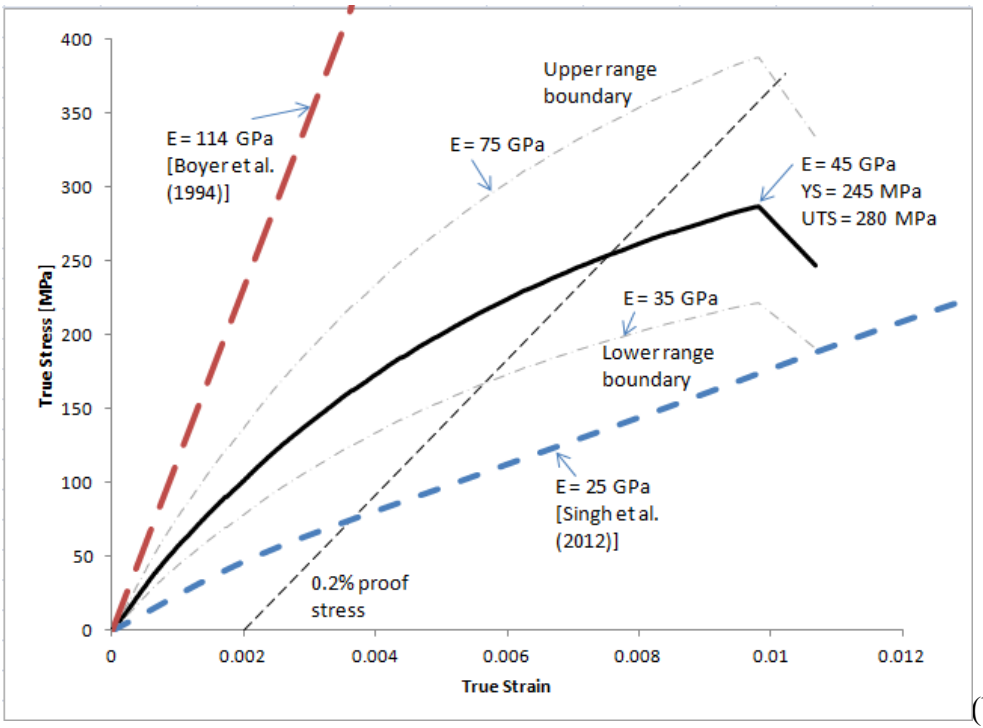

(b)

Figure 2.55: (a) True stress-true strain curves for standard value and other study; (b) Comparison of true stress-true strain curve determined in this study with the standard value and other study

It was shown in this study that the properties of the SLM products vary with the manufacturing parameters and conditions of material. Table 2.16 summarizes the full definition of SLM Ti-6Al-4V micro-strut specimens used in this study. This definition is based on the standard definition that was suggested by Tsopanos et al. (2010) but with additional information for type of strut specimen in this study. This full definition is extremely important for any SLM product since the mechanical properties are highly dependent on the manufacturing parameters and geometry, as well as other post-manufacturing treatment of the material.

Table 2.16: Full definition of SLM Ti-6Al-4V micro-strut

General definition for strut	Specific definition
Type of specimen	Strut
Parent material	Ti-6Al-4V (Ti64)
Laser power (Watt)	200
Laser exposure time (μs)	1000
Averaged strut diameter (μm)	375
Strut length (mm)	43 / 23
Build angle	35° / 90°
Heat treatment	As-received / Heat-treated (Process A, etc.)

The full definition can be written as:

Type of specimen/ Parent material/ Laser power (Watt)/ Laser exposure time (μs)/ Averaged strut diameter (μm)/ Strut length (mm)/ Build angle/ Heat-treatment

Therefore, for the 35° build angle as-received strut in this study, the definition would be:

Strut/ Ti64/ 200/ 1000/ 375/ 43/ 35°/As-received

REFERENCES OF CHAPTER 2

Arola, D. and Ramulu, M. (1999) 'An examination of the effects from surface texture on the strength of fiber reinforced plastics'. *Journal of Composite Materials*, 33: 102-123.

Arola, D. and Williams, C.L. (2002) 'Estimating the fatigue stress concentration factor of machined surfaces'. *International Journal of Fatigue*, 24: 923-930.

ASM Handbook (1992). 'Al (Aluminium) Ternary Alloy Phase Diagrams'. *Alloy Phase Diagrams*, 3: 3.8-3.22. ASM International.

ASTM D 3379-75 (Reapproved 1989) (1999) 'Standard test method for tensile strength and Young's modulus for high-modulus single-filament materials'. *Annual Book of ASTM Standards*, pp. 732-735.

ASTM Standard (2012) '*Standard specification for Addititive Manufacturing Titanium-6 Aluminum-4 Vanadium with Powder Bed Fusion*', ASTM International, DOI: 10.1520/F2924-12.

Barbour, R. (1978) *Glassblowing for laboratory technicians*, 2nd Edition. Oxford: Pergamon Press.

Becker, W.T. and McGarry, D. (2002) 'Mechanisms and Appearances of Ductile and Brittle Fracture in Metals', *Failure Analysis and Prevention*, Vol. 11, ASM Handbook, ASM International, p 587-626.

Brown, M.E. and Gallagher, P.K. (ed.) (2008) 'Recent advances, techniques and applications', *Handbook of Thermal Analysis and Calorimetry*, Volume 5, Elsevier Science, Amsterdam.

Boyer, R., Welsch, G., Collings E.W. (ed.) (1994). *Material Properties Handbook: Titanium Alloys*, ASM International: Material Park, OH. http://www.matweb.com (assessed on 5/2/2010)

Cansizoglu, O., Harrysson, O., Cormier, D., West, H., Mahale, T. (2008) 'Properties of Ti-6Al-4V non-stochastic lattice structures fabricated via electron beam melting'. *Materials Science and Engineering A*, 492: 468-474.

Diao, X.M., Furuno, T., Fujita, M. (1999) 'Digital image analysis of cross-sectional tracheid shapes in Japanese softwoods using the circularity index and aspect ratio'. *Journal of Wood Science*, 45: 98-105.

Facchini, L., Magalini, E., Robotti, P., Molinari, A. (2009) 'Microstructure and mechanical properties of Ti-6Al-4V produced by electron beam melting of pre-alloyed powders'. *Rapid Prototyping Journal*, 15(3): 171-178.

Facchini, L., Magalini, E., Robotti, P., Molinari, A., Hoges, S., Wissenbach, K. (2010) 'Ductility of a Ti-6Al-4V alloy produced by selective laser melting of prealloyed powders'. *Rapid Prototyping Journal*, 16/6: 450-459.

Gilbert, R. And Shannon, C.R. (1998) *Heat treating of titanium and titanium alloys*, ASM Handbook Online, Volume 4, ASM International.

Hasan, R., Mines, R., Shen, E., Tsopanos, S., Cantwell, W., Brooks, W., Sutcliffe, C. (2010) 'Comparison of the drop weight impact performance of sandwich panels with aluminium honeycomb and titanium alloy micro lattice cores'. *Applied Mechanics and Materials*, Vol. 24-25: 413-418.

Hollander, D.A., Walter, M.V., Wirtz, T., Sellei, R., Schmidt-Rohlfing, B., Paar, O., Erli, H.J. (2006) 'Structural, mechanical and in vitro characterization of individually structured Ti-6Al-4V produced by direct laser forming'. *Biomaterials*, 27: 955-963.

Hooputra, H., Gese, H., Dell, H., Werner, H. (2004) 'A comprehensive failure model for crashworthiness simulation of aluminium extrusions'. *International Journal of Crashworthiness*, 9(5): 449-463.

Instron (2013) '3340 Series Single Column Testing Systems for Low-force Testing'. Instron website http://www.instron.com/wa/product/3300-Single-Column-Testing-Systems.aspx (assessed on 21/5/2013).

Kalidindi, S.R., Abusafieh, A., El-Danaf, E. (1997) 'Accurate characterization of machine compliance for simple compression testing'. *Experimental Mechanics*, Vol. 37: 210-215.

Kerlins, V. and Phillips, A. (1987) 'Modes of Fracture', *Fractography*, Vol. 12, ASM Handbook, ASM International, 1987, p. 12-71.

Kude, V.P., and Khairnar, R.S. (2004) 'Fabrication of silicon based glass fibres for optimal communication'. *Bulletin of Material Science*, 27(1): 73-77.

Lampman, S. (1990). 'Wrought Titanium and Titanium Alloys'. *Properties and Selection: Nonferrous Alloys and Special-Purpose Materials*, 2: 592-633. ASM International.

http://products.asminternational.org.ezproxy.liv.ac.uk/hbk/index.jsp (assessed on 22/5/2013).

Lemaitre, L. and Chaboche, J.L. (1990) *Mechanics of Solid Materials*. Cambridge University Press, UK.

Li, C.T. and Langley, N.R. (1985) 'Improvement in fiber testing of high-modulus single-filament materials'. *Journal of American Ceramic Society*, Vol. 68: C-202-C-204.

Mines, R., Girard, Y., Fascio, V. (2009) 'On the development of conventional and micro lattice cellular metals as core materials in aerospace sandwich construction'. *Proceedings of the International European SAMPE*, Europe, pp. 248-256.

Murr, L.E., Quinones, S.A., Gaytan, S.M., Lopez, M.I., Rodela, A., Martinez, E.Y., Hernandez, D.H., Martinez, E., Medina, F., Wicker, R.B. (2009) 'Microstructure and mechanical behaviour of Ti-6Al-4V produced by rapid-layer manufacturing, for biomedical applications'. *Journal of the Mechanical Behaviour of Biomedical Materials*, 2: 20-32.

Murray, J.L. (1992) 'Fe-Ti (Iron-Titanium)', in *Fe (Iron) binary alloy phase diagrams*, ASM Handbooks, Volume 3, Alloy Phase Diagrams. ASM International.

Nikon (2013). 'Microscope Alignment for Kohler Illumination'. *MicroscopyU – The Source for Microscopy Education*. Nikon, USA. Website: http://www.microscopyu.com/tutorials/java/kohler/ (assessed on 28/5/2013).

Pattanayak, D.K., Fukuda, A., Matsushita, T., Takemoto, M., Fujibayashi, S., Sasaki, K., Nishida, N., Nakamura, T., Kokubo, T. (2011) 'Bioactive Ti metal analogous to human cancellous bone: Fabrication by selective laser melting and chemical treatments'. *Acta Biomaterialia*, 7: 1398-1406.

Petkar, B.M., Oka, P.G., Sundaram, V. (1980) 'The cross-sectional shapes of a cotton fiber along its length'. *Textile Research Journal*, 50: 541-543.

Polmear, I.J. (2006) *Light alloys: From traditional alloys to nanocrystals*, 4th Edition. Elsevier/Butterworth-Heinemann, Amsterdam, Holland.

Rehme, O. (2010) *Cellular Design for Laser Freeform Fabrication*. Cuvillier Verlag, Gottingen.

Sergueeva, A.V., Zhou, J., Meacham, B.E., Branagan, D.J. (2009) 'Gage length and sample size effect on measured properties during tensile testing'. *Materials Science & Engineering A*, Vol. 526: 79-83.

Shen, Y. (2009) 'High performance sandwich structures based on novel metal cores'. PhD Thesis, University of Liverpool, United Kingdom.

Singh, G., Sen, I., Gopinath, K., Ramamurty, U. (2012) 'Influence of minor addition of boron on tensile and fatigue properties of wrought Ti-6Al-4V alloy'. *Materials Science and Engineering: A*, 540: 142-151.

Skau, E.L. (1951) 'Simple expressions for the circularity and fullness of fibers'. *Textile Research Journal*, 21: 14-17.

Sutcliffe, C. (n.d) *Standard Operating Procedure for SLM250*, University of Liverpool, Doc. No. SOP01B.

Swift, H.W. (1952) 'Plastic instability under plane stress'. *Journal of the Mechanics and Physics of Solids*, 1: 1-18.

Tan, H. (2009) 'Hardening and flow rule', *Flow Theory of Plasticity*, Lecture notes, University of Aberdeen, UK. (available at http://homepages.abdn.ac.uk/h.tan/pages/teaching/plasticity/Flow.pdf)

Tsopanos, S., Mines, R., McKown, S., Shen, Y., Cantwell, W., Brooks, W., Sutcliffe, C.J. (2010) 'The influence of processing parameters on the mechanical properties of selectively laser melted micro-lattice structures'. *Journal of Manufacturing Science and Engineering ASME*, Vol. 132: 041011-1 – 041011-12.

Turek, D.E. (1993) 'On the tensile testing of high modulus polymers and the compliance correction'. *Polymer Engineering and Science*, Vol. 33: 328-333.

Ushijima, K., Cantwell, W.J., Mines, R.A.W., Tsopanos, S., Smith, M. (2011) 'An investigation into the compressive properties of stainless steel micro-lattice structures'. *Journal of Sandwich Structures and Materials*, 13: 303-329.

Van Bael, S., Kerckhofs, S., Moesen, G., Pyka, M., Schrooten, G., Kruth, J.P. (2011) 'Micro-CT-based improvement of geometrical and mechanical controllability of selective laser melted Ti6Al4V porous structures'. *Material Science and Engineering A*, 528: 7423-7431.

Vandenbroucke, B. and Kruth, J.P. (2007) 'Selective laser melting of biocompatible metals for rapid manufacturing of medical parts'. *Rapid Prototyping Journal*, 13/4: 196-203.

Vilaro, T., Colin, C., Bartout, J.D. (2011). 'As-Fabricated and Heat-Treated Microstructures of the Ti-6Al-4V Alloy Processed by Selective Laser Melting'. *Metallurgical and Materials Transactions A*, 42A: 3190-3199.

Vu, V.T. and Blachut, J. (2009) 'Plastic instability pressure of toroidal shells'. *Journal of Pressure Vessel Technology*, 131: 051203-1 - 051203-10.

Wu, X. and Hu, D. (2005) 'Microstructural refinement in cast TiAl alloys by solid state transformations'. *Scripta Materialia*, Vol. 52: 731-734.

Wu, X. (2006) 'Review of alloy and process development of TiAl alloys'. *Intermetallics*, 14: 1114-1122.

Yan, C., Hao, L., Hussein, A., Raymont, D. (2012) 'Evaluations of cellular lattice structures manufactured using selective laser melting'. *International Journal of Machine Tools and Manufacture*, Vol. 62: 32-38.

Yasa, E., Deckers, J., Kruth, J.P. (2011) 'The investigation of the influence of laser re-melting on density, surface quality and microstructure of selective laser melting parts'. *Rapid Prototyping Journal*, Vol. 17(5): 312 – 327.

CHAPTER 3: INVESTIGATION ON PROPERTIES AND BEHAVIOURS OF SLM Ti-6Al-4V BCC MICRO-LATTICE BLOCKS

3.1 INTRODUCTION

The use of the titanium alloy Ti-6Al-4V in the manufacture of micro-lattice structure using the selective laser melting process (SLM) for use as a light-weight load bearing material in sandwich structure cores suggests that this material has a promising future as a candidate aerospace material. Based on extensive studies on the SLM stainless steel SS316L micro-lattice structure in terms of architecture [McKown et al. (2007)], strength and impact performances [McKown et al. (2008); Mines et al. (2008); Shen (2009)], as well as manufacturing and theoretical optimizations [Tsopanos et al. (2010; Ushijima et al. (2011)], this current study of the SLM Ti-6Al-4V micro-lattice block is one of the early steps that supports the efforts of introducing this novel material into the real aerospace applications. An important performance issue in aerospace sandwich construction is the foreign object impact (FOI) performance such as a result of dropped tools, hail and bird strike [Mines et al. (1998)].

After the evaluation of single strut as discussed in Chapter 2, the next stage in the collapse of the foreign object impact panels' performance is the investigation of the behaviour of micro-lattice blocks. In this chapter, evaluation of the properties and characteristics that influence the performance of micro-lattice blocks with body centred cubic (BCC) arrangement were carried out. This BCC arrangement has the advantage of simplicity and reliability in manufacture [Tsopanos et al. (2010)] as well as better response to multi-axial deformation [Shen et al. (2010)]. As previously reported, the specific strength of SLM Ti-6Al-4V BCC micro-lattice core was competitive with that of the aluminium honeycomb core [Mines et al. (2009); Hasan et al. (2010)]. This was specifically true for the micro-lattice structure with high

manufacturing parameters, which were 200W laser power and 1000μs laser exposure time [Shen (2009)].

The compression loading was applied to the micro-lattice block structure due to the simple test for comparison, especially between the blocks with different processing parameters. The block structure displays similar failure modes with that from the FOI panel structure [Hasan et al. (2010)]. The current study focuses on the formation of nodal areas within the blocks since they are the important elements in a BCC structure. Besides, focus is also given to the progressive collapse mechanisms of the specific nodal areas as well as the general block structure.

It was observed that the SLM Ti-6Al-4V BCC micro-lattice blocks failed along 45° angle diagonal plane under compression loading [Shen (2009)]. The localized failure in this material has motivated this study to focus specifically at the node area with the surrounding struts. Based on knowledge from Chapter 2, the investigations were started from the manufacturing aspects of the SLM Ti-6Al-4V BCC micro-lattice blocks especially near the node areas, which relate the formation of the blocks and geometry to the structural strength and mechanical properties of the whole micro-lattice structure. The deliverable of this study is a full definition of geometry and quality of BCC micro-lattice blocks. Findings on deformation behaviours and modes of collapse or failure under loading are important and will be compared with FEA analysis on SLM Ti-6Al-4V BCC micro-lattice structural performance in Chapter 4.

3.2 MANUFACTURING DETAILS OF SLM Ti-6Al-4V BCC MICRO-LATTICE BLOCKS

As pointed out by Yadroitsev (2009), more than 130 parameters influence the selective laser melting (SLM) process. These can be classified into two major types of factors, namely, the processing parameters which include manufacturing aspects and processes, and secondly, the powder material characteristics. In the current study, the manufacturing aspects of the SLM Ti-6Al-4V BCC micro-lattice blocks are re-visited, in order to understand the history of past block builds that were used in previous studies [Shen (2009); Hasan et al. (2011)]. Focus is given to the formation of nodes and the surrounding struts.

3.2.1 Manufacturing process – Software applications

SLM is one of few solid freeform processes available commercially. Solid freeform process is defined as a process which involves a set of manufacturing techniques that are able to produce complex solid objects directly from a computer model, without aid from part-specific tooling [Beaman et al. (1997)]. The SLM process is assigned from computer software applications and specific powder material is selectively laser melted to form complicated parts. In this section, review of the software involved in the manufacturing process of the SLM was referred mostly to Tsopanos (2008). Figure 3.1 shows the flowchart of components involved in SLM process, which was adapted from Aris (2009).

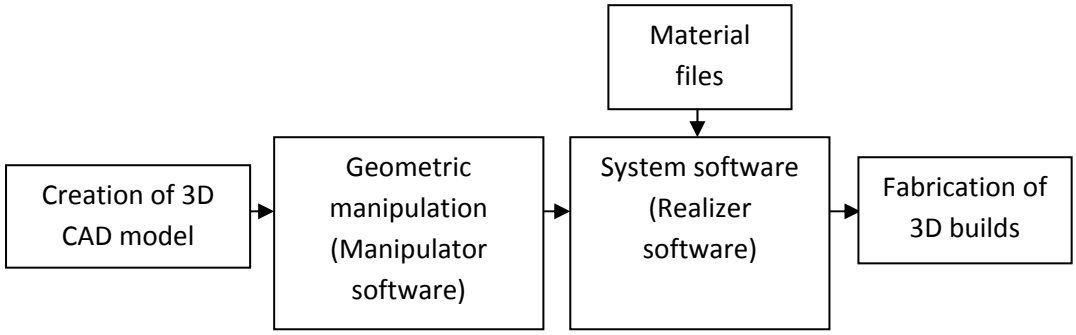

Figure 3.1: SLM process components for micro-lattice structure fabrication, adapted from Aris (2009)

In typical SLM process, the process normally begins with computer modelling of the 3D object in CAD software, installed in any workstation, away from manufacturing machine. For the current study of SLM Ti-6Al-4V BCC micro-lattice block, the graphic drawing of 3D micro-lattice was started from a lattice unit cell which in turn is comprised of the 3D strut arrangement in BCC topology as shown in Figure 3.2(a), before populating the cell for lattice block model drawing. This was done using the Manipulator software, which converted the 3D computer model into StereoLitography (STL) format, i.e. a triangulated representation of the 3D geometry held in CAD model [Tsopanos (2008)]. The complete lattice block drawing was then saved as a .part file.

The 3D lattice block drawing was then opened as .STL file using support software at the manufacturing machine workstation. During this step, the block geometry was duplicated and arranged in Cartesian coordinates. Structural supports in terms of short thin struts at bottom of blocks were generated and incorporated within the drawing of the blocks. These structural supports would be important in the removal process of manufactured blocks from the base substrate at the end of the production. The completed block drawing was then saved in the build files directory. Another important step in assigning build parameters was the slicing process. Tsopanos (2008) showed that the slicing process was automated separately from the layer thickness selection during part definition procedure, and this would significantly

affect both surface finish quality and productions build time. The STL format discussed earlier facilitated this slicing process and the build parameters information of each slice was then stored in a file known as material file, located in the material files directory. The material file was stored in a .dat file and can be read as a plain text file. An example of material file data for and definition of the build parameters is shown in Appendix 3A at the end of this thesis.

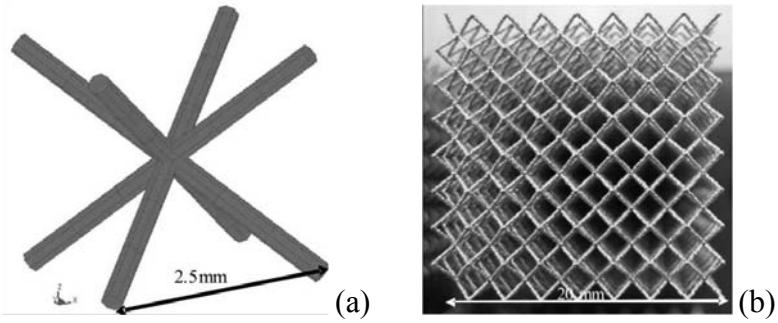

Figure 3.2: (a) Geometry of the BCC unit cell; (b) example of a micro-lattice cubic block [Tsopanos et al. (2010)]

After the slicing process, a complete build file was generated and could be opened in the Realizer software as the .f&s file. The .f&s file contained STL geometry, slices information, build parameters such as laser powers, and also geometrical data of a build. When the .f&s file was opened in the Realizer software, a graphic of the micro-lattice block was shown, and in addition, slice by slice or layer by layer details of the block manufacturing could be visualized. In each visualised layer, every laser point position was shown and this represented the real laser point for the micro-lattice build during the manufacturing process. In the other words, the Realizer software compiled all geometrical and fabrication related information before passing this on to the next step in the SLM process [Aris (2009)]. Figure 3.3 shows an example of computer screen shot of .f&s file for a BCC micro-lattice build. The configuration of struts and nodes that were manufactured from the laser melted powder process can be clearly seen from the laser points represented in the figure.

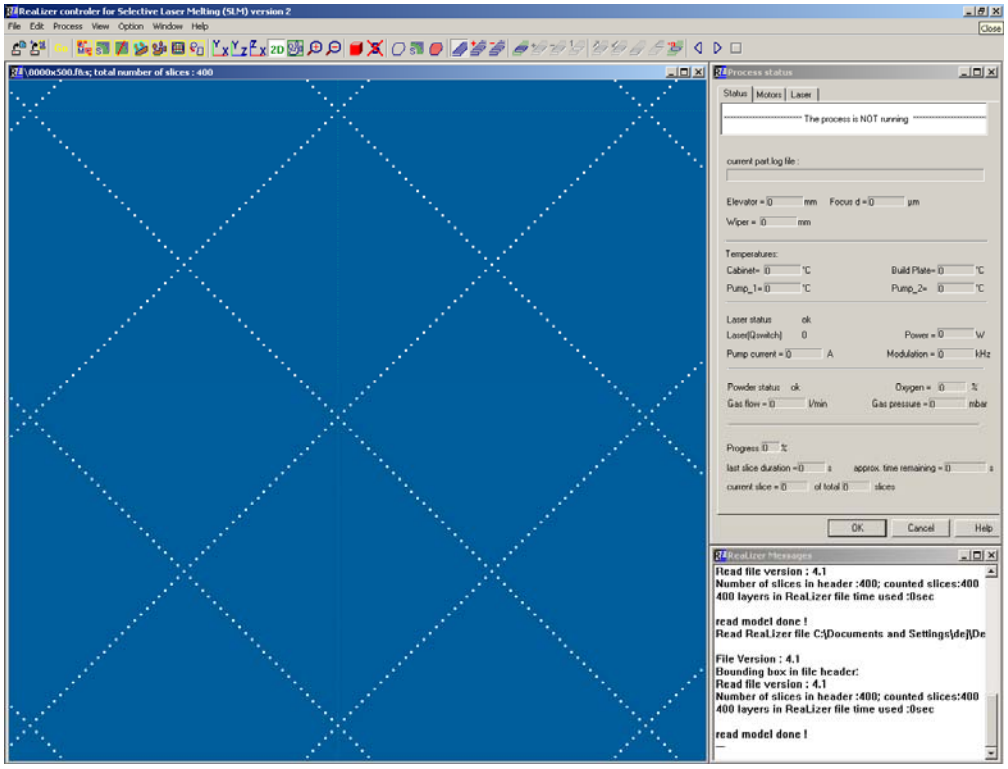

Figure 3.3: An example of screen shot of a build file of SLM Ti-6Al-4V BCC micro-lattice block which shows a part of side view of the block (each point represents single laser point during manufacturing)

3.2.2 Manufacturing process – Apparatus set-up

In the current study, the SLM Ti-6Al-4V BCC micro-lattice blocks were manufactured using the same apparatus as reported in Tsopanos et al. (2010). Figure 3.4(a) and (b) respectively show the schematic of the SLM process and the apparatus that was mentioned in the literature.

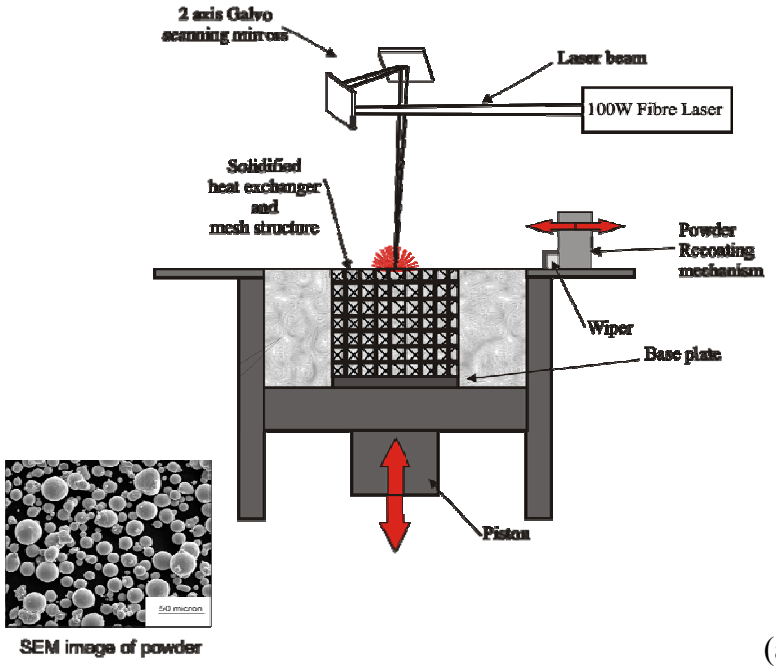

(a)

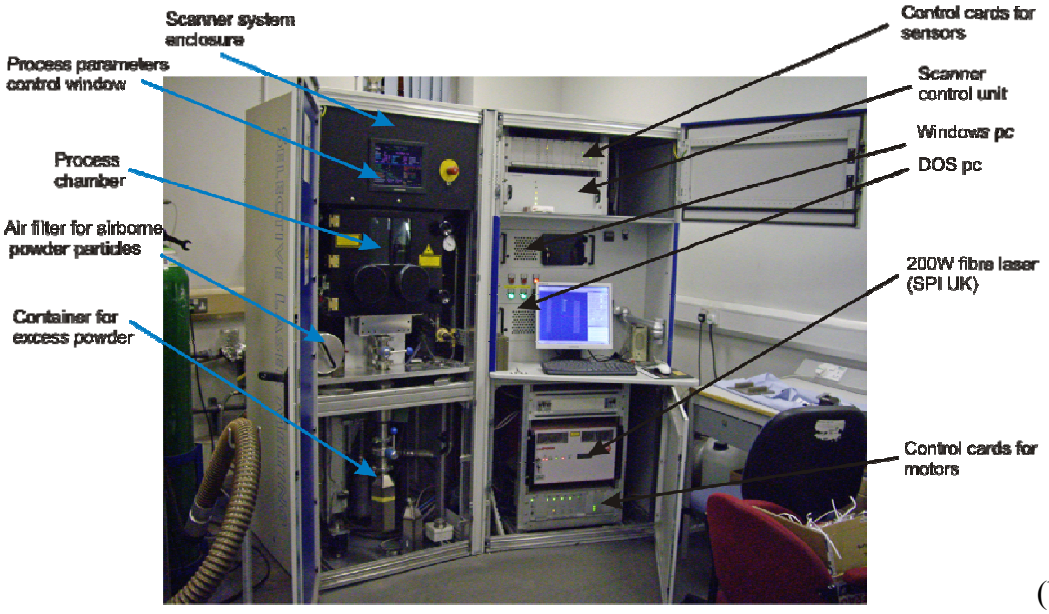

(b)

Figure 3.4: (a) Schematic of the SLM process; (b) the MCP Realizer II machine [Tsopanos et al. (2010)]

Figure 3.4(b) shows the SLM apparatus that has been mentioned in Chapter 2 section 2.2, which was the MCP Realizer II (commercial SLM workstation supplied by MCP (UK) Ltd.) with a build envelope of 250 mm X 250 mm X 240 mm. It was fitted with a 200 W continuous wave Ytterbium fiber laser operating at a wavelength of 1068 – 1095 nm and was the apparatus used by Tsopanos et al. (2010). The variable focussing optic is a Sill 300 mm focal length f-theta lens, which produce a focused beam spot size with diameter of 90 μm [Tsopanos et al. (2010)]. The layer by layer manufacturing process was carried out as schematically illustrated in Figure 3.4(a). The total manufacturing time required was dependent on product dimension and thickness. It was mentioned by Tsopanos et al. (2010) that a 20 mm cubed block took approximately 6 hours to manufacture since the build consisted of 400 layers of laser hatches of 50 μm thickness for each layer.

Four important aspects that were required to be ready before the SLM manufacturing process were the base substrate, build files, powder and gas supply. The base substrate was a support metal plate where the products were manufactured on and therefore was prepared from the same material as the product material. In this study, the base substrates were Ti-6Al-4V plates since the manufactured products were the Ti-6Al-4V micro-lattice blocks. The second aspect to be considered was the build files, which was the complete .f&s file that contained all geometrical and fabrication related information compiled in Realizer software, as explained in the previous section 3.2.1. The third considered aspect was the metal powder to be melted in SLM manufacturing process. In this micro-lattice block study, the powder was Titanium Powder Grade 5 ASTM (Ti-6Al-4V), produced by TLS Technik GmbH & Co., Germany, with the chemical composition of elements as shown in Table 2.1 of Chapter 2. It was ensured that the Ti-6Al-4V powder was full inside a designated container located at the top back of the SLM workstation. Meanwhile, the fourth aspect to be considered prior to SLM manufacturing was the argon gas supply near the SLM workstation. The argon gas was ensured to be in full tank with around 200-240 bar pressure, and tank with less than 100 bar pressure should be changed to a full one. It was mentioned by Tsopanos et al. (2010) that the argon gas was used in providing an argon atmospheric condition with no more than 0.2% oxygen under 10-15 mbars overpressure during SLM manufacturing. This condition was provided in

order to protect the SLM-processed products from oxidation during powder melting and solidification. Besides, the low oxygen condition was also meant for fire protection.

A general routine was followed before the manufacturing. First, the process chamber was inspected to be in clean condition. Excessive powder from previous build was vacuumed using a designated vacuum cleaner for a particular material. Powder containers such as overflow containers, main hopper and small hopper were also ensured to be in clean condition. Then, the metal base substrate was inserted on levelled platform and powder was filled in small hopper until a very thin layer covered the substrate. After that, the chamber was closed and argon gas was purged into the chamber by using a motorised pump. The purging process was left until it reached a steady condition. Meanwhile, the build file was loaded and the material file was assigned while waiting for the purging process to complete. Then, the main power supply for the laser was turned on, followed by switching on the laser button in the Realizer software. After this was done, all the lights at the laser panel turned to green. Prior to starting the manufacture, the oxygen level was ensured to be less than 0.2% under 10-15 mbars overpressure. A gas pump was used to recycle the argon atmosphere and a filter system removed powder particulate residues from the recycled gas [Tsopanos et al. (2010)]. Figure 3.5 highlights the four important aspects in the SLM process discussed together with the flow of general procedure that was followed in running the SLM process using the MCP Realizer II at the University of Liverpool.

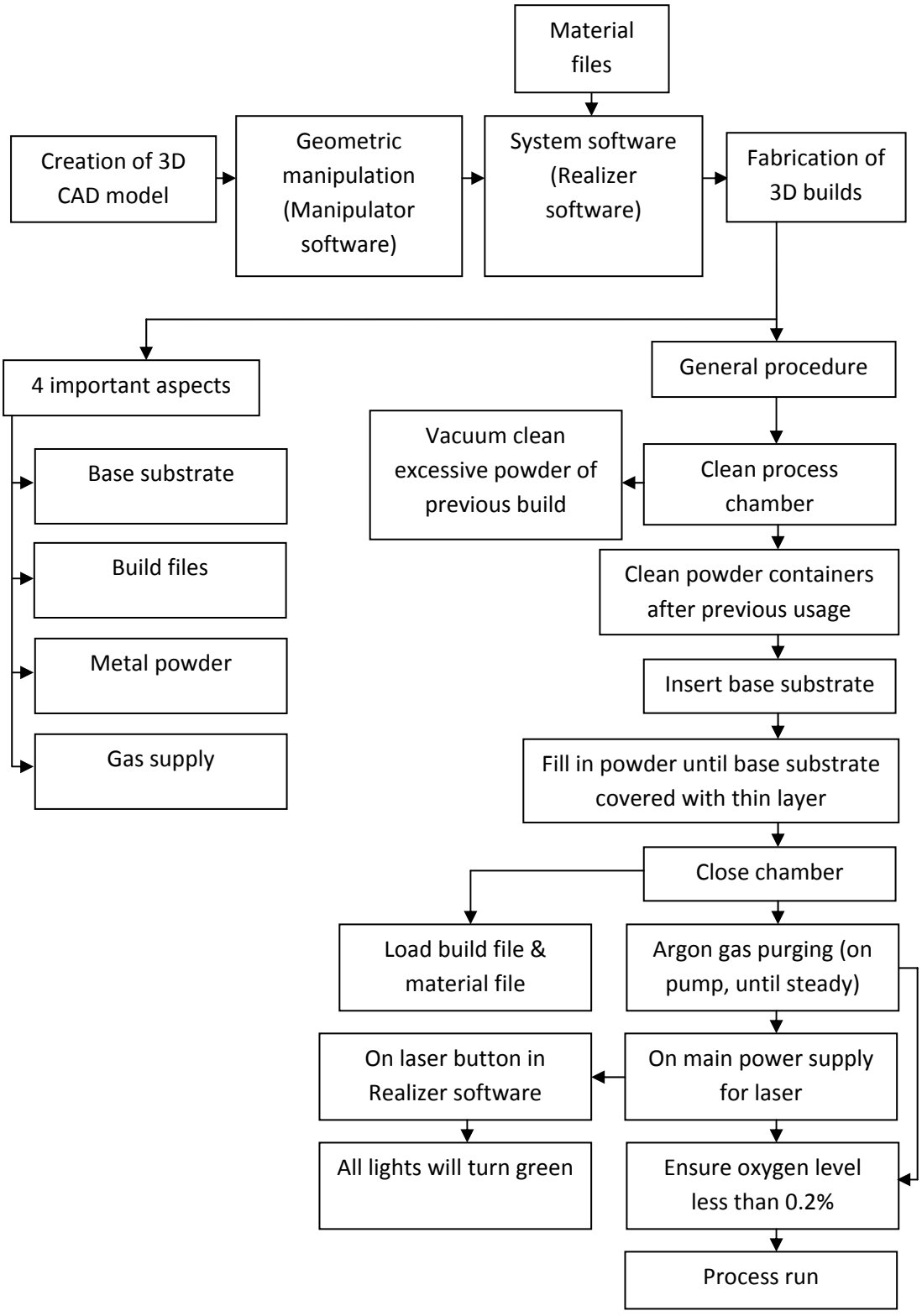

Figure 3.5: Four important aspects in SLM process and the flow of general procedure for SLM manufacturing that was applied in using the MCP Realizer II

It is important to notice that the MCP Realizer II was used for a range of powder materials. Therefore, the machine was carefully cleaned on change over, following a standard operating procedure [Sutcliffe (n.d)]. The comprehensive procedure covered all crucial manufacturing aspects that were briefly discussed in this current section. Besides the manufacturing aspects, another major factor which influences the processing parameters of the SLM process is the powder material characteristics. This factor was not directly discussed in this section nor in the standard operating procedure, Sutcliffe (n.d). Therefore, on top of the existing internal procedure, a recently published procedure regarding the specifications of SLM Ti-6Al-4V manufacturing can be referred to in the future, especially in the handling of used metal powder and maintenance of the chemical composition of the used powder [ASTM Standard (2012)].

3.3 QUALITY OF SLM Ti-6Al-4V BCC MICRO-LATTICE BLOCKS

As discussed in Chapter 2, the properties of the SLM Ti-6Al-4V micro-struts were related to the geometry and microstructure of the material, which was a result of the SLM manufacturing parameters. Analysis of the geometry of the SLM micro-strut has led to the quantification of the quality of this material, which as shown, can be improved with the improvement along the outer surface of the materials by the introduction of post-manufacturing heat-treatment process.

In this section, the investigation of quality of SLM Ti-6Al-4V BCC micro-lattice blocks was initiated from the formation of nodes at the 45° angle diagonal plane as shown in Figure 3.6. The motivation to investigate the formation of the nodes came from the observation of the failure of the SLM Ti-6Al-4V micro-lattice blocks along the diagonal plane, as shown in Figure 3.7(a) and (b) [Shen (2009)]. It can be seen in Figure 3.7(b) that failure occurred near the nodal areas. On top of the investigation on node formation, the quality of SLM Ti-6Al-4V BCC micro-lattice block was also analyzed based on the geometry of the builds including the diameter, surface roughness and circularity of the struts. The quality of micro-lattice block materials was then compared to that of single manufactured micro-strut materials from Chapter 2.

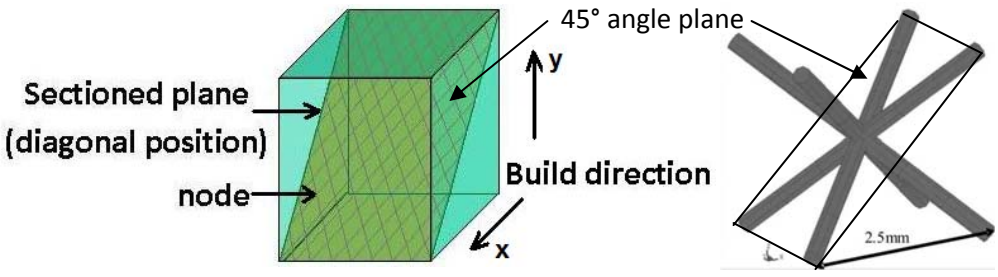

(a) (b)

Figure 3.6: Schematic of (a) 45° angle diagonal plane of BCC micro-lattice block; (b) 45° angle plane of BCC micro-lattice unit cell

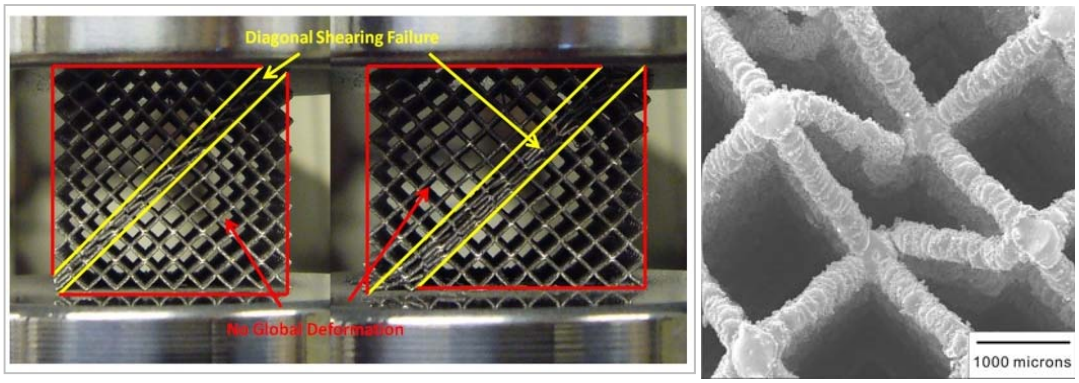

(a) (b)

Figure 3.7: (a) The 45° angle diagonal plane failure of the SLM Ti-6Al-4V BCC micro-lattice block (180 W X 500 µs) under compression [B(1-3)-180-500-AR]; (b) SEM image of SLM Ti-6Al-4V BCC micro-lattice block (200 W X 1000 µs) [B(1-3)-200-1000-AR] which shows failure near nodes area [Shen (2009)]

3.3.1 Analysis on Node Formation of the SLM Ti-6Al-4V BCC Micro-lattice Block

To analyze the node formation at the 45° angle diagonal plane, a metallurgical sample was prepared. Sectioning of sample using metallographic procedure was chosen in order to avoid the introduction of strain within the specimen. The as-received (180 W x 1000 µs) and the heat-treated (160 W x 1000 µs) SLM Ti-6Al-4V BCC micro-lattice blocks were resin mounted in order to firmly hold the struts and nodes position during the sectioning process. Sectioning process was done on the mounted blocks by grinding them with coarse emery paper (80 grits), starting at end points of the blocks in 45° angle, until the diagonal planes were reached. The specimens were then polished up to 50 nm surface finish and etched with hydrofluoric acid (HF) for 5 seconds in order to reveal the microstructure. Figure 3.8(a) to (d) show the images of the mounted block resin of the as-received material, before and after the metallographic sectioning.

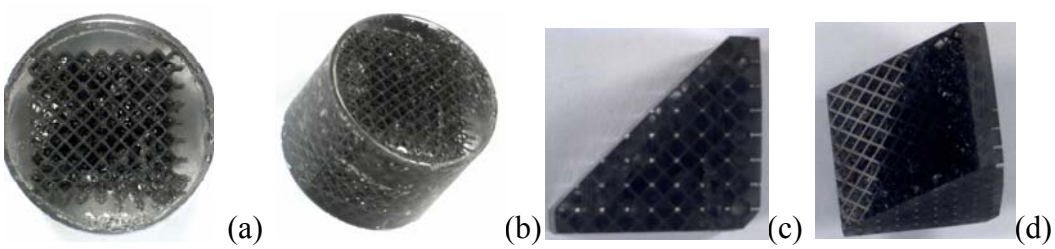

Figure 3.8: Resin mounted block of the as-received SLM Ti-6Al-4V BCC micro-lattice (180 W x 1000 µs) [B1-180-1000-AR-M] (a) from side view (b) at angle view; and (c) Diagonal plane from side view (d) at angle view

The sectioned diagonal plane of the as-received material (180 W x 1000 µs) revealed the details of node formation in a BCC micro-lattice block as shown in Figure 3.9. The x and y build directions were as shown in the figure, determined by the pattern of the globules of the struts. The black dots represented the estimated laser focus point at different times, and the thin lines represented the estimated globule boundaries. From the figure, the continuity of struts was considered good and there was little excess material. The quality of nodes depends on the laser scanning strategy [Tsopanos et al. (2010)]. It can be noted that only a single laser spot occurred at the centre of the node, in order to minimise material volume, and this agreed with that of laser points during manufacturing as shown in earlier Figure 3.3.

To summarise part of the manufacturing process, in Figure 3.9, the laser was switched on at point **A** for t=1000 µs. The laser was then moved to point **B** and switched on for 1000 µs. The laser was then moved on to other nodes and blocks. A number of blocks or a mixture of specimens (micro-struts and blocks) can be manufactured at any one time [Tsopanos et al. (2010)]. The laser was returned to point **C** in 30-60 seconds, and by this time the globule at **A** has solidified. The introduction of laser power at **C** melted the powder and partially melted the globule **A**. Note that the build direction was at an inclination of 45° angle. There was a complex thermo-mechanical process within the area, and this was discussed in detail by Yadroitsev (2009) and Rehme (2010). The thermo-mechanical process affects the quality of micro-struts and nodes, as well as their geometry and properties.

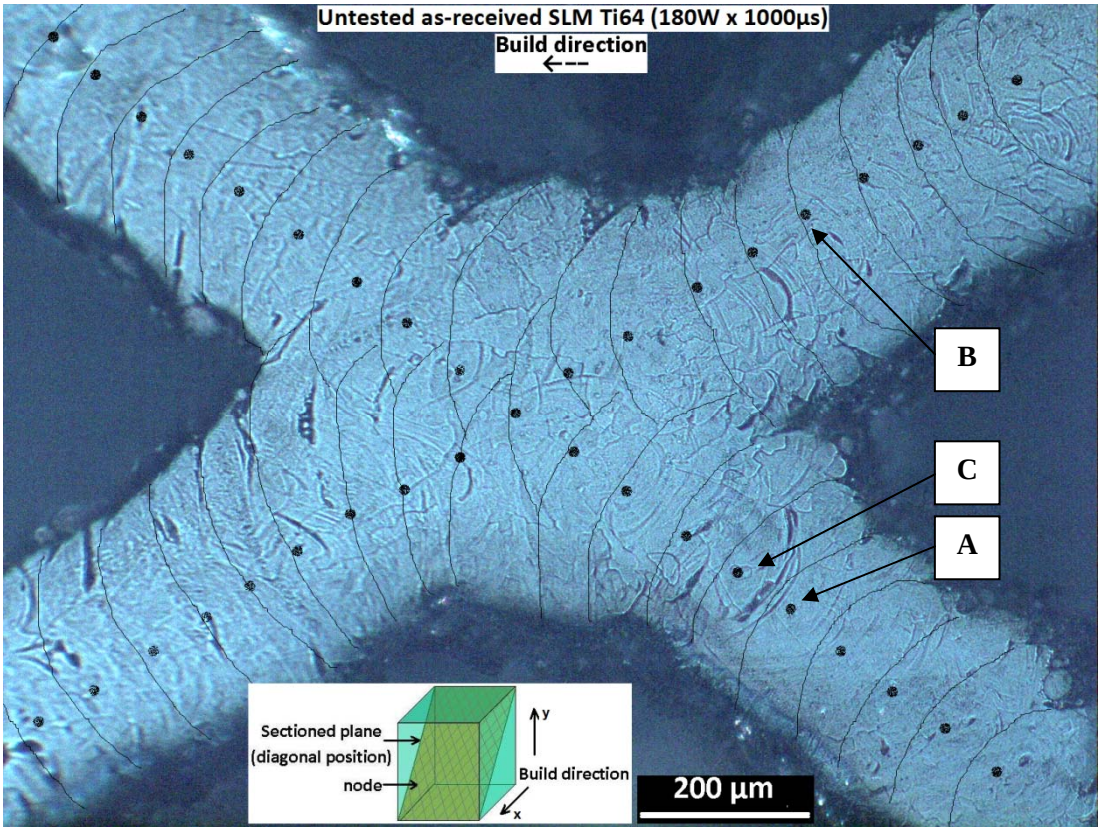

Figure 3.9: Details of node formation in SLM Ti-6Al-4V BCC micro-lattice block (180 W X 1000 µs) [B1-180-1000-AR-M]

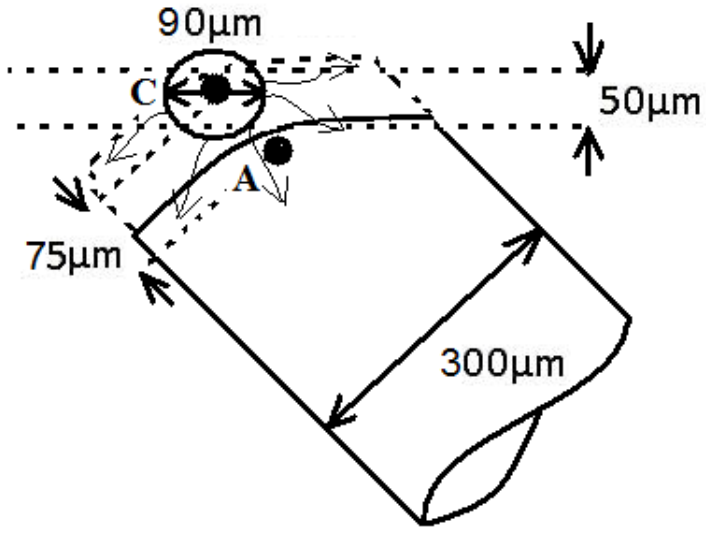

Figure 3.10: Approximation of dimensioned schematic drawing for globule formation (points A and C in Figure 3.9); layer thickness = 50 µm, laser beam spot size = 90 µm, distance between melted surface = 75 µm, strut diameter = 300 µm

Figure 3.10 shows the approximation of the dimensioned schematic drawing for the construction of the globule at point **C**. The globule was formed from the melting of the selected Ti-6Al-4V powder with 50 μm thickness. As shown in the schematic, the heat conduction from the laser beam with 90 μm spot size dissipated into the powder and melted the surrounding powder for up to the diameter size of the strut, which was approximately 300 μm. The distance between the surface of the melted powder and the previously solidified surface was about 75 μm, which was the diagonal distance of the 50 μm powder thickness in a BCC configuration. It can be seen that a part of the solidified surface of globule **A** was also melted during the formation of globule **C**. Therefore, there was an overlap between the two globules which fused the globules together.

Figure 3.11 shows a sectioned node of the heat-treated SLM Ti-6Al-4V BCC micro lattice block with 160 W x 1000 μs parameters. The effects of heat-treatment can be seen along the outer surfaces where the fusion of discontinuities and bonded particles were observed. The microstructure of the heat-treated micro-lattice block was comparable to that of the heat-treated single strut as discussed in Chapter 2. However, a slightly different arrangement of β phase in the heat-treated micro-lattice block was observed as compared to that of the heat-treated single strut. This could be due to the effect of different initial manufacturing parameters of both the materials, which led to different cooling rates during the formation of materials. It is known that the microstructure formations of titanium alloys are very sensitive to cooling rates [Gilbert and Shannon (1998)]. Table 3.1 compares the differences in microstructures of the micro-lattice blocks and single struts.

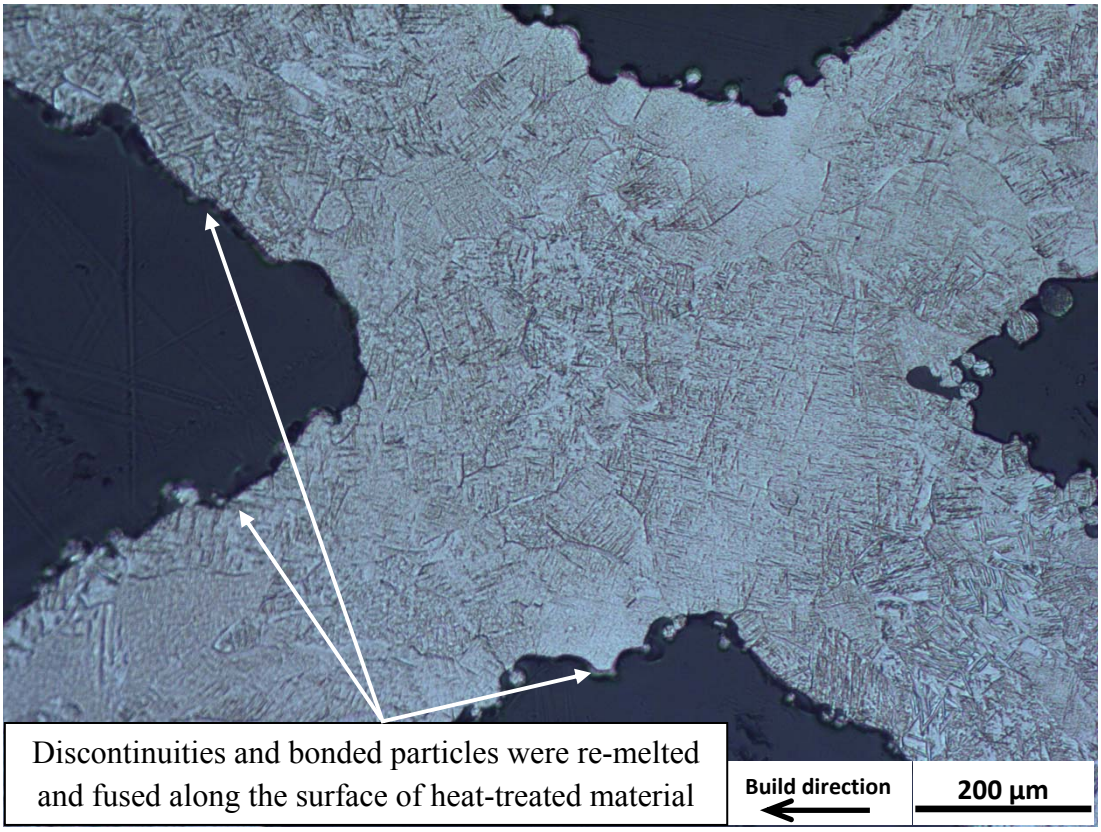

Figure 3.11: Sectioned node of the heat-treated SLM Ti-6Al-4V BCC micro lattice block (160 W x 1000 µs) [B1-160-1000-HT-M]

Table 3.1: Microstructure comparison between the SLM Ti-6Al-4V BCC micro-lattice blocks and single manufactured SLM Ti-6Al-4V micro-struts from Chapter 2

BCC micro-lattice blocks	Single manufactured struts
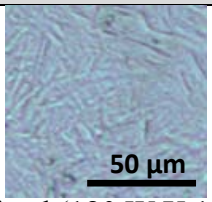 As-received (180 W X 1000 µs) [B1-180-1000-AR-M]	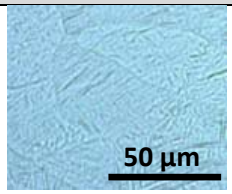 As-received (200 W X 1000 µs) [S1-35-200-1000-AR-M]
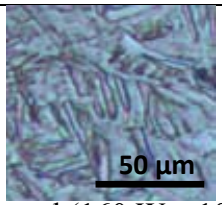 Heat-treated (160 W x 1000 µs) [B1-160-1000-HT-M]	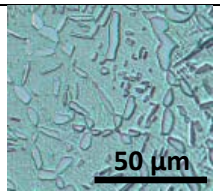 Heat-treated (200 W x 1000 µs) [S1-90-200-1000-HT(B)-M]

3.3.2 Analysis of Geometry of Struts in SLM Ti-6Al-4V BCC Micro-lattice Blocks

Analysis of geometry involved the measurements of diameter, surface roughness, circularity as well as dimensional accuracy of struts in SLM Ti-6Al-4V BCC micro-lattice blocks. The diameter of struts in the BCC micro-lattice blocks was analysed using the shadow measurement method in order to be comparable with that of the single manufactured micro-struts in Chapter 2. The surface roughness and circularity of the struts were also determined using similar procedures. Figure 3.12 shows an SEM image of the strut arrangements in the 45° angle diagonal plane of the as-received micro-lattice block (160 W x 1000 µs). The struts diameters can be directly measured from the image, as indicated in the figure. Strut diameters for 50 struts (average of three readings per strut) were measured and distributed as shown in Figure 3.13.

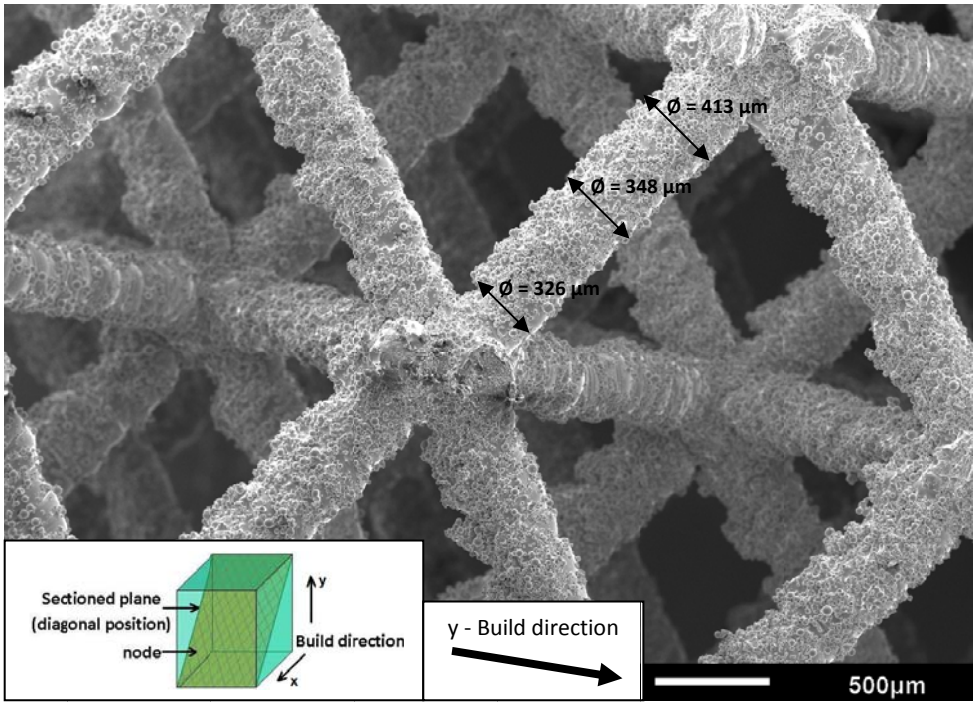

Figure 3.12: Struts arrangements in 45° angle diagonal plane of the as-received SLM Ti-6Al-4V BCC micro-lattice block (160 W x 1000 µs) [B(1-2)-160-1000-AR]

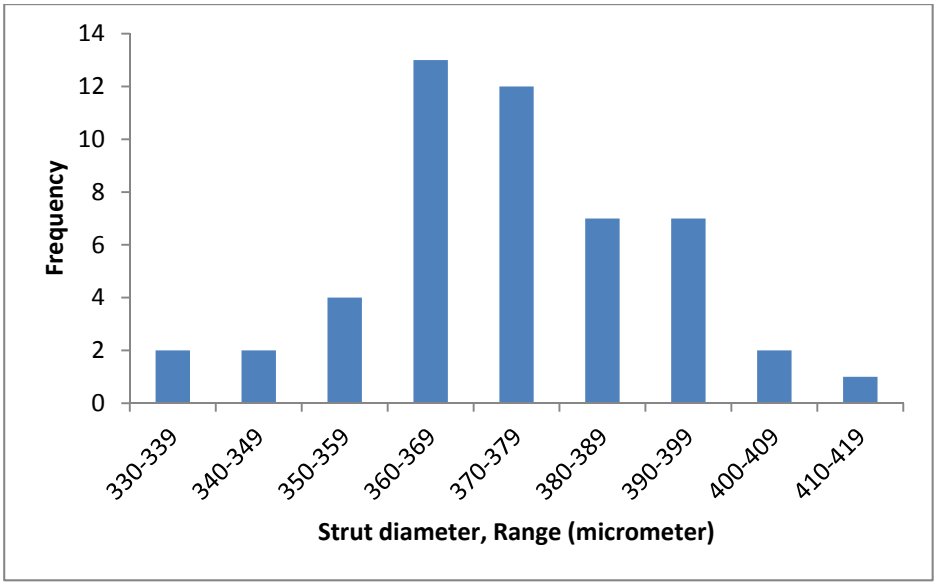

Figure 3.13: Distribution of strut diameters in as-received SLM Ti-6Al-4V BCC micro-lattice block (160 W x 1000 µs) [B(1-2)-160-1000-AR]

From Figure 3.13, it can be seen that most of the strut diameters in the as-received micro-lattice block were between the ranges of 360 to 379 µm. Besides, a noticeable number of strut diameters were between the ranges of 380 to 399 µm. The average diameter of the struts was found to be (374.24 ± 17.7) µm. This gave a good agreement with the diameter measurements of the singly manufactured struts discussed in Chapter 2.

Meanwhile, Table 3.2 shows diameter variations and surface roughness parameters within struts of both the as-received and heat-treated micro-lattice blocks, using the shadow measurement method as discussed in Chapter 2. From this method, the average strut diameter for the as-received micro-lattice blocks was determined as (373.1 ± 29.95) µm, with minimum and maximum values of 321 µm and 429 µm respectively. The average strut diameter for the heat-treated micro-lattice blocks was determined as (339.41 ± 17.57) µm, with minimum and maximum values of 307 µm and 371 µm respectively.

Table 3.2: Diameter variations and surface roughness parameters within struts of both the as-received and heat-treated SLM Ti-6Al-4V BCC micro-lattice blocks (using the shadow measurement method)

As-received blocks (160 W x 1000 µs) [B(1-2)-160-1000-AR]	Heat-treated blocks (160 W x 1000 µs) [B(1-2)-160-1000-HT]
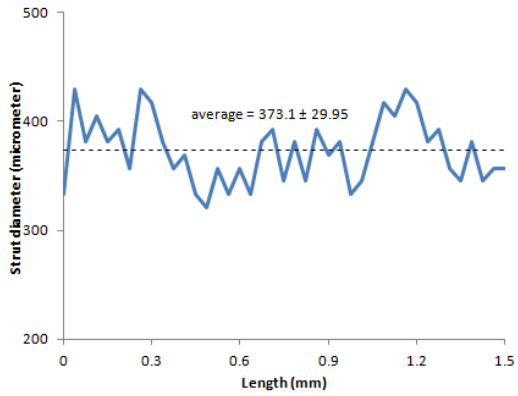 Strut diameter variation	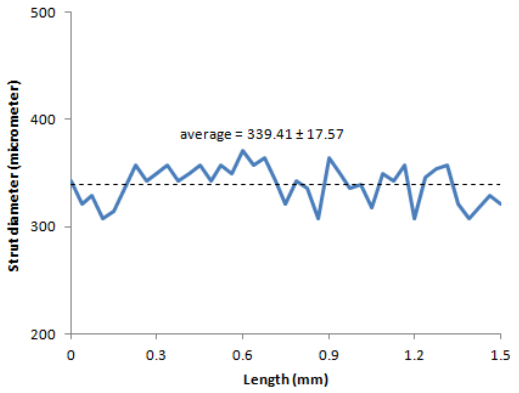 Strut diameter variation
Average diameter = (373.1 ± 29.95) µm Minimum diameter = 321 µm Maximum diameter = 429 µm	Average diameter = (339.41 ± 17.57) µm Minimum diameter = 307 µm Maximum diameter = 371 µm
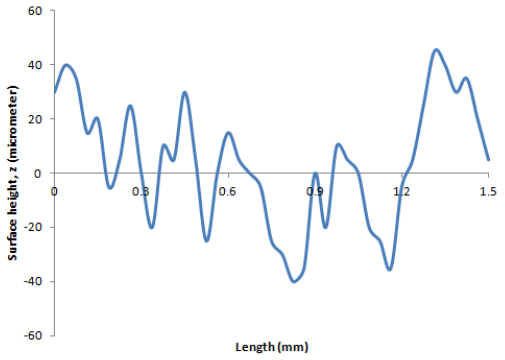 Surface roughness profile	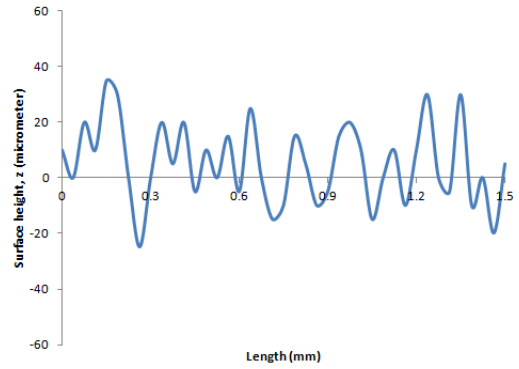 Surface roughness profile
R_a = 18.3 µm	R_a = 11.8 µm
R_y = 85 µm	R_y = 60 µm
R_z = 64 µm	R_z = 46 µm

It can be seen that the average strut diameters determined from both direct measurement and shadow measurement methods for the as-received micro-lattice

blocks were found comparable to each other, which were (374.24 ± 17.7) μm and (373.1 ± 29.95) μm, respectively. In order to include all measured diameter values within the considered ranges, it was decided to choose the minimum and maximum values as 321 μm and 429 μm, respectively.

As discussed in Chapter 2, Kude and Khairnar (2004) proposed a formula for strut diameter estimation, which can be obtained from the maximum measured radius and minimum measured radius values (Equation 2.5). Besides the diameter estimation, they also developed a formula for determination of a strut's non-circularity (Equation 2.6). Table 3.3 tabulates the estimated strut diameter and circularity values for both the as-received and heat-treated SLM Ti-6Al-4V BCC micro-lattice blocks using formulas from Kude and Khairnar (2004).

Table 3.3: The estimated strut diameter and circularity values for both the as-received and heat-treated SLM Ti-6Al-4V BCC micro-lattice blocks using formulas from Kude and Khairnar (2004)

Geometry	As-received blocks (160 W x 1000 μs) [B(1-2)-160-1000-AR]	Heat-treated blocks (160 W x 1000 μs) [B(1-2)-160-1000-HT]
Diameter (μm)	378.87	340.51
Non-circularity (%)	28.5%	18.8%
Circularity (%)	71.5%	81.2%

As mentioned in Chapter 1, the influences of SLM parameters on mechanical properties of stainless steel micro-lattice block structures were studied by Tsopanos et al. (2010). They derived an equation to estimate strut diameter, d, of the SLM stainless steel (SS316L) BCC micro-lattice blocks, in terms of mass of the block, m_b, density of the steel, ρ_s, number of cells along the cube side, N^3, and the cell length, L. In this study, the equation was applied to the Ti-6Al-4V material, with density ρ_t, taken as 4430 kg/m^3 [Boyer et al. (1994)]. Since several blocks in this study have a

slightly different number of cells as compared to the blocks in the Tsopanos et al. (2010) study, the formula was revised as in Equation 3.1, where N_1, N_2 and N_3 were the number of cells along the width, length and height directions.

$$d = \sqrt{\frac{m_b}{\rho_t.\pi .N_1 \times N_2 \times N_3 .L .\sqrt{3}}} \quad [3.1]$$

It should be noted that this formula was meant for the as-received material, since post-manufacturing heat-treatment was not taken into account in the derivation. Table 3.4 lists the estimated strut diameters for SLM Ti-6Al-4V micro-lattice blocks with several manufacturing parameters, calculated using the derived formula from Tsopanos et al. (2010).

Table 3.4: Estimated strut diameters for SLM Ti-6Al-4V micro-lattice blocks using formula from Tsopanos et al. (2010)

Manufacturing parameters	Unit cell size [L]	Block dimension (mm^3)	Number of cells [$N_1.N_2.N_3$]	Average mass of block [m_b]	Calculated diameter
200 W x 1000 µs [B(1-3)-200-1000-AR]	2.5 mm	20 x 20 x 20	8 x 8 x 8	2.90 g	307 µm
180 W x 1000 µs [B1-180-1000-AR]	2.5 mm	20 x 20 x 20	8 x 8 x 8	3.25 g	325 µm
160 W x 1000 µs [B(1-2)-160-1000-AR]	2.5 mm	20 x 20 x 19	8 x 8 x 7.5	3.33 g	339 µm

From Table 3.4, it can be seen that the estimated diameter values were different compared to the diameter values determined using other methods that were discussed earlier in this section. Higher strut diameter values were estimated for blocks with lower laser power (W) parameters. The effect of manufacturing parameters on the diameter of struts in SLM Ti-6Al-4V micro-lattice blocks will be further discussed in section 3.4.1.

3.3.3 Comparison of Quality of Struts in Micro-lattice Blocks with Single Manufactured Struts

As the quality of SLM Ti-6Al-4V micro-lattice blocks depends on the quality of strut geometries; the diameter, surface roughness and circularity of struts in micro-lattice blocks and single manufactured struts were compared. Table 3.5 compares the geometries of both struts materials.

Table 3.5: Comparison of quality of struts in BCC micro-lattice blocks with single manufactured struts for SLM Ti-6Al-4V material

Material	As-received			Heat-treated		
	Struts in micro-lattice (160 W x 1000 µs) [B(1-2)-160-1000-AR]	Single struts (200 W x 1000 µs) [S(1-15)-35-200-1000-AR]	% diff.	Struts in micro-lattice (160 W x 1000 µs) [B(1-2)-160-1000-HT]	Single struts (200 W x 1000 µs) [S(1-9)-35-200-1000-HT(B)]	% diff.
Diameters from measurements	(373.1 ± 29.95) µm	(374.14 ± 26.15) µm	0.3%	(339.41 ± 17.57) µm	(322.56 ± 16.6) µm	5.2%
Diameters from Kude & Khairnar (2004) formula	378.87 µm	378.32 µm	0.1%	340.51 µm	316.94 µm	7.4%
Circularity	71.5%	73.6%	2.9%	81.2%	77.9%	4.2%
R_a	18.3 µm	16.8 µm	8.9%	11.8 µm	11.5 µm	2.6%
R_y	85 µm	70 µm	21.4%	60 µm	60 µm	0%
R_z	64 µm	59 µm	8.5%	46 µm	46 µm	0%

It was shown that the quality of struts in the micro-lattice blocks was comparable to that of single manufactured struts. All of the properties differed by less than 10%, except for the R_y value for the as-received material. This shows that the single manufactured struts with 35° build angle can represent the struts arranged in BCC

micro-lattice blocks, and hence can be used to estimate the properties of the parent materials for micro-lattice structures. It should be noted that, the small differences in the properties of struts could be contributed by the different manufacturing laser power (W) of the micro-lattice blocks and single struts.

3.4 COMPRESSION TEST ON SLM Ti-6Al-4V BCC MICRO-LATTICE BLOCKS

Uniaxial quasi-static compression tests were conducted on the SLM Ti-6Al-4V BCC micro-lattice blocks specimens. The samples were placed between lubricated compression platens on an Instron 4024 universal test machine. The crosshead displacement rate was 0.25mm/min. Load was recorded by the load-cell and an extensometer attached to the upper and lower compression platens recorded the displacement during the test. The compression strength was determined by dividing the peak force by the initial cross section of the samples. Figure 3.14(a) and (b) show the compression test set-up. It should be noted that in the micro-tensile test of struts in Chapter 2, direct reading of displacement was taken from the machine, thus a compliance correction method was necessary. In the compression test of blocks in Chapter 3, the displacement was recorded from the extensometer attached to the upper and lower platens of the machine, thus the compliance correction for the machine was not applied.


(a)

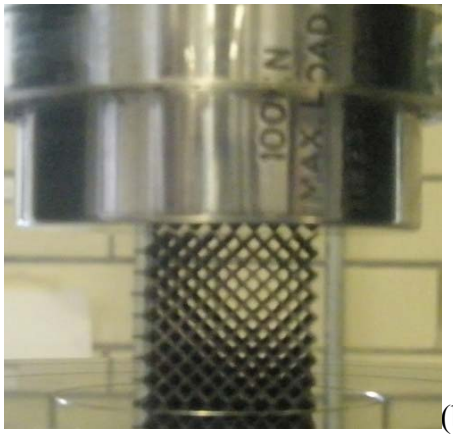
(b)

Figure 3.14: (a) The Instron 4024 universal test machine for compression tests; (b) SLM Ti-6Al-4V BCC micro-lattice block prior to compression test

3.4.1 Compression Tests Results

Table 3.6 extracts the compression tested specimens from the earlier Table 1.3 of Chapter 1. The table arranges the number of specimens according to different laser powers and laser exposure parameters. Meanwhile, Figure 3.15(a) to (c) show the stress-strain curves for the SLM Ti-6Al-4V BCC micro-lattice blocks specimens with different manufacturing parameters and post-processing treatments.

Table 3.6: Compression tested block specimens according to laser powers and laser exposures parameters

Laser parameters	500 µs	1000 µs
160 W	-	2 x As-received [B(1-2)-160-1000-AR] 2 x Heat-treated [B(1-2)-160-1000-HT]
180 W	3 x As-received [B(1-3)-180-500-AR] 3 x HIPped [B(1-3)-180-500-HIP]	1 x As-received [B1-180-1000-AR]
200 W	-	3 x As-received [B(1-3)-200-1000-AR] 3 x HIPped [B(1-3)-200-1000-HIP]

There were effects due to the differences of laser powers (160 W, 180 W and 200 W), laser exposure times (500 µs and 1000 µs) and post-processing treatments (heat-treatment and HIP) shown by the results in stress-strain curves of Figure 3.15(a) to (c). At the similar laser exposure time (1000 µs), higher maximum stresses were observed in specimens with lower laser powers (160 W and 180 W in Figure 3.15(a) compared to 200 W in Figure 3.15(b)). Meanwhile, Figure 3.15(c) shows the stress-strain curves for material with lower manufacturing parameter, which was found to be more ductile. The pattern was different from that shown in Figure 3.15(a) and (b) since it failed layer by layer at 45° diagonal plane, therefore there are series of peaks for each layer failure. In comparison, abrupt failure occurred in material with higher laser parameter (Figure 3.15(a) and (b)). Table 3.7 summarizes the SLM Ti-6Al-4V BCC micro-lattice blocks results derived from the stress-strain curves.

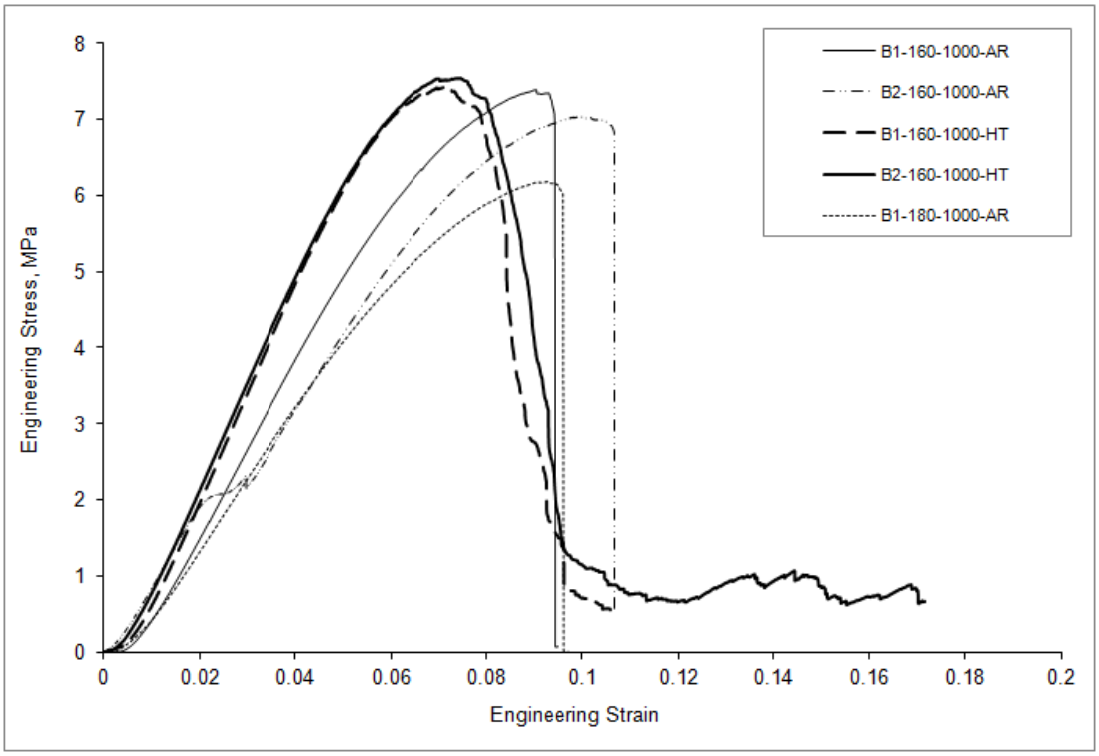
B1-160-1000-AR
B2-160-1000-AR
B1-160-1000-HT
B2-160-1000-HT
B1-180-1000-AR
Engineering Stress, MPa
Engineering Strain
0
1
2
3
4
5
6
7
8
0
0.02
0.04
0.06
0.08
0.1
0.12
0.14
0.16
0.18
0.2

(a)

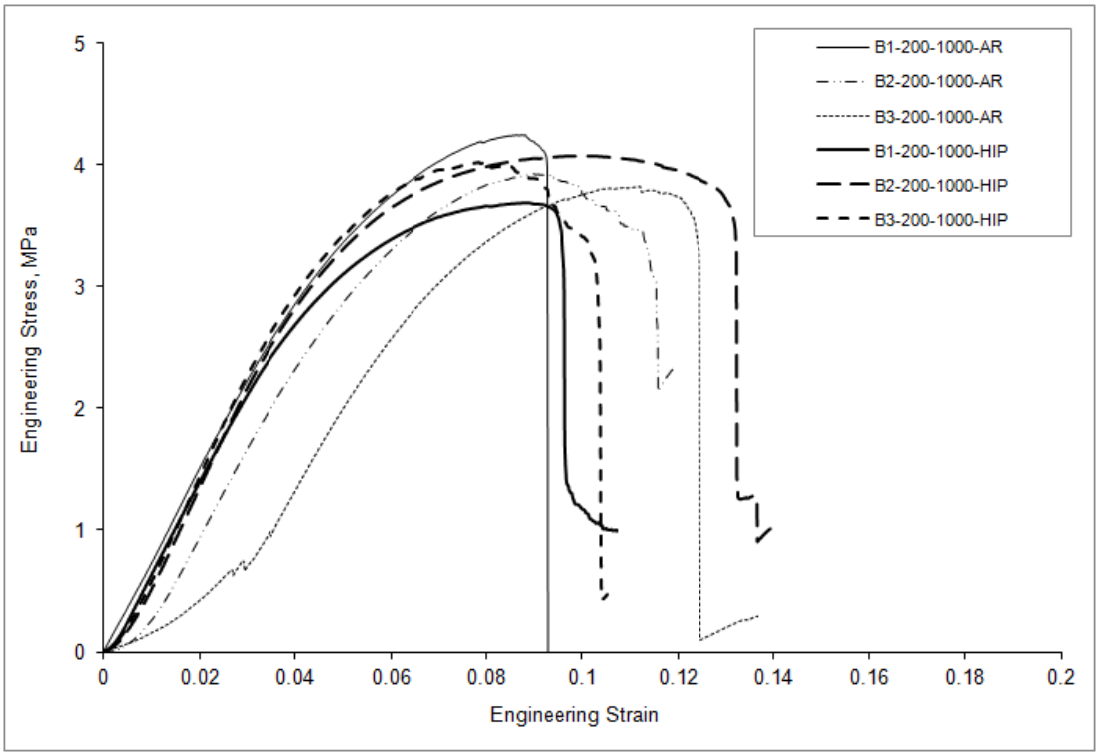
B1-200-1000-AR
B2-200-1000-AR
B3-200-1000-AR
B1-200-1000-HIP
B2-200-1000-HIP
B3-200-1000-HIP
Engineering Stress, MPa
Engineering Strain
0
1
2
3
4
5
0
0.02
0.04
0.06
0.08
0.1
0.12
0.14
0.16
0.18
0.2

(b)

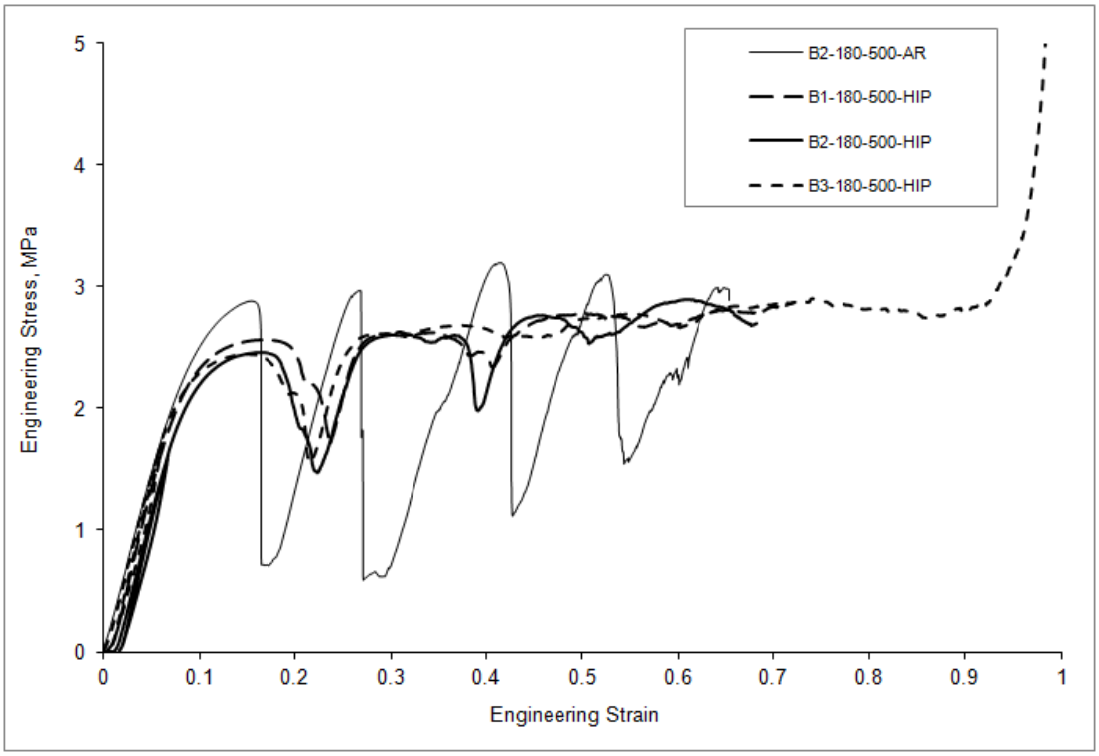

(c)

Figure 3.15: Stress-strain curves for SLM Ti-6Al-4V BCC micro-lattice blocks (a) [B(1-2)-160-1000-AR], [B(1-2)-160-1000-HT] and [B1-180-1000-AR]; (b) [B(1-3)-200-1000-AR] and [B(1-3)-200-1000-HIP]; (c) [B2-180-500-AR] and [B(1-3)-180-500-HIP] [adapted from Shen(2009)]

Table 3.7: Summary of the SLM Ti-6Al-4V BCC micro-lattice blocks results

Material ID	Max. Stress, σ_{ult} [MPa]	Stiffness, E [MPa]	Strain at max. Stress	Fracture strain	Mass, m [g]	Estimated diameter, d [μm]	Estimated lattice density, ρ [g/cm^3]	Specific strength, σ_{ult} / ρ [kN.m/kg]	Specific stiffness, E / ρ [kN.m/kg]
B1-160-1000-HT	7.5	119.3	0.072	0.080	3.40	343	0.447	16.78	266.89
B2-160-1000-HT	7.6	116.9	0.075	0.082	3.40	343	0.447	17.00	261.52
B1-160-1000-AR	7.4	96.8	0.091	0.092	3.40	343	0.447	16.55	216.55
B2-160-1000-AR	7.0	82.1	0.100	0.106	3.30	338	0.434	16.13	189.17
B1-180-1000-AR	6.2	77.1	0.095	0.096	3.20	322	0.400	15.50	192.75
B1-200-1000-AR	4.3	68.0	0.088	0.093	2.90	307	0.363	11.85	187.33
B2-200-1000-AR	3.8	59.4	0.093	0.118	2.90	307	0.363	10.47	163.66
B3-200-1000-AR	3.8	50.0	0.110	0.125	2.90	307	0.363	10.47	137.74
B1-200-1000-HT	4.1	68.4	0.080	0.104	2.90	307	0.363	11.29	188.48
B2-200-1000-HT	4.1	70.8	0.110	0.140	2.90	307	0.363	11.29	195.12
B3-200-1000-HT	3.75	68.0	0.090	0.100	2.90	307	0.363	10.33	187.33
B1-180-500-AR	2.75	21.0	0.150	0.160	2.28	272	0.285	9.65	73.68
B2-180-500-AR	2.80	24.0	0.150	0.160	2.28	272	0.285	9.82	84.21
B3-180-500-AR	2.90	31.3	0.175	0.180	2.28	272	0.285	10.18	109.65
B1-180-500-HT	2.60	22.0	0.180	0.200	2.28	272	0.285	9.12	77.19
B2-180-500-HT	2.50	21.0	0.175	0.180	2.28	272	0.285	8.77	73.68
B3-180-500-HT	2.50	22.0	0.160	0.175	2.28	272	0.285	8.77	77.19

Note: The stiffness (E) unit (MPa) of micro-lattice materials in this study is comparable to other studies [Shen et al. (2010); Tsopanos et al. (2010); Ushijima et al. (2011)]. The lattice structure is considered as block material, and it is not a solid material. The properties of the solid material were derived from the single strut as discussed in Chapter 2. In Chapter 3, the stiffness is determined for the lattice structure, not for the solid material.

In Table 3.7, the maximum stress σ_{ult}, stiffness E, strain at maximum stress as well as fracture strain values were determined from the stress-strain curves of the block specimens. The estimated diameter d values were derived from the mass m values and block dimensions, calculated using the formula mentioned in Equation 3.1, which is a modified formula of Tsopanos et al. (2010). It should be noted that the formula was derived based on the effects of manufacturing parameters to the micro-lattice blocks, and there was no consideration of the effects of heat-treatment to the materials. Therefore, from Table 3.7, it can be seen that the estimated diameter value for the micro-lattice blocks with the same manufacturing parameters was similar, although it was shown in this study (section 3.3.2) that the heat-treatment improved the surface roughness and diameter variations of the struts, which led to a smaller average value of the diameter of the struts within the heat-treated micro-lattice blocks compared to that of the as-received blocks. Based on the results in Table 3.7, the estimated diameter, specific strength (σ_{ult} / ρ) and specific stiffness (E / ρ) values for the SLM Ti-6Al-4V micro-lattice blocks with different laser powers were plotted as shown in Figure 3.16(a), (b) and (c).

There is an interest to determine the single strut properties from the micro-lattice block properties as tabulated in Table 3.7. Equations developed by Ushijima et al. (2011) are therefore applied (these equations will be also applied in Chapter 4, Section 4.6.1). The re-arranged Ushijima et al. (2011) equations are as shown in Equation 3.2 and 3.3, where the Young's Modulus and compressive stress for the single strut are given by E_{strut} and σ_{strut} respectively. The stiffness of micro-lattice block is given by $E_{micro\text{-}lattice}$ (taken from E value in Table 3.7), while the compressive stress of micro-lattice block is given by $\sigma_{micro\text{-}lattice}$ (taken from σ_{ult} value in Table 3.7). The strut's diameter is given by d, and length of the unit cell is given by L.

$$E_{strut} = \frac{E_{micro-lattice}}{\sqrt{3}\,\pi} \cdot \frac{1+2(L/d)^2}{(d/L)^2} \qquad [3.2]$$

$$\sigma_{strut} = \frac{\sigma_{micro-lattice} \cdot 3L^3}{4\sqrt{2}d^3} \qquad [3.3]$$

The derived properties of the single strut using the micro-lattice block properties (four selected IDs from Table 3.7) are tabulated in Table 3.8 and compared with the standard properties [Boyer et al. (1994)] as well as properties of strut determined in Chapter 2 (as listed in Table 2.15).

Table 3.8: Comparison of micro-strut properties derived from theoretical equations, micro-tensile test (determined in Chapter 2) and standard properties

Ti-6Al-4V properties	Young's modulus E	Ultimate stress σ
From micro-tensile test in Chapter 2 (as-received material)	45 GPa	280 MPa
Standard properties (tensile test) [Boyer et al. (1994)]	114 GPa	950 MPa
From micro-lattice block compressive properties (Equations [3.2] and [3.3])		
Selected Material ID (from Table 3.7)		
B1-160-1000-AR	101 GPa	521 MPa
B1-180-1000-AR	104 GPa	496 MPa
B1-200-1000-AR	111 GPa	378 MPa
B1-180-500-AR	55 GPa	308 MPa

From the results in Table 3.8, it can be seen that the strut Young's Modulus and ultimate stress which are determined using the micro-lattice block compressive properties give higher values from that determined using strut tensile test in Chapter 2. The micro-lattice blocks with high laser exposure time (1000 μs) lead to the strut Young's Modulus values which are comparable to the standard value and the ultimate stress of 50% from the standard value. However, the micro-lattice block with low laser exposure time (500 μs) leads to the strut Young's Modulus value which is similar with that determined in micro-tensile strut test of Chapter 2 in this study. The mixed results of the strut properties derived from the micro-lattice blocks suggest that the theoretical equations developed by Ushijima et al. (2011) can be

used in the estimation of individual micro-strut in the lattice. However, the determination of the properties from the strut material as discussed in Chapter 2 gives more consistent results, despite of the low values as compared to the standard properties.

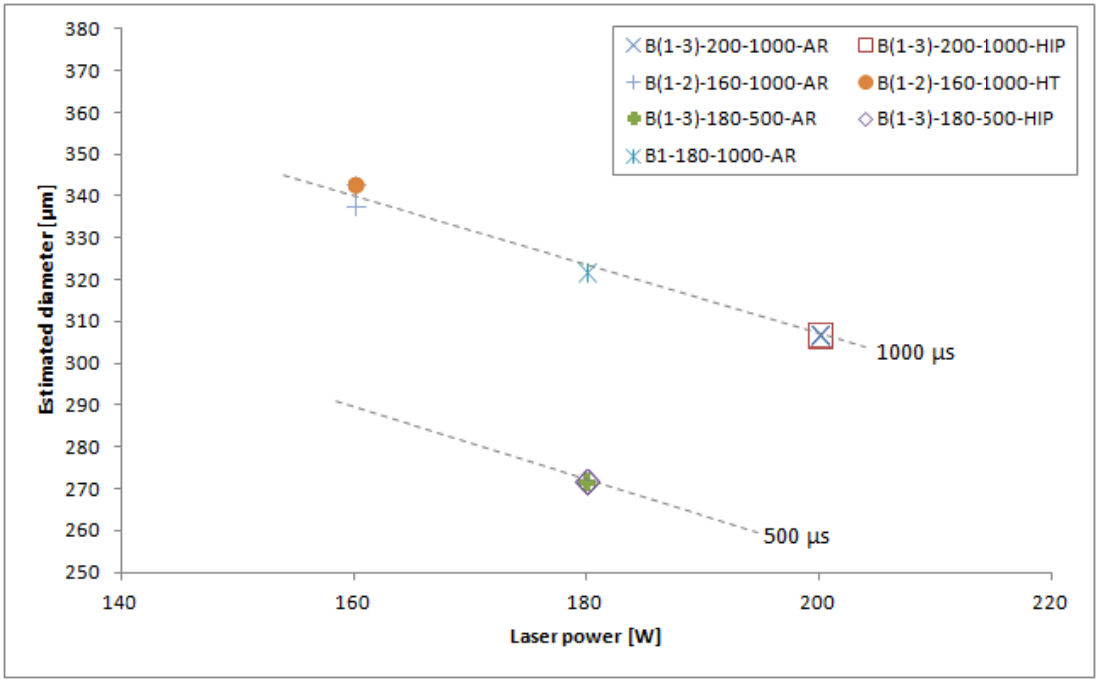

(a)

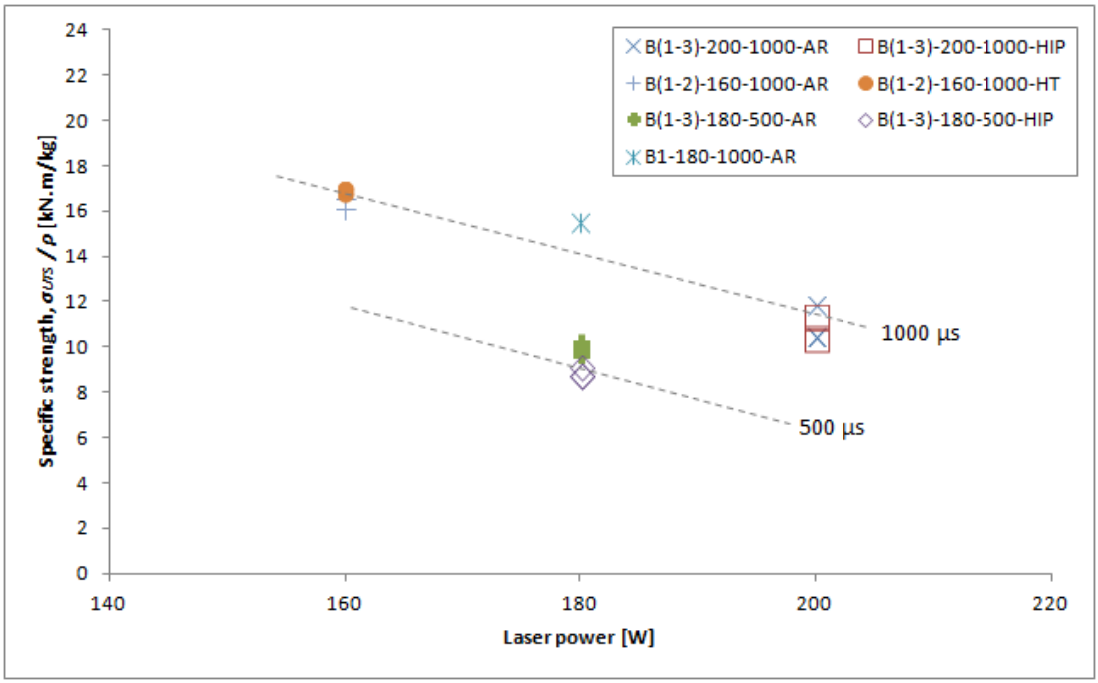

(b)

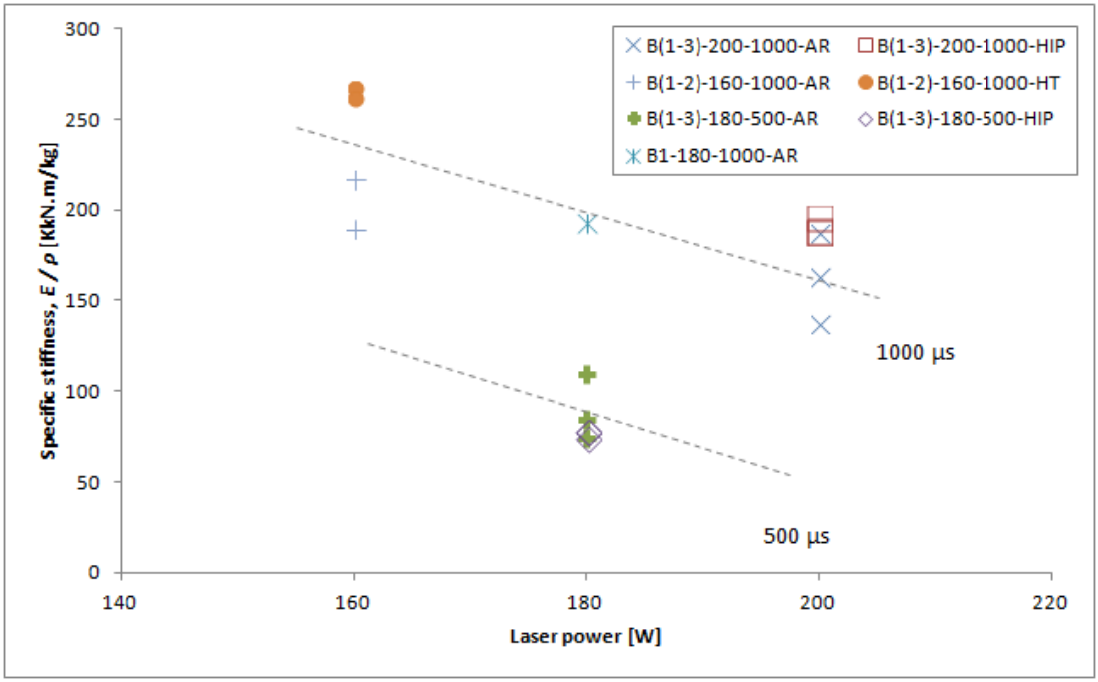

(c)

Figure 3.16: Variations in (a) estimated strut diameters; (b) specific strengths; (c) specific stiffness; of the SLM Ti-6Al-4V micro-lattice blocks with different laser powers

From Figure 3.16(a), at laser exposure time of 1000 µs, the estimated strut diameters were higher for blocks with 160 W laser power as compared to blocks with laser power of 200 W. Since there was no variation in laser power of blocks with laser exposure time of 500 µs, the results of blocks with that exposure time were estimated to be similar with that of blocks with 1000 µs exposure time. Lines representing interactions of estimated diameters with laser powers were drawn for both the 500 µs and 1000 µs laser exposure times. It was shown that the strut diameters of the SLM Ti-6Al-4V micro-lattice blocks increase as the laser power decreased and the laser exposure time increased. The results are difference with that of the SLM SS316L micro-lattice blocks, where the strut diameters were reported to be increased as both the laser power and laser exposure times increased [Tsopanos et al. (2010)]. These results were due to the complexity in thermo-mechanical process of the SLM Ti-6Al-4V BCC micro-lattice structures. The sensitivity of titanium alloy to different conditions and atmospheres were amongst the possible factors that contributed to the difference in the mechanisms between the SLM Ti-6Al-4V micro-lattice blocks and

the SLM SS316L micro-lattice blocks. There are currently numerous studies around the globe which aim to understand the mechanisms of the SLM Ti-6Al-4V materials, and the interests to the studies were shown by a large number of recent publications [Song et al. (2012); Leuders et al. (2012); Fogagnolo et al. (2012); Simonelli et al. (2012); Vrancken et al. (2012)].

Following the results of estimated diameters, the specific strengths and the specific stiffness at similar exposure times were also increased with decrease in laser powers, as shown in Figure 3.16(b) and 3.16(c) respectively. The difference in the relations of the strength and stiffness of the SLM Ti-6Al-4V micro-lattice blocks in this study (strength and stiffness increase as laser power decreases) compared to that of the SLM SS316L (strength and stiffness increase as laser power increases) [Tsopanos et al. (2010)] suggests that the mechanisms in titanium alloy materials are more complicated than the stainless steel. It was found that the findings in this study match with the melting mechanisms suggested by Song et al. (2012). In the study, Song et al. (2012)] summarized three different melting mechanisms of Ti-6Al-4V powder, as a result of difference laser energies (laser powers and speeds) during the SLM processing. The mechanisms are as listed below and defined in a processing map shown in Figure 3.17.

I. *Melting with cracks* – This is a high energy input zone. At a high laser power combined with a relatively low scanning speed, the single Ti-6Al-4V track could be completely melted and even broke up due to the excessive shrinkage and the high residual stresses, producing many visible cracks.
II. *Continuous melting* – The energy input was so comfortable that continuous single tracks were obtained by means of the complete melting of Ti-6Al-4V powders.
III. *Partial melting* – The insufficient energy input could not induce significant melting of Ti-6Al-4V powders. This will inevitably induce a laminated structure formed by Ti-6Al-4V powders.

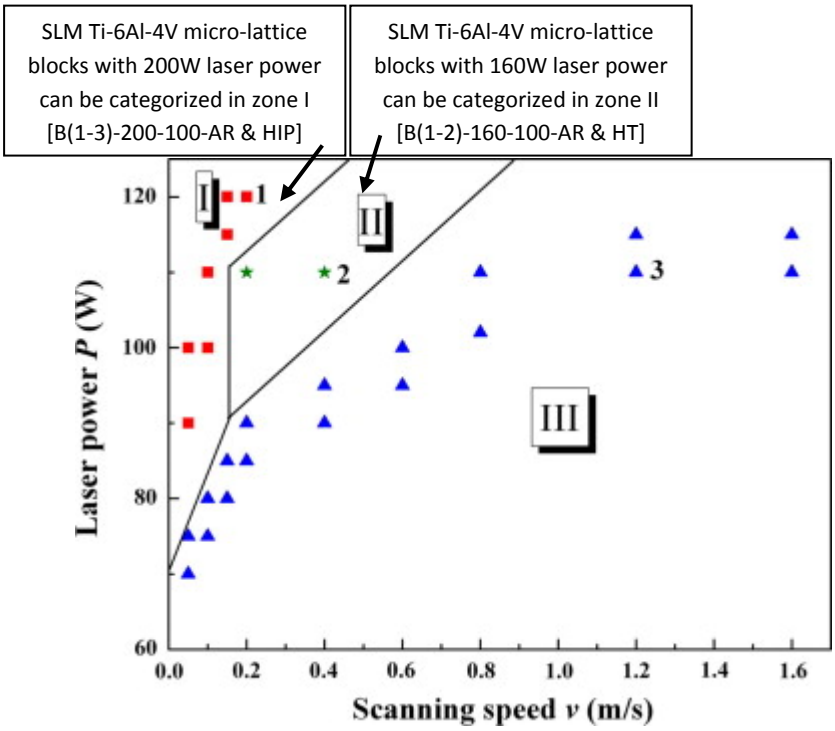

Figure 3.17: Mechanisms of single tracks for selective laser melted Ti-6Al-4V (zone I – *melting with cracks*; zone II – *continuous melting*; zone III – *partial melting*) versus laser power and scanning speed [Song et al. (2012)]

The results of the SLM Ti-6Al-4V micro-lattice blocks as shown in Figure 3.16(a) to (c) were compared to the processing map by Song et al. (2012). It is suggested that the micro-lattice blocks with 160 W laser power can be categorized in zone II, while the micro-lattice blocks with 200 W laser power can be categorized in zone I of the processing map in Figure 3.17. The definitions of zone I and II could be the reasons of the decrease in strength and stiffness of the SLM Ti-6Al-4V micro-lattice blocks with the increase in laser power. This suggests that, the highest laser power will not give the optimum properties of the SLM Ti-6Al-4V micro-lattice blocks, and different set of SLM manufacturing parameters would be needed for different types of applications.

The effects of different post-processing treatments can be also seen from the stress-strain curves of the SLM Ti-6Al-4V micro-lattice blocks (Figure 3.15(a) to (c)). It

was mentioned by Shen (2009) that the HIP process has stabilised the stress-strain response of the blocks with lower manufacturing parameters, i.e. 180 W x 500 μs, as shown in Figure 3.15(c). However, there was no improvement shown as a result of HIP process for the blocks with higher manufacturing parameters, i.e. 200 W x 1000 μs (Figure 3.15(b)). The deformation and mode of failure of both the as-received and HIPped blocks with 200 W x 1000 μs were found to be similar. In literature, it was reported that HIP treatment led to significant improvement in the SLM Ti-6Al-4V material due to the reduction of pores size [Leuders et al. (2012)]. In the current study, it should be noted that the BCC micro-lattice blocks are actually cubic shaped blocks with regular arrangement of pores, different from the bulk specimen materials used in Leuders et al. (2012) study. As the HIP works by closing pores in bulk materials, it is expected that it does not give effect to the micro-lattice materials as the 'pores' in the micro-lattices are not meant to be closed. This suggests that the HIP process would not be the appropriate post-manufacture treatment to the SLM Ti-6Al-4V micro-lattice blocks.

On the other hand, with the introduction of simple heat-treatment process in this study, a more progressive manner of failure was observed in the SLM Ti-6Al-4V BCC micro-lattice blocks with higher laser parameters (Figure 3.15(a)). A 'Ductile tearing' type of failure was seen in the stress-strain curves of the heat-treated blocks, compared to both the as-received and HIPped blocks. This suggests that there was some improvement in the heat-treated block deformation and failure modes (Figure 3.15(a)), compared to that of the as-received and HIPped blocks (Figure 3.15(b)).

The heat-treated blocks failed with slightly different behaviour compared to the as-received blocks. The heat-treated blocks were in attached condition, while the as-received blocks were completely fractured into two main pieces, as shown in Figure 3.18. This indicated that the ductility of the heat-treated materials was improved. For comparison, there was no improvement observed in the failure of the HIPped blocks (200 W x 1000 μs).

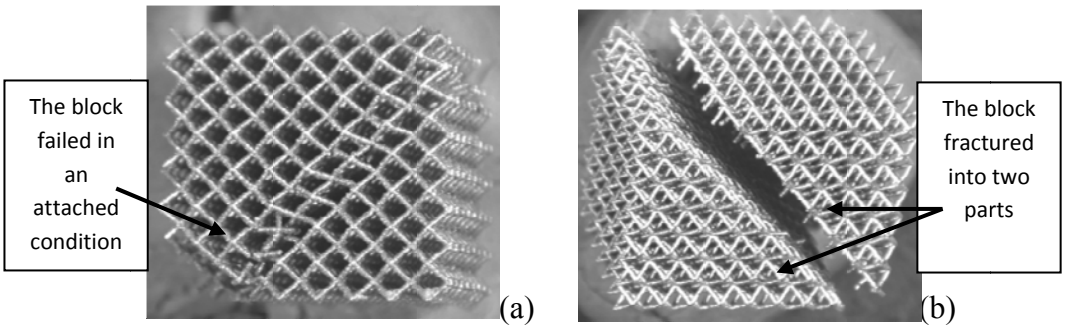

Figure 3.18: The failed conditions of SLM Ti-6Al-4V BCC micro-lattice blocks; (a) heat-treated material [B1-160-1000-HT]; (b) as-received material [B1-160-1000-AR]

Under compressive loads, it was observed that the SLM Ti-6Al-4V BCC micro-lattice block specimens failed due to bending of struts ends along the 45° angle planes, as shown in Figure 3.18. These struts failed under tensile stress conditions after the maximum stress points. The failure mechanisms will be discussed in the following section.

It should be noted that different complicated failure mechanisms could be obtained from different arrangements of core-skin bonding in the real aerospace applications. However, in this study, it was decided to test a simple case which has well defined collapse behaviour, without getting into complexities of buckling and instability.

3.4.2 Fracture Surfaces and Failure Mechanisms of SLM Ti-6Al-4V Micro-Lattice Blocks

As discussed in the previous section, the SLM Ti-6Al-4V BCC micro-lattice blocks failed at 45° angle diagonal plane, towards the end of struts near the nodal areas. Figure 3.19 shows an SEM image of a failed strut in a BCC micro-lattice block (160Wx1000µs) under compression load. It can be seen that the strut failed due to bending, adjacent to the nodal area. Compared to the failure of single struts under tensile load as discussed in Chapter 2, the struts in BCC micro-lattice block arrangement experience a different failure mechanism. The loading conditions are simplified as in the schematic illustration of Figure 3.20.

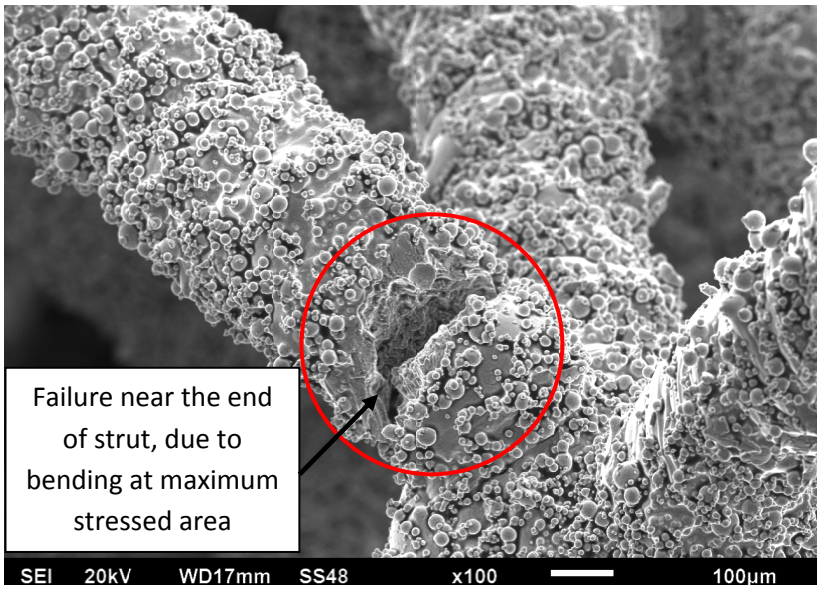

Figure 3.19: SEM image of a failed strut in SLM Ti-6Al-4V BCC micro-lattice block (160Wx1000µs) under compression load [B1-160-1000-AR]

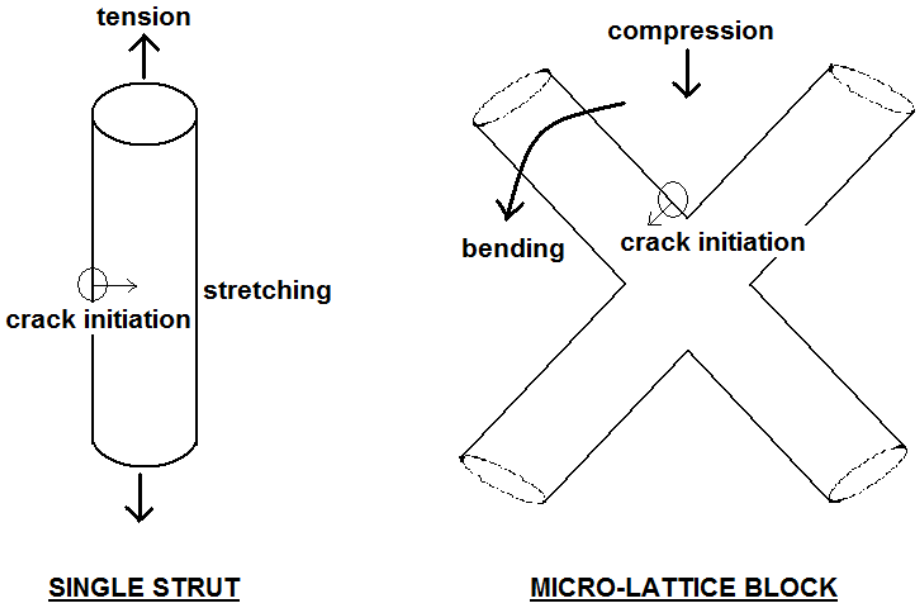

Figure 3.20: Comparison between failure of a single strut under tensile loading and strut in a micro-lattice block under compression loading

As mentioned in Becker and Garry (2002), although the appearance of microscale brittle and ductile fractures in parts failed in bending are not different from those of tensile loading condition, the sequence of the zones can be more complex than in tensile specimen. Figure 3.21(a) and (b) show a failure surface of the as-received SLM Ti-6Al-4V BCC micro-lattice block (160Wx1000µs) at different magnifications. From the surface, the initiation of fracture was expected to start at point 1, which was the location of maximum stress during strut bending, or the tension side. Then the fracture progressed towards the other side or the compression side of the bending failure. Figure 3.21(c) is a higher magnification of Figure 3.21(a) and (b), which shows the evidence of ductile fracture due to the existence of ductile dimples on the fracture surface. Figure 3.21(d) shows a top view of a fractured metal rod due to bending, given in Becker and Garry (2002), which is comparable to the fracture surface found in this study (Figure 3.21(b)).

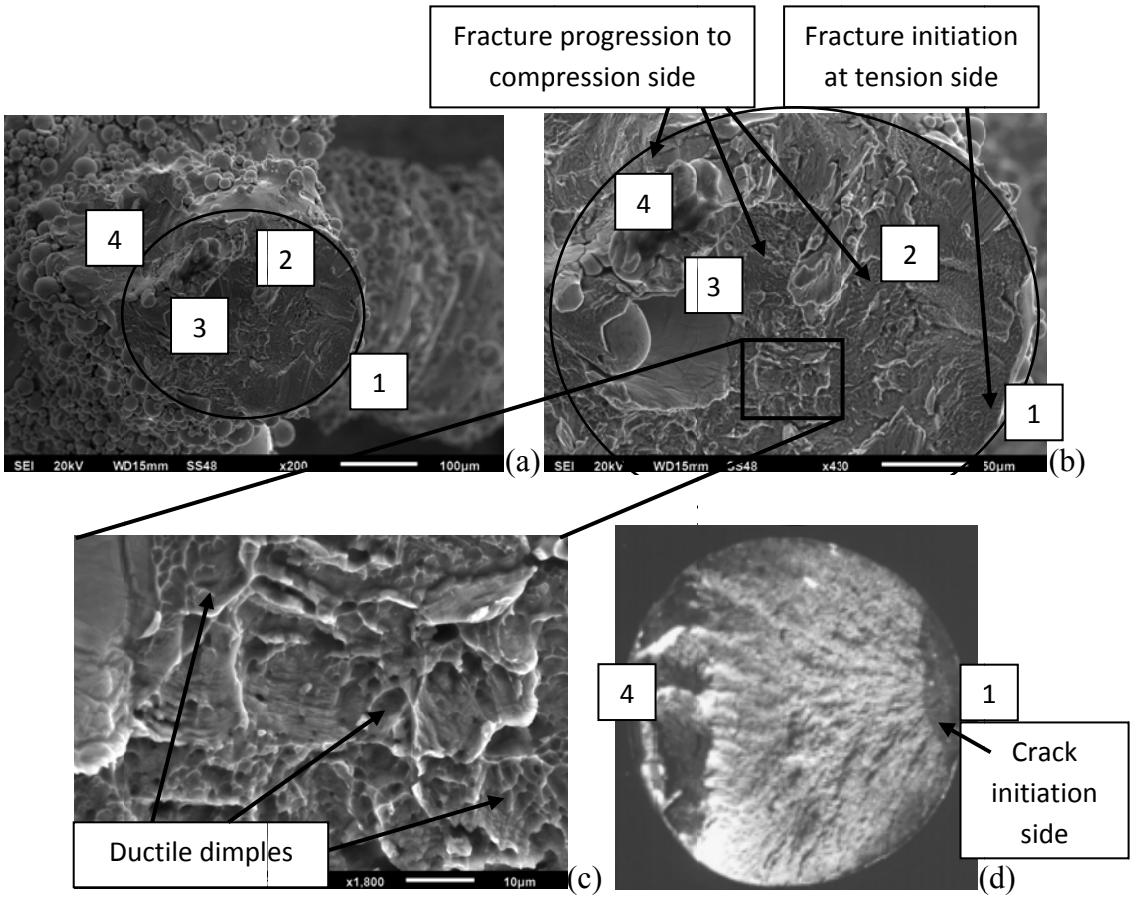

Figure 3.21: (a), (b), (c) Fracture surface of a failed strut in the as-received SLM Ti-6Al-4V BCC micro-lattice block (160Wx1000µs) [B1-160-1000-AR] at different magnifications; (d) A comparable fracture surface of metal rod due to bending failure; 1 = tension side, 4 = compression side [Becker and Garry (2002)]

Ductile fracture surface was also observed from the heat-treated SLM Ti-6Al-4V BCC micro-lattice blocks (160Wx1000µs). Ductile dimples can be seen from different magnifications of Figure 3.22(a), (b) and (c). The initiation of fracture was started at the tension side (point 1), and progressed towards the compression side (point 2). The sequence of the fracture zones was found similar to that of the strut in the as-received micro-lattice block which failed due to bending near the node area.

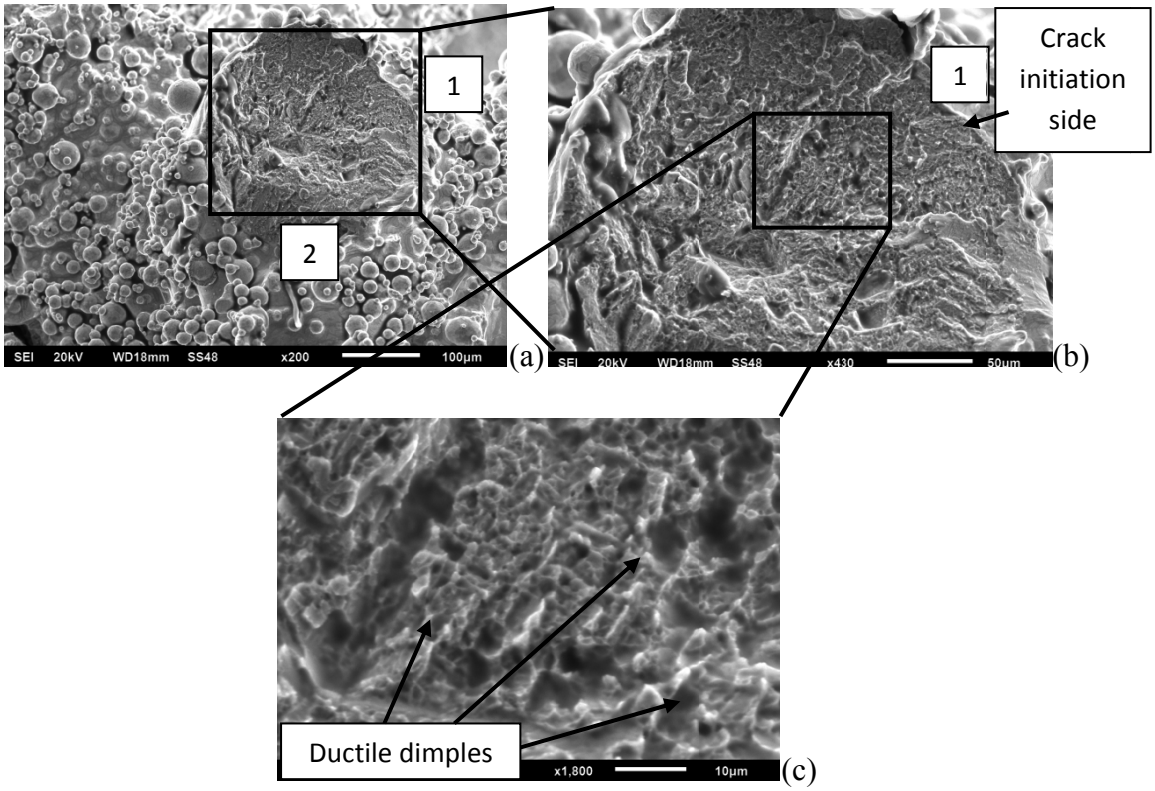

Figure 3.22: (a), (b) (c) Fracture surface of a failed strut in heat-treated SLM Ti-6Al-4V BCC micro-lattice block (160Wx1000µs) [B1-160-1000-HT] at different magnifications; 1 = tension side, 2 = compression side

3.4.3 Justifications for Rupture Criterion

The failure mechanisms of the single micro-struts under tensile loading and the struts within the BCC micro-lattice blocks under compressive loading were shown in earlier Figure 3.20. Both stretching mechanism for the single struts and bending mechanism for the struts in BCC blocks were initiated from cracks at maximum load locations. In both conditions, failure took place at low strains. Although limited necking was observed due to the low strain (as discussed in section 2.4.8), the failure surfaces showed ductile dimples, which indicated that the materials were ductile. In this case, ductile criterion was chosen in the prediction of failure for the BCC micro-lattice blocks, which was due to the failure of struts near the nodal areas.

There are several studies aim to predict fracture due to ductile crack formation. Hooputra et al. (2004) suggested a comprehensive failure model for ductile material using the IDS (Instability, Ductile and Shear) failure criteria, from the assumption that the equivalent fracture strain ε_{eq}^{**} is a function of the stress triaxiality η,. In the study, thin-walled double chamber aluminium extrusions were used. Imperfection such as localised necking, which led to a local neck and followed by fracture, was mentioned to be the main fracture mechanism in ductile sheet metals. The study suggested that a correct representation of the plastic deformation and failure of individual component parts including the imperfection is essential for the failure prediction of structures consist of small components such as the aluminium chamber. In other studies, Bao and Wierzbicki (2004) evaluated the effectiveness and accuracy of several ductile criteria. It was mentioned that different functions are necessary to predict crack formation for different ranges of stress triaxiality. Weighting functions in a wide range of stress states were suggested to be obtained from the determination of fracture locus in the space of equivalent strain to fracture and stress triaxiality. From a calibration study of seven fracture models, Wierzbicki et al. (2005) suggested that the constant equivalent strain method can be used in situation when the stress triaxiality and/or the deviatoric state parameter vary in very narrow ranges. A recent study by Giglio et al. (2012) calibrated the ductile fracture locus for Ti-6Al-4V titanium alloy using the Boa-Wierzbicki failure criterion. The standard classical tensile test specimens with four difference geometries were tested in different load conditions using a multiaxial test machine. The stress triaxiality at failure was driven by the specimen geometry in the calibration, by a limited range of a combination of axial and torque load using the multiaxial test machine.

For the current study, the failure of the struts in the BCC blocks under compressive loading will be predicted from the failure of the single manufactured struts under tensile loading. This is based on the suggestion by Hooputra et al. (2004), which mentioned that the plastic deformation and failure of individual component parts is essential in the failure prediction of a structure. Since the failure of the struts was initiated from the cracks at the surface, geometrical imperfection should be considered in the prediction. Detailed study of geometry and dimensional accuracy

of struts was conducted to quantify the imperfections. Due to constraint in the number of specimens and type of test that involved, data from the tension test of single struts was used in the calibration of the plastic strain.

The assumption given by Hooputra et al. (2004) was applied, which stated that the equivalent fracture strain ε_{eq}^{**} is a function of the stress triaxiality η. Since the stress triaxiality was not determined in this study, the constant equivalent strain method was used as suggested by Wierzbicki et al. (2005). The equivalent fracture strain ε_{eq}^{**} can be assumed to be as the same with the equivalent plastic strain at the onset of instability, ε_{eq}^{*}. The equivalent plastic strain at the onset of instability ε_{eq}^{*} can be taken from the equivalent plastic strain $\bar{\varepsilon}^{p}$ at fracture, given by the stress-strain curves obtained in the tensile test study. It was shown in Chapter 2 section 2.4.7 that the equivalent plastic strain $\bar{\varepsilon}^{p}$ is related to the equivalent stress $\bar{\sigma}$ in a uniaxial loading (equation 2.30 and 2.31). Therefore, in this study, the equivalent plastic strain $\bar{\varepsilon}^{p}$ from the fracture of the single struts can be use in the failure prediction of the BCC micro-lattice block materials.

3.5 IMPROVEMENTS IN SLM Ti-6Al-4V BCC MICRO-LATTICE BLOCKS

Table 3.9 lists the improvements that have been achieved after the introduction of heat-treatment on the SLM Ti-6Al-4V BCC micro-lattice blocks (160Wx1000µs). There were improvements in the geometry of struts in the micro-lattice blocks, given by the increase in circularity and decrease in surface roughness by 13.6% and 35.5% respectively. The improvements in geometry led to the improvement in initial modulus value by 23.2%, with the maximum stress of the heat-treated block similar to that of the as-received block. Unfortunately, there was a reduction in failure strain of the heat-treated block. However, as reported in the previous section, the heat-treated block failed in a more progressive manner, with an attached parts condition, while the as-received block fractured abruptly into two pieces, which indicated that there was improvement in ductility of the heat-treated material.

Table 3.9: Improvements due to the introduction of heat-treatment on the SLM Ti-6Al-4V micro-lattice blocks

Properties	As-received strut [B(1-2)-160-1000-AR]	Heat-treated strut [B(1-2)-160-1000-HT]	Difference from the As-received
Diameter (shadow measurement method)	(373.1 ± 29.95) µm	(339.41 ± 17.57) µm	-9.0%
Diameter (Kude and Khairnar (2004) formula)	378.87 µm	340.51 µm	-10.1%
Circularity	71.5%	81.2%	+13.6%
Surface roughness, R_a	18.3 µm	11.8 µm	-35.5%
Initial Modulus, E	96.8 MPa	119.3 MPa	+23.2%
Maximum stress	7.4 MPa	7.5 MPa	+1.4%
Strain at failure, ε_f	0.092	0.082	-10.9%

Shen (2009) reported that the HIPped process slightly stabilises the responses of the SLM Ti-6Al-4V BCC micro-lattice blocks with lower parameters (180 W x 500 µs),

but gave no improvement to the micro-lattice with high parameters (200 W x 1000 μs). Compared to the HIPped process, the simple heat-treatment introduced in this study (discussed in detail in Chapter 2, section 2.2.2) has shown more promising compression test results. However, a more stable stress-strain curve of SLM Ti-6Al-4V BCC micro-lattice material with high parameter (200 W x 1000 μs) is preferred. To further improve the quality and geometry of the SLM Ti-6Al-4V BCC micro-lattice block material, it is suggested that:

- The current heat-treatment process is revised by introducing one more step of solution treatment-quenching-precipitation process in order to produce more circular and equiaxed microstructures for a better plasticity in material.
- The duration of precipitation treatment is slightly increased to promote the grain growth in order to improve ductility of the material, therefore stabilising the stress-strain response. However, further increase in ductility will decrease the strength of material.
- The current SLM standard procedure [Sutcliffe (n.d)] is really enforced especially during cleaning on change over powder material. Furthermore, the suggestions in handling of used metal powder and maintaining the chemical composition of the used powder [ASTM Standard (2012)] can be followed.
- As mentioned in Chapter 2, the laser re-melting technique [Yasa et al. (2011)] can be considered to be applied at every layer during micro-lattice structure manufacturing in order to improve the outer surfaces and porosity of the material, but this technique will definitely increase the total manufacturing processing time. The complexity in thermo-mechanical process during the SLM will also increase.

3.6 SUMMARY OF CHAPTER 3

One stage closer to Foreign Object Impact (FOI) panel performance is by analyzing the behaviour of the SLM Ti-6Al-4V micro-lattice blocks under compression load. In this study, only the BCC configuration was analyzed due to simplicity and reliability in manufacture [Tsopanos et al. (2010)]. Moreover, the BCC micro-lattice blocks were reported to have a bending dominated response [McKown et al. (2008)], which is preferable in impact energy absorption. The preliminary study of the SLM Ti-6Al-4V BCC micro-lattice blocks reported that the material failed at 45° angle diagonal planes [Shen (2009)]. The study reported in this chapter aims to understand the failure of this material, and to suggest possible improvements for the material.

The manufacture of the SLM Ti-6Al-4V BCC micro-lattice block was re-visited, in order to trace the processing of the limited ready specimens. The finding of a unique cross-section of micro-lattice nodes at 45° angle diagonal planes revealed the formation of the material and gave an insight on the material's quality. The geometry (diameter and circularity) as well as surface properties of struts in the micro-lattice blocks were measured and they were found to be comparable to that of the single manufactured struts discussed in Chapter 2. The suggested heat-treatment in this study showed promising improvements on strut quality in the micro-lattice blocks.

Compression tests were done on several micro-lattice blocks with different parameters and post-processing treatments. In the SLM Ti-6Al-4V BCC micro-lattice blocks, increase in diameter size and specific strengths were observed with the decrease in laser powers and increase in laser exposure times, different to that of the SS316L micro-lattice blocks reported by Tsopanos et al. (2010). This finding is comparable to the suggested SLM Ti-6Al-4V melting mechanisms suggested by Song et al. (2012). A simple heat-treatment procedure was applied in this study, and it was found that there was some difference in deformation and failure modes of blocks as compared to the HIP treatment reported in Shen (2009). It was shown that struts in the SLM Ti-6Al-4V BCC micro-lattice blocks failed due to bending at the

highest tensile stress near the nodal areas. Dimpled fracture surfaces of the struts showed that ductile failure took place in the material. Therefore, ductile facture model by Hooputra et al. (2004) was suggested to be applied in the failure prediction of the material.

All in all, this chapter relates the geometry, properties and performance of the micro-lattice blocks with the micro-struts which were discussed in Chapter 2. The mode of deformation and failure of the micro-lattice blocks provides a background as well as an input for the analysis which will be presented in Chapter 4.

REFERENCES OF CHAPTER 3

Aris, M.S. (2009) *The Development of Active Heat Transfer Enhancement Devices from Shape Memory Alloys in a Selective Laser Melting Process*, PhD Thesis, University of Liverpool, United Kingdom.

ASTM Standard (2012) '*Standard specification for Addititive Manufacturing Titanium-6 Aluminum-4 Vanadium with Powder Bed Fusion*', ASTM International, DOI: 10.1520/F2924-12.

Bao, Y. and Wierzbicki, T. (2004) 'A comparative study on various ductile crack formation criteria'. *Transactions of the ASME*, 126: 314-324.

Beaman, J.J., Barlow, J.W., Bourell, D.L., Crawford, R.H., Marcus, H.L., Mcalea, K.P. (1997) *Solid freeform fabrication: a new direction in manufacturing*, Kluwer Academic.

Becker, W.T. and McGarry, D. (2002) 'Mechanisms and Appearances of Ductile and Brittle Fracture in Metals', *Failure Analysis and Prevention*, Vol. 11, ASM Handbook, ASM International, p 587-626.

Boyer, R., Welsch, G., Collings E.W. (ed.) (1994). *Material Properties Handbook: Titanium Alloys*, ASM International: Material Park, OH. http://www.matweb.com (assessed on 5/2/2010)

Fogagnolo, J.B., Sallica-Leva, E., Lopes, E., Jardini, A.L., Caram, R. (2012) 'The effect of the laser process parameters in the microstructure and mechanical properties of Ti6Al4V produced by selective laser sintering/melting', *Proceedings of METAL 2012*, Brno, Czech Republic, EU.

Giglio, M., Manes, A., Vigano, F. (2012) 'Ductile fracture locus of Ti-6Al-4V titanium alloy'. *International Journal of Mechanical Sciences*, 54:121-135.

Gilbert, R. And Shannon, C.R. (1998) *Heat treating of titanium and titanium alloys*, ASM Handbook Online, Volume 4, ASM International.

Hasan, R., Mines, R., Shen, E., Tsopanos, S., Cantwell, W., Brooks, W., Sutcliffe, C. (2010) 'Comparison of the drop weight impact performance of sandwich

panels with aluminium honeycomb and titanium alloy micro lattice cores'. *Applied Mechanics and Materials*, 24-25: pp. 413-418.

Hasan, R., Mines, R., Shen, E., Tsopanos, S., Cantwell, W. (2011) 'Comparison on compressive behaviour of aluminium honeycomb and titanium alloy micro lattice blocks'. *Key Engineering Materials*, 462-463: Pp. 213-218.

Hooputra, H., Gese, H., Dell, H., Werner, H. (2004) 'A comprehensive failure model for crashworthiness simulation of aluminium extrusions'. *International Journal of Crashworthiness*, 9(5): 449-463.

Kude, V.P., and Khairnar, R.S. (2004) 'Fabrication of silicon based glass fibres for optimal communication'. *Bulletin of Material Science*, 27(1): 73-77.

Leuders, S., Thone, M., Riemer, A., Niendorf, T., Troster, T., Richard, H.A., Maier, H.J. (in press – corrected proof, November 2012) 'On the mechanical behaviour of titanium alloy TiAl6V4 manufactured by selective laser melting: Fatigue resistance and crack growth performance'. *International Journal of Fatigue*,

http://dx.doi.org.ezproxy.liv.ac.uk/10.1016/j.ijfatigue.2012.11.011

McKown, S., Cantwell, W.J., Brooks, W.K., Mines, R.A.W., Tsopanos, S., Sutcliffe, C.J. (2007) 'High performance sandwich structures with hierarchical lattice cores'. *Proceedings of the 28th International European SAMPE*, Europe. 396-401.

McKown, S., Shen, Y., Brooks, W.K., Sutcliffe, C.J., Cantwell, W.J., Langdon, G.S., Nurick, G.N., Theobald, M.D. (2008) 'The quasi-static and blast loading response of lattice structures'. *International Journal of Impact Engineering*, 35: 795-810.

Mines, R.A.W., Worrall, C.M., Gibson, A.G. (1998) 'Low velocity perforation behaviour of polymer composite sandwich panels'. *International Journal of Impact Engineering*, 21(10): 855-879.

Mines, R.A.W., McKown, S., Tsopanos, S., Shen, E., Cantwell, W., Brooks, W., Sutcliffe, C. (2008) 'Local effects during indentationh of fully supported

sandwich panels with micro lattice cores'. *Applied Mechanics and Materials*, 13-14: 85-90.

Mines, R., Girard, Y., Fascio, V. (2009) 'On the development of conventional and micro lattice cellular metals as core materials in aerospace sandwich construction'. *Proceedings of the International European SAMPE*, Europe, pp. 248-256.

Rehme, O. (2010) *Cellular Design for Laser Freeform Fabrication*. Cuvillier Verlag, Gottingen.

Simonelli, M., Tse, Y.Y., Tuck, C. (2012) 'Further understanding of Ti-6Al-4V selective laser melting using texture analysis', *Proceedings of SFF Symposium*, pp: 480-491, Cockrell School of Engineering, The University of Texas at Austin, USA.

Shen, Y. (2009) *High performance sandwich structures based on novel metal cores*, PhD Thesis, University of Liverpool, United Kingdom.

Shen, Y., McKown, S., Tsopanos, S., Sutcliffe, C.J., Mines, R.A.W., Cantwell, W.J. (2010) 'The mechanical properties of sandwich structures based on metal lattice architectures'. *Journal of Sandwich Structures and Materials*, 12: 159-180.

Song, B., Dong, S., Zhang, B., Liao, H., Coddet, C. (2012) 'Effects of processing parameters on microstructure and mechanical property of selective laser melted Ti6Al4V'. *Materials & Design*, 35: 120-125.

Sutcliffe, C. (n.d) *Standard Operating Procedure for SLM250*, University of Liverpool, Doc. No. SOP01B.

Tsopanos, S. (2008) *Micro heat exchangers by selective laser melting*, PhD Thesis, University of Liverpool, United Kingdom.

Tsopanos, S., Mines, R.A.W., McKown, S., Shen, Y., Cantwell, W.J., Brooks, W., Sutcliffe, C.J. (2010) 'The influence of processing parameters on the mechanical properties of selectively laser melted stainless steel microlattice

structures'. *Journal of Manufacturing Science and Engineering*, 132: 041011-1 - 140111-12.

Ushijima, K., Cantwell, W.J., Mines, R.A.W., Tsopanos, S., Smith, M. (2011) 'An investigation into the compressive properties of stainless steel micro-lattice structures'. *Journal of Sandwich Structures and Materials*, 13: 303-329.

Vrancken, B., Thijs, L., Kruth, J.P., Humbeeck, J.V. (2012) 'Heat treatment of Ti6Al4V produced by selective laser melting: Microstructure and mechanical properties', *Journal of Alloys and Compounds*, 541: 177-185.

Wierzbicki, T., Bao, Y., Lee, Y.W., Bai, Y. (2005) 'Calibration and evaluation of seven fracture models'. *International Journal of Mechanical Sciences*, 47: 719-743.

Yadroitsev, I. (2009) *Selective laser melting – Direct manufacturing of 3D-objects by selective laser melting of metal powders*, Lambert Academic Publishing, Germany.

Yasa, E., Deckers, J., Kruth, J.P. (2011) 'The investigation of the influence of laser re-melting on density, surface quality and microstructure of selective laser melting parts'. *Rapid Prototyping Journal*, Vol. 17(5): 312 – 327.

CHAPTER 4: SIMULATION ANALYSIS OF BCC UNIT CELL MICRO-LATTICE STRUCTURE

4.1 INTRODUCTION

Mines et al. (2007) mentioned that a feature of the stiffness and progressive collapse of the micro-lattice structures is their multiple modes of failure, embracing elastic buckling, plastic buckling, plastic collapse, and tensile rupture. These modes of failure depend on the micro-lattice architecture, mechanical properties of the parent material and mode of loading. In a theoretical analysis of the prediction of the initial stiffness and plastic collapse strength of the SLM stainless steel BCC micro-lattice blocks under compressive loading, Ushijima et al. (2011) focussed on a single mode of failure, which was the plastic hinge collapse near the BCC nodes.

In the current study, this chapter aims to quantify the effects of the parent material properties in the collapse of the micro-lattice structures. The plastic flow and failure of the struts within the SLM Ti-6Al-4V BBC unit cells were investigated for both the as-received and heat-treated materials. The unit cell size that was considered in this study was 2.5 mm. For comparison, the best possible performance of the BCC unit cell is quantified using the standard properties of the titanium alloy material [Boyer et al. (1994)].

A simulation analysis of the deformation behaviour of the SLM Ti-6Al-4V BCC micro-lattice unit cells was carried out in order to further understand the progressive collapse and failure mechanism of the material. Mechanical and rupture properties of the single struts analyses from Chapter 2, as well as micro-lattice blocks response and failure studies from Chapter 3 were used as input and comparison in failure prediction of the BCC unit cell under compressive loading. It was reported in the previous chapters that fracture surfaces with ductile dimples were observed for the

failed SLM Ti-6Al-4V micro-struts, therefore, the material was considered to have failed due to ductile mechanism despite the low failure strains.

In this chapter, the simulation analysis was done for the BCC unit cell micro-lattice structure using the Abaqus/CAE 6.10 and Abaqus/CAE 6.11 software. The quasi-static finite element (FE) model of the SLM Ti-6Al-4V BCC unit cell was based on a validated model of the SLM stainless steel BCC unit cell by Smith (2012). The explanations for the model developments (sections 4.3 and 4.4) were mostly referenced from Smith (2012). The Abaqus/Standard was used since only static analysis was conducted in this study.

4.2 REALITY VERSUS VIRTUAL CONDITIONS

The difference in mechanical properties of both the as-received and heat-treated SLM Ti-6Al-4V BCC micro-lattice materials was the main consideration in this study as this was considered to be the key in quantifying the effects of the parent material properties to the collapse of the micro-lattice structures. This was thoroughly discussed in both Chapter 2 and Chapter 3. An important finding for the parent material is the improvements in geometry and other mechanical properties, as the result of the application of heat-treatment process. The heat-treatment was shown to improve the surface variations and some imperfections of the SLM manufactured struts due to the manufacturing mechanism and build angle arrangements; thus leading to the improvement in the mechanical properties of the materials.

As mentioned in Chapter 3, the selectively laser melted BCC micro-lattice blocks with nominal dimensions of 20 mm cubed were compressed at a displacement rate of 0.25mm/min in an Instron 4024 universal test machine using flat platens. The load was measured using a load cell and the platen displacement was measured using a clip gauge. Stress was expressed as load over original area and strain was expressed as platen displacement over original block length. These measurements assume no

block expansion during the compression and that the elastic strain is constant. It was observed that failure occurred at low strains for both the as-received and heat-treated SLM Ti-6Al-4V BCC micro-lattice blocks. However, a more progressive manner of failure was observed in the heat-treated SLM Ti-6Al-4V BCC micro-lattice blocks. Figure 4.1(a) to (d) show the block failure modes of both the as-received and heat-treated blocks. It should be noted that the as-received block failed in an abrupt manner, thus the failure condition could not be captured at the machine platens manually.

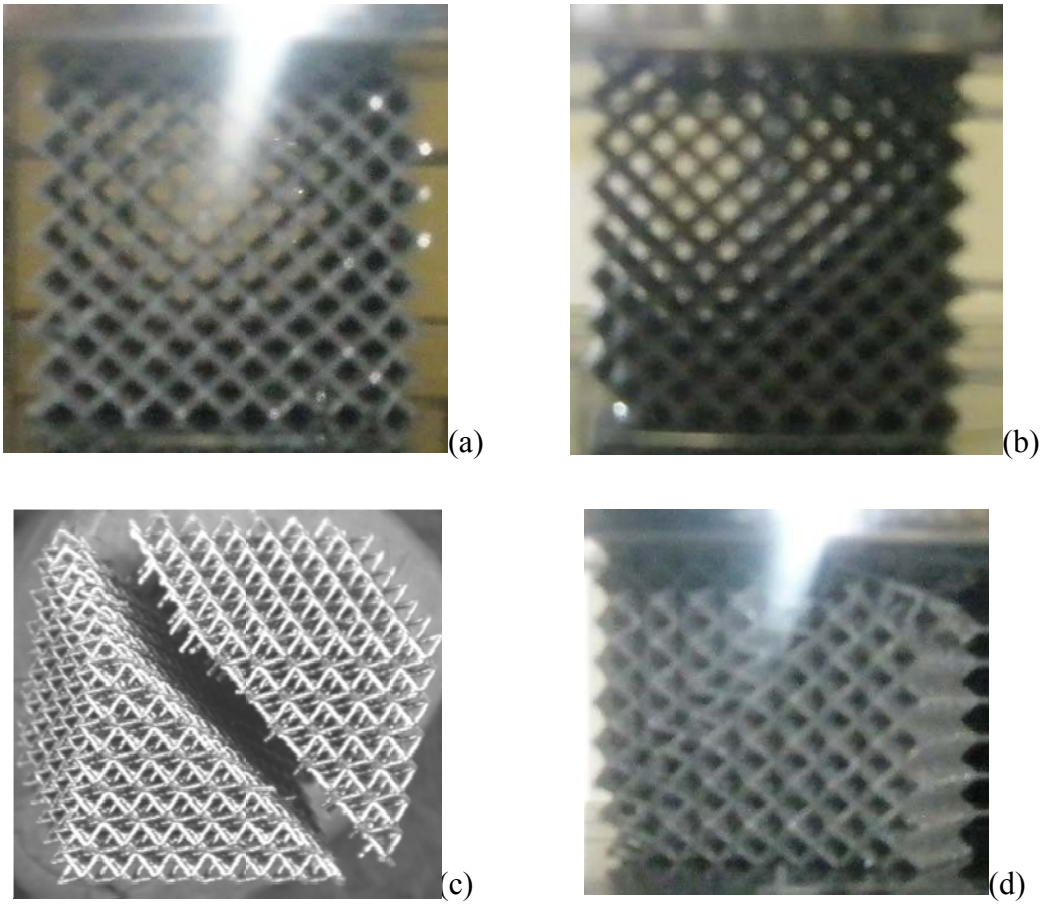

Figure 4.1: The collapse of SLM Ti-6Al-4V micro-lattice structures; (a) As-received block prior to failure (~0.08 strain) [B1-160-1000-AR]; (b) Heat-treated block prior to failure (~0.08 strain) [B1-160-1000-HT]; (c) The failed as-received block; (d) The failed heat-treated block (>0.082 strain)

In this chapter, the discussion involves the unit cells with 2.5 mm size, in the unconstrained BCC micro-lattice blocks. It was based on a validated model of the SLM stainless steel BCC unit cell by Smith (2012). Similar to studies by Ushijima et al. (2011), it is assumed that the plastic hinge forms near the nodes, and the central portion of the struts is dominated by an elastic deformation and that the unit cell is free to expand. In this way, the individual struts rotate in a vertical plane, and no lateral (3D) deformation occurs. As far as the SLM Ti-6Al-4V unit cell is concerned, abrupt failure behaviour is observed for the as-received material, as shown in Figure 4.1(c). This could be the effect of the residue elements and geometrical imperfections in the manufactured material (discussed in Chapter 2) and indicates some kind of instability, but the heat-treatment was shown to mitigate this effect and a more progressive behaviour can be observed in Figure 4.1(d).

To summarize, the failure mode given by the stainless steel BCC unconstrained block with unit cell size 2.5 mm as shown in Figure 4.2 is modelled in this study, based on works by Smith (2012). As pointed out by Ushijima et al. (2011), other strut's failure modes could occur for different cell sizes and block boundary conditions. For the abrupt collapse of the Ti-6Al-4V micro-lattice, the equivalent plastic strain determined from the single strut study in Chapter 2 of this work will be used, and failure will be interrogated from the FE results in order to compare with the block compression failure.

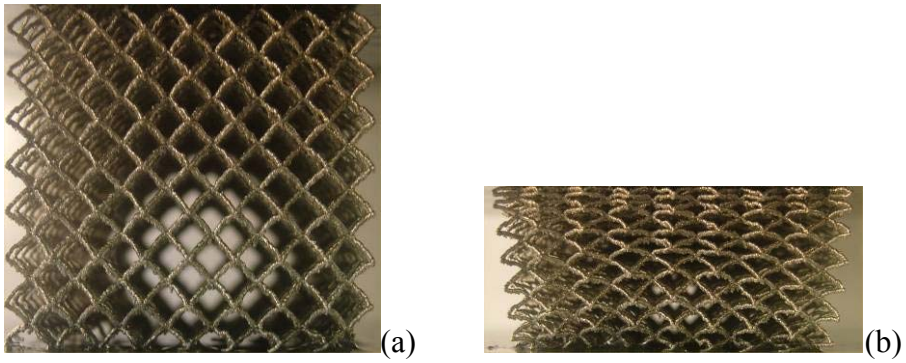

Figure 4.2: The SLM stainless steel BCC unconstrained block with 2.5 mm unit cell size; (a) at 0% crush; (b) at 50% crush [adapted from Shen (2009)]

4.3 CONSTITUTIVE MODEL FOR ELASTO-PLASTIC MATERIAL

In spite of low fracture strains, the fracture surfaces of the SLM Ti-6Al-4V BCC micro-lattice blocks showed ductile dimples which indicated that the material failed due to ductile mechanism. Therefore, an isotropic elasto-plastic model was chosen for the finite element modelling of the material. The model is commonly used for metal plasticity calculations, either as a rate-dependant or as a rate-independent model, and has a particularly simple form [Abaqus Theory Manual (2009)].

4.3.1 Isotropic Elasticity

A linear elastic model was used to describe the elastic response of the material in the FE models. A linear elastic material model is valid for small elastic strains (normally less than 5%); can be isotropic, orthotropic, or fully anisotropic; and can have properties that depend on temperature and other field variables.

To model the elastic response of the lattice structures, an isotropic, temperature independent model was used. For materials that exhibit a linear elastic material behaviour, the total stress is defined from the total elastic strain as,

$$\sigma = D^{el}\varepsilon^{el} \qquad [4.1]$$

Where σ is the total stress, D^{el} is the fourth order elasticity tensor and ε^{el} is the total elastic strain [Abaqus Analysis User's Manual (2010)].

For isotropic linear elasticity, the stress-strain relationship is given by,

$$\begin{Bmatrix} \varepsilon_{11} \\ \varepsilon_{22} \\ \varepsilon_{33} \\ \gamma_{12} \\ \gamma_{13} \\ \gamma_{23} \end{Bmatrix} = \begin{bmatrix} 1/E & -v/E & -v/E & 0 & 0 & 0 \\ -v/E & 1/E & -v/E & 0 & 0 & 0 \\ -v/E & -v/E & 1/E & 0 & 0 & 0 \\ 0 & 0 & 0 & 1/G & 0 & 0 \\ 0 & 0 & 0 & 0 & 1/G & 0 \\ 0 & 0 & 0 & 0 & 0 & 1/G \end{bmatrix} \begin{Bmatrix} \sigma_{11} \\ \sigma_{22} \\ \sigma_{33} \\ \sigma_{12} \\ \sigma_{13} \\ \sigma_{23} \end{Bmatrix} \quad [4.2]$$

Here, the elastic properties are defined by the Young's modulus, E, and the Poisson's ratio, v, of the material. The shear modulus, G, can be expressed in terms of E and v as,

$$G = E/2(1 + v) \quad [4.3]$$

To ensure stability in the model, the material properties must fall within certain limits. The stability criterion requires that $E > 0$, $G > 0$ and $-1 > v > 0.5$.

The elastic material properties used in the FE models are presented in Section 4.4.6. In Abaqus, the keyword for elasticity is *ELASTIC as shown in the input file in Appendix 4A.

4.3.2 Plasticity

To model the plastic response of the lattice structures, a classical isotropic metal plasticity model was used. The classical metal plasticity models use Mises or Hill yield surfaces with associated plastic flow, which allow for isotropic and anisotropic yield, respectively. The models use perfect plasticity or isotropic hardening behaviour, and can be used when rate-dependent effects are important. The classical metal plasticity models are intended for applications such as crash analyses, metal forming, and general collapse studies. In Abaqus, the keyword for plasticity is *PLASTIC as shown in the input file in Appendix 4A.

4.3.3 Yield

The Mises yield surface was used to define isotropic yielding. This is defined by the value of the uniaxial yield stress as a function of the uniaxial equivalent plastic strain. The Mises yield surface assumes that yielding of the metal is independent of the equivalent pressure stress; and this observation is confirmed experimentally for most metals (except metal foams) under positive pressure stress [Abaqus Analysis User's Manual (2010)].

4.3.4 Strain Hardening

Isotropic hardening was used to describe the post-yield behaviour of the material in the lattice structures. An isotropic material has a yield surface that increases in size uniformly in all directions, such that as plastic strain occurs, the yield stress increases in all of the stress directions. To define isotropic hardening, the yield stress, σ^0, is given in tabular form as a function of the plastic strain. The yield stress at any strain state is then interpolated from the data table, and it remains constant for plastic strains exceeding the last value given in tabular data.

Decomposition of the total increment of strain is:

$$d\varepsilon = d\varepsilon^{el} + d\varepsilon^{pl} \qquad [4.4]$$

For a rate-dependent material, the strain rate relationship, $\acute{\varepsilon}^{pl}$ follows the uniaxial flow rate definition, that is:

$$\acute{\varepsilon}^{pl} = h(q, \varepsilon^{pl}, \theta) \qquad [4.5]$$

Where h is a known function, q is the von-Mises equivalent stress, ε^{pl} is an equivalent plastic strain and θ is the temperature.

The plastic material properties used in the FE models were extracted from curves presented in Figure 4.6 of Section 4.4.6.

4.3.5 Nonlinear Structural Analysis

A linear analysis infers a linear relationship between the applied loads and the response of the system. Linear analysis is a convenient approximation that is often adequate for simple design purposes. A nonlinear structural problem is one in which the structure's stiffness changes as it deforms. In reality, all physical structures are nonlinear and therefore linear analysis is often inadequate for many structural simulations. There are three sources of non-linearity that are included in the FE models in this study; material nonlinearity, boundary non-linearity, and geometric non-linearity.

Most materials exhibit a linear stress-strain relationship at low levels of strain but as the strain increases, the material yields, at which point the response becomes nonlinear. Material nonlinearity can also be related to factors other than strain. Strain-rate dependency, temperature and material failure are also forms of material nonlinearity. Boundary nonlinearity occurs if the boundary conditions change during the analysis. This type of nonlinearity is common in analysis involving contact. Boundary nonlinearities are extremely discontinuous; and when contact occurs during a simulation, there is a large and instantaneous change in the response of the structure. Geometric nonlinearity occurs when there are changes in geometry during the analysis, which affect the response of the structure. This can be caused by large deflections or rotations, pre-stress within a structure and 'snap-through' effects.

4.3.6 Failure Criterion

Ductile criterion was referred in failure prediction of the material. As explained in Chapter 1, the ductile criterion is a phenomenological model for predicting the onset of damage due to nucleation, growth and coalescence of voids. In Abaqus, the ductile criterion was based on studies reported in Hooputra et al. (2004). The plastic strain based parameter that was derived in the studies was from the application of initial imperfection which was assumed to be triggering the instability and forming a localised necking; the main mechanism that was leading to fracture in ductile sheet metals.

In this study, the ductile criterion was manually applied in conjunction with the Mises yield surfaces which was defined by the value of the uniaxial yield stress as a function of the uniaxial equivalent plastic strain. The relations between the equivalent yield stress and the equivalent plastic strain were derived in Equation [2.30] and [2.31] of Chapter 2. Using the determined equivalent plastic strain, failure will be interrogated from the FE results and compared with the block compression failure in Chapter 3.

4.4 QUASI-STATIC FINITE ELEMENT MODELS OF BCC UNIT CELLS

This section presents details of the finite elements simulation procedures to model the BCC unit cells under the quasi-static compressive loading. The stainless steel SS316L BCC unit cell model which was developed and validated by Smith (2012) was adapted in this study, but modifications in geometry and material properties were done to suit with the titanium alloy Ti-6Al-4V BCC unit cells. Table 4.1 listed the finite element models in this study.

Table 4.1: The finite element models for BCC unit cells in this study

Model ID	Type	Remarks
Model A	SS316L – 195 μm strut diameter	Developed and validated by Smith (2012)
Model B	As-received Ti-6Al-4V – 380 μm strut diameter	Geometry and material properties were different from Model A
Model C	Heat-treated Ti-6Al-4V – 380 μm strut diameter	Material properties were different from Model B
Model D	Best performance Ti-6Al-4V – 380 μm strut diameter	Standard material properties [Boyer et al. (1994)]

Three-dimensional quasi-static simulations were performed using the ABAQUS/standard software package [Abaqus Analysis User's Manual (2010)]. Eight-node continuum (3D brick) elements were used to capture both the unit cell geometry and the stress-strain distribution within the struts. The models aim to describe the progressive collapse of the SLM Ti-6Al-4V BCC unit cell micro-lattice structures under compressive loads.

4.4.1 Model Geometry

Individual unit cells meshed with 3D brick elements were modelled using an idealised structural geometry, in which the struts have a constant diameter and are assumed to be perfectly straight. Unit cells with size of 2.5 mm and BCC topology were modelled. Model B, C and D were geometrically modified from Model A, where the diameters were increased to 380 µm as shown in Figure 4.3. The 380 µm diameter size was chosen to represent the Ti-6Al-4V strut diameter and it was within the range of average strut diameters estimated in Chapter 2 and 3. With the same element size, the total elements of Model B, C and D (380 µm diameter) were increased to 24640 elements compared to 5760 elements of Model A (195 µm diameter). Table 4.2 presents the key properties of the FE models in this study.

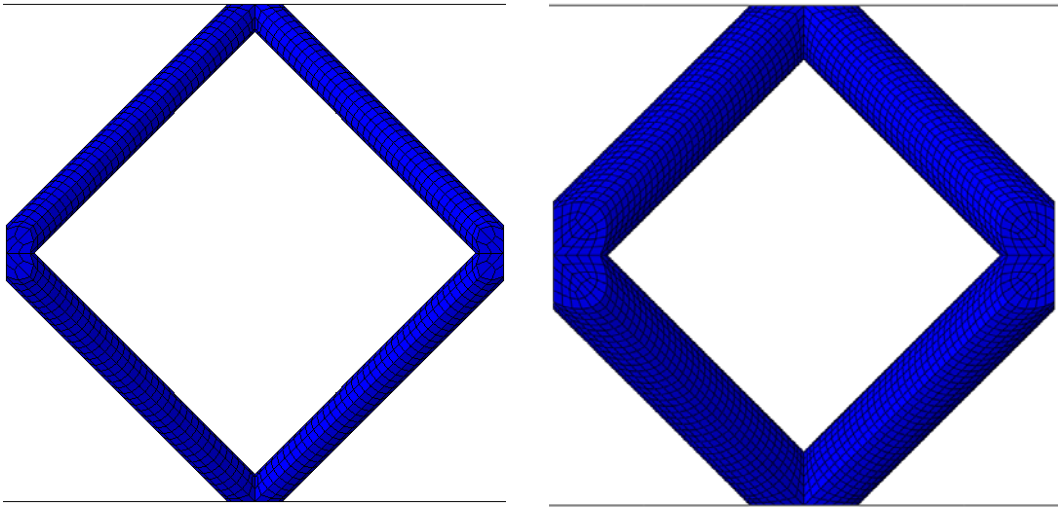

(a) (b)

Figure 4.3: (a) BCC unit cell with 195 µm strut diameter (Model A); (b) modified BCC unit cell with 380 µm strut diameter (Model B, C and D)

Table 4.2: Key properties of the BCC unit cell FE models

Model ID	E (GPa)	σ_y (MPa)	Source of properties	Strut diameter (mm)	Cell size (mm)	Average element size (mm)	Number of elements
Model A	140 (SS316L)	144	Tsopanos et al. (2010)	0.195	2.5	0.05	5760
Model B	45 (Ti-6Al-4V)	245	Chapter 2	0.380	2.5	0.05	24640
Model C	65 (Ti-6Al-4V)	340	Chapter 2	0.380	2.5	0.05	24640
Model D	114 (Ti-6Al-4V)	880	Boyer et al. (1994)	0.380	2.5	0.05	24640

In the Abaqus software, the 3D BCC unit cell structures were created by drawing an inclined circular cross-section strut. The pattern function was used to create four inclined struts, forming half of the unit cell. This was then reflected along a horizontal plane and the two components were merged together to create a complete unit cell. The 3D geometry was partitioned, reducing the unit cell into simple shapes, thereby allowing a regular mesh to be generated without excessively warped elements [Smith (2012)].

For computational efficiency, the compression platens used in the compression tests were represented by rigid plates. The rigid plate does not undergo any deformation during the analysis as expected, but can undergo large rigid body motions.

4.4.2 Model Assembly, Loading and Boundary Conditions

The unit cells and rigid plates were arranged in the assembly shown in Figure 4.4(a). A displacement boundary condition was applied to progressively crush the unit cells, which was assigned to the reference point, placed at the centre of the upper rigid plate, and this was set to move the plate down in the vertical direction at a constant rate. The reference point was used to record the displacement and reaction force from the unit cell. This was converted to engineering stress-strain data using the dimensions of the unit cell. The upper plate displacement for Model A was -2.2 mm, while for Model B, C and D, the plate displacement was reduced to -1.5 mm due to less space between the struts. Boundary conditions were applied to the edges of the 3D brick unit cell in order to account for the constraint applied by the surrounding unit cells. Figure 4.4(b) shows the boundary conditions used to model the six nodal regions where two or more struts meet. The presence of surrounding unit cells was accounted for by ensuring that the faces, at the edge of the unit cell, all remain in the same plane during deformation [Smith (2012)]. More explanations for the boundary conditions and constraints are given in Note for caption of Figure 4.4 at the following page and in the Appendix 4A.

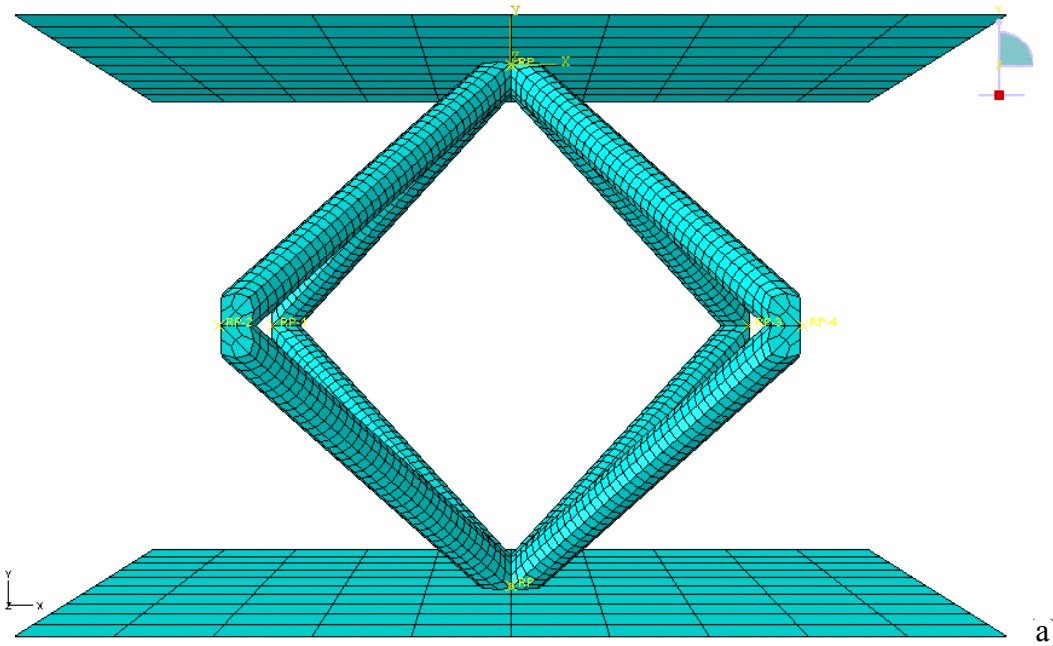

a)

(b)

Figure 4.4: (a) Assembly arrangements for the FE model (Model A); (b) Plot showing the boundary conditions applied to the 3D brick element models (Model A)

Note for caption of Figure 4.4: The upper image(a) is the meshed version of the part in the lower image(b). Green is for meshed and blue is for the unmeshed assembly in Abaqus colour coding. The thin yellow lines at the four corners are the symbols for boundary conditions assigned to the model. The yellow axes lines with written x, y and z are the local coordinate for the model. The yellow font 'RP' stands for reference point, which has been assigned at the four corners of the unit cell.

Constraints have been assigned to the reference points (RPs), in which, the movements of the surfaces are restricted in all planes, but the RPs are allowed to translate only in z direction. Further explanation for the constraint condition is referred to illustration from Ushijima et al. (2011) as shown in Figure 4.5.

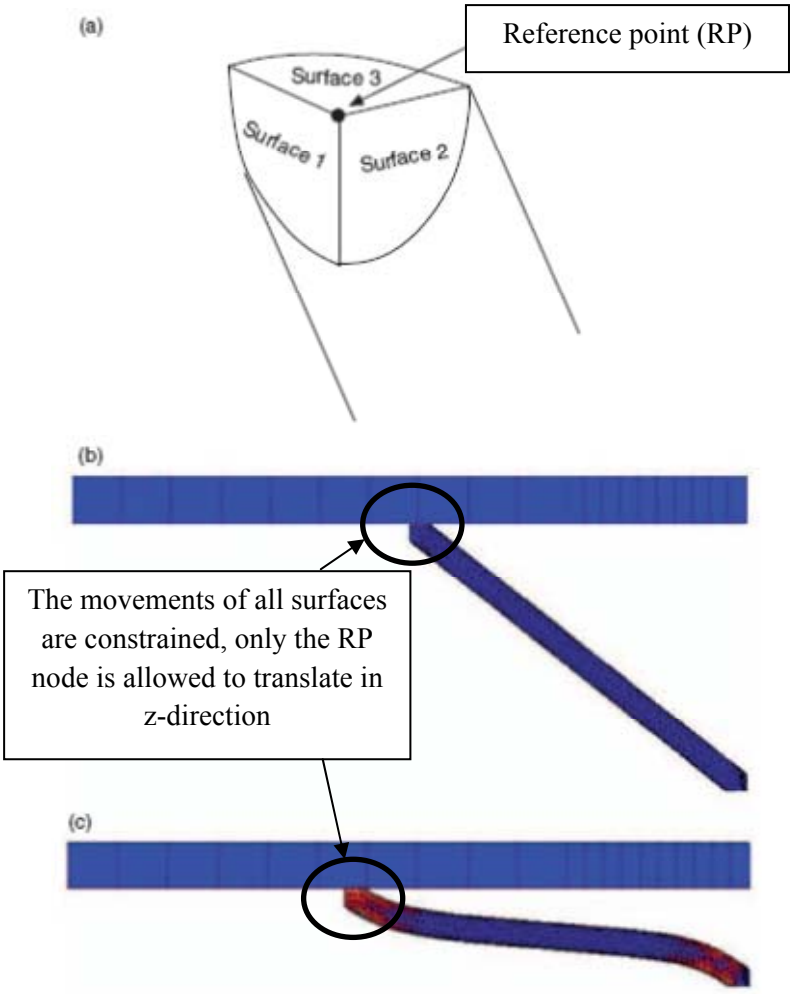

Figure 4.5: One-eighth from the model in Figure 4.4: (a) Micro-strut's constraint condition; (b) undeformed strut; (c) deformed strut for 3D finite element model [adapted from Ushijima et al. (2011)]

Note: When a micro-lattice block is compressed, the movement for each strut is simplified as in the model, due to the boundary conditions given from the neighbouring struts. This unit cell model is only applicable to BCC unconstrained condition of micro-lattice block.

4.4.3 Element Types

The 3D solid element type C3D8R element was used to model the BCC unit cells. This element is the 8-node linear hexahedral (brick), reduced integration with hourglass control. It provides constant volumetric strain throughout the element, which prevents mesh 'locking' when the material response is approximately incompressible. Reduced integration uses a lower-order integration to form the element stiffness and reduces running time. However, hourglassing can be a problem with reduced integration elements since they have only one integration point, and it is possible for them to distort in such a way that the strains calculated at the integration point are all zero which leads to uncontrolled distortion of mesh. This is the reason for including hourglass control, but they should be used with reasonably fine meshes.

Conceptually, these brick elements model small blocks of material in a component. Since they may be connected to other elements on any of their faces, brick elements, like bricks in a building, can be used to build models of virtually any shape, subjected to any loading conditions [Smith (2012)].

4.4.4 Element generation

An element mesh was generated from the model geometry using the meshing tools within the Abaqus software. Total numbers of generated elements were as listed in Table 4.2. Viscoelastic hourglass controls were applied to the 3D brick elements within the mesh to reduce hour-glassing and excessive warping, as mentioned in the earlier section.

4.4.5 Mesh sensitivity

For the BCC unit cells based on 3D brick elements, the study of element size effects in relation to the response of the structure was carried out by Smith (2012), where the importance of mesh sensitivity was shown. In Smith's study, it was concluded that the strain hardening response of the unit cell, along with the plateau stress, Young's modulus, yield and CPU time, were some of the factors that needed to be considered when choosing an appropriate element size as listed in earlier Table 4.2. It was shown by Smith (2012) that the element size of 0.05 which was applied to Model A in this study gave a reasonable result within a considerable time.

4.4.6 Material Properties

As mentioned in the earlier Table 4.2, for Model A, the material properties determined in the study of Tsopanos et al. (2010) were used as the input data. The engineering stress-strain relationship as shown in Figure 4.6(a) was derived using a combination of experimental data and FE analysis. The engineering stress-strain was converted to the true stress-strain curve in order to be used as the input for Model A in Abaqus [Smith (2012)]. For Model B and C, the corrected experimental properties which were the true stress-strain curves for both the as-received and heat-treated SLM Ti-6Al-4V micro-struts as determined in Chapter 2 were applied. The data from curves as described in section 2.4.7 were used as inputs for Model B and C, and shown in Figure 4.6(b) and (c). On the other hand, the input for Model D was taken from the standard properties of Ti-6Al-4V material [Boyer et al. (1994)], for the prediction of the best properties for the micro-lattice structure. In all stages of the analysis, it is important to ensure that the true stress-strain curves are used as the input data for the Abaqus FE models.

As shown in Figure 4.6(b) and (c), the true stress-strain input data for the SLM Ti-6Al-4V micro-struts are continuous curves. In Abaqus, the stress-strain response is

decomposed into two parts and the stress-strain input is considered to be a bilinear curve. The first part is the elastic part which is a linear relation of stress-strain up to yield point, modelled with the *ELASTIC keyword in the input file (Appendix 4A). The second part is the post-yield part which is modelled to follow perfect plasticity behaviour. The growth of plasticity is according to the stress-strain data from *PLASTIC tabular data input, as given in the input file (Appendix 4A). More discussions for the stress-strain input data are generally under section 4.6.1, especially in Figure 4.12, Figure 4.13 and Table 4.7.

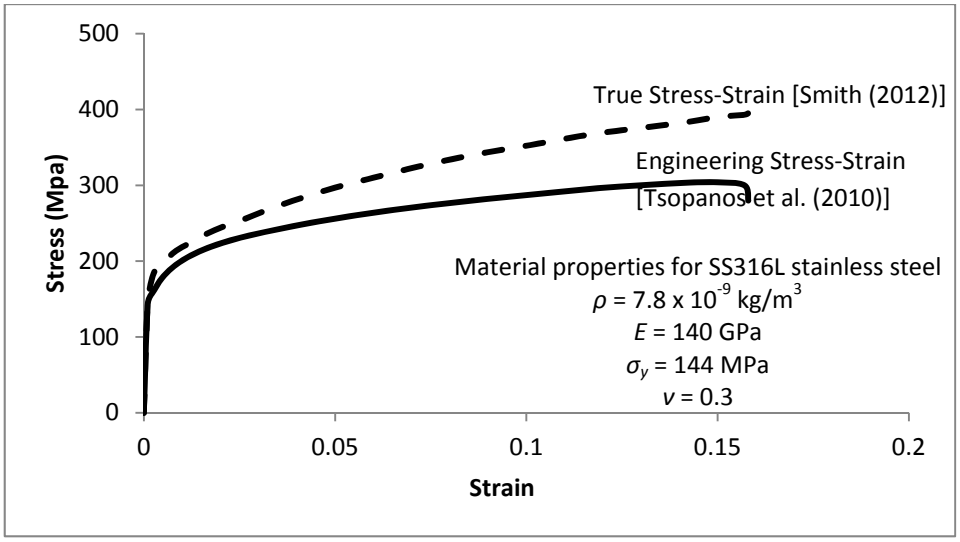

(a)

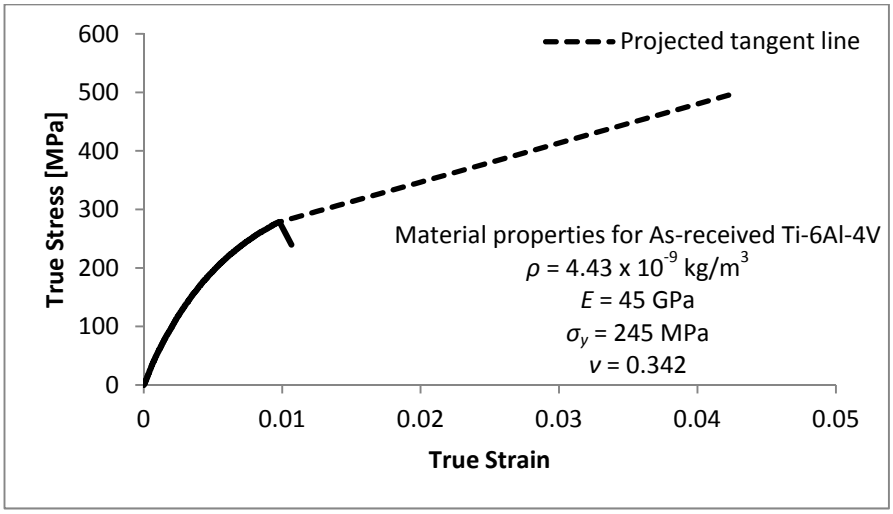

(b)

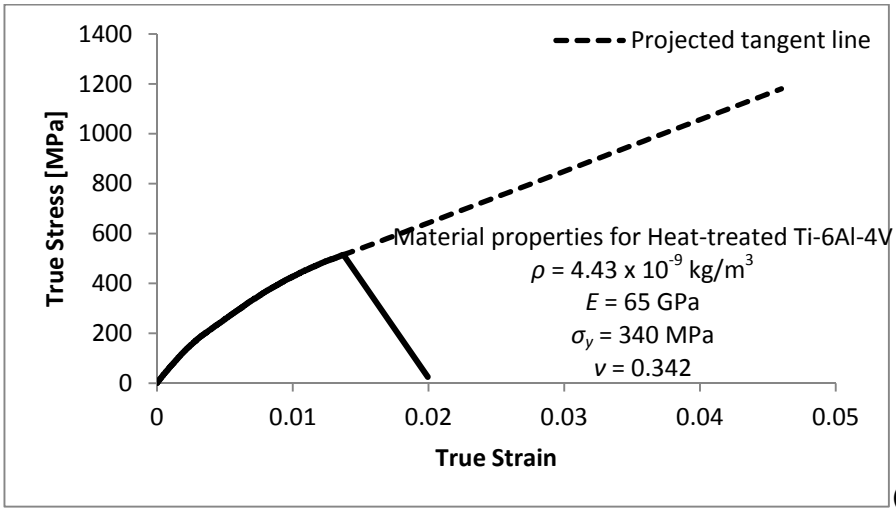

(c)

Figure 4.6: Stress-strain curves of micro-struts for input data of (a) Model A [Tsopanos et al. (2010)]; (b) Model B (Chapter 2); (c) Model C (Chapter 2)

4.4.7 Modelling Interaction

A contact pair algorithm was used for modelling contact in the FE models. The contact pair interaction can refer to a contact interaction property, which defines the tangential behaviour (friction formulation) and the normal behaviour (contact pressure-clearance relationship). The contact properties were set to 'hard' in the normal direction and frictionless in the tangential direction. The hard contact property allows for any contact pressure between two surfaces when the clearance is zero and there is no pressure when the clearance is greater than zero.

Friction between surfaces in contact is modelled in Abaqus using the Coulomb friction model. The model characterises the frictional behaviour between the surfaces using a coefficient of friction. Sliding between the surfaces is zero until the surface traction reaches a critical shear stress value, τ_{crit}, which is defined as:

$$\tau_{crit} = \mu p \qquad [4.6]$$

Where, μ is the coefficient of friction and p is the contact pressure between the two surfaces. A friction coefficient of zero means that the surfaces are frictionless and are free to slide across one another.

4.4.8 Modelling Data Output and Stress-strain Definition for a Unit Cell Model

The output from the FE models is specified by creating output requests. Finite element analyses can create very large amounts of output. Abaqus can control and manage this output so that only data required to interpret the results of the simulation are produced. An output request defines which variables are outputted during the analysis. This data can be outputted from specific regions, integration points or reference points and the rate at which it is recorded can also be defined. There are two types of output requests; field output or history output.

Field outputs are generated from the data that is spatially distributed over the whole model or over regions of the model. The amount of field output during an analysis is often large and therefore a low frequency is recommended for field data to be written to the output database. This data displays images of the structure at each requested interval, for example, displacement or stress and strain distributions as the structure deforms. In the quasi-static models, displacement, stress and strain field outputs were requested for the whole model.

History outputs are used to request the output of variables from the whole model or specific points of the model at high frequency. When creating a history output request, the individual components of the variables can be specified. In this study, the displacement data for the relevant direction for the rigid compression platens and the reaction forces were requested in a history output at the rigid plate reference point [Smith (2012)].

A similar definition of the experimental stress-strain for the micro-lattice blocks was applied to the response of the micro-lattice blocks of the FE models. The stress was expressed as load over original area therefore the reaction force output from the FE model was divided by the cross-sectional area of the BCC unit cell. The strain was calculated as the displacement output over the original length of the BCC unit cell model.

4.5 RESULTS FROM QUASI-STATIC FINITE ELEMENT SIMULATIONS OF MODEL A

Results of Model A, which used the 3D brick elements of BCC unit cell for stainless steel SS316L micro-lattice structure, were validated in the Smith (2012) study. Smith (2012) compared the response of both the 3D brick element and the beam element models with the results from experiments, as shown in Figure 4.7. It was shown that the quasi-static response of the 2.5 mm BCC unit cell structures can be accurately described using finite element modelling with the 3D brick element type. Table 4.3 extracted the key properties of the results. In Figure 4.7, it should be noted that the accuracy of the FE results compared to the experimental results is decreased with the decrease of cell size. Ushijima et al. (2011) mentioned that shear and other effects are becoming important in modelling of micro-lattice structure with small cell size, which was not specifically addressed in the FE models of Smith (2012).

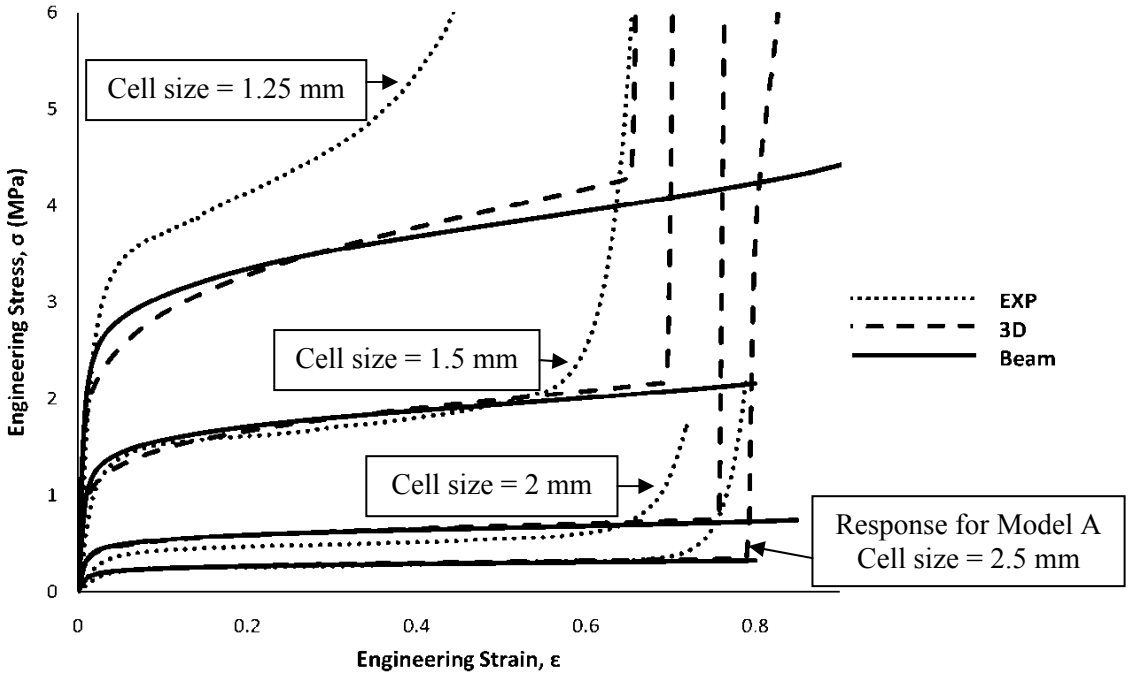

Figure 4.7: Stress-strain curves comparing the experimental and FE results for SS316L BCC unit cells in Smith (2012) study. Response for Model A in the current study is given by the 3D stress-strain curve for the 2.5 mm cell size.

Table 4.3: Key properties of validated Model A from Smith (2012)

Properties	Experiment	FE simulation	% Differences
E (MPa)	10.6	13.0	22.6%
$\sigma_{0.2\%}$ (MPa)	0.16	0.17	6.3%

The collapse of the BCC unit cell corresponds with the FE model is shown in Figure 4.8, which can be seen to compare well with the experimental images. As shown in the figures, the unit cell collapsed due to bending at the end of the struts near the nodes. This indicated that the ends of the struts were the area with the highest stress concentrations under the compressive load.

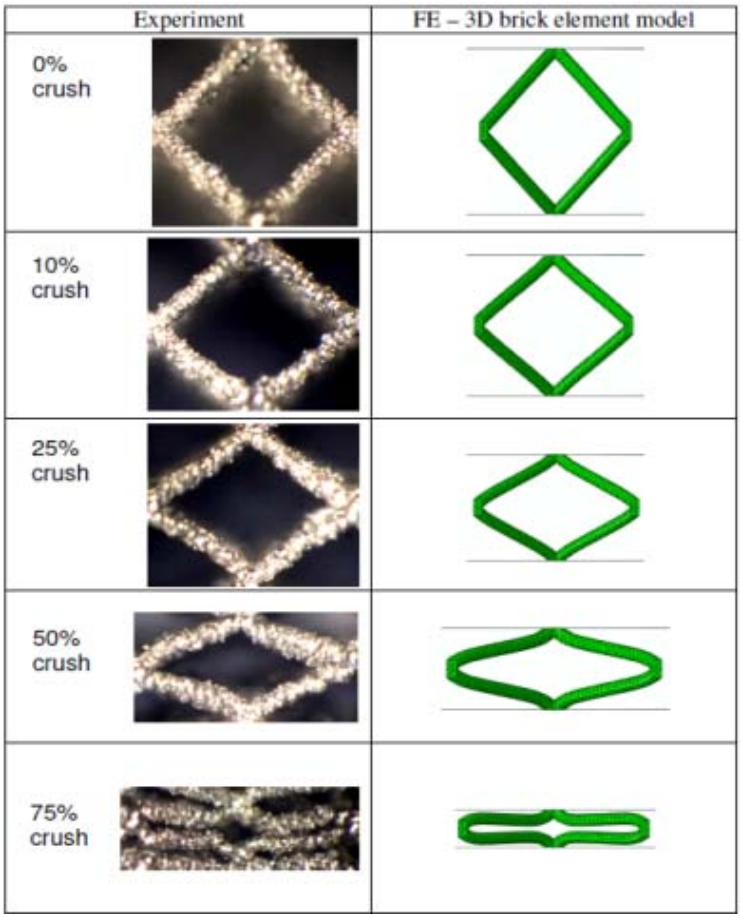

Figure 4.8: The quasi-static crush behaviour of the BCC unit cell at increasing levels of deformation (Model A) [adapted from Smith (2012)]

Figure 4.9 shows the equivalent plastic strains at the corresponding sections of the maximum stressed area (near node area) at 10%, 25%, 50% and 75% crush to show the growth of plasticity in Model A.

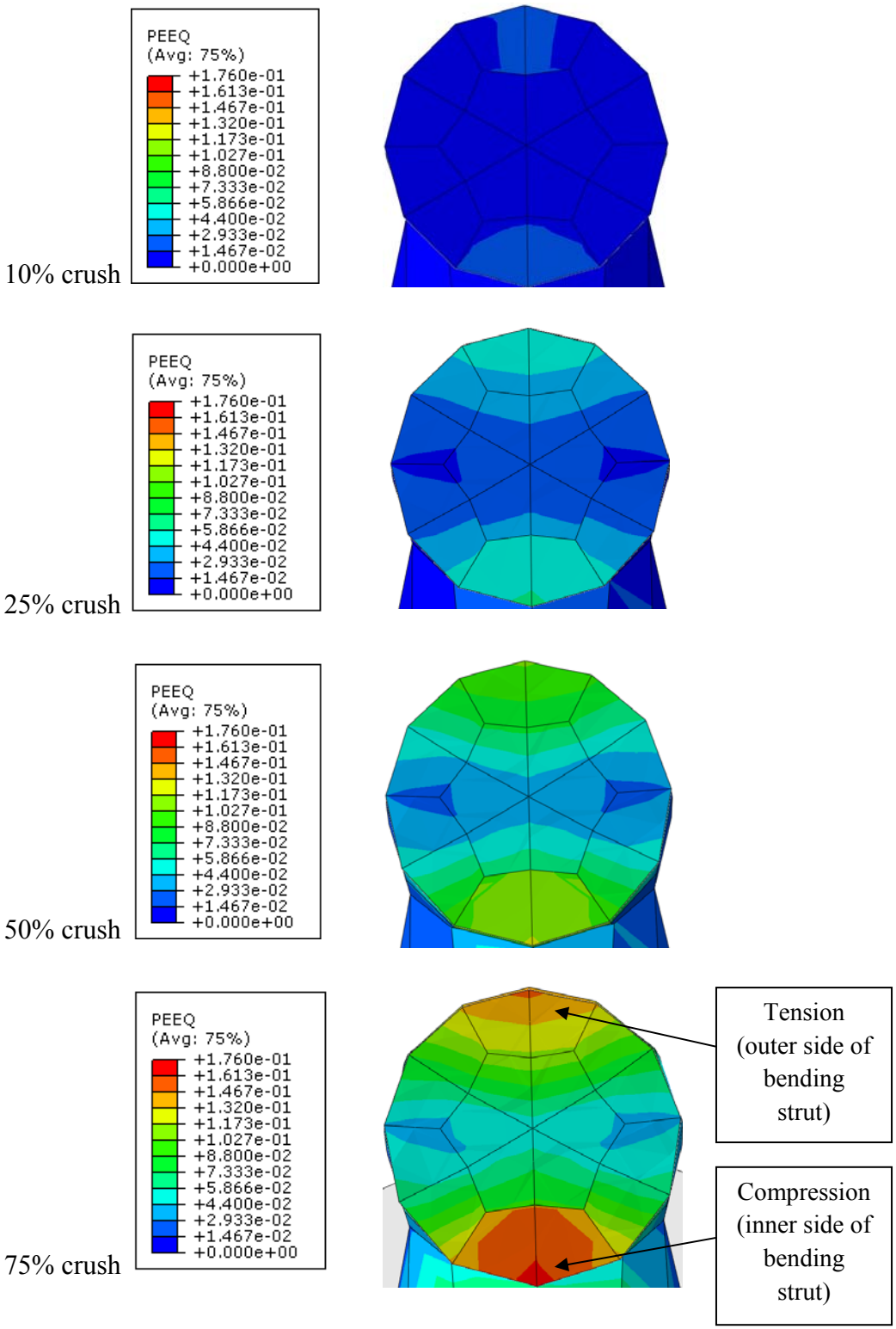

Figure 4.9: Growth of plasticity in Model A

From Figure 4.9, at 75% crush, the strain across the elements can be observed. As discussed in Chapter 3 section 3.4.2, one side of the strut experienced tension while the other side of the strut experienced compression. The values of PEEQ across the strut's cross section are plotted and shown in Figure 4.10. It can be seen that the PEEQ distribution varies almost linearly from the tension side to the compression side of the strut. This distribution matches with strain distribution across a bending beam from the established theory of plasticity [Chakrabarty (2006)].

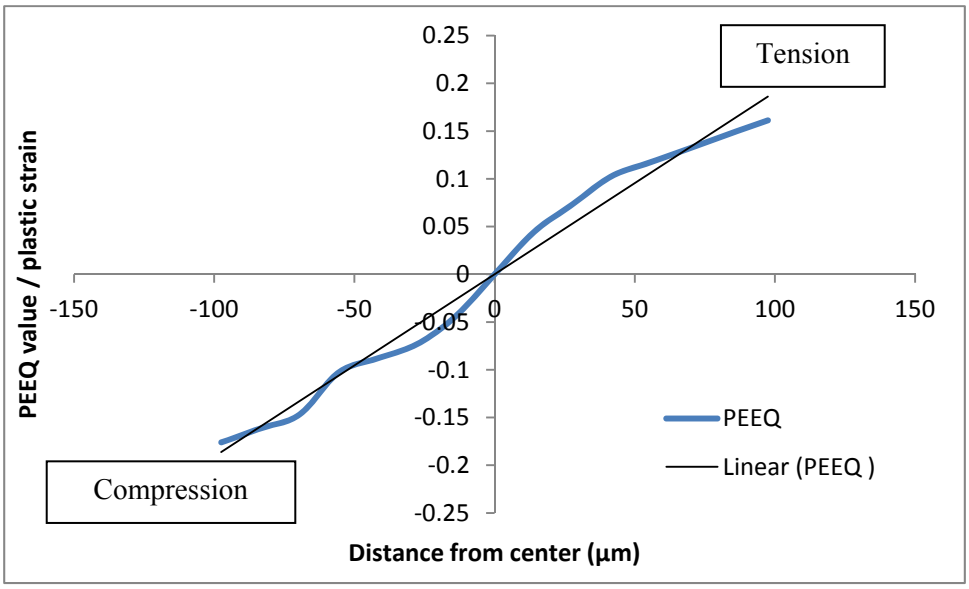

Figure 4.10: Strain distribution across strut of Model A

4.6 RESULTS FROM QUASI-STATIC FINITE ELEMENT SIMULATIONS OF MODEL B AND MODEL C

In this section, results from the FE simulations of Model B and C were compared to the experimental block compression data of the SLM Ti-6Al-4V micro-lattice structures from Chapter 3. Table 4.4 lists the input data from Chapter 2 for both Model B and C, with the respective block compression data from Chapter 3 for comparisons. It should be noted that only single unit cells were modelled in the FE simulations, therefore close comparisons should be done with the BCC cells along the deformed 45° angle planes within the micro-lattice blocks.

Table 4.4: Relations between input data, FE models and comparisons with experimental results of SLM Ti-6Al-4V micro-lattice blocks

Input data from Chapter 2		FE Model		Comparison with results from Chapter 3	
Material	Parameters / strut diameter	Model	Strut diameter	Material	Parameters / strut diameter
As-received single struts [Material ID: S(1-15)-35-200-1000-AR]	200 W x 1000 µs Diameter: (374.14 ± 26.15) µm Single manufactured strut	Model B	380 µm Single unit cell	As-received block [Material ID: B1-200-1000-AR]	200 W x 1000 µs Diameter (estimated): 307 µm 8 x 8 x 8 unit cells
Heat-treated single strut [Material ID: S(1-9)-35-200-1000-HT(B)]	200 W x 1000 µs Diameter: (322.56 ± 16.60) µm Single manufactured strut	Model C	380 µm Single unit cell	Heat-treated block [Material ID: B1-160-1000-HT]	160 W x 1000 µs Diameter: (339.41 ± 17.57) µm 8 x 8 x 7.5 unit cells

4.6.1 Comparisons with Experimental Results

Figure 4.11 shows the comparison of the FE results for Model B and C with the respective experimental results of the as-received and heat-treated SLM Ti-6Al-4V micro-lattice blocks. The experimental curves show that the collapse of the materials occurs after the elastic regions yield and reach the maximum stress values. Since the damage criterion is not applied to the FE models, the predicted stress-strain curves only show the noticeable steep rise in the elastic region followed by a stress plateau without any failure points. In Figure 4.11, plasticity starts at points A due to the yield stress of the materials; while points B represent the ultimate stress from the input curves as shown in Figure 4.12 and 4.13 respectively. From Figure 4.12 and 4.13, it is shown that the plastic input data (*PLASTIC) models the response of the material as linear up to the yield, and the plasticity starts after the yield point onwards. For comparison, in reality, the input curve is continuous.

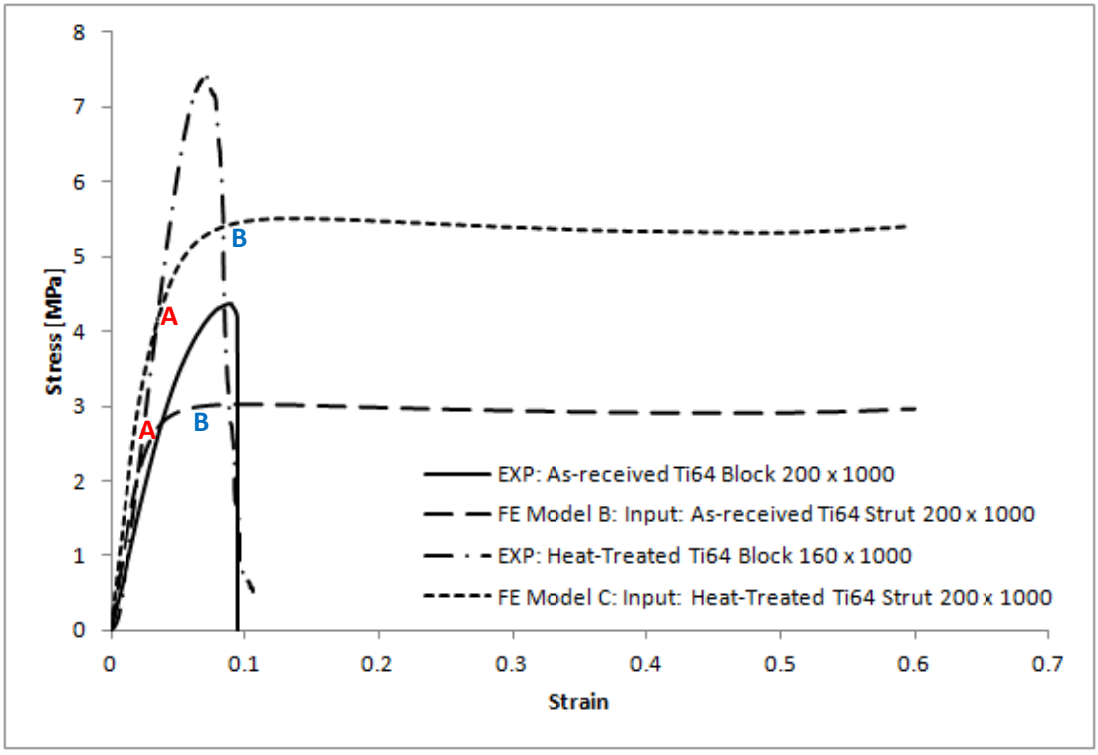

Figure 4.11: Stress-strain curves comparing experimental and FE results for both as-received and heat-treated SLM Ti-6Al-4V BCC micro-lattice structures

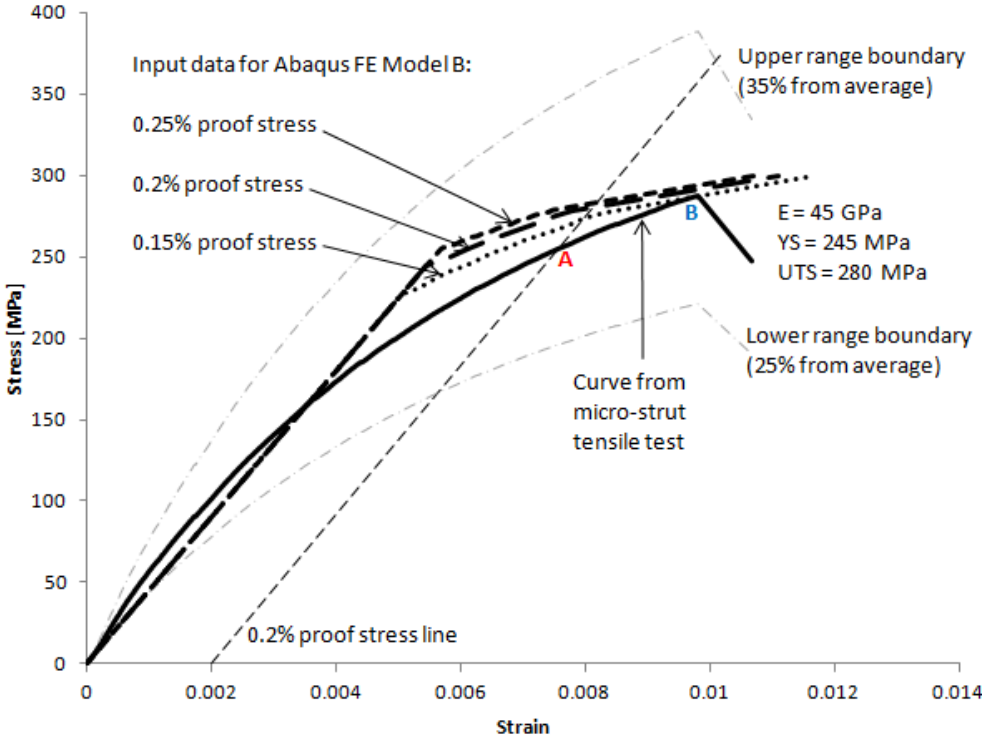

Figure 4.12 (Repetition of Figure 2.38): True stress-strain curve for the as-received SLM Ti-6Al-4V micro-strut with input data for Abaqus Model B

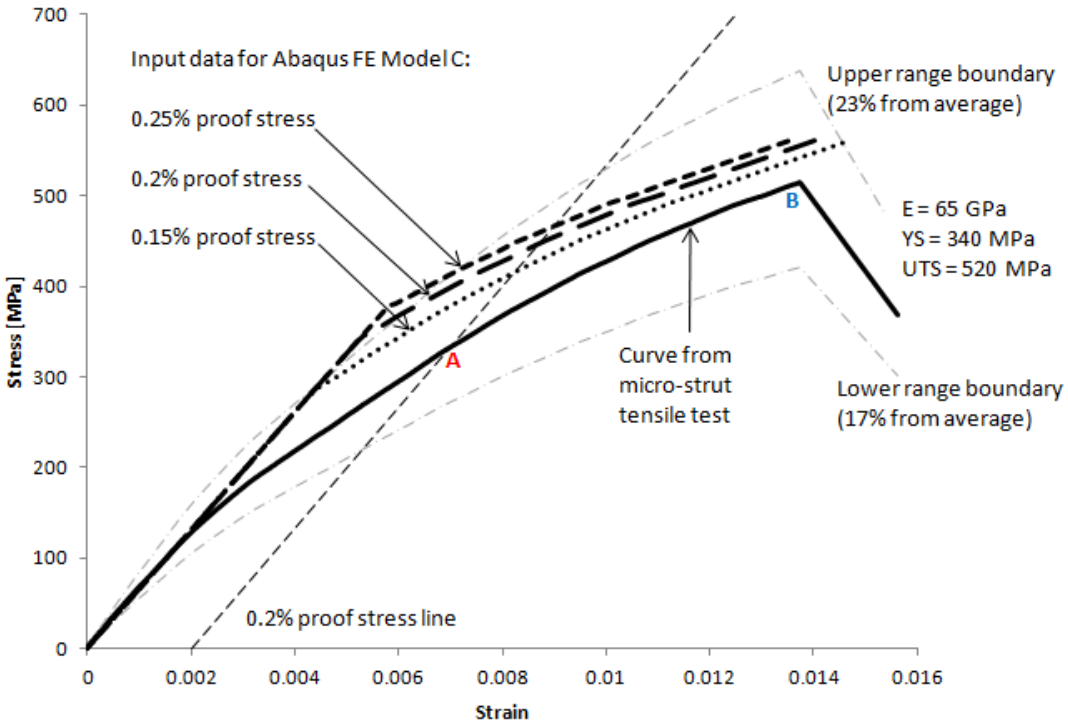

Figure 4.13 (Repetition of Figure 2.40): True stress-strain curve for the heat-treated SLM Ti-6Al-4V micro-strut with input data for Abaqus Model C

Table 4.5: Comparisons of experimental and FE results for SLM Ti-6Al-4V BCC micro-lattice blocks

Properties	Experiment	FE model	% Difference (FE – Exp.)
As-received (AR) material [B1-200-1000-AR] / Model B			
Stiffness	68 MPa	100 MPa	+ 47%
Initial collapse	3.6 MPa	2.7 MPa	- 25%
Final collapse	4.3 MPa	3.0 MPa	- 30%
Heat-treated (HT) material [B1-160-1000-HT] / Model C			
Stiffness	119 MPa	145 MPa	+ 22%
Initial collapse	6.5 MPa	4.4 MPa	- 32%
Final collapse	7.5 MPa	5.5 MPa	- 27%

Table 4.5 lists the differences between the experimental and the FE results. It can be seen that there were noticeable differences between the values of stiffness, initial collapse and final collapse for both the experimental and FE results. This indicates the difficulty in the estimation of the initial material properties which were derived from the tensile test of the micro-struts as been thoroughly discussed in Chapter 2. Since the assigned boundary conditions of the models are considered reasonable for the BCC unit cell (as discussed in section 4.4.2), the factors that contribute to the differences in the results could be the node geometry and strut diameter of the FE models.

As mentioned in section 4.4.1, an idealised structural geometry was used in the 3D brick element models, where the struts are assumed to have a constant diameter and to be perfectly straight. In reality, there are variations in the strut diameter values, which led to the variations in mechanical properties of the SLM manufactured struts, showed by the upper and lower boundaries as in Figure 4.12 and 4.13.

In order to estimate the sensitivity of the diameter variations to the mechanical properties of the SLM Ti-6Al-4V micro-lattice model, the analytically developed equations for the BCC SS316L micro-lattice cell can be applied [Ushijima et al. (2011)]. The stiffness of a BCC unit cell E_{BCC}, and the corresponding plastic collapse strength $\sigma_{pl,BCC}$, are shown in Equation 4.7 and 4.8 respectively. The Young's Modulus of the material is given by E, yield strength is given by σ_0, strut's diameter is given by d, and length of the unit cell is given by L.

$$E_{BCC} = \sqrt{3}\pi E.\frac{(d/L)^2}{1+2(L/d)^2} \quad [4.7]$$

$$\sigma_{pl,BCC} = \frac{4\sqrt{2}d^3\sigma_0}{3L^3} \quad [4.8]$$

Table 4.6: Diameter variations effects to mechanical properties of Ti-6Al-4V blocks

Note: The minimum and maximum diameter values are calculated from ±2σ (σ values are stated in Table 4.4)

As-received (AR) block [B1-200-1000-AR] / Model B						
	Experiment	FE	Theory [Ushijima et al. (2011)]			
Laser parameters	200W x 1000µs	200W x 1000µs	200W x 1000µs			
Diameter [µm]	307 (Table 3.7)	380	380	321.84 (min.)	374.14 (ave.)	426.44 (max.)
				(section 2.4.1)		
E_{BCC} [MPa]	68	100	65	33	61	102
$\sigma_{pl,BCC}$ [MPa]	3.6	2.7	1.6	1.0	1.5	2.3
Heat-treated (HT) block [B1-160-1000-HT] / Model C						
	Experiment	FE	Theory [Ushijima et al. (2011)]			
Laser parameters	160W x 1000µs	200W x 1000µs	200W x 1000µs			
Diameter [µm]	343 (Table 3.7)	380	380	289.36 (min.)	322.56 (ave.)	355.76 (max.)
				(section 2.4.1)		
E_{BCC} [MPa]	119	145	93	32	49	72
$\sigma_{pl,BCC}$ [MPa]	6.5	4.4	2.3	1.0	1.4	1.8

Table 4.6 shows the effects of diameter variations to the mechanical properties of SLM Ti-6Al-4V BCC micro-lattice blocks, from the equations developed theoretically by Ushijima et al. (2011). It is shown that the stiffness E_{BCC} and plastic collapse $\sigma_{pl,BCC}$ values are varied due to the variations of diameter. Even a slight change in diameter will result in different value of mechanical properties. From the table, it can be seen that the theoretical estimation give a good prediction of the stiffness value E_{BCC} for the as-received SLM Ti-6Al-4V micro-lattice blocks. The average diameter gives a result similar to the experimental value while the maximum diameter gives a result similar to that of the FE model. However, the theoretical estimations under predict the plastic collapse $\sigma_{pl,BCC}$ values for the as-received block, and both the stiffness E_{BCC} and plastic collapse $\sigma_{pl,BCC}$ values for the heat-treated block. Figure 4.14 summarizes the stiffness values of the as-received SLM Ti-6Al-4V BCC micro-lattice blocks from the experiment, FE model as well as theoretical predictions from different diameter values.

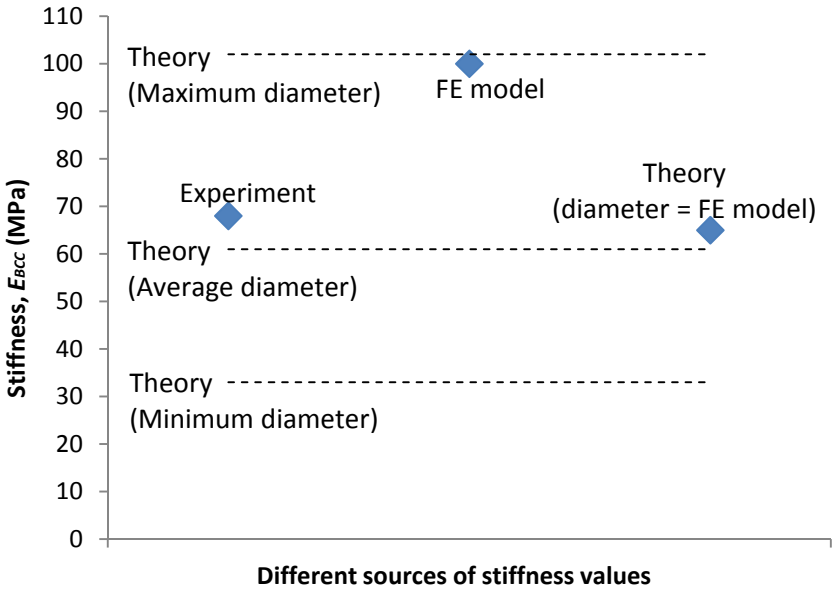

Figure 4.14: Stiffness values of the as-received SLM Ti-6Al-4V BCC micro-lattice blocks from the experiment, FE model and theoretical predictions from different diameter values

Besides the variations of strut diameter values, another factor that is expected to contribute to the differences between the FE and the experimental results is the configuration of the node geometry. Since the struts in the FE model are assumed to have a constant diameter and to be perfectly straight, the nodes are also considered to have straight edges due to the intersections of the struts. In reality, the node edges are not exactly straight and there are accumulations of materials at the node areas due to the melting mechanism of the powder during the SLM process. The extra mass at the node areas could have contributed to the strength of the micro-lattice structure. As shown in Table 4.5, the collapse strength values for the experimental results are higher than that of the FE results by around 30%. Figure 4.15 shows the 45° angle cross-section of the FE model for the BCC unit cell. The node region shows sharp and straight edges, as indicated by the circles. Meanwhile, Figure 4.16 shows the existence of extra mass at the node area of the SLM Ti-6Al-4V BCC micro-lattice block.

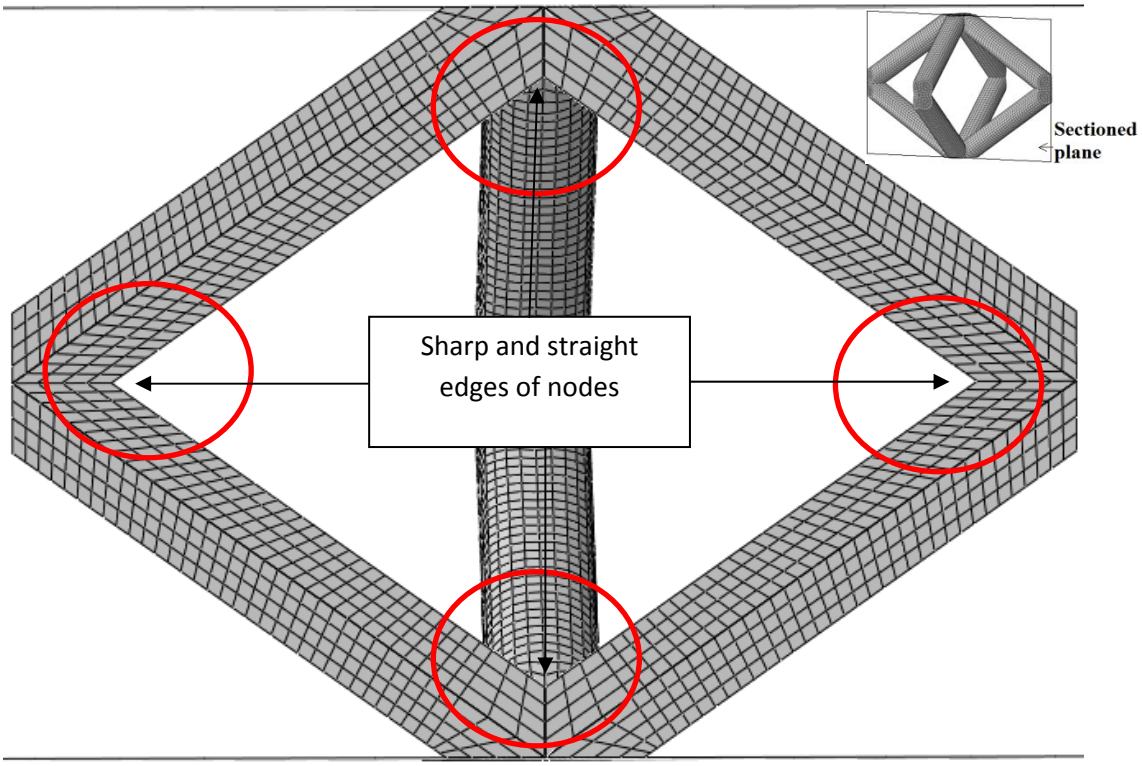

Figure 4.15: The 45° angle cross-section of the FE model for the BCC unit cell (Model B)

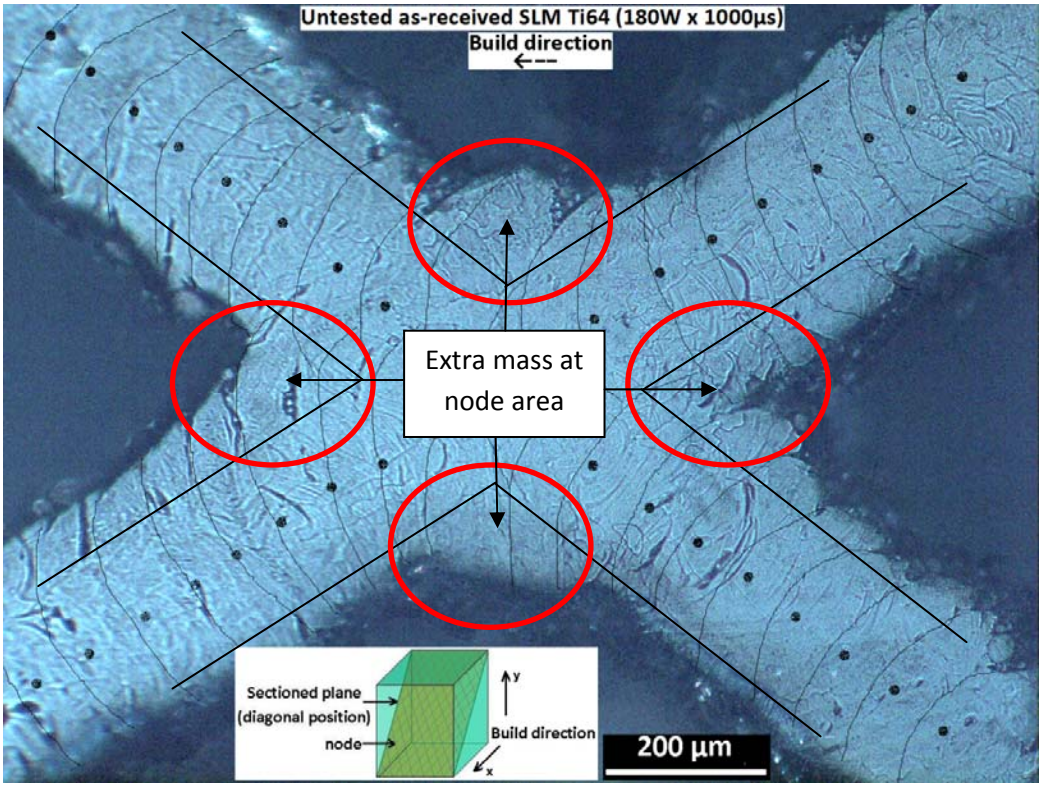

Figure 4.16 (Repetition of Figure 3.9): The existence of extra mass at node area of SLM Ti-6Al-4V BCC micro-lattice block (180 W X 1000 µs) [B1-180-1000-AR-M]

From the comparison of the cross-sections at the node area of the experiment and the FE model, it is suggested that there is an effect of the accumulation of mass at the node area to the strength of the micro-lattice blocks. In future, an additional geometry around the node area could be considered for the FE model representation. From theoretical aspect, the effect of extra fillet material on the stiffness of the micro-lattice structure could be determined using beam deflection analysis by singularity functions [Budynas and Nisbett (2008)].

Other than the geometrical aspects contributions to the differences in results between the experiment and the FE model, the sensitivity of flow stress in the FE input data was also analyzed. The yield stresses of the input data at 0.15% and 0.25% proof stresses were used and compared with the currently defined yield stress at 0.2% proof stress. Table 4.7 shows the FE model input properties for the three different proof stresses.

Table 4.7: FE model input properties for the three different proof stresses

Input for As-received material (FE Model B)		
0.15% proof stress	0.2% proof stress	0.25% proof stress
*Density 4.43e-09, *Elastic 45000., 0.342 *Plastic 225., 0. 229., 0.0002 233., 0.00042 238., 0.00064 242., 0.00087 245., 0.00109 249., 0.00131 253., 0.00153 256., 0.00176 260., 0.00199 263., 0.00223 266., 0.00246 269., 0.00269 273., 0.00292 276., 0.00316 278., 0.0034 300., 0.00666	*Density 4.43e-09, *Elastic 45000., 0.342 *Plastic 245., 0. 250., 0.00038 255., 0.00067 260., 0.00099 265., 0.00137 270., 0.00174 275., 0.00209 278., 0.00235 300., 0.00564	*Density 4.43e-09, *Elastic 45000., 0.342 *Plastic 255., 0. 256., 0.00011 258., 0.00023 260., 0.00034 262., 0.00046 263., 0.00058 265., 0.00069 266., 0.00081 268., 0.00092 269., 0.00104 271., 0.00116 273., 0.00127 274., 0.00139 276., 0.00151 277., 0.00163 278., 0.00175 279., 0.00179 300., 0.00501
Input for Heat-treated material (FE Model C)		
0.15% proof stress	0.2% proof stress	0.25% proof stress
*Density 4.43e-09, *Elastic 65000., 0.342 *Plastic 280., 0. 296., 0.00041 311., 0.00082 327., 0.00123 341., 0.00165 357., 0.00208 371., 0.00249 385., 0.00293 398., 0.00336 411., 0.0038 424., 0.00425 436., 0.0047 449., 0.00515 460., 0.00561 471., 0.00608 482., 0.00655 493., 0.00702 502., 0.00751 515., 0.00812 560., 0.01039	*Density 4.43e-09, *Elastic 65000., 0.342 *Plastic 340., 0. 350., 0.00029 360., 0.00057 370., 0.00086 380., 0.00119 390., 0.00151 400., 0.00183 410., 0.00215 420., 0.00251 430., 0.00289 440., 0.00324 450., 0.00361 460., 0.00402 470., 0.00444 480., 0.00485 490., 0.00527 500., 0.00581 510., 0.00627 514., 0.00648 560., 0.00878	*Density 4.43e-09, *Elastic 65000., 0.342 *Plastic 375., 0. 380., 0.00017 390., 0.00051 400., 0.00082 410., 0.00115 420., 0.00149 429., 0.00182 438., 0.00216 448., 0.00249 456., 0.00284 465., 0.0032 473., 0.00355 481., 0.00389 490., 0.00425 500., 0.00479 504., 0.00497 508., 0.00515 512., 0.00534 515., 0.0055 560., 0.00777

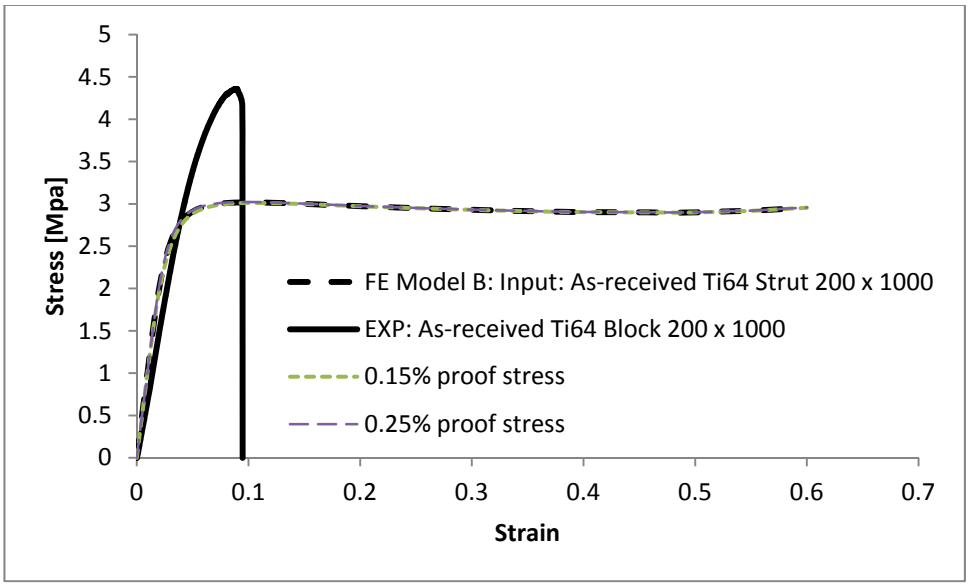

(a)

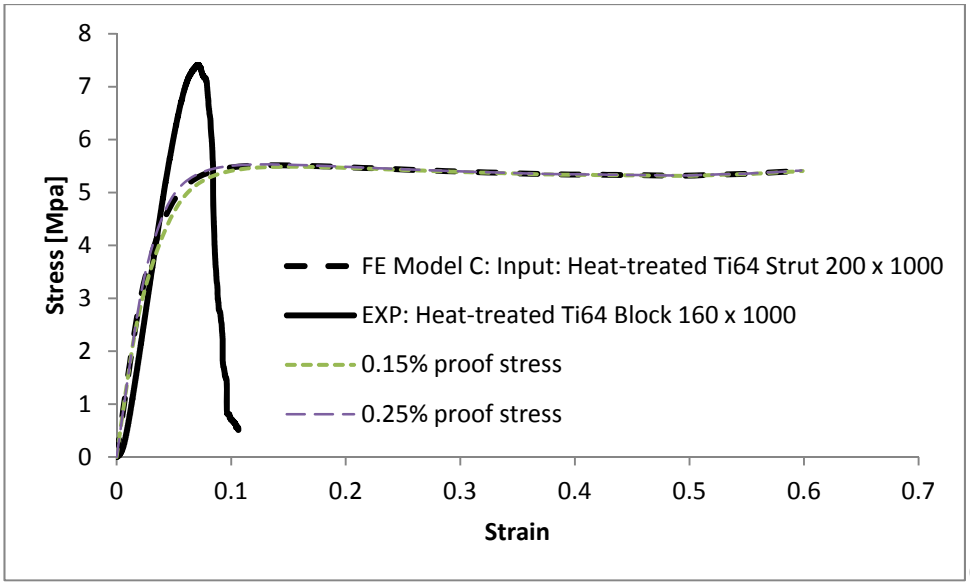

(b)

Figure 4.17: FE results with input data from three different proof stresses, 0.15%, 0.2% and 0.25%; (a) As-received material (Model B); (b) Heat-treated material (Model C)

Figure 4.17 shows the FE results with input data from the three different proof stresses. It can be seen that there is unnoticeable difference between the FE results from the three different proof stresses for both the as-received and heat-treated

material. As shown in Figure 4.12 and 4.13, the differences in input data from these three proof stresses are also small.

Theoretically, Ushijima et al. (2011) showed that the collapse of a BCC micro-lattice block structure is proportional to the flow stress of the material, as shown in previous Equation [4.8]. As discussed earlier in Table 4.6, the theoretical plastic collapse estimation under predicts both the experimental and FE results. However, the estimation still shows the effect of flow stress on the plastic collapse of the micro-lattice structure in this study. Table 4.8 shows the comparison between the experimental yield stress and the effects of flow stress in the yield values from both the FE model and theoretical estimation.

Table 4.8: Comparison between the experimental yield stress and the effects of flow stress in the yield values from both FE model and theoretical estimation (σ_0 is the flow stress of the input material; $\sigma_{pl,BCC}$ is the plastic collapse of micro-lattice block)

Material	Flow stress/ plastic collapse	Experiment	Proof stress					
			0.15%		0.2%		0.25%	
			FE	Theory	FE	Theory	FE	Theory
As-received	σ_0 [MPa]	-	225	225	245	245	255	255
	$\sigma_{pl,BCC}$ [MPa]	3.6	2.7	1.5	2.7	1.6	2.5	1.7
Heat-treated	σ_0 [MPa]	-	280	280	340	340	375	375
	$\sigma_{pl,BCC}$ [MPa]	6.5	4.4	1.9	4.4	2.3	4.4	2.5

4.6.2 Collapse and Deformation

The experimental results of the SLM Ti-6Al-4V BCC micro-lattice blocks showed that both the as-received and heat-treated materials failed at about 0.1 strains or 10% deformations (Figure 4.17). As mentioned in section 4.2, the as-received block failed in an abrupt manner into two main pieces, therefore, the progression in collapse could not be captured. Meanwhile, the heat-treated blocks showed a more progressive collapse and in an intact condition, therefore, up to 20% deformation was recorded. Figure 4.18 compares the experimental and FE (Model C) images for the collapse of a BCC unit cell within a heat-treated SLM Ti-6Al-4V micro-lattice block. It should be noted that dark areas in the FE model indicated the growth of plasticity within the struts.

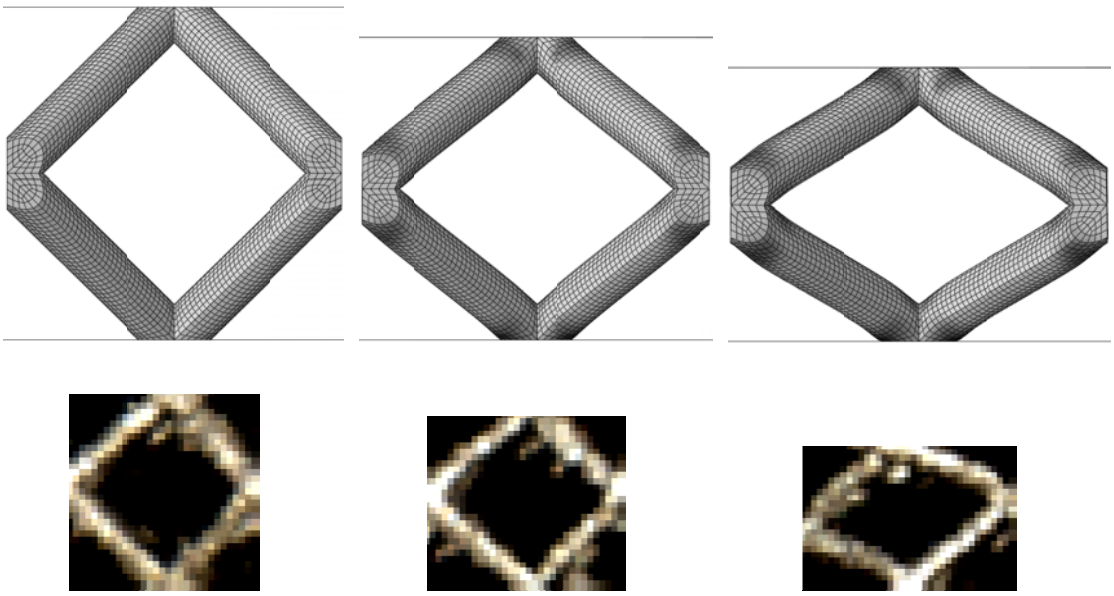

(a) 0% crush (b) 10% crush (c) 20% crush

Figure 4.18: Comparison of collapse behaviour from the experiment (heat-treated) and FE (Model C) of the BCC unit cell under a quasi-static compression load up to 20% crush (the unit cell photos were extracted from Figure 4.1(d))

Based from Figure 4.18, it can be seen that plasticity took place at the end of the struts of the BCC unit cell. These were the maximum stressed areas. The growths of

plasticity across the cross-sections of these maximum stressed areas up to 20% crush are shown in Figure 4.19. In the figure, it is shown that the plastic strain grows from the side part of the strut towards the middle area. The side part of the strut was the area where the crack was initiated, as reported in Chapter 3 section 3.4.2.

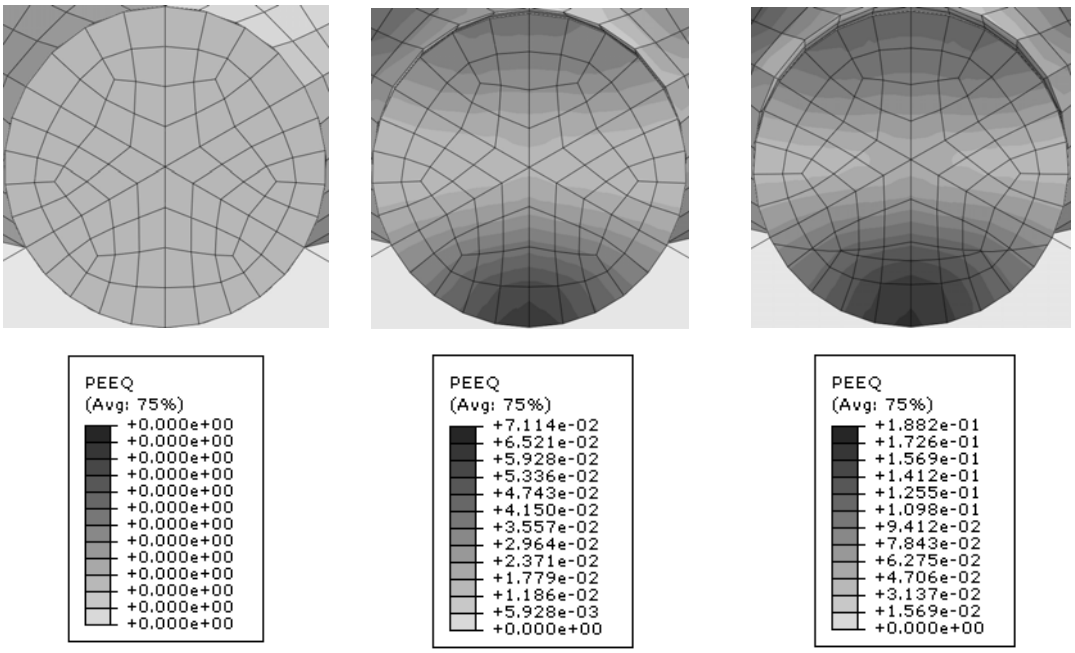

(a) 0% crush (b) 10% crush (c) 20% crush

Figure 4.19: Growth of plasticity across the maximum stressed area at the end of the strut in BCC unit cell (Model C)

Since the micro-lattice structure failed at approximately 10% crush, the plastic strain distribution along the FE model strut was captured at this deformation. Figure 4.20 shows the 45° angle cross-section of the BCC unit cell of Model B at 10% crush. The plastic strain distributions along the strut are shown in Figure 4.21, for three parts; A1, A2 and A3. It is shown that the strain component is highly localized in the bent area which is at the end of the strut, and reaches a maximum value of approximately 0.052 for the 10% crush of micro-lattice unit cell (Model B). Meanwhile, the plastic strain distribution across the highly localized part experiencing strain is shown in Figure 4.22 (along direction B1 of Figure 4.20). It is confirmed that the strain is highly localized at one side of the bent strut (at the beginning of line A1), where the crack initiated.

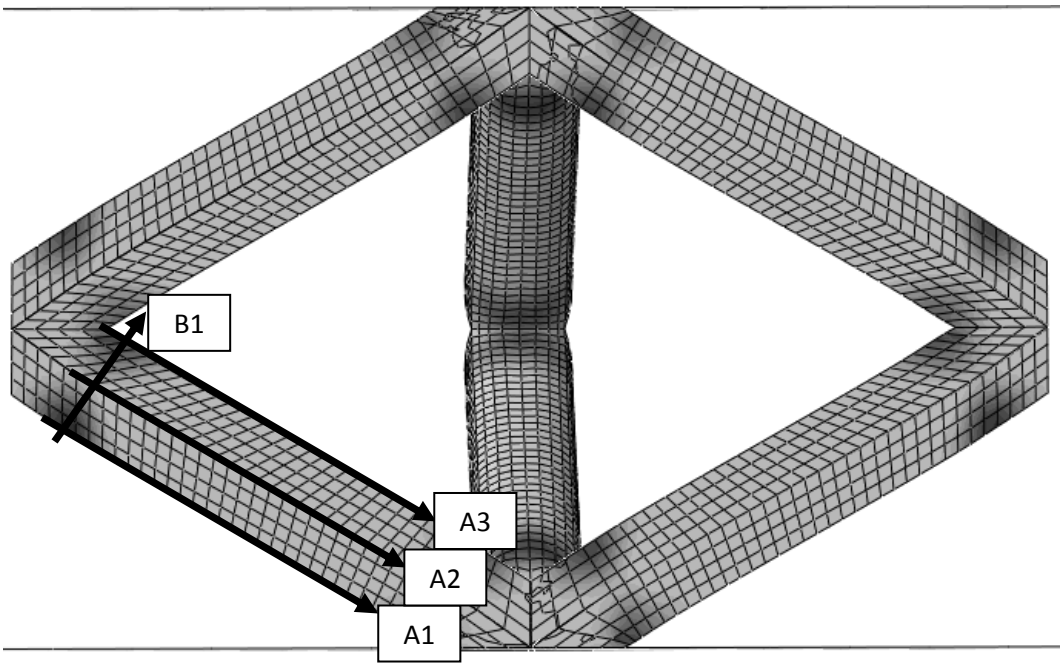

Figure 4.20: The 45° angle cross-section of the FE model at 10% crush (Model B), with four directions of strain distributions; A1, A2, A3 (details in Figure 4.21) and B1 (details in Figure 4.22)

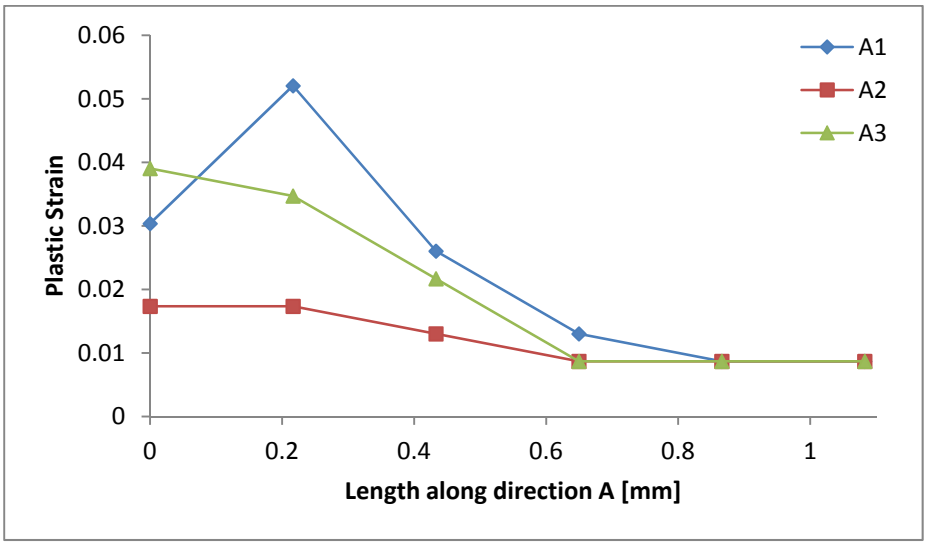

Figure 4.21: The plastic strain distributions along the strut, for three parts; A1, A2 and A3 as indicated in Figure 4.20

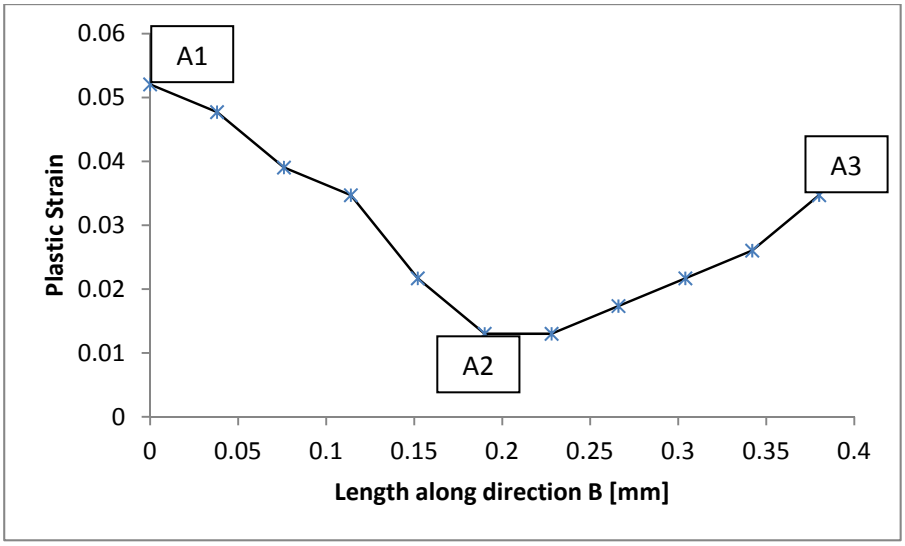

Figure 4.22: The plastic strain distribution across the direction B1 of Figure 4.20 (The labels A1, A2 and A3 indicate the crossings of the three lines with B1 in Figure 4.20)

It should be noted that the FE model only represents a unit cell of the BCC micro-lattice block. In the experiment, the highly localized strain occurred along the 45° angle of the micro-lattice block, as shown in Figure 4.1(d). A better representation could be achieved from the use of two-layer cell FE model. It was shown by Smith (2012) that the two-layer cell using beam element model can highlight the formation of shear bands at 45° angle for the BCC structure with vertical pillars (BCC-Z). This is shown in Figure 4.23. However, if the 3D brick element with the 380 μm strut diameter is used, the two-layer cell will comprise of four times of the total element number as compared to the current unit cell model, which means that it will be approximately 100000 elements altogether. This is a massive number of elements and the computational cost will be increased. Another alternative for the FE model of multiple unit cells is with the use of beam element rather than the 3D brick element. However, the beam element model could not offer the details of the three dimensional deformation as been explained in this section. Therefore, it can be said that the 3D brick element model which is based on a single BCC unit cell offers a reasonable comparison to the experimental block compression test with 8 x 8 x 8 BCC unit cells, although there are differences in the response between both the experiment and the FE model. The details of plastic growth which indicates the

initiation of crack in the micro-strut can be clearly shown from the single unit cell model with the 3D brick element type. It should be noted that the current study is only looking at a single cell collapse of Ti-6Al-4V BCC micro-lattice structure, since multiple cells collapse will introduce lots of complicated new effects regarding the usage of titanium material.

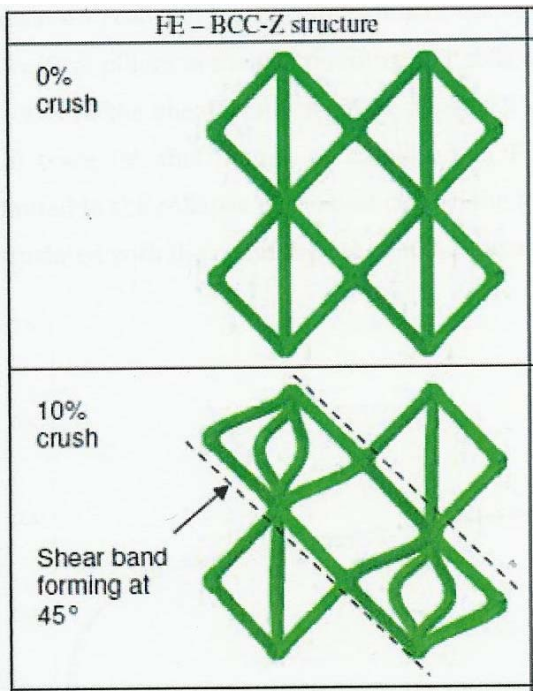

Figure 4.23: Two-layer cell using beam element model for BCC-Z, which highlights the formation of shear bands at 45° angle [adapted from Smith (2012)]

4.6.3 Prediction of Failure

The failure of the SLM Ti-6Al-4V BCC unit cell is based on the ductile criterion, where the plastic strain is the main parameter. By using the pre-determined equivalent plastic strain from Chapter 2, the estimation of failure will be done from the interrogation of the FE result and will be compared to the experimental block compression failure. Table 4.9 lists the equivalent plastic strain values derived from the uniaxial tensile tests of the single struts in Chapter 2 for both the as-received and heat-treated materials.

Table 4.9: List of equivalent plastic strain values from uniaxial tensile test of SLM Ti-6Al-4V single struts

Material	Reference	Relation between equivalent stress, $\bar{\sigma}$, and equivalent plastic strain, $\bar{\varepsilon}^p$	Stress at strut failure, $\bar{\sigma}_f$	Equivalent plastic strain at strut failure, $\bar{\varepsilon}_f^p$
As-received	Equation 2.30, Chapter 2	$\bar{\sigma} = [0.245 + 7.8721\bar{\varepsilon}^p]\text{GPa}$	280 MPa (UTS in Figure 4.10)	0.00445
Heat-treated	Equation 2.31, Chapter 2	$\bar{\sigma} = [0.34 + 29.098\bar{\varepsilon}^p]\text{GPa}$	520 MPa (UTS in Figure 4.11)	0.00619

From the FE modelling outputs, results of the maximum equivalent plastic strain, PEEQ at the maximum stressed part of strut near the nodal area were plotted against the percentage of deformation up to 20% crush for both the as-received (Model B) and heat-treated (Model C) materials, as shown in Figure 4.24(a) and (b)

respectively. The values of equivalent plastic strain at single strut failure ($\bar{\varepsilon}_f^p$) in Table 4.9 were then taken as the maximum equivalent plastic strain (PEEQ) for the FE modelling outputs (Figure 4.24), and the deformations at which the failure initiates were estimated.

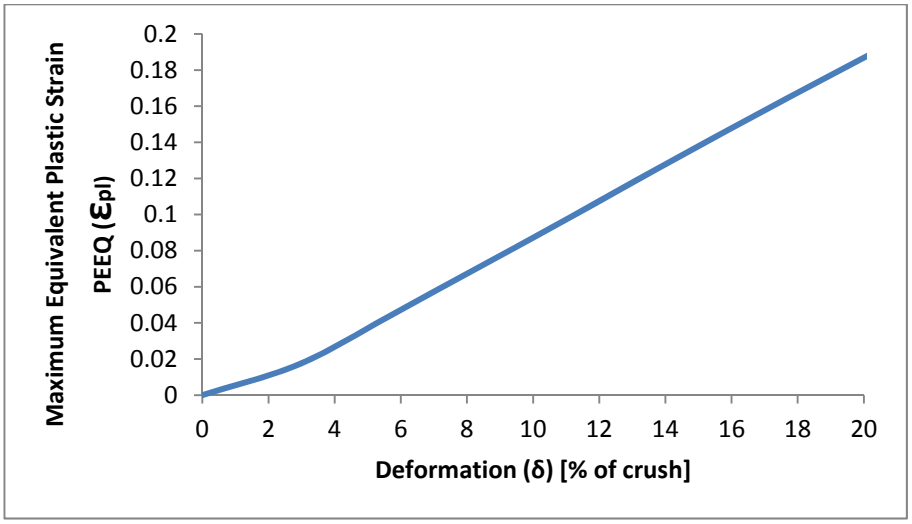

(a)

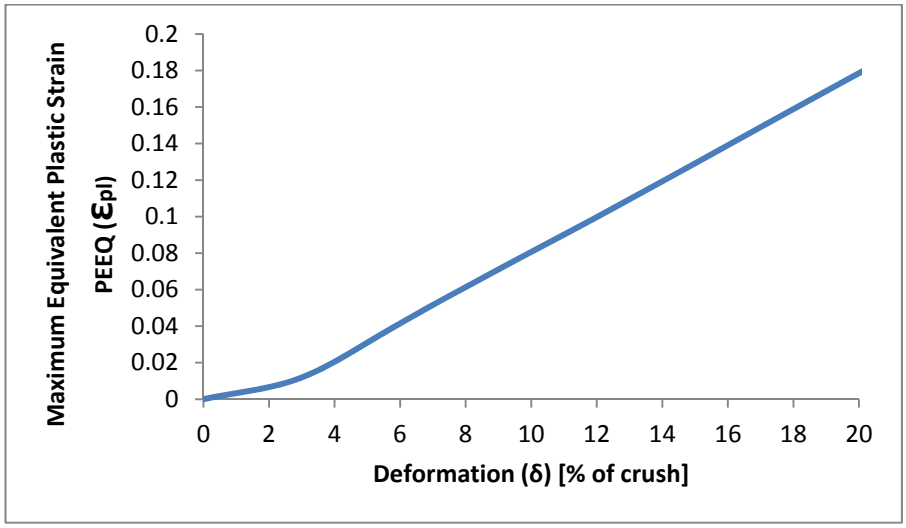

(b)

Figure 4.24: The maximum equivalent plastic strain, PEEQ at the maximum stressed strut against the percentage of deformation up to 20% crush from the FE of (a) Model B and; (b) Model C

With the $\bar{\varepsilon}_f^p$ values from Table 4.9, failure for Model B (Figure 4.24(a)) was estimated at 1% deformation, while failure for Model C (Figure 4.24(b)) was

estimated at 2% deformation. These predicted values are very low (a factor of ten less) as compared to the experimental values, where both of the as-received and heat-treated materials failed at approximately 0.1 strains or at 10% deformation (Figure 4.17). Figure 4.25 shows the stress-strain curves for both FE models with the estimation of failure.

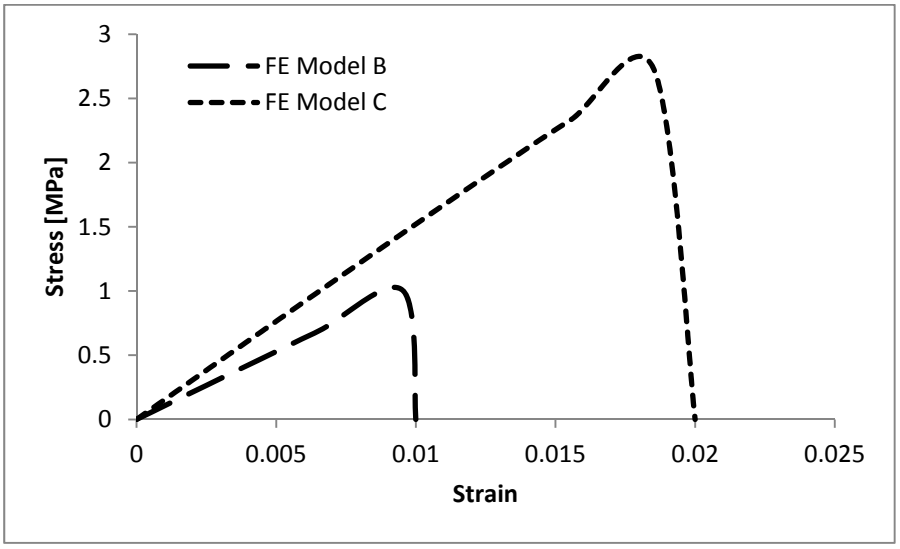

Figure 4.25: Stress-strain curves for Model B and C with the estimation of failure

From the results, it is shown that the failure strain of the uniaxial tensile test of the single struts is different from that of the micro-lattice blocks under compression test. The difference between the two tests is the constraint, one resulted the stretching of the strut (tensile test) and another one resulted the bending of the strut (compression test), as discussed in section 3.4.2. In this study, the equivalent plastic strain at strut failure, $\bar{\varepsilon}_f^p$, was determined from a relation between the equivalent stress, $\bar{\sigma}$, and the equivalent plastic strain, $\bar{\varepsilon}^p$, using the strain hardening curves of the uniaxial tensile test, as discussed in section 2.4.7. It was expected that the equivalent plastic strain from the tensile test was similar to that from the compression test. However, it was found that the change in constraints from tension to bending resulted in a different extent of critical strains for both test. It was mentioned in Thuillier et al. (2011) that in bending, the strain limit prediction derived from an instability criterion is

inaccurate and a criterion based on a critical void volume fraction, which can be identified from macroscopic tests, was suggested.

To summarize, in this chapter, sensitivity analyses were performed in various aspects including the plasticity of the material which was derived from the proof stress, the diameter of the struts where comparison was done based on equations from theoretical analysis, and the node geometry of the micro-lattice blocks which was compared to the cross-section of the manufactured material. Besides, the rupture criterion was selected based on evaluations of the micro-lattice struts and blocks failure. Unfortunately, the failure prediction of the SLM Ti-6Al-4V BCC micro-lattice block is found inaccurate and this shows the complexity of rupture model for the material. There are several aspects that can be considered in the next step for the rupture analysis of the material, which are listed as below.

- The experimental calibration of rupture and fracture from the strut test is a factor of ten down compared to the parameter in the micro-lattice block collapse. An FE model for the strut test could be performed for the calibration and derivation of fracture parameter, ε_p, from the strut test.
- The selection of another rupture criterion can be considered. It is shown in this study that the plastic strain is not a good estimation to address the rupture from tension to bending. In order to accurately derive the fracture parameter, another criterion such as the criterion based on a critical void volume fraction proposed by Thuillier et al. (2011) can be considered. It is mentioned that the void volume fraction evolution law is classically split into two contributions, one for nucleation and the other one for growth of cavities. More than three parameters are required for this criterion; hence more sophisticated tests including the hydraulic bulge test need to be performed. These sophisticated tests are too complicated to be done, by taking into account the issues in geometry and manufacturing of the SLM Ti-6Al-4V micro-lattice material. The issues need to be sorted out before further tests can be implemented. It should be noted that the discussion in the current study is specific for the SLM Ti-6Al-4V BCC micro-lattice block with 2.5 mm cell size and

manufacturing parameters between 160W/1000μs and 200W/1000μs. For some other parameters, some more sophisticated model may be needed.

- In this study, a classical isotropic metal plasticity model was used. Another constitutive relation for the plasticity model in the Abaqus can also be considered such as a porous metal plasticity model. The porous metal plasticity model is based on Gurson's porous metal plasticity theory with void nucleation and defines the plastic flow on the basis of a potential function that characterizes the porosity in terms of relative density. This model was used by Thuillier et al. (2011) in conjunction with the application of the critical void volume fraction based criterion. Again, more parameters need to be determined from more tests. For the current SLM Ti-6Al-4V micro-lattice structure, this would be too complicated due to the geometrical and manufacturing issues as discussed in Chapter 2 and 3.

4.7 BEST PROPERTIES PREDICTION FOR SLM Ti-6Al-4V BCC MICRO-LATTICE BLOCK FROM MODEL D

As discussed in Chapter 2, the properties of the strut materials in this study are found to be low when compared to the properties in other studies (Table 2.13). However, it had been shown in this study that the heat-treatment process introduced an improvement to the variability of the struts within the SLM Ti-6Al-4V BCC micro-lattice blocks, thus leading to an improvement in the properties, as shown by the stress-strain response of the block material. Further improvement to the geometry and variability of the struts will of course improve the response of the SLM Ti-6Al-4V micro-lattice blocks. Properties as close as the standard properties as possible [Boyer et al. (1994)] would be preferred and the best response expected from the micro-lattice structures can be represented by the response of Model D as shown in Figure 4.26.

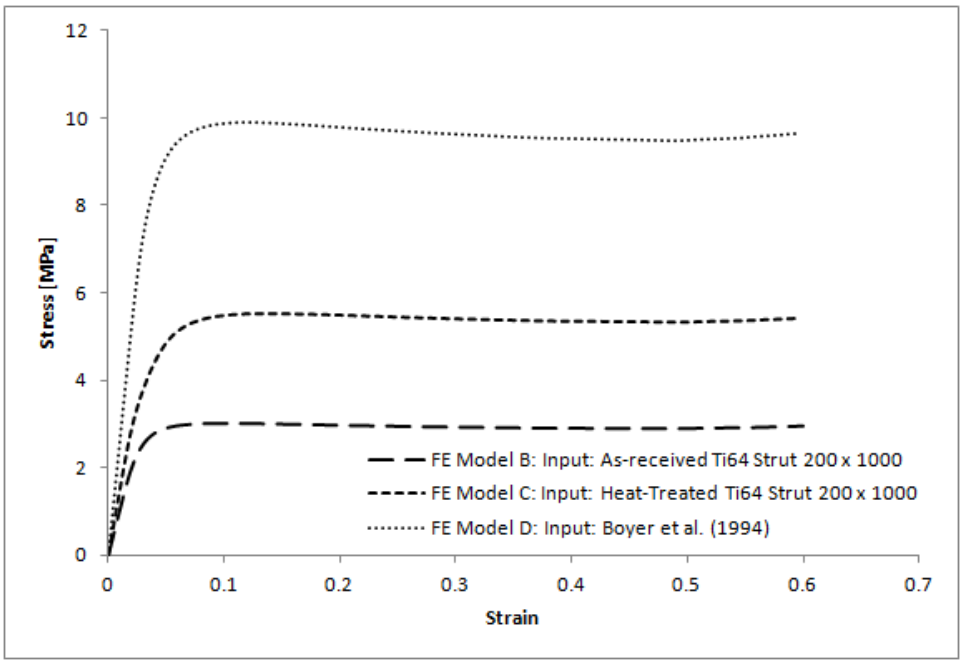

4.26: The best expected response of the SLM Ti-6Al-4V BCC micro-lattice block from Model D with the input from standard properties

4.8 SUMMARY OF CHAPTER 4

This simulation analysis of the SLM Ti-6Al-4V micro-lattice blocks was represented by a BCC unit cell model based on a validated model from the stainless steel SS316L micro-lattice study [Smith (2012)]. The 3D presentation of plastic growth in the struts was shown, and it was found that the end parts of the struts near the nodal area were the parts with highest plastic strain. This indicated that these were the parts that experienced maximum stress and also where the failure initiated. This supports the experimental findings of the failure initiation site, as discussed in Chapter 3.

For failure prediction, the pre-determined equivalent plastic strain from Chapter 2 was used and failure was interrogated from the FE result. It was found that this procedure gave a low value strain when compared to the experimental block compression failure, thus the predicted failure was a factor of ten out when compared to the experimental failure. However, the effect of improvement in properties due to the heat-treatment process can be seen from the stress-strain curves with the failure prediction.

As discussed in Chapter 2 and 3, there are many factors which contribute to the performance of the micro-lattice structures produced from the selective laser melting process. It was shown in this study that the improvement in geometry and variability of the basic unit for the micro-lattice structure, which is the strut, will improve the performance of the micro-lattice material. In this chapter, the best performance expected from the SLM Ti-6Al-4V BCC micro-lattice structure was shown by the response of Model D, with the input from the standard properties [Boyer et al. (1994)]. There is hope that with the improvements in manufacturing procedure which will improve the geometry and variability in the production of struts from single laser beam melting, the properties of the micro-lattice structures will be improved so as to become much closer to the standard properties.

REFERENCES OF CHAPTER 4

Abaqus Analysis User's Manual (2010) Abaqus 6.10 Online Documentation. Dassault Systemes Simulia Corp. Providence, RI, USA.

Abaqus Theory Manual (2009) Abaqus 6.9-EF Online Documentation. Dassault Systemes Simulia Corp. Providence, RI, USA.

Boyer, R., Welsch, G., Collings E.W. (ed.) (1994). *Material Properties Handbook: Titanium Alloys*, ASM International: Material Park, OH. http://www.matweb.com (assessed on 5/2/2010)

Budynas, R.G. and Nisbett, J.K. (2008). *Shigley's Mechanical Engineering Design* (8th edition in SI unit), McGraw-Hill, Singapore.

Chakrabarty, J. (2006). *Theory of Plasticity* (3rd edition), Butterworth-Heinemann, Jordan Hill, GBR.

Hooputra, H., Gese, H., Dell, H., Werner, H. (2004) 'A comprehensive failure model for crashworthiness simulation of aluminium extrusions'. *International Journal of Crashworthiness*, 9(5): 449-463.

Mines, R.A.W., McKown, S., Cantwell, W., Tsopanos, S., Brooks, W., Sutcliffe, C.J. (2007) 'On the progressive collapse of micro-lattice structures'. *Proceedings of the 13th International Conference on Experimental Mechanics, Alexandroupolis*, Greece, Paper No. 158.

Shen, Y. (2009) *High performance sandwich structures based on novel metal cores*, PhD Thesis, University of Liverpool, United Kingdom.

Smith, M.I.H. (2012) *The compressive response of novel lattice structures subjected to static and dynamic loading*, PhD Thesis, University of Liverpool, United Kingdom.

Thuillier, S., Le Maout, N., Manach, P.Y. (2011) 'Influence of ductile damage on the bending behaviour of aluminium alloy thin sheets'. *Materials and Design*, 32: 2049-2057.

Tsopanos, S., Mines, R., McKown, S., Shen, Y., Cantwell, W., Brooks, W., Sutcliffe, C.J. (2010) 'The influence of processing parameters on the mechanical properties of selectively laser melted micro-lattice structures'. *Journal of Manufacturing Science and Engineering ASME*, Vol. 132: 041011-1 – 041011-12.

Ushijima, K., Cantwell, W.J., Mines, R.A.W., Tsopanos, S., Smith, M. (2011) 'An investigation into the compressive properties of stainless steel micro-lattice structures'. *Journal of Sandwich Structures and Materials*, 13: 303-329.

CHAPTER 5: CONCLUSIONS, RECOMMENDATIONS AND FUTURE WORKS

5.1 CONCLUSIONS

The research activities which were reported in this thesis focused on the study of the behaviour and properties of the Selective Laser Melting (SLM) titanium alloy Ti-6Al-4V micro-lattice structure as core material in sandwich construction for aerospace applications. Issues which affect the behaviour of the SLM Ti-6Al-4V micro-lattice structure were defined and clarified in detail. Works and findings were done within the scope and objectives of the research. The conclusions were listed as below:

C1. The viability of the SLM Ti-6Al-4V micro-lattice structure for foreign object impact (FOI) application in sandwich structure construction of aerospace material was investigated.

Previous research studies in the application of the SLM process to produce micro-lattice core material for sandwich structure in FOI applications were started with stainless steel material [McKown et al. (2007); Mines (2008)]. Since titanium alloy is more preferable for future aerospace build material [Wu (2006)], the current research is a next step to the preliminary research efforts on the SLM micro-lattice structures. It was found that a combination of the manufacturing parameters of 200 Watts (W) and 1000 microseconds (μs) for the Ti-6Al-4V micro-lattice structure core resulted in a more localized impact area in the sandwich constructions as compared to the competing aluminium honeycomb core [Hasan et al. (2010)].

In the current research, both the titanium alloy single manufactured micro-struts and BCC micro-lattice blocks with similar manufacturing parameters as in previous research were tested and analyzed. The stress-strain curves were determined from tensile tests of the strut materials. It was found that the strength of the as-received material was about one third of the strength of the standard titanium alloy [Boyer et

al. (1994)]. However, the strength was improved to about 60% of the standard value after the introduction of a simple heat-treatment process. The heat-treated micro-lattice blocks failed in a more progressive manner as compared to the as-received blocks. The determined properties of the strut materials were then used as the input data in a finite element simulation of BCC unit cell model, and it was found that the FE simulation results were comparable to the experimental micro-lattice block results.

Original contribution: The current SLM Ti-6Al-4V micro-lattice structures have been shown to be able to compete with aluminium honeycomb from the point of view of Foreign Object Impact performance in aerospace sandwich panel constructions. This performance can be improved with the improvement of quality of the Ti-6Al-4V parent material, which is the micro-strut.

In this study, the effect of yield stress of Ti-6Al-4V micro-lattice material on the FOI performance is highlighted. The improvement of yield stress of the heat-treated micro-lattice has shown that this material offers promising properties, when referring to a developed relation by Ushijima et al. (2011) as shown in Equation 5.1.

$$\sigma_{pl} = \frac{\rho^*}{\rho_p}\frac{4\sqrt{6}}{9}\sigma_0\frac{d}{L} \qquad [5.1]$$

Where ρ^* is the density of the lattice, ρ_p is the density of the parent material, σ_0 is the yield stress of the parent material, d is the strut diameter and L is the cell length. Hence, for collapse mode without rupture, a doubling of yield stress will double the block collapse stress. Assuming a cylindrical volume of deformation for panel perforation, this would lead to a halving of the dent depth for a given impact energy. This would bring the Ti-6Al-4V micro-lattice into direct competition with the honeycomb, as shown in Figure 1.21 of Chapter 1.

C2. The dimensional accuracy and circularity of the SLM Ti-6Al-4V micro-struts as well as the microstructure of the materials were quantified.

The micro-struts in a body centred cubic (BCC) micro-lattice structure are in an arrangement of 35° angles from the centre node [Rehme (2010)]. Due to the overlaps

in the angle of build [Cansizoglu et al. (2008)], there are variations in the strut diameter within the micro-lattice structure manufactured from the SLM process. In this study, the dimensional accuracy and circularity of the SLM Ti-6Al-4V micro-struts which were singly built at the 35° angle were determined. The variability in the strut diameter values was related to the surface quality of the SLM manufactured material. These variations were used in the lower and upper boundaries estimations for the mechanical properties of the struts. It was shown that the dimensional accuracy, circularity and surface roughness of the SLM manufactured struts can be improved with the application of heat-treatment process.

The observation for the microstructure of the SLM Ti-6Al-4V micro-strut was also done. The microstructure was found to be similar to that reported by Facchini et al. (2010), with 'as-cast' needle-like martensitic structure, which was different from the standard annealed Ti-6Al-4V α/β material [Boyer et al. (1994)]. Dendritic structures were observed among the martensite structure of the SLM Ti-6Al-4V material in this study. From the energy dispersive spectroscopy (EDS) analysis, iron (Fe) element was detected in the dendritic region. Some chromium (Cr), a non-Ti-6Al-4V element, was also detected in that region. This finding showed that the manufacturing process of the SLM Ti-6Al-4V material was extremely sensitive. The residues which were suspected from the cleaned powder feed system, contributed to the existence of the Cr element in the dendritic region. The microstructure of the SLM Ti-6Al-4V micro-strut was improved by a post-manufacture heat-treatment process. A simple 'solution treatment-quenching-aging' procedure to the strut was proposed, where the strut was placed in a vacuum-sealed quartz tube. The resultant microstructure of the heat-treated strut was observed to be closer to that normally found in the α/β Ti-6Al-4V alloy [Polmear (2006)]. It was also found that the segregation of elements was redistributed, and the dendritic region was disappeared. The EDS analysis of the heat-treated material showed that the Fe element was evenly distributed and there was no Cr element detected throughout the sampling length of the strut.

Original contribution: The quality of the SLM Ti-6Al-4V micro-strut was quantified in this study. This includes the dimensional accuracy, surface quality, material microstructure, trace residue elements, and hence variability in material and structural performance. This study filled the gap between the various aspects of

research within the area of SLM manufacturing, titanium alloy material, as well as microstructure properties of the micro-lattice strut material, where an integrated approach was applied in addressing the issues.

C3. Mechanical properties of the SLM Ti-6Al-4V micro-struts were measured and the stress-strain curves were obtained. Besides, the SLM Ti-6Al-4V micro-lattice blocks were tested under compression load and the performance of the materials were evaluated.

It was highlighted by Zhou et al. (2004) that it is necessary to characterize the mechanical properties of individual struts in an aluminium alloy lattice block structure rather than using the bulk alloy properties, since it was found that the chemical analysis of an individual strut was different from that of the bulk material. In the current study of SLM Ti-6Al-4V micro-lattice structure, it was also found that the microstructure and element analysis of the individual strut was different from the standard annealed Ti-6Al-4V alloy material [Boyer et al. (1994)]. Although the microstructure was found similar with that of other research [Facchini et al. (2010)], there is a difference in the material properties of the material used in this research.

The mechanical properties of the material in this study were determined from the tensile tests of the individual micro-struts. The elastic modulus (E) for the SLM Ti-6Al-4V micro-struts was investigated using the experimental compliance correction methods as found in the literatures [Sergueeva et al. (2009); Kalidindi et al. (1997); Turek (1993)]. The yield strength (σ_y) and ultimate tensile strength (UTS) values were also determined. The variabilities in strut diameters and dimensions were applied in the estimations of the lower and upper boundaries of the properties. The values of E, σ_y and UTS for the material in this study was determined as 40%, 32% and 30% respectively from the standard values [Boyer et al. (1994)]. These low property values were suspected to result from the quality issues related to the SLM manufactured materials. It was found that a post-manufacture heat-treatment process improved the microstructure of the SLM Ti-6Al-4V micro-struts as well as the properties of the material. Tensile test results of the heat-treated strut showed that the values of E, σ_y and UTS increased up to 60%, 39% and 55% of their respective

standard values. Although they were still low, they were considered to be fairly good, taking into consideration the existence of the residue elements in the material.

An investigation of properties of the SLM Ti-6Al-4V micro-lattice material was further explored with the tested micro-lattice blocks under compression load. It was observed that the SLM Ti-6Al-4V micro-lattice blocks experienced a 'brittle-like' struts failure at the end parts of the struts, near the nodal areas. The failure surface was examined under the scanning electron microscope (SEM), and it was found that there were ductile dimples on the surface, which indicated that a ductile failure mechanism occurred. Since the failure took place near the micro-lattice node areas, the manufacturing quality in that area was investigated. The layer by layer node manufacturing was discussed and the cross-section of the node was observed under the optical microscope, to relate the effects of manufacturing parameters with the node-struts formation in the BCC micro-lattice structures. The quantified dimensional accuracy, circularity and surface roughness of the struts were related to the failure at these node-strut areas. It was found that the performance and collapse of the SLM Ti-6Al-4V BCC micro-lattice blocks under compressive loading depended on the properties (E, σ_y and UTS) and dimensions of the micro-struts within the block materials.

In the micro-lattice study of stainless steel material [Tsopanos et al. (2010)], it was shown that the strength and properties of the micro-lattice blocks increased with the increase of laser manufacturing parameters of the SLM process. However, in the current study, it was shown that a different relation applies to the SLM Ti-6Al-4V micro-lattice block materials. The strength and properties increased with the increase of laser manufacturing time, but was found to decrease with the increase of laser power. This finding was similar to that of Song et al. (2012) which found that the melting mechanism for the Ti-6Al-4V powder at a very high laser energy produced SLM products which were fully dense but with the formation of cracks within the material. These cracks led to the decrease in the strength and properties of the SLM Ti-6Al-4V material.

Original contribution: The mechanical properties of the SLM Ti-6Al-4V BCC micro-lattice structure were determined from the individual struts, with the application of the compliance correction method in a simple tensile test procedure. A

detailed study of the quality of the node formation in the BCC micro-lattice block was another original contribution in this study. The manufacturing route of the SLM micro-lattice structure was revealed from the 45° angle cross-section of the block. There is potential of possible improvements with the improvements in the dimensional accuracy and circularity of the micro-struts within the micro-lattice structures.

C4. The progressive collapse of the SLM Ti-6Al-4V BCC micro-lattice structure was analyzed from the finite element (FE) simulation of elastic, plastic and rupture deformation for a BCC unit cell.

A validated FE model of stainless steel (SS316L) BCC unit cell from other research [Smith (2012)] was adapted for the titanium alloy Ti-6Al-4V material in the current study. The 3D brick element was used for the model. Similar boundary conditions were applied, but the size of struts was changed from 195 μm diameter to 380 μm, to represent a larger diameter of the SLM Ti-6Al-4V micro-struts. For the modified model, the strut properties from the detailed definition of micro-struts were used. The plastic strain based rupture criterion was applied, and the equivalent plastic strain was determined from the individual micro-struts tests. The failure of the micro-lattice structure was manually interrogated in the analysis of the unit cell, but this method gave the estimated fracture strain ten times lower than the experimental value. To conclude the findings in this study, the elasto-plastic response of the unit cell model was suggested to be used in the prediction of the best possible performance of the SLM Ti-6Al-4V BCC micro-lattice structure.

Original contribution: In this study, the validated model from another study was modified to suit with the real conditions of the titanium alloy micro-lattice structure. The ductile rupture criterion was selected for the Ti-6Al-4V micro-lattice block collapse model. The properties which were derived from the individual struts were used as the input for the FE model, and the result was compared to the experimental values. The effect of the properties of parent material on the micro-lattice block collapse was quantified.

As shown in Figure 4.17 of Chapter 4, the simulation results are not a close match with the outputs from experiments. There are differences in the virtual geometry of the model as compared to the real geometry of the micro-lattice material. The dimensions of the strut in the model are also simplified from the complex SLM processed micro-lattice strut dimensions. Analysis of micro-strut leads to low E values as compared to standard value of Ti-6Al-4V alloy. The trend of low E value is also observed in the earlier micro-lattice studies [Shen (2009); Tsopanos et al. (2010)]. Lastly, the plastic properties and rupture of the model are using projected values from the sudden rupture of the experimental material. The projection is done since the classical plasticity model is adapted for the simulation. All in all, although there are differences between the experiment and simulation values, the model used in this study has shown an acceptable approximation of the collapse of the Ti-6Al-4V micro-lattice structure.

5.2 RECOMMENDATIONS

It was shown that the behaviour and properties of the SLM Ti-6Al-4V BCC micro-lattice structure depend on the parent material properties which were resulted from the manufacturing routes and parameters. An improvement in manufacturing process includes the layer strategy and laser beam quality can improve the properties of the micro-lattice materials. If the manufacturing details were maintained the same, the properties which affect the behaviours can be improved with the improvements of the geometrical accuracy and microstructure of the material, with a simple post-manufacture heat-treatment process as suggested in this study. In order to further explore the potential of the SLM Ti-6Al-4V micro-lattice structure as core material in the sandwich constructions for FOI in aerospace applications, it is recommended that the following issues be addressed:

R1. The manufacturing strategy for the micro-lattice material can be improved in order to produce micro-struts with better quality of dimensional accuracy and circularity. A new arrangement can be suggested to minimise the 'stair-case' effects due to the layer by layer manufacturing.

R2. The improvement of the Ti-6Al-4V micro-lattice material produced from the SLM process can be further studied with the introduction of other possible heat-treatment processes. The heat-treatment procedure suggested in this study can be repeated by one or two more cycles in order to improve the outer surface variations of the micro-struts, as well as to refine and produce a microstructure with more equiaxed grains.

R3. The SLM processing route and parameters which were revised in this study refer to the manufacturing of specimen that was about four years ago. The processing issue such as the existence of residue elements which were related to the machine cleanliness were investigated in this study, and it is suggested that a thorough examination on materials produced by the SLM process is practiced in order to maintain and improve the product quality [ASTM Standard (2012)].

R4. The 3D brick element type FE model can be used to predict the progressive collapse of the SLM Ti-6Al-4V BCC micro-lattice block. The model can be further improved with the considerations of strut geometry imperfections and node geometry size of the BCC micro-lattice block. Failure of the SLM Ti-6Al-4V BCC micro-lattice block can be further studied using the void volume fraction criterion [Thuillier et al. (2011)], especially when the manufacturing issues that were address in this study are resolved.

Besides all of the above recommendations, there are also different approaches that could be taken if the topic were to be tackled again. Firstly, a significant effort can

be given to closely control the manufacturing aspect, especially in quality issues. A more fundamental study can be done in the model or analysis of formation of struts and blocks from the complicated SLM process using Ti-6Al-4V material. Secondly, a more detailed approach can be suggested to improve the micro-strut testing and measurement. An improved test using the same facilities as reported in Gumruk and Mines (2013) can be adapted. Besides, other approaches with more detailed study using optical non-contact strain measurements can also be considered [Wattrisse et al. (2001); Orteu (2009)]. Other than that, it is found that the block compression test was good in addressing the foreign object impact of micro-lattice structure, although there is limitation in the analysis. The FEA model was also considered well for the fundamental study of the collapse of the material, although there are also some limitations as compared to the real micro-lattice condition. In future, the plasticity and rupture modelling can be validated in more detail.

5.3 SUMMARY AND FUTURE WORKS

In summary, the quality of the SLM Ti-6Al-4V BCC micro-lattice structure can be further improved, with the improvements of the variations in geometry and microstructure due to the manufacturing strategy and procedure. In the future, the quality assurance method needs to be developed and applied in the production of the SLM micro-lattice structures, regardless of the scale of the production. An improved quality will improve the mechanical properties of the micro-lattice material, making it to be significantly close to the standard values.

In this study, the BCC topology of the micro-lattice structure is not an optimal configuration, but it offers simplicity and reliability for the manufacturing as well as the experimental testing. The high manufacturing parameters of the specimen used in this study is also not the optimal parameter for the SLM Ti-6Al-4V material, and it is important to closely study the melting mechanism for the single laser beam manufacture of the micro-lattice structure. For future, the relation between the processes, material and structure performances can be further defined, and a

complete account of the material route from powder to final structure can be obtained. The performance of the tested SLM Ti-6Al-4V BCC micro-lattice structures in this study, together with the expected best performance for the material are annotated in Figure 5.1. The summary of the results and findings for the materials in this study are listed in Table 5.1, which can be referred in future works for further improvements of the materials.

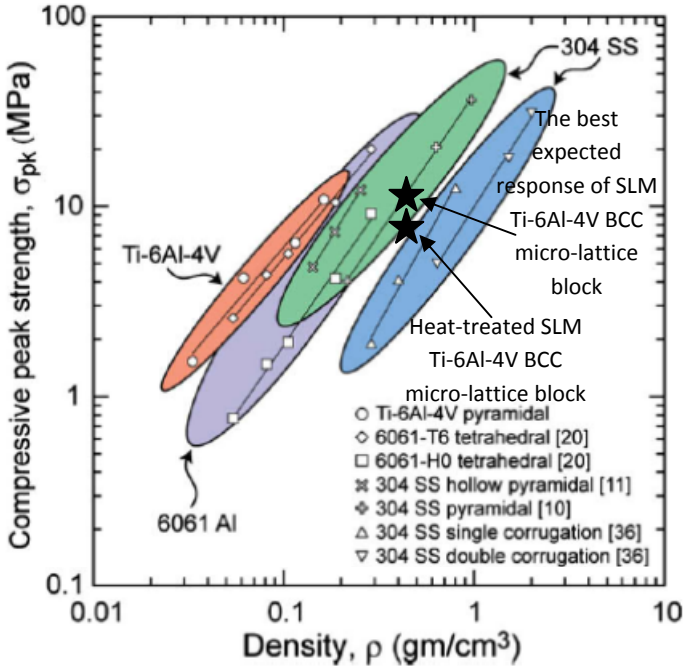

Figure 5.1 (Repetition of Figure 1.14): Compressive peak strength versus density for various sandwich core topologies [Queheillalt and Wadley (2009)]

Table 5.1: Summary of results and findings for the SLM Ti-6Al-4V materials

	As-received (AR)	Heat-treated (HT)	Optimal / Further Improvement
Single Struts			
Circularity (35°)	74%	78%	Improved circularity in HT
Dimensional accuracy (35°)	86%	90%	Improved accuracy in HT, means less diversity in dimension
Surface quality, R_a (35°)	16.8 µm	11.15 µm	Reduced surface roughness in HT, means less irregularity, less stress concentration, thus improved strength
Microstructure	'Needle-like' martensite α-phase	More balance α and β phase	Improved α and β phase in HT, but more circular grains are needed for better ductility
Diameter (200 W x 1000 µs)	(374.14 ± 26.15) µm	(322.56 ± 16.60) µm	Smaller diameter of HT due to less surface irregularity
E	(45 ± 16) GPa	(65 ± 15) GPa	Improved stiffness of HT is 57% of standard
	Textbook: 114 GPa [Boyer et al. (1994)]		
σ_y	(245 ± 86) MPa	(340 ± 78) MPa	Improved yield of HT is 39% of standard
	Textbook: 880 MPa [Boyer et al. (1994)]		
σ_{uts}	(280 ± 98) MPa	(520 ± 120) MPa	Improved strength of HT is 55% of standard
	Textbook: 950 MPa [Boyer et al. (1994)]		
ε_f	1%	1.5%	Improved ductility of HT is 11% of standard
	Textbook: 14% [Boyer et al. (1994)]		
Micro-lattice blocks			
Strut diameter (160 W x 1000 µs)	(373.10 ± 29.95) µm	(339.41 ± 17.57) µm	Smaller diameter of HT due to less surface irregularity
Estimated ρ	0.447 g/cm^3		Density derived from averaged mass/weight
E / ρ (160 W x 1000 µs)	217 kN.m/kg	262 kN.m/kg	Increased stiffness of HT block
σ_{ult} / ρ (160 W x 1000 µs)	16.55 kN.m/kg	17.00 kN.m/kg	Increased strength of HT block
ε_f / ρ (160 W x 1000 µs)	0.206 cm^3/g	0.183 cm^3/g	Reduced failure strain of HT block
Manufacturing effects in blocks			
Laser power 500 < W < 1000	Increase strength as power increase		
Laser exposure time 160 < µs < 200	Increase strength as exposure time decrease		
Strut diameter (estimated)	307 µm	307 µm	No difference in estimated diameters derived from averaged mass/weight

REFERENCES OF CHAPTER 5

ASTM Standard (2012) '*Standard specification for Addititive Manufacturing Titanium-6 Aluminum-4 Vanadium with Powder Bed Fusion*', ASTM International, DOI: 10.1520/F2924-12.

Boyer, R., Welsch, G., Collings, E.W. (Eds.) (1994) Material Properties Handbook *Titanium Alloys*. ASM International: Material Park, OH. http://www.matweb.com

Cansizoglu, O., Harrysson, O., Cormier, D., West, H., Mahale, T. (2008) 'Properties of Ti-6Al-4V non-stochastic lattice structures fabricated via electron beam melting'. *Materials Science and Engineering A*, 492: 468-474.

Facchini, L., Magalini, E., Robotti, P., Molinari, A., Hoges, S., Wissenbach, K. (2010) 'Ductility of a Ti-6Al-4V alloy produced by selective laser melting of prealloyed powders'. *Rapid Prototyping Journal*, 16/6: 450-459.

Gumruk, R. And Mines, R.A.W. (2013) 'Compressive Behaviour of Stainless Steel Micro-lattice Structures'. *International Journal of Mechanical Sciences*, 68: 125-139.

Hasan, R., Mines, R., Shen, E., Tsopanos, S., Cantwell, W., Brooks, W., Sutcliffe, C. (2010) 'Comparison of the drop weight impact performance of sandwich panels with aluminium honeycomb and titanium alloy micro-lattice cores'. *Applied Mechanics and Materials*, 24-25: 413-418.

Kalidindi, S.R., Abusafieh, A., El-Danaf, E. (1997) 'Accurate characterization of machine compliance for simple compression testing'. *Experimental Mechanics*, Vol. 37: 210-215.

McKown, S., Cantwell, W.J., Brooks, W.K., Mines, R.A.W., Tsopanos, S., Sutcliffe, C.J. (2007) 'High performance sandwich structures with hierarchical lattice cores'. *Proceedings of the 28th International European SAMPE*, Europe. 396-401.

Mines, R.A.W. (2008) 'On the characterization of foam and micro-lattice materials used in sandwich construction'. *Strain*, 44: 71-83.

Orteu, J.J. (2009) '3-D computer vision in experimental mechanics'. *Optics and Lasers in Engineering*, 47: 282-291.

Polmear, I.J. (2006) *Light alloys: From traditional alloys to nanocrystals*. 4th ed, Elsevier/Butterworth-Heinemann, Amsterdam.

Queheillalt, D.T. and Wadley, H.N.G. (2009) 'Titanium alloy lattice truss structures'. *Material and Design* 30: 1966-1975.

Rehme, O. (2010) *Cellular Design for Laser Freeform Fabrication*. Cuvillier Verlag, Gottingen.

Sergueeva, A.V., Zhou, J., Meacham, B.E., Branagan, D.J. (2009) 'Gage length and sample size effect on measured properties during tensile testing'. *Materials Science & Engineering A*, Vol. 526: 79-83.

Smith, M.I.H. (2012) *The compressive response of novel lattice structures subjected to static and dynamic loading*, PhD Thesis, University of Liverpool, United Kingdom.

Song, B., Dong, S., Zhang, B., Liao, H., Coddet, C. (2012) 'Effects of processing parameters on microstructure and mechanical property of selective laser melted Ti6Al4V'. *Materials & Design*, 35: 120-125.

Thuillier, S., Le Maout, N., Manach, P.Y. (2011) 'Influence of ductile damage on the bending behaviour of aluminium alloy thin sheets'. *Materials and Design*, 32: 2049-2057.

Tsopanos, S., Mines, R.A.W., McKown, S., Shen, Y., Cantwell, W.J., Brooks, W., Sutcliffe, C.J. (2010) 'The influence of processing parameters on the mechanical properties of selectively laser melted stainless steel microlattice structures'. *Journal of Manufacturing Science and Engineering*, 132: 041011-1 - 140111-12.

Turek, D.E. (1993) 'On the tensile testing of high modulus polymers and the compliance correction'. *Polymer Engineering and Science*, Vol. 33: 328-333.

Wattrisse, B., Chrysochoos, A., Muracciole, J.M., Nemoz-Gaillard, M. (2001) 'Analysis of Strain Localization during Tensile Tests by Digital Image Correlation'. *Experimental Mechanics*, 41(1): 29-39.

Wu, X. (2006) 'Review of alloy and process development of TiAl alloys'. *Intermetallics*, 14: 1114-1122.

Zhou, J., Shrotriya, P., Soboyejo, W.O. (2004) 'On the deformation of aluminum lattice block structures: from struts to structures'. *Mechanics of Materials*, 36: 723-737.

LIST OF PUBLICATIONS

JOURNALS

- R.A.W. Mines, S. Tsopanos, Y. Shen, **R. Hasan**, S.T. McKown (2013) 'Drop Weight Impact Behaviour of Sandwich Panels with Metallic Micro-lattice Cores'. *International Journal of Impact Engineering*, 60: 120-132.

- **Rafidah Hasan**, Robert Mines, Peter Fox (2011) 'Characterization of selectively laser melted Ti-6Al-4V micro-lattice struts'. *Procedia Engineering* (ICM11). Vol. 10. Pp. 536-541. Elsevier.

- **Rafidah Hasan**, Robert Mines, Eva Shen, Sozon Tsopanos, Wesley Cantwell (2011) 'Comparison on compressive behaviour of aluminium honeycomb and titanium alloy micro lattice blocks'. *Key Engineering Materials*. Vol. 462-463. Pp. 213-218. Trans Tech Publications, Switzerland.

- **R. Hasan**, R.Mines, E.Shen, S. Tsopanos, W. Cantwell, W. Brooks, C. Sutcliffe (2010) 'Comparison of the drop weight impact performance of sandwich panels with aluminium honeycomb and titanium alloy micro lattice cores'. *Applied Mechanics and Materials*. Vol. 24-25. Pp. 413-418. Trans Tech Publications, Switzerland.

- **R. Hasan**, R.A.W. Mines, S. Tsopanos (2010) 'Determination of elastic modulus value for selectively laser melted titanium alloy micro strut'. *Journal of Mechanical Engineering Technology* (JMET ISSN 2180-1053). Vol. 2 No. 2 (December 2010). Universiti Teknikal Malaysia Melaka, Malaysia.

CONFERENCE PROCEEDINGS

- R. Mines, **R. Hasan** (2012) 'The measurement and interpretation of material and structural behaviours in micro-lattice structures manufactured using selective laser melting'. *15th International Conferences on Experimental Mechanics* (ICEM15). 22-27 July 2012. Porto, Portugal.

- **Rafidah Hasan**, Robert Mines, Peter Fox (2011) 'Characterization of selectively laser melted Ti-6Al-4V micro-lattice struts'. *11th International Conference on the Mechanical Behaviour of Materials* (ICM11). 5-9 June 2011. Como Lake, Italy.

- **R. Hasan**, R.Mines, E.Shen, S. Tsopanos, W. Cantwell, W. Brooks, C. Sutcliffe (2010) 'Comparison of the drop weight impact performance of sandwich panels with aluminium honeycomb and titanium alloy micro lattice cores'. *7th BSSM International Conference on Advances in Experimental Mechanics*. 7-9 September 2010. School of Engineering, University of Liverpool, UK.

- **Rafidah Hasan**, Robert Mines, Eva Shen, Sozon Tsopanos, Wesley Cantwell (2010) 'Comparison on compressive behaviour of aluminium honeycomb and titanium alloy micro lattice blocks'. *Proceedings of The 8th International Conference on Fracture and Strength of Solids* (FEOFS2010). 7-9 June 2010. Kuala Lumpur, Malaysia.

- **Rafidah Hasan**, Robert Mines, Mohd Ruzaimi Mat Rejab, Wesley Cantwell (2010) 'Design of Micro-lattice structures for optimal foreign impact performance in sandwich structures'. *Proceedings of The 1st Annual UK-Malaysia-Ireland Engineering Science Conference* (UMIES2010). Pp. 69. 23-25 June 2010. Queen's University Belfast, Ireland.

Appendix 3A

An example of a material file data [Louvis, E. (n.d.) *Material File Definition*, University of Liverpool].

MATERIAL FILE DEFINITION

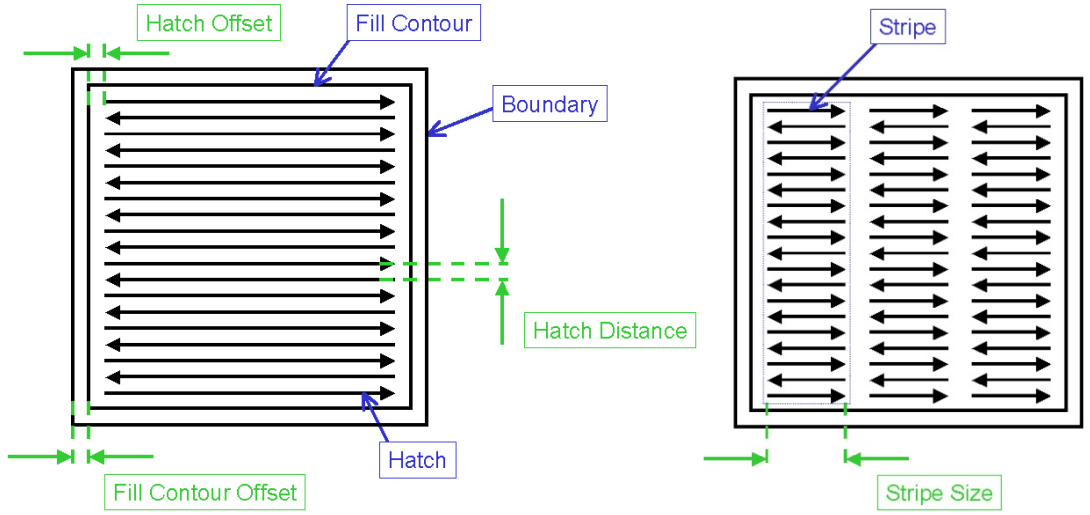


```
[EXPOSURE]
exposure_50=50µLAYER
```

Definition of corresponding section for a slice thickness covered by this material file

```
[50µLAYER]
expoBoundary=200
expoHatch=150
expoBoundarySolid=200
expoFillContourSolid=200
expoHatchSolid=150
expoInnerSupport=300
expoPointSequence=300
expoSkinHatch=200
expoSupport=300
```

Example of settings used for 50 µm slices/layers
Exposure time for boundary on powder (in µs)
Exposure time for hatch lines on powder (in µs)
Exposure time for outer contour (in µs)
Exposure time for fill contours (in µs)
Exposure time for hatch lines (in µs)
Exposure time for built-in supports (in µs)
Exposure time for point sequences (in µs)
Exposure time for skin hatches (in µs)
Exposure time for externally generated supports

```
pdistBoundary=30
pdistHatch=30
pdistBoundarySolid=30
pdistFillContourSolid=30
pdistHatchSolid=30
pdistInnerSupport=30
pdistPointSequence=30
pdistSkinHatch=30
pdistSupport=30
```

Point distances for each geometry referred to as in the exposure time section (in µm)

laserPowerBoundary=4000 laserPowerBoundarySolid=4000 laserPowerFillContourSolid=4000 laserPowerHatch=4000 laserPowerHatchSolid=4000 laserPowerInnerSupport=2500 laserPowerPointSequence=2500 laserPowerSkinHatch=4000 laserPowerSupport=2500	Control current for laser power for each geometry referred to as in the exposure time section (in mA)
lensPosBoundary=1550 lensPosBoundarySolid=1550 lensPosFillContourSolid=1550 lensPosHatch=1613 lensPosHatchSolid=1613 lensPosInnerSupport=1533 lensPosPointSequence=1533 lensPosSkinHatch=1550 lensPosSupport=1533	Lens position for each geometry referred to as in the exposure time section (in 1/100 mm)
numberOfExposuresBoundarySolid=1 numberOfExposuresFillContourSolid=1 numberOfExposuresHatchSolid=1 numberOfExposuresInnerSupport=1 numberOfExposuresPointSequence=1 numberOfExposuresSkinHatch=1 numberOfExposuresSupport=1	Number of exposures for each geometry referred to as in the exposure time section
laserFrequenceBoundarySolid=0 laserFrequenceFillContourSolid=0 laserFrequenceHatchSolid=0 laserFrequenceInnerSupport=0 laserFrequencePointSequence=0 laserFrequenceSkinHatch=0 laserFrequenceSupport=0	not active
[HATCH]	
spotSize=0.199	Beam effected zone / thinnest wall (in mm)
default_withBeamCompensation=1	Compensate for width of this beam effected zone (on/off)
hatchSortBlockSize=800	Number of hatches sorted in one block – the more the longer the sort process
minHatchLength=0.100000	Shortest hatch length to be processed

default_hatch_sortType=1	Hatch strategy: 0 = unsorted, 1 = rows first, 2 = columns first, 3 = shortest distance, 4 = checker board
default_hatch_shrinkFactorSolid=0.113	Shrinkage of layers during solidification to be compensated for
default_hatch_typeSolid=1	Type of hatches: 0 = off, 1 = x/y alternating between layers, 2 = x and y on each layer
default_hatch_contour_fill_countSolid=0	Number of contour following hatch lines
default_hatch_contour_fill_offsetSolid=0.08	Offset of a fill contour from outer contour (mm)
default_hatch_offsetSolid=0.08	Offset of hatches from contours (in mm)
default_hatch_xDistanceSolid=0.05	Distance between hatch lines in x direction (mm)
default_hatch_yDistanceSolid=0.05	Distance between hatch lines in y direction (mm)
default_hatch_withStripesSolid=0	Hatch in stripes (on/off)
default_hatch_stripeSizeSolid=10.000000	Width of the stripes (in mm)
hatchSortBlockCheckerBoardSteps=10.000000	Number of lines in one square
hatchStripesRightLeft=0 hatchStripesUpDown=0	Unidirectional or meandering horizontal and vertical hatch lines (on/off)
default_hatch_weakSizeLimit=0.05	Overhang above which hatch on powder parameters are used
default_hatch_shrinkFactor=0.113 default_hatch_type=2 default_hatch_contour_fill_count=0 default_hatch_contour_fill_offset=0.08 default_hatch_offset=0.08 default_hatch_xDistance=0.05 default_hatch_yDistance=0.05 default_hatch_withStripes=0 default_hatch_stripeSize=4.000000	Parameters for hatches on powder, same effect of individual lines as for solid hatches
default_skinHatchLimit=25.00000	Width above which skin hatch will be considered
default_skin_hatch_type=0 default_skin_hatch_offset=0.030000 default_skin_hatch_xDistance=0.05 default_skin_hatch_yDistance=0.05 default_skin_hatch_withStripes=0 default_skin_hatch_stripeSize=3.000000	Parameters for skin hatches on surfaces, same effect of individual lines as for regular hatches
	Parameters for built-in shell feature
default_wallHatched=1	Hatch shell between boundary lines (on/off)
default_hatch_innerSupport=1	Pin-supports inside hollow structure (on/off)
default_hatch_wallThickness=1.000000	Wall thickness (in mm)
default_hatch_innerSupport_xDistance=2.0000	x-distance between support pins (in mm)
default_hatch_innerSupport_yDistance=2.0000	y-distance between support pins (in mm)

[PARAMETER]
debugWarmUp=0
longDistance=0.000000
warmUpDistance=0.000000
warmUpTimeFactor=1.000000

[SUPPORTER]
baseGridHeightInMM=2.000000
bridgeHeight=1
connectSupportLines=0
crossBitSize=1.00000
debugSuppo=0
defaultCX=1.30000
defaultCY=1.30000
defaultCutSuppoContourOffset=0.300000
defaultCutSuppoHatchMinLength=0.300000
defaultFloor=15
defaultGeoType=1
defaultGridOffset=-0.200000
defaultMinSliceDistance=0.1
defaultPinSize=0.200000
defaultSVH=256
defaultSingePinSize=0.300000
defaultSinglePinSize=0.300000
defaultSlimProfilesToBeBridged=3.000000
defaultSocket=25
defaultTipSize=0.200000
defaultTolerance=0.000000
evenNumberOfCells=1
extraBridgePass=1
maxCubeSize=3.000000
maxVoxelSizeAtPart=6.00000
meander=1
minButterfly=12
minCubeToPart=1
minSVH=3
minTipPinSize=0.0500000
sortSupport=2
supportPerforation=0
useSplit=0
verbose=1
withBaseGrid=0

General parameters – should only be modified if instructed to do so

Appendix 4A

An example of input file for quasi-static finite element model of a BCC Unit Cell (Model A).

```
*Heading
** Job name: BCC-2-5mm-Rafidah Model name: BCC-L-25-D-02-8-4
** Generated by: Abaqus/CAE 6.10-2
*Preprint, echo=NO, model=NO, history=NO, contact=NO
*Part, name=BCC-2-5mm-DIA-195microns
*End Part
**
*Part, name="Rigid Plate"
*End Part
**
**
** ASSEMBLY
**
*Assembly, name=Assembly
**
*Instance, name="Rigid Plate-1", part="Rigid Plate"
 -4.30877610035907e-07,           0.,           0.
 -4.30877610035907e-07,           0.,           0.,
0.99999956912239,           0.,           0.,          90.
*Node
      1,           2.,           2.,           0.
      2,          -2.,           2.,           0.
      3,          -2.,          -2.,           0.
      4,           2.,          -2.,           0.
      5,   1.60000002,           2.,           0.
      6,   1.20000005,           2.,           0.
      7,  0.800000012,           2.,           0.
      8,  0.400000006,           2.,           0.
      9,           0.,           2.,           0.
----------------------------------
    121,  0.398692071, 0.0865500048,           0.
    122, -0.182551235, -0.252560765,           0.
    123,  0.420116991, -0.526383221,           0.
    124,  0.141134858, -0.280317783,           0.
    125,   1.60483313,  -1.60733461,           0.
    126, -0.0292776842, 0.0243827272,           0.
    127, -0.0602132119, -0.441991061,           0.
*Element, type=R3D3
1, 124, 127, 117
2, 123,  99, 120
*Element, type=R3D4
  3,  96,  82,  78, 111
  4,  31, 125,  41,  30
  5,  34,  35,  58,  42
  6,  59,  28,  29,  60
  7,  44,  17,  18,  51
  8,  47,  46,  68,  69
  9,  17,  44,  46,  16
 10,  16,  46,  47,  15
 ---------------------------
100, 126, 113, 118, 122
```

Parts of model

(1) BCC unit cell

(2) Rigid plate

Element type for rigid plate

```
101, 124, 116, 121, 126
102, 110, 107, 114, 119
103, 111, 102, 115, 121
104, 124, 126, 122, 127
105, 113, 126, 119, 114
106, 124, 117, 123, 116
107, 127, 108, 104, 117
*Node
    128,           0.,           0.,           0.
*Nset, nset="Rigid Plate-1-RefPt_", internal
128,
*Elset, elset="Rigid Plate-1", generate
   1,  107,    1
*End Instance
**
*Instance, name=BCC-Unit-Cell-131108-1, part=BCC-2-5mm-DIA-
195microns
       -1.25,           0.,        -1.25
*Node
      1, 0.0731478557,  -1.17685211,   2.30743957
      2,  0.112952076,  -1.13704777,   2.38704801
      3,   1.14660656, -0.103393391,   1.35339344
      4,   1.10680246, -0.143197581,     1.273785
      5, 0.0333436951,  -1.09724367,   2.34724379
      6,   1.06699824, -0.0635891408,   1.31358922
      7,  0.192560583,  -1.17685211,   2.42685223
      8,  0.119412698,  -1.24999988,          2.5
      9,           0.,  -1.24999988,          2.5
     10,  0.152756304,  -1.09724367,   2.46665621
----------------------------------------
   8067,     1.425143,  -2.36789393,   1.16093087
   8068,   2.37969327,  -1.32647538,  0.034566585
   8069,    1.2797873,  -2.42830396,   1.13447261
   8070,   1.36552739,  -2.42830396,    1.2202127
   8071,    1.2797873,  -2.38447237,   1.17830396
   8072,   1.36552739,  -2.47021246,   1.17830396
   8073,   1.32169604,  -2.38447237,    1.2202127
   8074,   1.32169604,  -2.47021246,   1.13447261
*Element, type=C3D8R
  1, 2649,  217, 2614, 6316,  181,    1,  216, 2579
  2, 6316, 2614, 2615, 6315, 2579,  216,  215, 2580
  3, 6315, 2615, 2616, 6314, 2580,  215,  214, 2581
  4, 6314, 2616, 2617, 6313, 2581,  214,  213, 2582
  5, 6313, 2617, 2618, 6312, 2582,  213,  212, 2583
  6, 6312, 2618, 2619, 6311, 2583,  212,  211, 2584
  7, 6311, 2619, 2620, 6310, 2584,  211,  210, 2585
  8, 6310, 2620, 2621, 6309, 2585,  210,  209, 2586
----------------------------------------
5754, 6291, 2574, 6296, 8073, 2527,  177, 2526, 6139
5755, 6298, 2577, 6294, 8074, 2578,  180, 2575, 6297
5756, 6294, 2570, 6287, 8074, 2575,  116, 2278, 6297
5757, 6287, 2571, 6298, 8074, 2278,  161, 2578, 6297
5758, 6033, 2360, 6287, 8074, 2420,  165, 2570, 6294
5759, 6298, 2419, 6033, 8074, 2577,  176, 2420, 6294
5760, 6298, 2571, 6287, 8074, 2419,  168, 2360, 6033
*Nset, nset=_PickedSet2, internal, generate
    1,  8074,     1
*Elset, elset=_PickedSet2, internal, generate
    1,  5760,     1
** Section: Section-1
*Solid Section, elset=_PickedSet2, material=STEEL
```

Element type for BCC unit cell

Total number of elements

```
1.,
*End Instance
**
*Instance, name="Rigid Plate-2", part="Rigid Plate"
 -4.30877610035907e-07,          -2.5,           0.
 -4.30877610035907e-07,          -2.5,           0.,
0.99999956912239,          -2.5,           0.,          90.
*Node
      1,           2.,           2.,           0.
      2,          -2.,           2.,           0.
      3,          -2.,          -2.,           0.
      4,           2.,          -2.,           0.
      5,   1.60000002,           2.,           0.
      6,   1.20000005,           2.,           0.
      7,  0.800000012,           2.,           0.
----------------------------------
    122, -0.182551235, -0.252560765,           0.
    123,  0.420116991, -0.526383221,           0.
    124,  0.141134858, -0.280317783,           0.
    125,   1.60483313,  -1.60733461,           0.
    126, -0.0292776842, 0.0243827272,           0.
    127, -0.0602132119, -0.441991061,           0.
*Element, type=R3D3
1, 124, 127, 117
2, 123,  99, 120
*Element, type=R3D4
  3,  96,  82,  78, 111
  4,  31, 125,  41,  30
  5,  34,  35,  58,  42
  6,  59,  28,  29,  60
  7,  44,  17,  18,  51
  8,  47,  46,  68,  69
------------------------------
104, 124, 126, 122, 127
105, 113, 126, 119, 114
106, 124, 117, 123, 116
107, 127, 108, 104, 117
*Node
    128,           0.,           0.,           0.
*Nset, nset="Rigid Plate-2-RefPt_", internal
128,
*Elset, elset="Rigid Plate-2", generate
   1,  107,    1
*End Instance
**
*Node
      1,  -1.25999999,        -1.25,  -1.25999999
*Node
      2,  -1.25999999,        -1.25,   1.25999999
*Node
      3,   1.25999999,        -1.25,  -1.25999999
*Node
      4,   1.25999999,        -1.25,   1.25999999
*Nset, nset=_PickedSet227, internal, instance="Rigid Plate-1"
 128,
*Nset, nset=RP-set, instance="Rigid Plate-1"
 128,
*Nset, nset=_PickedSet361, internal, instance="Rigid Plate-2"
 128,
*Nset, nset=PR-set-bottom, instance="Rigid Plate-2"
 128,
```

```
*Nset, nset=_PickedSet380, internal
 1,
*Nset, nset=_PickedSet382, internal
 1,
*Nset, nset=_PickedSet384, internal
 2,
*Nset, nset=_PickedSet386, internal
 2,
*Nset, nset=_PickedSet388, internal
 3,
*Nset, nset=_PickedSet390, internal
 3,
*Nset, nset=_PickedSet392, internal
 4,
*Nset, nset=_PickedSet394, internal
 4,
*Nset, nset=_PickedSet396, internal, instance="Rigid Plate-1"
 128,
*Nset, nset=_PickedSet398, internal
 1,
*Nset, nset=_PickedSet400, internal
 1,
*Nset, nset=_PickedSet402, internal
 2,
*Nset, nset=_PickedSet404, internal
 2,
*Nset, nset=_PickedSet406, internal
 3,
*Nset, nset=_PickedSet408, internal
 3,
*Nset, nset=_PickedSet410, internal
 4,
*Nset, nset=_PickedSet412, internal
 4,
*Nset, nset=_PickedSet422, internal, instance=BCC-Unit-Cell-131108-1
    1,    2,    3,    4,    5,    6,    7,    8,    9,   10,   11,
12,   13,   14,   15,   16
------------------------------
   17,   18,   19,   20,   21,   22,   23,   24,   25,   26,   27,
 7144, 7145, 7146, 7147, 7148, 7149, 7150, 7151, 7152, 7153, 7154,
7155, 7156, 7157, 7158, 7159
 7160, 7161, 7162, 7163, 7164, 7165, 7166, 7167, 7168, 7169, 7170,
7171, 7172, 7173, 7174, 7175
 7176, 7177, 7178, 7179, 7180, 7181, 7182, 7183, 7184, 7185, 7186
*Nset, nset=_PickedSet422, internal, generate
 1,  4,  1
*Elset, elset=_PickedSet422, internal, instance=BCC-Unit-Cell-
131108-1
    1,    2,    3,    4,    5,    6,    7,    8,    9,   10,   11,
12,   13,   14,   15,   16
------------------------------------
2865, 2866, 2867, 2868, 2869, 2870, 2871, 2872, 2873, 2874, 2875,
2876, 2877, 2878, 2879, 2880
 2991, 2992, 2997, 2998, 3000, 3009, 3010, 3012, 3561, 3564, 3711,
3714, 3717, 3718, 3720, 3729
 3730, 3732, 4281, 4284, 4431, 4434, 4437, 4438, 4440, 4449, 4450,
4452, 5001, 5004, 5151, 5154
 5157, 5158, 5160, 5169, 5170, 5172, 5721, 5724
*Nset, nset=_PickedSet423, internal, instance=BCC-Unit-Cell-131108-1
    8,    9,   12,   14,   36,   39,   41,   42,   60,   63,   65,
66,   84,   87,   89,   90
```

```
   99,  100,  101,  102,  103,  104,  105,  106,  107,  108,  109,
110,  111,  112,  113,  114
---------------------------------------
8032, 8033, 8034, 8035, 8036, 8037, 8038, 8039, 8040, 8041, 8042,
8043, 8044, 8045, 8046, 8047
 8048, 8049, 8050, 8051, 8052, 8053, 8054, 8055, 8056, 8057, 8058,
8059, 8060, 8061, 8062, 8063
 8064, 8065, 8066, 8067, 8068, 8069, 8070, 8071, 8072, 8073, 8074
*Elset, elset=_PickedSet423, internal, instance=BCC-Unit-Cell-
131108-1
  111,  112,  117,  118,  120,  129,  130,  132,  681,  684,  831,
834,  837,  838,  840,  849
  850,  852, 1401, 1404, 1551, 1554, 1557, 1558, 1560, 1569, 1570,
1572, 2121, 2124, 2271, 2274
-----------------------------------------
 5721, 5722, 5723, 5724, 5725, 5726, 5727, 5728, 5729, 5730, 5731,
5732, 5733, 5734, 5735, 5736
 5737, 5738, 5739, 5740, 5741, 5742, 5743, 5744, 5745, 5746, 5747,
5748, 5749, 5750, 5751, 5752
 5753, 5754, 5755, 5756, 5757, 5758, 5759, 5760
*Nset, nset=_PickedSet444, internal, instance=BCC-Unit-Cell-131108-1
  116,  118,  120,  122,  141,  142,  161,  162,  180, 1673, 1682,
1687, 1688, 1691, 1981, 1984
 1985, 1988, 2278, 2281, 2282, 2285, 2575, 2576, 2578, 4902, 4907,
5366, 5371, 5830, 5835, 6293
 6297,
*Elset, elset=_PickedSet444, internal, instance=BCC-Unit-Cell-
131108-1
 3583, 3584, 3585, 3595, 3596, 3597, 4303, 4304, 4305, 4315, 4316,
4317, 5023, 5024, 5025, 5035
 5036, 5037, 5743, 5744, 5745, 5755, 5756, 5757
*Elset, elset=__PickedSurf223_SPOS, internal, instance="Rigid Plate-
1", generate
   1,  107,    1
*Surface, type=ELEMENT, name=_PickedSurf223, internal
__PickedSurf223_SPOS, SPOS
*Elset, elset=__PickedSurf363_SNEG, internal, instance="Rigid Plate-
2", generate
   1,  107,    1
*Surface, type=ELEMENT, name=_PickedSurf363, internal
__PickedSurf363_SNEG, SNEG
*Elset, elset=__PickedSurf379_S3, internal, instance=BCC-Unit-Cell-
131108-1
 2122, 2158, 2160, 5164, 5174, 5177
*Elset, elset=__PickedSurf379_S4, internal, instance=BCC-Unit-Cell-
131108-1
 2121, 2124, 2159, 5161, 5165, 5166, 5175
*Elset, elset=__PickedSurf379_S2, internal, instance=BCC-Unit-Cell-
131108-1
 5178,
*Surface, type=ELEMENT, name=_PickedSurf379, internal
__PickedSurf379_S3, S3
__PickedSurf379_S4, S4
__PickedSurf379_S2, S2
*Elset, elset=__PickedSurf381_S4, internal, instance=BCC-Unit-Cell-
131108-1
 1561, 1565, 1566, 1575, 5151, 5154
*Elset, elset=__PickedSurf381_S3, internal, instance=BCC-Unit-Cell-
131108-1
 1564, 1574, 1577, 5152
```

```
*Elset, elset=__PickedSurf381_S2, internal, instance=BCC-Unit-Cell-
131108-1
 1578, 5755, 5756, 5757
*Surface, type=ELEMENT, name=_PickedSurf381, internal
__PickedSurf381_S4, S4
__PickedSurf381_S3, S3
__PickedSurf381_S2, S2
*Elset, elset=__PickedSurf383_S4, internal, instance=BCC-Unit-Cell-
131108-1
  841,  845,  846,  855, 3003, 3006
*Elset, elset=__PickedSurf383_S3, internal, instance=BCC-Unit-Cell-
131108-1
  844,  854,  857, 3004
*Elset, elset=__PickedSurf383_S2, internal, instance=BCC-Unit-Cell-
131108-1
  858, 3595, 3596, 3597
*Surface, type=ELEMENT, name=_PickedSurf383, internal
__PickedSurf383_S4, S4
__PickedSurf383_S3, S3
__PickedSurf383_S2, S2
*Elset, elset=__PickedSurf385_S3, internal, instance=BCC-Unit-Cell-
131108-1
 1402, 1438, 1440, 3145, 3146, 3147, 3148, 3149, 3150, 3151, 3152,
3153, 3154, 3155, 3156, 3157
 3158, 3159, 3160, 3161, 3162, 3199, 3200, 3201, 3202, 3203, 3204,
3205, 3206, 3207, 3208, 3209
 3210, 3211, 3212, 3213, 3214, 3215, 3216, 3217, 3218, 3219, 3220,
3221, 3222, 3223, 3224, 3225
 3226, 3227, 3228, 3229, 3230, 3231, 3232, 3233, 3234
*Elset, elset=__PickedSurf385_S4, internal, instance=BCC-Unit-Cell-
131108-1
 1401, 1404, 1439, 3163, 3164, 3165, 3166, 3167, 3168, 3169, 3170,
3171, 3172, 3173, 3174, 3175
 3176, 3177, 3178, 3179, 3180
*Elset, elset=__PickedSurf385_S2, internal, instance=BCC-Unit-Cell-
131108-1, generate
 4297,  4299,     1
*Surface, type=ELEMENT, name=_PickedSurf385, internal
__PickedSurf385_S3, S3
__PickedSurf385_S4, S4
__PickedSurf385_S2, S2
*Elset, elset=__PickedSurf387_S3, internal, instance=BCC-Unit-Cell-
131108-1
 2842, 2878, 2880, 4454, 4457
*Elset, elset=__PickedSurf387_S4, internal, instance=BCC-Unit-Cell-
131108-1
 2841, 2844, 2879, 4455
*Elset, elset=__PickedSurf387_S2, internal, instance=BCC-Unit-Cell-
131108-1
 4458, 5737, 5738, 5739
*Surface, type=ELEMENT, name=_PickedSurf387, internal
__PickedSurf387_S3, S3
__PickedSurf387_S4, S4
__PickedSurf387_S2, S2
*Elset, elset=__PickedSurf389_S4, internal, instance=BCC-Unit-Cell-
131108-1
 2295, 2867, 4431, 4434
*Elset, elset=__PickedSurf389_S3, internal, instance=BCC-Unit-Cell-
131108-1
 2294, 2297, 2866, 2868, 4432
```

```
*Elset, elset=__PickedSurf389_S2, internal, instance=BCC-Unit-Cell-
131108-1
 2298, 5035, 5036, 5037
*Surface, type=ELEMENT, name=_PickedSurf389, internal
__PickedSurf389_S4, S4
__PickedSurf389_S3, S3
__PickedSurf389_S2, S2
*Elset, elset=__PickedSurf391_S3, internal, instance=BCC-Unit-Cell-
131108-1
  718,  720, 3734, 3737
*Elset, elset=__PickedSurf391_S4, internal, instance=BCC-Unit-Cell-
131108-1
  719, 3735
*Elset, elset=__PickedSurf391_S2, internal, instance=BCC-Unit-Cell-
131108-1
  115,  116,  117,  118, 3738, 5017, 5018, 5019
*Surface, type=ELEMENT, name=_PickedSurf391, internal
__PickedSurf391_S3, S3
__PickedSurf391_S4, S4
__PickedSurf391_S2, S2
*Elset, elset=__PickedSurf393_S4, internal, instance=BCC-Unit-Cell-
131108-1
  265,  266,  267,  268,  269,  270,  271,  272,  273,  274,  275,
276,  277,  278,  279,  280
  281,  282,  319,  320,  321,  322,  323,  324,  325,  326,  327,
328,  329,  330,  331,  332
  333,  334,  335,  336,  337,  338,  339,  340,  341,  342,  343,
344,  345,  346,  347,  348
  349,  350,  351,  352,  353,  354, 2854, 2856, 3711, 3714
*Elset, elset=__PickedSurf393_S3, internal, instance=BCC-Unit-Cell-
131108-1
  283,  284,  285,  286,  287,  288,  289,  290,  291,  292,  293,
294,  295,  296,  297,  298
  299,  300, 2855, 3712
*Elset, elset=__PickedSurf393_S2, internal, instance=BCC-Unit-Cell-
131108-1, generate
 4315,  4317,     1
*Surface, type=ELEMENT, name=_PickedSurf393, internal
__PickedSurf393_S4, S4
__PickedSurf393_S3, S3
__PickedSurf393_S2, S2
*Elset, elset=__PickedSurf435_S3, internal, instance=BCC-Unit-Cell-
131108-1
  706,  708,  718,  720, 1426, 1428, 1438, 1440, 2146, 2148, 2158,
2160, 2866, 2868, 2878, 2880
*Elset, elset=__PickedSurf435_S4, internal, instance=BCC-Unit-Cell-
131108-1
  707,  719, 1427, 1439, 2147, 2159, 2867, 2879
*Surface, type=ELEMENT, name=_PickedSurf435, internal
__PickedSurf435_S3, S3
__PickedSurf435_S4, S4
*Elset, elset=__PickedSurf436_S3, internal, instance=BCC-Unit-Cell-
131108-1
 2272, 2283, 2286, 4455, 4458, 5002
*Elset, elset=__PickedSurf436_S4, internal, instance=BCC-Unit-Cell-
131108-1
 2271, 2274, 2284, 4456, 5001, 5004
*Surface, type=ELEMENT, name=_PickedSurf436, internal
__PickedSurf436_S3, S3
__PickedSurf436_S4, S4
```

```
*Elset, elset=__PickedSurf437_S4, internal, instance=BCC-Unit-Cell-
131108-1
 2296, 2841, 2844, 4431, 4434, 4444
*Elset, elset=__PickedSurf437_S3, internal, instance=BCC-Unit-Cell-
131108-1
 2295, 2298, 2842, 4432, 4443, 4446
*Surface, type=ELEMENT, name=_PickedSurf437, internal
__PickedSurf437_S4, S4
__PickedSurf437_S3, S3
*Elset, elset=__PickedSurf438_S3, internal, instance=BCC-Unit-Cell-
131108-1
  112,  114,  124, 3735, 3738, 4282
*Elset, elset=__PickedSurf438_S4, internal, instance=BCC-Unit-Cell-
131108-1
  111,  123,  126, 3736, 4281, 4284
*Surface, type=ELEMENT, name=_PickedSurf438, internal
__PickedSurf438_S3, S3
__PickedSurf438_S4, S4
*Elset, elset=__PickedSurf439_S4, internal, instance=BCC-Unit-Cell-
131108-1
  135,  138,  682, 3711, 3714, 3724
*Elset, elset=__PickedSurf439_S3, internal, instance=BCC-Unit-Cell-
131108-1
  136,  681,  684, 3712, 3723, 3726
*Surface, type=ELEMENT, name=_PickedSurf439, internal
__PickedSurf439_S4, S4
__PickedSurf439_S3, S3
*Elset, elset=__PickedSurf440_S3, internal, instance=BCC-Unit-Cell-
131108-1
 1552, 1563, 1566, 5175, 5178, 5722
*Elset, elset=__PickedSurf440_S4, internal, instance=BCC-Unit-Cell-
131108-1
 1551, 1554, 1564, 5176, 5721, 5724
*Surface, type=ELEMENT, name=_PickedSurf440, internal
__PickedSurf440_S3, S3
__PickedSurf440_S4, S4
*Elset, elset=__PickedSurf441_S4, internal, instance=BCC-Unit-Cell-
131108-1
 1576, 2121, 2124, 5151, 5154, 5164
*Elset, elset=__PickedSurf441_S3, internal, instance=BCC-Unit-Cell-
131108-1
 1575, 1578, 2122, 5152, 5163, 5166
*Surface, type=ELEMENT, name=_PickedSurf441, internal
__PickedSurf441_S4, S4
__PickedSurf441_S3, S3
*Elset, elset=__PickedSurf442_S4, internal, instance=BCC-Unit-Cell-
131108-1
  831,  834,  844, 3015, 3018, 3562
*Elset, elset=__PickedSurf442_S3, internal, instance=BCC-Unit-Cell-
131108-1
  832,  843,  846, 3016, 3561, 3564
*Surface, type=ELEMENT, name=_PickedSurf442, internal
__PickedSurf442_S4, S4
__PickedSurf442_S3, S3
*Elset, elset=__PickedSurf443_S4, internal, instance=BCC-Unit-Cell-
131108-1
  856, 1401, 1404, 2991, 3003, 3006
*Elset, elset=__PickedSurf443_S3, internal, instance=BCC-Unit-Cell-
131108-1
  855,  858, 1402, 2992, 2994, 3004
*Surface, type=ELEMENT, name=_PickedSurf443, internal
```

```
__PickedSurf443_S4, S4
__PickedSurf443_S3, S3
*Elset, elset=__PickedSurf447_S3, internal, instance=BCC-Unit-Cell-
131108-1
  117,  129,  699,  702,  711,  714,  836,  839,  840,  848,  851,
1021, 1022, 1023, 1024, 1025
 1026, 1027, 1028, 1029, 1030, 1031, 1032, 1033, 1034, 1035, 1036,
1037, 1038, 1237, 1238, 1239
 ------------------------
 3198, 3397, 3398, 3399, 3400, 3401, 3402, 3403, 3404, 3405, 3406,
3407, 3408, 3409, 3410, 3411
 3412, 3413, 3414, 3577, 3580, 3582, 3591, 3716, 3719, 3720, 3728,
3731, 4298, 4300, 4302, 4311
 4436, 4439, 4440, 4448, 4451, 5018, 5020, 5022, 5031, 5156, 5159,
5160, 5168, 5171, 5738, 5740
 5742, 5751
*Elset, elset=__PickedSurf447_S4, internal, instance=BCC-Unit-Cell-
131108-1
  116,  119,  120,  128,  131,  697,  701,  709,  713,  837,  849,
967,  968,  969,  970,  971
  972,  973,  974,  975,  976,  977,  978,  979,  980,  981,  982,
983,  984, 1039, 1040, 1041
----------------------------------------
3357, 3358, 3359, 3360, 3415, 3416, 3417, 3418, 3419, 3420, 3421,
3422, 3423, 3424, 3425, 3426
 3427, 3428, 3429, 3430, 3431, 3432, 3433, 3434, 3435, 3436, 3437,
3438, 3439, 3440, 3441, 3442
 3443, 3444, 3445, 3446, 3447, 3448, 3449, 3450, 3579, 3590, 3592,
3594, 3717, 3729, 4299, 4310
 4312, 4314, 4437, 4449, 5019, 5030, 5032, 5034, 5157, 5169, 5739,
5749, 5752, 5754
*Elset, elset=__PickedSurf447_S2, internal, instance=BCC-Unit-Cell-
131108-1
  132,  247,  248,  249,  250,  251,  252,  253,  254,  255,  256,
257,  258,  259,  260,  261
  262,  263,  264,  265,  266,  267,  268,  269,  270,  271,  272,
273,  274,  275,  276,  277
  278,  279,  280,  281,  282,  283,  284,  285,  286,  287,  288,
------------------------------------
 5527, 5528, 5529, 5530, 5531, 5532, 5533, 5534, 5535, 5536, 5537,
5538, 5539, 5540, 5541, 5542
 5543, 5544, 5545, 5546, 5547, 5548, 5549, 5550, 5551, 5552, 5553,
5554, 5555, 5556, 5557, 5558
 5559, 5560, 5561, 5562, 5563, 5564, 5565, 5566, 5567, 5568, 5569,
5570, 5571, 5572, 5573, 5574
*Surface, type=ELEMENT, name=_PickedSurf447, internal
__PickedSurf447_S3, S3
__PickedSurf447_S4, S4
__PickedSurf447_S2, S2
*Surface, type=NODE, name=_PickedSet423_CNS_, internal
_PickedSet423, 1.
*Surface, type=NODE, name=_PickedSet422_CNS_, internal
_PickedSet422, 1.
*Rigid Body, ref node="Rigid Plate-1"."Rigid Plate-1-RefPt_",
elset="Rigid Plate-1"."Rigid Plate-1"
*Rigid Body, ref node="Rigid Plate-2"."Rigid Plate-2-RefPt_",
elset="Rigid Plate-2"."Rigid Plate-2"
** Constraint: C-top
*Coupling, constraint name=C-top, ref node=_PickedSet396,
surface=_PickedSurf435
*Kinematic
```

```
** Constraint: C1-X
*Coupling, constraint name=C1-X, ref node=_PickedSet398,
surface=_PickedSurf436
*Kinematic
** Constraint: C1-Z
*Coupling, constraint name=C1-Z, ref node=_PickedSet400,
surface=_PickedSurf437
*Kinematic
** Constraint: C2-X
*Coupling, constraint name=C2-X, ref node=_PickedSet402,
surface=_PickedSurf438
*Kinematic
** Constraint: C2-Z
*Coupling, constraint name=C2-Z, ref node=_PickedSet404,
surface=_PickedSurf439
*Kinematic
** Constraint: C3-X
*Coupling, constraint name=C3-X, ref node=_PickedSet406,
surface=_PickedSurf440
*Kinematic
** Constraint: C3-Z
*Coupling, constraint name=C3-Z, ref node=_PickedSet408,
surface=_PickedSurf441
*Kinematic
** Constraint: C4-X
*Coupling, constraint name=C4-X, ref node=_PickedSet410,
surface=_PickedSurf442
*Kinematic
** Constraint: C4-Z
*Coupling, constraint name=C4-Z, ref node=_PickedSet412,
surface=_PickedSurf443
*Kinematic
*End Assembly
**
** MATERIALS
**
*Material, name=STEEL
*Density
 7.8e-09,
*Elastic
140000., 0.3
*Plastic
    144.,      0.
 183.773, 0.0015
 195.401,  0.003
 203.721, 0.0045
 210.429,  0.006
 216.146, 0.0075
 221.181,  0.009
 224.249,   0.01
 247.561,   0.02
 269.014,   0.03
  286.31,   0.04
 301.052,   0.05
 314.035,   0.06
 325.716,   0.07
 336.387,   0.08
 346.247,   0.09
 355.439,    0.1
 364.069,   0.11
 372.217,   0.12
```

Material properties

Elasticity

Plasticity

```
 379.948,   0.13
 387.313,   0.14
 394.354,   0.15
 401.104,   0.16
 407.594,   0.17
 413.847,   0.18
 419.885,   0.19
 425.727,    0.2
**
** INTERACTION PROPERTIES
**
*Surface Interaction, name=IntProp-1
1.,
*Friction
0.,
*Surface Behavior, penalty
**
** INTERACTIONS
**
** Interaction: Contact-bottom-plate
*Contact Pair, interaction=IntProp-1
_PickedSet423_CNS_, _PickedSurf363
** Interaction: Contact-top-plate
*Contact Pair, interaction=IntProp-1
_PickedSet422_CNS_, _PickedSurf223
** Interaction: Contact-unit-cell
*Contact Pair, interaction=IntProp-1
_PickedSurf447,
** ----------------------------------------------------------------
**
** STEP: Step-1
**
*Step, name=Step-1, nlgeom=YES, inc=20000
*Static
0.0005, 1., 1e-08, 0.005
**
** BOUNDARY CONDITIONS
**
** Name: Fix-bottom-plate Type: Displacement/Rotation
*Boundary
_PickedSet361, 1, 1
_PickedSet361, 2, 2
_PickedSet361, 3, 3
_PickedSet361, 4, 4
_PickedSet361, 5, 5
_PickedSet361, 6, 6
** Name: Fix-bottom-unit-cell Type: Displacement/Rotation
*Boundary
_PickedSet444, 1, 1
_PickedSet444, 2, 2
_PickedSet444, 3, 3
_PickedSet444, 4, 4
_PickedSet444, 5, 5
_PickedSet444, 6, 6
** Name: Move-top-plate Type: Displacement/Rotation
*Boundary
_PickedSet227, 1, 1
_PickedSet227, 2, 2, -2.2
_PickedSet227, 3, 3
_PickedSet227, 4, 4
_PickedSet227, 5, 5
```

Modelling Interaction

Simulation analysis procedure for static, non-linear analysis

Boundary conditions

The value of -2.2 indicates that the top plate is moved for 2.2mm downward the z-direction. In other lines, no value in z-direction indicates no movement.

```
_PickedSet227, 6, 6
**
** OUTPUT REQUESTS
**
*Restart, write, number interval=50, time marks=NO
**
** FIELD OUTPUT: F-Output-1
**
*Output, field, variable=PRESELECT, number interval=20, time
marks=NO
**
** HISTORY OUTPUT: H-Output-3
**
*Output, history
*Energy Output
ALLIE, ALLWK
**
** HISTORY OUTPUT: H-Output-2
**
*Node Output, nset=RP-set
RF2, U2
*End Step
```

Modelling data output